Enabling 3D magnetic circuits by the additive manufacturing of soft magnetic material

Alexander Goodall

The University Of Sheffield.

University of Sheffield

Materials Science & Engineering

A thesis submitted for the degree of Doctor of Philosophy

December 2022

Abstract

Additive manufacturing has been revolutionary in enabling complex structural components such as lattice structures and topologically optimised parts, however the utilisation of functional materials such as soft magnetic materials is only just being realised. 3D magnetic flux pathways in electrical machines have been illusive due to the high eddy current losses caused by thick cross-sections, and the inability to process electrical steel laminations into 3D structures. By processing soft magnetic materials with additive manufacturing, geometry can be tailored to avoid large bulk cross sections and reduce eddy currents whilst maintaining a 3D flux pathway, enabling the creation of new electrical machine architectures in the pursuit of higher power density and efficiency, which may enable the decarbonisation of the transport sectors including commercial aircraft.

This thesis demonstrates the processing of high silicon electrical steel (Fe-6.5 wt%Si) using laser powder bed fusion and characterises the magnetic properties of this material. The importance of surface roughness on the magnetic susceptibility is investigated, showing that contours may be used to improve the as-built surface finish, but post-processing methods such as polishing are required to obtain the best magnetic properties. The samples in this study exhibited a weak crystallographic texture and the orientation of the samples in the build chamber displayed little impact on the magnetic susceptibility.

Two methods are used in this study to reduce eddy currents and enable components with 3D magnetic flux pathways to be manufactured. The first is by designing thin-walled cross-sections, which use air as an insulating medium to reduce the thick cross section of the material. This method is demonstrated in lab experiments showing a reduction of the eddy current loss coefficient to 0.0005 using a novel hexagonal cross section. A Hilbert pattern was implemented into an axial flux electrical machine, demonstrating loss performance comparable to thick electrical steel laminations below 500 Hz, increasing torque density by 13% by achieving a reduction in volume of magnetic material of 33%. The second method uses process control to create stochastic cracking within the material, demonstrating excellent loss behaviour of 2.2 W/kg (50 Hz, 1T) with stacking factors >97%. The mechanical integrity was confirmed to be adequate for implementation into the axial flux machine tested with a UTS of 25 MPa when embedded with epoxy resin. These methods can be implemented into electrical machines enabling the creation of new architectures, with the hope to increase power density and efficiency.

This is the first time that additively manufactured soft magnetic material has been characterised in an electrical machine, overcoming the issues of large cross sections. Although the soft magnetic material has not displayed loss behaviour as good as electrical steel laminations, it does enable 3D magnetic circuits within electrical machines which may be exploited to improve the performance of the machine. Further optimisation of the stochastic cracking method of eddy current management by aligning the cracks with the flux direction will yield further improvements, and may compete with the thinnest laminations. Due to the current cost and limitations of additive manufacturing, this technology is only likely to be implemented into the highest value electrical machines, such as those in top end automotive and aerospace, where benefits in performance are of upmost importance. This development in processing of soft magnetic material is the missing piece to enable fully additively manufactured motors, which could revolutionise electrical machine architecture.

“The future belongs to those who believe in the beauty of their dreams”

E. Roosevelt

Acknowledgements

I would like to extend enormous thanks to each person involved in this project in any way! Though there is not space to name them all, more than a few deserve a special mention.

Firstly, to my academic supervisors. Prof. Iain Todd, for constantly challenging me to do more even when I thought it not necessary, I regretfully admit this always improved my work. And for allowing me the freedom and support to develop and chase my own research themes. To Prof. Dan Allwood for continued support, especially in self-development and pastoral matters. And to Prof. Geraint Jewell for taking the time to educate me regarding electrical engineering (without any obligation to do so.

Secondly to my colleagues, without their technical support and fruitful discussions this project would have taken double the time. I'm grateful for the enthusiasm and curiosity of Lova Chechik, the intelligence and wisdom of Felicity Freeman, know-how and helpfulness of George. To Elaine Livera, Frances Livera, Lucy Farquhar and others for an enjoyable and supportive work environment.

I would also like to thank all my friends in Sheffield and further afield, who kept me distracted outside of the lab and kept me sane throughout the tumultuous times of Covid and thesis writing. Especially to those who can keep up with me on a mountain bike, and safely hold a climbing rope. To Gordon Weight, whom did his best to prevent me from making it to the end of my PhD with his ability to almost cut a climbing rope whilst I am attached to it. To Sam Chandler, Callum Evans, James Jackson and Edward Hird for doing a stellar job to help me make it to the end of my PhD.

Finally, I'd like to express my appreciation and recognition for my family. My parents who have been model parents, supporting me through every twist and turn of this unpredictable life without asking too much about my questionable life choices. My brother Simon, who is in part responsible for the PhD as I try to find my way out of his academic shadow, and my sister Stephanie for honesty, friendship, and a source of inspiration.

Contents

1 Introduction 1

2 Research context 3

2.1 Additive manufacturing methods 3

2.2 Magnetism 5

2.3 Soft magnetic materials 7

2.4 Characterisation of soft magnetic materials manufactured by AM 9

2.5 Use of soft magnetic materials manufactured by AM in electrical machines 14

2.6 Summary 19

3 Magnetocrystalline Anisotropy and Surface Roughness 20

3.1 Journal details and author contributions: 20

3.2 Background 20

3.3 Paper 22

4 Geometrical control of eddy currents in additively manufactured Fe-Si 39

4.1 Journal details and author contributions: 39

4.2 Background 39

4.3 Further methodology 40

4.4 Paper 42

5 Loss performance of an additively manufactured axial flux machine stator with an eddy-current limiting structure 63

5.1 Journal details and author contributions: 63

5.2 Background 63

5.3 Paper 65

6 Cracking of soft magnetic FeSi to reduce eddy current losses in stator cores 82

6.1 Journal details and author contributions: 82

6.2 Background 82

6.3 Paper 83

7 Mechanical properties of stochastically cracked components 102

7.1 Journal details and author contributions: 102

7.2 Background 102

7.3 Paper 103

8 Discussion, Conclusions and future work 116

8.1 Discussion 116

8.2 Conclusions 118
8.3 Future work 120
9 References 122

List of Figures and tables

Figure 2-1 Schematic of L-PBF process chamber. Adapted from https://upload.wikimedia.org/wikipedia/commons/3/33/Selective_laser_melting_system_schematic.jpg 4
Figure 2-2 Schematic showing laser scanning of a powder bed, highlighting the melt penetration of previous layers. Reproduced from (9) (fig.8.3). 5
Figure 2-3 – Magnetic behaviour of ferromagnetic, ferrrimagnetic, paramagnetic and diamagnetic materials (16) . 5
Figure 2-4 – Ordering of magnetic moments in magnetic materials (16) 6
Figure 2-5 - Typical BH loop of a soft magnetic material, reproduced from (17) 6
Figure 2-6 – Magnetic domains in ferromagnetic material (16) 7
Table 1 – Overview of magnetic properties of common soft magnetic materials 8
Figure 2-7 Generated eddy currents are larger in a solid cross-section (left) than a laminated structure (right). https://en.wikipedia.org/wiki/Eddy_current#/media/File:Laminated_core_eddy_currents_2.svg 9
Figure 2-8 - Number of publications per year found using Scopus search terms, additive AND manufacturing AND soft AND magnet*, and also including Fe*Si*. 10
Figure 2-9 - Metallurgy of high silicon electrical steel showing porosity and cumulative crack length c.c.l. at different line energy densities (Laser power/Laser speed) of 70, 140, 280 and 420 J/m. Reproduced from (21)11
Figure 2-10 – Coercive force and permeability for as-built samples (left) and heat-treated samples (right). Reproduced from (26) 12
Figure 2-11 - Permeability and coercivity in the as-built and heat-treated condition, at a number of flux densities at 1, 10 and 50 Hz. Reproduced from (28). 13
Figure 2-12 - Yield strength of binary FeCo showing both conventionally processed and AM processed data, showing a 300% increase in yield strength and large increase in ductility. Reproduced from (36).= 14
Figure 2-13 - Topology optimised PMM rotor showing optimisation results (a), post smoothing (b) and manufactured component (c). Reproduced from (39). 15
Figure 2-14 - Topology optimisation results (left) and implemented cross-sectional geometry (right) of a toroidal ring sample. Reproduced from (38). 15
Figure 2-15 - The slotted structure shown by Goll et al, showing the micrograph of the printed sample (a) and the simulated eddy current behaviour of the ideal cross-section (b). Reproduced from (26). 16
Figure 2-16 - Different strategies for geometrical control of eddy currents including parallel plates, Mesh, and Hilbert patterns. The Hilbert pattern showed the lowest eddy current coefficient. Reproduced from (27). ... 17
Figure 2-17 Stator half shells of the transverse flux machine shown by Kresse et al (51) that are additively manufactured. Reproduced from (51). 18
Figure 3-1 – Sample orientation, machine coordinate system and labelling nomenclature(a) with a photo of the samples in the as-built condition (b). 24
Figure 3-2 - Density vs build angle (a) with micrographs of 0° sample (b) and 15° sample (c) showing high density with a small amount of porosity present. 28
Figure 3-3 - EBSD data of 0° (a), 15° (b), 30° (c), 45° (d), 60° (e), 75° (f) and 90° (g). Showing maps of the XZ plane with grain orientation in the XY plane, demonstrating a strong <001> texture in the 0° sample but there is weak texture in the other samples. 29
Figure 3-4 – Calculated changes in J_{50} (magnetic polarisation at 5000 A/m) with magnetisation angle (angle between the long edge of the sample and the magnetisation direction) using EBSD data, demonstrating a small change of less than 3% between all samples and orientations. 30
Figure 3-5 – First quadrant of the MH loop for as-built samples with varying build angle, 0-90°, demonstrating a reducing magnetic performance from 0° to 75°, with the 90° sample being an anomaly. Decreasing performance is indicated by a lower magnetisation at the knee point, and a reduced gradient before the knee point. 31
Figure 3-6 – Normalised susceptibility of as-built (AB), heat treated – 1hr @ 1150°C (HT), and heat treated with polishing (HT + P), demonstrating a small increase in susceptibility with heat treatment and a large increase with polishing. There is also a decrease in performance with increasing build angle away from vertical (0°). Results are normalised to 0° as-built sample. 32

Figure 3-7 – First quadrant of the MH loop for the as-built, heat-treated, and heat-treated + polishing samples all built at an angle of 0°, showing that heat-treatment has a small positive effect but polishing gives a large improvement with a higher susceptibility and saturation knee point. 32
Figure 3-8 – Surface roughness study showing a sample without contours (a), a sample with 2 contours (b), surface roughness vs build angle (c) demonstrating an increasing roughness with build angle for the as-built samples, and surface roughness vs contour volumetric energy density (d), demonstrating a significant improvement in surface roughness with contouring but little difference between 1 or 2 contours. 33
Figure 3-9 – First quadrant of MH loop demonstrating an improved magnetic performance with a lower roughness in both the as-built and heat-treated states. Heat-treatment has a small positive effect on the magnetic performance also. The highest and lowest roughness of the samples was 44 Sa and 5 Sa respectively. 34
Figure 3-10 - EBSD data of as-built (a) and heat-treated (b) samples with a build angle of 0°, showing partial recrystallisation after heat-treatment for 1h. First quadrant of the MH loop for the heat treated samples (c), along with average grain size vs build angle (d) and annealing time (e). 36
Table 2 - Fe-6.5 wt% Si Powder Details 44
Figure 4-1 - Parameters relating to L-PBF sample processing showing build plane and build direction, laser scan direction, hatch spacing and layer rotation angle 44
Figure 4-2 Altair flux 3D model used to simulate eddy current losses in toroidal samples, showing the different volume regions and the coils and symmetry used. 46
Figure 4-3 - Example of XCT short-circuiting analysis showing the binarized image with an example short-circuit and total length highlighted. 47
Figure 4-4 Results showing the effect of changing laser parameters on the density of Fe-Si samples. Error bars show standard error. The samples increase in density up to 70 J/mm^3, whereby increasing energy density does not improve density. There are two outliers with density below 92% with an energy density of above 70 J/mm^3 due to melt pools which have been modelled to be thinner than the hatch spacing. Lack of fusion (b) results from low energy density whereas cracking (d) occurs from too high energy density. 48
Figure 4-5 BH loops of the AB and HT condition at 1T 5Hz, and 0.9T 1000Hz, showing the specific losses (W/kg) demonstrating that HT gives an improvement at 5Hz but performs worse at 1000Hz. As this setup can only use a field of 5000A/m, the 1000Hz samples were measured at a lower flux density of 0.9T. 49
Figure 4-6 - Loss behaviour at flux density of 1T for various frequencies, showing that the HT gives an improvement in losses at low frequencies but above 400Hz, the AB condition demonstrates lower losses. 50
Figure 4-7 - Energy loss per cycle showing that the linear fit can successfully obtain C_{eddy} and $C_{hysteresis}$ 50
Figure 4-8 – Solid (a,e), Hexagonal (b,f), slotted (c,g) and Hilbert (d,h) cross-section showing a micrograph of the AB sample after removal from the baseplate (e,f,g,h), and the cross-section as per the design (a,b,c,d). Micrographs show the build direction (Figure 4-1) 52
Figure 4-9 - Display of eddy current density inside the bulk section and complex cross-sections, demonstrating a clear reduction in eddy current density for all the complex cross-sections. This enables the current paths to be observed showing the difference between the hexagonal section which constrains the eddy currents to smaller areas, and the slotted and Hilbert sections which force the currents over longer paths. Full images of each can be found in **Appendix 1** including arrows indicating current flow direction. 52
Figure 4-10- Eddy current losses during electromagnetic simulations of the complex cross-sections compared to the bulk cross-section, performed at a flux density of 1T with varying frequencies. All the complex cross-sections showed an improvement over the bulk, with the hexagonal cross-section showing the lowest losses at approximately 6% of the losses of the bulk cross-section. 53
Figure 4-11 - BH loops of bulk and hexagonal cross-sections at 50Hz, showing that although the hexagonal section has significantly lower losses, it requires a larger field to obtain the same flux density. The initial permeability is better for the hexagonal sample however the knee point of the BH loop is at a lower flux density, at approximately 0.5-0.6 T rather than 0.7-0.8 for the bulk cross-section. 53
Figure 4-12 - Errors in resolution of cross-section such as shorting, missing air gaps or cracking/porosity. 54
Figure 4-13 – XCT data of slotted ring showing the electrical shorting between areas which should be isolated. The voxel size attained is 16.72 µm due to the relatively thick sample. 54
Figure 4-14 – Hilbert and modified Hilbert cross-sections, where the modified cross-section has no surfaces which would overhang by more than 45°. Micrographs of these sections demonstrate that the modified Hilbert section is more similar to the intended design. Losses are shown (e), whereas the Hilbert section shows lower

losses in the simulation, the modified Hilbert section shows lower losses in the physical sample, due to more accurate representation to the desired geometry. 55
Figure 4-15 – Diagram showing the increasing size of the air gap between sections which need to be electrically isolated, demonstrating that the larger the gap, the less undesirable electrical shorting between areas which should not be connected. However, the larger the gap the less material in a given area and the lower the stacking factor. 56
Figure 4-16 - Loss behaviour of hexagonal cross sections AB with differing air gaps and designs from Figure 4-15. The lowest losses are for the HH section with 200um gaps, as can be seen in Figure 4-15 this has the best electrical isolation between the different sections. The VH sections show the losses reducing with an increasing air gap size, however this also reduces the SF from 87% to 74%. 57
Figure 4-17 - Full size image showing solid cross-section eddy current density with arrows to show current direction 59
Figure 4-18 Full size image showing hexagonal cross-section eddy current density with arrows to show current direction, using a more suitable scale than Figure 4-9. 60
Figure 4-19 Full size image showing slotted cross-section eddy current density with arrows to show current direction, using a more suitable scale than Figure 8. 61
Figure 4-20 Full size image showing Hilbert cross-section eddy current density with arrows to show current direction, using a more suitable scale than Figure 8. 62
Figure 5-1 – 3D FEA model showing stator, rotor, permanent magnets and stator windings. 69
Figure 5-2 - Hilbert shape filling curve used to manage eddy currents, showing a test to check for the minimum sized gap in the XY plane (a), the resultant Hilbert cross-sectional geometry when the pattern is built in the XY plane (b) and XZ plane (c), along with the schematic showing the minimum gap design rule (d) and the graphical representation of the minimum gap design rule (e). 71
Figure 5-3 - BH loops of toroid samples with Hilbert cross-sectional geometry, for the as-built state (a) and heat-treated state (b). BH loops were measured at several frequencies 5-1000Hz at a flux density of 1T. 72
Figure 5-4 – Experimentally measured loss behaviour of the Hilbert ring manufactured by AM, in the as-built and heat-treated conditions, compared with data calculated for two thicknesses of laminations. 73
Figure 5-5 - Hilbert stator for AFPM machine designed to be manufactured using AM (a,b). The stator has a toothed region which has a uniform air gap size for the XY plane of the AM machine (d), with a back iron region with non-uniform air gaps showing more clearance in the Z direction than the X direction (c). 74
Figure 5-6 - Images of the Hilbert stator showing the as-built component still attached to the build plate (a), the part after removal from the build plate (d), and the successfully resolved tooth profile (c), both showing severe oxidisation. The stator is also shown in the wound state ready for rig testing (b). 75
Table 3 - Time and cost of manufacturing Hilbert AM and 0.127mm electrical steel lamination 75
Figure 5-7 - Torque performance of AM Hilbert stator and 0.127mm laminations stator (a), demonstrating a reduction in torque of approximately 20% throughout the whole operating range. Loss performance (b) measured at several frequencies showing that the AM Hilbert stator has higher core loss than the 0.127mm laminations, but is comparable to 0.35mm laminations through a range of frequencies. 76
Figure 5-8 - Increasing the slot fill factor is demonstrated using L-PBF of pure copper, doubling the slot fill factor 78
Figure 5-9 – Delamination from bonding and machining shown for the 0.127mm laminated stator, and build defects of the AM Hilbert stator showing a weld line from splitting the component into four segments, and small errors where the geometry is not exactly as intended 79
Figure 5-10 - Demonstrator motor created mostly with AM, showing a soft magnetic FeSi stator core and rotor back iron, an aluminium housing and rotor. The bearings and permanent magnets are not created using AM. 80
Table 4 - Fe-6.5 wt%Si Powder Details 85
Table 5 - Sample processing parameters and scan strategy 85
Figure 6-1 Sample size shown along with X and Y resistivity samples, and scan strategies used in this study which include scan strategies that do not have any later rotation, such as bidirectional (B) and stripe (S), along with scan strategies with a 90˚ layer rotation such as bidirectional with rotation (BR) and stripe with rotation (SR). Stripe width was kept constant at 5mm in this study 86

Figure 6-2 Crack analysis workflow showing the cropped image from the XCT data (a), the auto-thresholded and binarised image (b), and the outlines of the particles analysed by ImageJ (c). This shows that only cracks are identified but that the total cracks are underestimated as some faint cracks are not identified, and some larger cracks have their length underestimated. 87
Figure 6-3 Schematic showing tortuosity calculation, the path which must travel around the cracks within the sample. A potential is imposed at the input and output, whilst an insulating wall of 1 voxel thickness is applied at the surfaces parallel to the current direction (X) 88
Figure 6-4 Laser speed vs crack density showing that the slower the laser speed, the higher the crack density within the sample. It is likely at higher laser speeds cracking will stop as LOF starts to become apparent. At lower laser speeds than 300 heavy balling occurs, and the samples are not built successfully. By changing the scan strategy whilst maintaining laser speed, there is an effect on the crack density within the samples. 90
Figure 6-5 Graph showing that in general the more cracks a sample has, the higher the effective resistivity. The sample at the highest laser speed 5_800_B exhibited both cracking and LOF defects. This may explain why the first data point has a higher resistivity than the second, even though it showed a lower crack density 90
Figure 6-6 Optical micrograph of 2_300_B sample (a) XY plane showing that the cracking shows a distinct pattern with the cracks running in preferred directions of 45 and 135˚. As there are a large number of cracks, it would be unsuitable to infer the crack distribution throughout the whole sample using only one micrograph. Sample 5_800_B (b) showing both cracking and LOF defects. 91
Figure 6-7 The electrical tortuosity calculated from the XCT data shows approximately a linear relationship, demonstrating that the scan strategy can create more tortuous pathways without increasing the crack density, as the sample with the S scan strategy shows. 91
Figure 6-8 Difference in effective resistivity between X and Y samples, showing that with a bidirectional scan strategy, the samples have a higher resistance in the X direction, parallel to the scan direction. By introducing a rotation into the scan strategy, the anisotropy is reduced. The reference sample has higher than expected resistivity in the Y sample. 93
Figure 6-9 An example XCT slice from sample 3_400_B in the XY plane (a) and XZ plane (c) and their respective histograms (b, d), showing that in the XY plane there is a strong preference for cracks which are between 45-135˚, showing a spread centred around 90˚ (normal to the scan direction),, whereas in the XZ plane, cracks have a much smaller spread around 90˚. 93
Figure 6-10 Optical microscopy images of samples 3_400_B (a), 6_400_BR (c), 8_400_S (e) and 9_400_SR (g) with their respective crack density histograms (b,d,f,h) showing the orientation of the cracks within the sample in the XY plane. 6_400_BR shows cracks mostly in the 45˚ and 135˚ directions whereas 8_400_SR shows cracking mostly in either the 0˚ or 90˚ direction. 94
Figure 6-11 The percentage change in effective resistivity of each sample post heat-treatment, showing that on average there is less than a 10% difference between pre and post heat treated samples. 95
Figure 6-12 YZ view of EBSD data showing orientation maps for samples 3_400_B (a) and 8_400_SR (b) and pole figures respectively (c,d). The grain orientation is plotted with respect to the XY plane, showing that 3_400_B has a <111> texture in the build direction (Z), whereas 8_400_SR has a stronger <001> texture in the build direction (Z). 96
Figure 6-13 BH loops of bulk, cracked and Hilbert rings at 50Hz, 1T. The Hilbert ring shows lower losses than bulk (area), and the cracked section shows lower losses than both of the other samples. For both the cracked and Hilbert samples, the permeability (gradient) is reduced when compared to the bulk, especially after the knee point in the loop 97
Figure 6-14 Loss behaviour of bulk, Hilbert and cracked samples at 1T, showing that the Hilbert section provides an improvement over bulk, however the cracked ring yields lower losses through the whole frequency range tested than both the other samples. 98
Figure 6-15 Micrographs of cross-sections of a Hilbert style pattern (a) with a stacking factor of 83.5% and a cracked section (b) using parameters 6_400_BR with a stacking factor of 97%, showing that the cracked section can yield a much higher stacking factor whilst still having lower losses. The Hilbert section has some porosity as the parameters used were optimised for bulk sections, rather than thin walls. 98
Table 6 - Loss behaviour of various materials at 50Hz and 1T 100
Figure 7-1 – Details of the additively manufactured blocks, that tensile test samples were machined from. 105

Figure 7-2 – Tensile test results of as-built Fe-6.5wt%Si with solid cross-section, showing an average UTS of 57 MPa. 107
Figure 7-3 - Tensile test results showing stress vs displacement (a). All samples show a linear elastic region, followed by a small area of yielding and a sharp decrease in stress carrying capacity. The effect of data smoothing is shown in (b) along with the suspected failure modes of each area of the curve. Stress concentrates into distinct bands, with examples from sample 1 as shown(c) and sample 2 (d), demonstrating the likelihood of underlying cracks perpendicular to the force. Areas of white have exceeded the scale and are not yet cracks. 108
Figure 7-4 – DIC showing the progression of cracks through the gauge section, along with simplified sketches explaining the strain patterns observed 109
Figure 7-5 - Localised strain values prior to new crack initiation during tensile test, showing the local maximum strain is 8-10%. 110
Figure 7-6 - Stress-displacement data for the samples reinforced with epoxy resin, demonstrating an average UTS of above 25MPa. 111
Table 7 – Overview of ultimate tensile properties found in this study. 111

List of Acronyms

AB	as built
AC	alternating current
AFM	abrasive flow machining
AFPM	axial flux permanent magnet
AM	additive manufacturing
AWG	american wire gauge
BCC	body centred cubic
BH	magnetic flux density against magnetizing force
BR	bidirectional with rotation
BS	british standard
CAD	computer aided design
CCD	charge coupled device
CNC	computer numerical control
DC	direct current
DED	directed energy deposition
DIC	digital image correlation
DSC	differential scanning calorimetry
EB-PBF	electron beam powder bed fusion
EBSD	electron backscatter diffraction
EDM	electrode discharge machining
EMs	electrical machines
FDM	fused deposition modelling
FE	finite element
FEA	finite element analysis
FEG	field emission gun
GO	grain orientated
GS	grain size
HT	heat treatment
ID	inner diameter
L-PBF	laser powder bed fusion
LOF	lack of fusion
MEA	more electric aircraft
MH	magnetic moment against magnetising force
MUD	multiples of uniform density
OD	outer diameter

PBF	powder bed fusion
PMM	permanent magnet motor
RPM	revolutions per minute
S	stripe
SE	standard error
SEM	scanning electron microscope
SF	stacking factor
SMCs	soft magnetic composite
SR	stripe with rotation
UTS	ultimate tensile strength
VED	volumetric energy densities
VSM	vibrating sample magnetometry
WGS	weighted grain size
XCT	X-ray computed tomography
XRD	X-ray diffraction
XRM	X-ray microscope

1 Introduction

With climate change and energy scarcity looming ahead, many sectors are turning to electrical power to reduce demands on fossil fuels and reduce harmful emissions. Electrical machines (EMs) are a key enabling technology in this transition, currently consuming over 50% of industrial energy consumption (1). To electrify our transport sectors including commercial aircraft (2), improvements in power density and fault tolerance will be required. The architecture of EMs has remained mostly unchanged since the early 1900s, due in part, to the restriction to a 2D magnetic circuit caused by the use of electrical steel laminations as a loss management method.

Additive manufacturing (AM) is a transformative technology enabling the next industrial revolution, Industry 4.0 (3), with an unprecedented freedom over geometrical design, spatial grading and control of microstructure. The AM of soft magnetic materials is still in its infancy, with the first studies published in 2012/13 by Zhang et al (4–6), however there is high promise for AM to process soft magnetic materials with excellent magnetic properties (7), enabling a 3D magnetic circuit. Eddy current loss management is a key challenge to the implementation of 3D magnetic circuits, materials such as soft magnetic composites (SMCs) have been investigated but lack the magnetic properties required for high power density EMs.

This study sets out to enable the use of electrical steel (Fe-Si), the most commonly used soft magnetic material (8), in a 3D magnetic circuit of an EM with performance comparable to that of electrical steel laminations. There are several challenges present to overcome to achieve this objective. Firstly, the processing of the material must be understood in order to create high quality components with material properties rivalling that of electrical steel laminations. Secondly, and more challenging, is avoidance of large cross-sections of bulk material which cause large eddy current losses. AM does not have the ability to process material as thin as rolling, and also has a much larger surface roughness, both which are known to limit the magnetic performance in Fe-Si. To work towards the overall objective, a number of smaller objectives are identified.

- Understand the processing of high silicon electrical steel (Fe-6.5 wt%Si) using L-PBF, and the resulting magnetic properties of the bulk material, including how characteristics such as crystalline anisotropy and surface roughness affect these properties. Create processing methods to control the intensity of the <100> texture, and use this to improve magnetic performance by creating components with spatially varied microstructure.

- Identify methods for reducing the eddy current loss in additively manufactured soft magnetic material, to achieve performance comparable to electrical steel. It may be difficult to build the complex shapes required to manage eddy current losses without using supports which would short across the insulating air gaps, therefore post processing methods to remove supports will also be investigated. Understand whether the mechanical properties of this material would survive the duty cycle of an electric machine.

- Demonstrate the use of additive manufacturing in the context of electrical machines. Implement a soft magnetic core manufactured with AM quantifying the performance and comparing to a comparable machine using electrical steel laminations.

This thesis is submitted as a series of papers either submitted to, or prepared ready for submission to peer reviewed journals. The author contributions are covered in full in each chapter. The author of this thesis is primarily responsible for most aspects including conceptualisation, methodology,

data collection and analysis and is the first author of all of these papers. Figures and references have been renumbered to be consistent throughout the thesis. As such the reference list has been removed from each paper in preference of one reference list at the end of the thesis.

Chapter 2 covers a high-level review of the relevant literature, with a more detailed interrogation of the most relevant papers. A detailed introduction is available in each chapter's paper; hence it would be unsuitable to repeat this in a comprehensive literature review.

Chapter 3 covers magnetic characterisation of high silicon electrical steel, focussing on the effects of crystallographic texture, surface finish and heat treatment methods, using vibrating sample magnetometry (VSM) as the method for magnetic characterisation and electron backscatter diffraction (EBSD) to observe the microstructure and crystallographic texture.

With the some of the materials magnetic properties characterised, Chapter 4 further characterises magnetic properties using ring samples tested with a permeameter to fully understand bulk material magnetic properties. Following this, multi-physics electromagnetic simulations are used to design a number of cross-sectional geometries aimed at reducing eddy current losses. These designs are then manufactured and tested experimentally to quantify their performance.

Chapter 5 the implements one of these cross-sectional designs into the stator of an axial flux EM, covering the technical design and manufacturing of the stator. The losses of this component are then characterised by rig testing using a CNC mill bed.

Chapter 6 investigates a different method of eddy current loss reduction by using control of process parameters during AM to cause stochastic cracking within the brittle high silicon electrical steel. Methods for controlling the orientation and density of these cracks are investigated, and these cracks are shown to artificially increase electrical resistivity. This chapter is closed by magnetic characterisation of the stochastically cracked material in the form of a ring sample, quantifying the loss behaviour and magnetic properties.

As concerns with mechanical integrity exist when using the stochastic cracking method, Chapter 7 characterises the mechanical properties by utilizing uniaxial tensile testing with digital image correlation (DIC), to show whether this material can withstand the loading requirements of an axial flux motor.

Finally, chapter 8 brings together the conclusion of these studies, commenting on their applicability to EMs and highlighting future work that can be completed to further that reported in this thesis.

2 Research context

2.1 Additive manufacturing methods

Additive manufacturing has developed enormously in the last few decades from a rapid prototyping process mostly for polymers, to full production systems capable of processing metallic (9)and ceramic components (10). AM is now a broad term encompassing a number of manufacturing techniques including fused deposition modelling (FDM), binder jetting, directed energy deposition (DED), powder bed fusion (PBF) and vat polymerisation (11). Although some research has demonstrated the processing of soft magnetic materials using polymer based techniques (12–15), this work focuses on the processing of soft magnetic materials which are generally metallic to obtain the best properties for electric machines. The main techniques applicable to processing metallic materials are:

- Directed energy deposition – "additive manufacturing process in which focused thermal energy is used to fuse materials by melting as they are being deposited" (11). DED normally uses a high-power laser (>1 kW) to melt feedstock, as it is deposited onto the workpiece. DED has a large spot size and melt pool size, limiting the resolution of features to approximately 0.5-1 mm. This is generally used as a near net shaping technique, whereby parts in the as-built condition will be post processed using manufacturing techniques such as machining.
    - Wire DED – the feedstock material is metallic wire
    - Powder DED – the feedstock material is metallic powder
- Binder jetting – "additive manufacturing process in which a liquid bonding agent is selectively deposited to join powder materials" (11). Binder jetting can process metallic materials by suspending them in a binder, then producing a 'green part', which is then placed in a furnace to remove the binder and bond the powder. This creates large shrinkages from the green state, and hence dimensional accuracy and full density can be difficult to obtain.
- Powder bed fusion – "additive manufacturing process in which thermal energy selectively fuses regions of a powder bed" (11). Powder bed fusion generally has a higher dimensional accuracy than DED and can process parts with complex geometries owing to the support of either the powder bed or manufactured supports.
    - Laser powder-bed-fusion (L-PBF) – using a medium power laser (100-500 W) with a small spot size, typically 50 – 100 µm. Dimensional accuracy is very high, but build rates can be slow
    - Electron beam powder-bed-fusion (EB-PBF) – uses an electron beam to melt the material in the powder bed, typically with very fast scan rates (>2 m/s). Requires larger amounts of powder as the powder bed often sinters during the build

This work exclusively uses L-PBF, which was identified to be the most suitable system for processing metallic soft magnetic materials. The high resolution and dimensional accuracy enable the creation of fine features which may be used to manage eddy currents, and laser processing parameters can be used to spatially grade the microstructure. EB-PBF was unsuitable as it cannot be used with magnetic powders due to the high fields used to direct the electron beam. Binder jetting may have been an equal alternative, but L-PBF was chosen based on availability at the institution.

L-PBF is a digital manufacturing process that takes a CAD model and slices it into a number of finite layers. For each of the layers, the laser scans the powder bed inside the cross-sectional area of the desired shape, causing the metallic powder to melt and resolidify as a single entity. The build

platform (fabrication piston Figure 2-1) then steps down by the layer thickness, usually 30-60 µm, and a new layer of powder is spread on top. The method of spreading the powder varies between systems, but is normally a mechanical roller or wiper blade, that takes powder from some kind of powder reservoir and deposits it over the build area. To scan the cross-sectional area, the laser completes a number of hatches, which are usually straight lines. These hatches are separated by the hatch spacing and are repeated until the whole area has been melted. The laser penetrates through multiple layers in order to ensure the latest layer is fully bonded to the material below (Figure 2-2). Multiple process parameters are available for control, and this study uses the parameters below to influence the amount of energy entering the power bed. These parameters are combined using Equation 1 to give a volumetric energy density (VED), which allows comparison between different sets of parameters, representing the total energy into for a given volume of powder. Different values of VED are required for different materials and geometries, with lack of fusion often the result of insufficient VED, while cracking and keyhole porosity are the result of excessive VED.

- Laser power (Q) - the power of the laser incident on the powder bed
- Laser speed (v) – the speed the laser traverses a single hatch
- Hatch spacing (h) – spacing between adjacent hatches
- Layer thickness (l) – the thickness between sequential layers

$$VED = \frac{Q}{vlh}$$

Equation 1

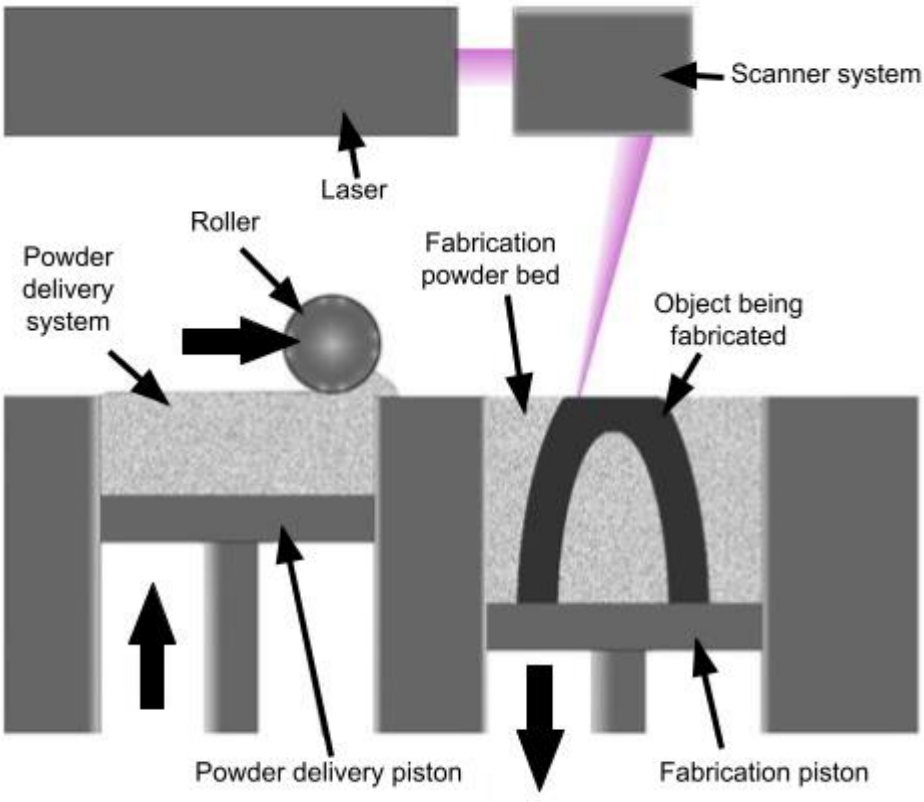

Figure 2-1 Schematic of L-PBF process chamber. Adapted from https://upload.wikimedia.org/wikipedia/commons/3/33/Selective_laser_melting_system_schematic.jpg

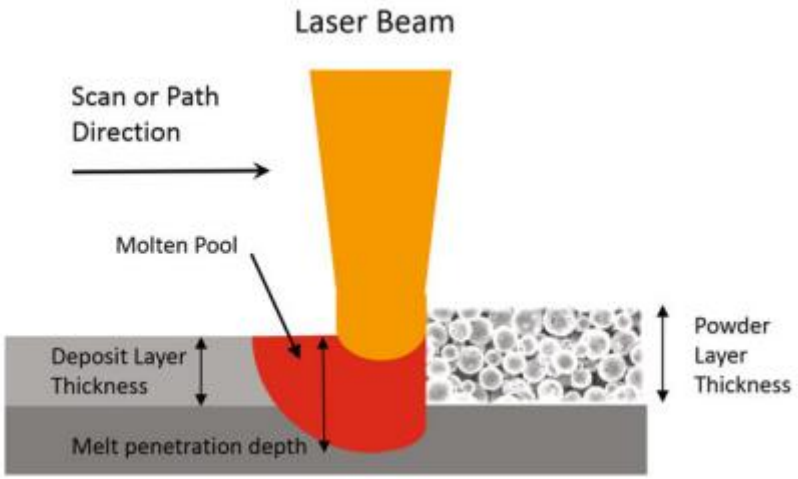

Figure 2-2 Schematic showing laser scanning of a powder bed, highlighting the melt penetration of previous layers. Reproduced from (9) (fig.8.3).

2.2 Magnetism

This project focuses on the additive manufacturing of soft magnetic materials, hence a short background into magnetism is necessary. Magnetic materials can be broadly classified into four main categories based on their magnetic behaviour: ferromagnetic, ferrimagnetic, paramagnetic, and diamagnetic and exhibit magnetic responses to an applied field as shown in Figure 2-3. Ferromagnetic materials, such as iron, nickel, and cobalt, exhibit spontaneous magnetization due to the alignment of their atomic magnetic moments in a parallel manner (Figure 2-4). When excited by an external magnetic field *H* they give a large magnetic response, where the magnetisation *M* is in the same direction as the external field, and they also display some hysteresis. Ferrimagnetic materials exhibit a similar behaviour, but instead of having aligned magnetic moments, they have magnetic moments of uneven amplitude, ordered antiparallel causing a net magnetic moment (Figure 2-4). Paramagnetic materials, such as aluminium, possess weak magnetic properties and exhibit a small temporary magnetization when subjected to an external magnetic field. No ordering of the magnetic moments within the material occurs without an applied field (Figure 2-4). Diamagnetic materials, such as copper, give a small magnetic response in the opposite direction to the applied field.

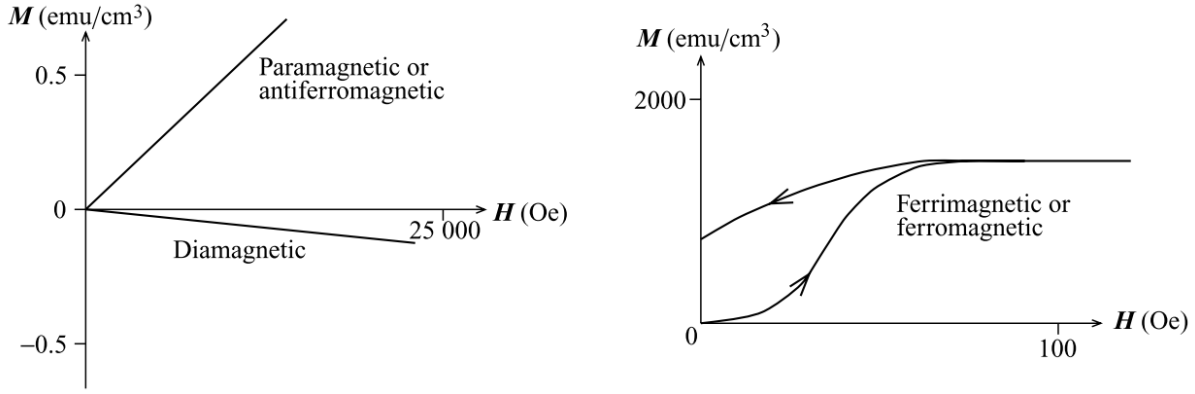

Figure 2-3 – Magnetic behaviour of ferromagnetic, ferrrimagnetic, paramagnetic and diamagnetic materials (16)

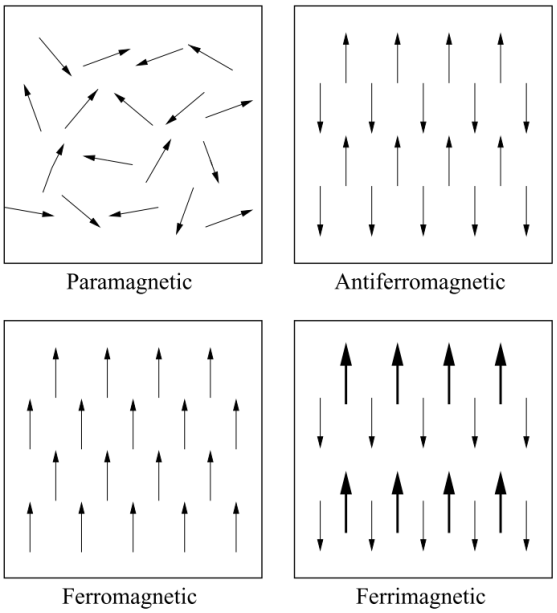

Figure 2-4 – Ordering of magnetic moments in magnetic materials (16)

Ferromagnetic materials are of the most significance to this study and will be the focus of the rest of this section. Magnetic materials are often characterised by the BH loop, also known as the hysteresis loop, which is the relationship between the magnetic field strength *H* and the resulting magnetic induction *B* in a magnetic material. It provides valuable insights into the material's magnetic behaviour and properties. A typical BH loop is shown in Figure 2-5, where the height of the loop is the saturation magnetisation, the gradient at B= 0 T is the maximum relative permeability and the difference between the x axis intercepts is the coercive force. The dashed line in this figure shows the initial magnetisation from a demagnetised state. Losses are given by the area of the loop, which includes both eddy current losses and hysteresis losses.

The crystallographic texture of a magnetic material plays a vital role in determining its magnetic properties. In ferromagnetic materials, favourable crystallographic textures can enhance magnetic properties such as coercivity. For example, in electrical steel, a strong <100> texture is desirable and results in an increase in permeability and a reduction in losses. Texture control techniques, such as rolling and annealing processes, can be employed to manipulate the crystallographic orientation and improve magnetic properties, and material with this strong <100> texture, also known as Goss texture, are known as grain orientated (GO) electrical steel.

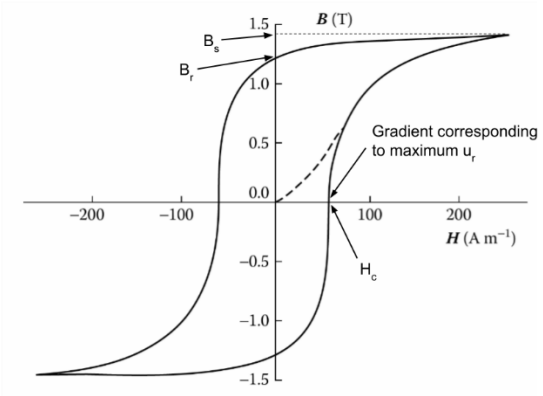

Figure 2-5 - Typical BH loop of a soft magnetic material, reproduced from (17)

In ferromagnetic materials, the magnetic domains are regions where atomic magnetic moments are aligned in the same direction. Domains are formed as it is energetically favourable for the domains not to be perpendicular to external surfaces as displayed in Figure 2-6 (16). Domain walls are the boundaries between these domains, and their motion significantly affects the material's magnetic properties. When subjected to an external magnetic field, domain walls first move to allow the domains in the closest direction to the applied field to grow. Following this, domains in unfavourable directions are annihilated by the growth of those in more favourable orientations. The last stage of magnetisation is for these domains to rotate to match the direction of the applied field. The ability of domain walls to move easily affects both permeability, and coercivity, with a higher permeability if the domain wall motion is easier. Permeability μ is a measure of a material's ability to conduct magnetic flux, and it determines the ease with which a material can be magnetized. Coercivity H_c on the other hand, represents the resistance of a material to changes in magnetization and is crucial for applications involving magnetic switching and storage. These two properties are intrinsically linked.

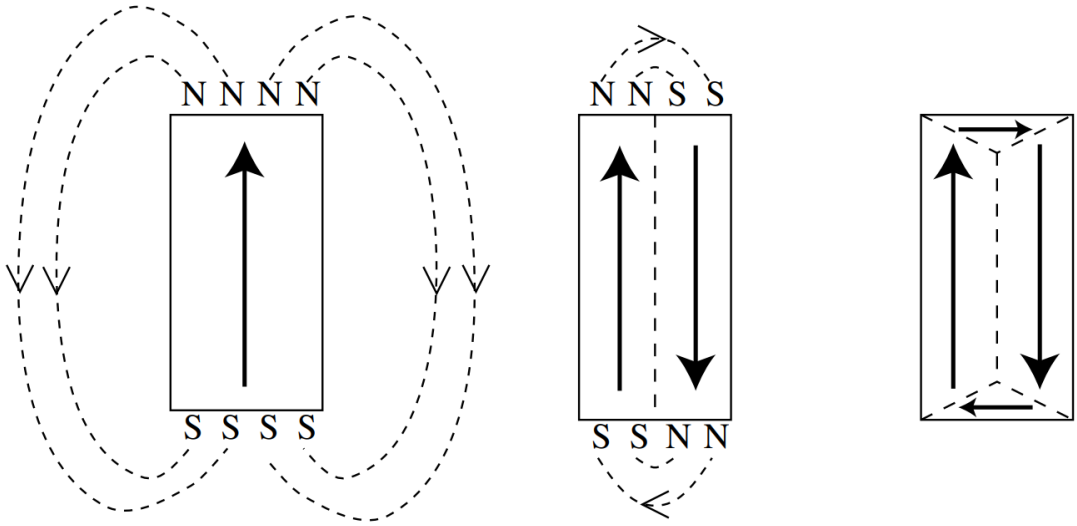

Figure 2-6 – Magnetic domains in ferromagnetic material (16)

2.3 Soft magnetic materials

Soft magnetic materials are an important class of materials for use in electronic and electrical engineering, where electrical energy is converted to or from kinetic energy using magnetism. Soft magnetic materials are characterised by having high relative permeability(μ_r) up to 30,000, high saturation magnetisation (M_{sat}) of 1.5 – 2.5 T, and coercive force (H_c) less than 1000 A/m. These ferromagetic materials magnetise easily but cannot sustain the high magnetic field without an external field, and hence also de-magnetise easily. This is advantageous for alternating current (AC) devices, whereby the direction of the magnetising field changes direction quickly. The three most common soft-magnetic materials are FeSi (electrical steel), FeNi and FeCo. These materials each have their own advantages, with FeCo having the highest known saturation magnetisation and FeNi having the highest known permeability (17). However, FeSi is the most commonly used (18) due to its excellent loss behaviour, combined with relatively high permeability and saturation magnetisation. An overview of common materials and their properties is available in Table 1.

Table 1 – Overview of magnetic properties of common soft magnetic materials

Material Name	Composition	Saturation magnetisation, M_{sat} (T)	Initial Permeability μ_i	Coercive force, H_c (A/m)
Electrical steel	FeSi Si 1-4%	2.0 (19)	4,000 (19)	10 - 200 (19)
High silicon electrical steel	Fe-6.5 wt%Si	1.8 (20)	29,000 (20)	10 – 100 (20)
Permendur	Fe-50 wt%Co	2.4 (19)	2,000 (19)	50 - 200 (19)
Permalloy	Fe-80 wt%Ni	0.75 - 1.0 (19)	100,000 (19)	<10 (19)
Pure Iron	Fe	2.16 (19)	1000 (19)	10 (19)
Pure Cobalt	Co	1.8 (19)	70 (19)	100 (19)
Pure Nickel	Ni	0.61 (19)	250 (19)	15 (19)

FeCo is mostly used with a 50/50 blend, also known as Permendur, whilst it often has small amounts of vanadium added to improve ductility. FeNi can be used with many compositions but it's often Fe-80 wt%Ni (permalloy) that is used when high permeability is required. FeSi is normally used with low silicon content of approximately 3%. Fe-6.5 wt%Si has been shown to have promising magnetic properties for future applications (20), however it is rarely used currently due to difficulties in processing due to brittle ordered phases B2 and D03 that form with the increased silicon content. Fe-3 wt%Si avoids these ordered phases and is single phase BCC α-iron, irrespective of cooling rates (20). One of the key properties of a soft magnetic material is the BH loop, characterisation of which can give access to the most important magnetic properties of permeability, saturation magnetisation, coercive force and core loss (hysteresis and eddy current). The BH loop changes based on both frequency and amplitude of flux density (B), meaning characterisation can become quite complex and should be done for an appropriate range for the intended use.

Hysteresis losses are due to the energy lost through domain wall motion, especially past features such as inclusions and dislocations which cause domain wall pinning. These losses are proportional to the frequency, and hence scale linearly with frequency. The hysteresis losses can be classified by measuring a BH loop with a quasi-static magnetisation, normally <<1 Hz.

Eddy currents are induced in a conductive material when they experience a changing magnetic field, such as that in an AC machine due to Faradays law of induction. The induced eddy currents cause losses in the form of joule heating of the material and are proportional to the square of the frequency. Eddy current losses can be reduced by increasing the resistance of the eddy current path or medium, or by allowing the eddy current to form over smaller cross-sectional areas (17). Hence, it is possible to measure and separate eddy current and hysteresis losses by taking measurements of the BH loop at several frequencies, the calculation of which is demonstrated in section 2.3 of chapter 4.

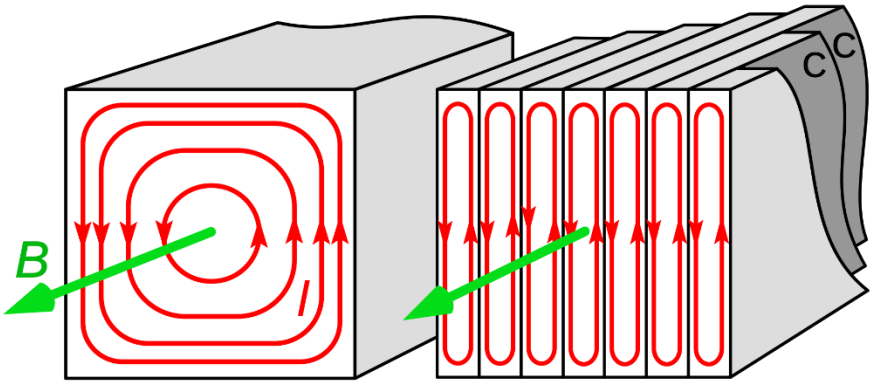

Figure 2-7 Generated eddy currents are larger in a solid cross-section (left) than a laminated structure (right). https://en.wikipedia.org/wiki/Eddy_current#/media/File:Laminated_core_eddy_currents_2.svg

When using soft magnetic materials in AC machines, it is common to use thin sheets of material, 0.1-0.5 mm thick called electrical steel laminations. These are electrically insulated, in order to reduce the eddy current losses, which depend on the geometry of the material. This has been practiced for many decades and lots of research has been completed to improve the processing, therefore the performance of electrical steel laminations is very good. However, there are limitations with this methodology, namely the restricting of magnetic circuits to two dimensions due to the planar nature of the laminations. In order to allow 3D magnetic flux pathways, other avenues have been investigated such as soft magnetic composites (SMC). SMCs are magnetic particles that have been coated with an insulating layer, therefore show very little eddy current loss due to a very high electrical resistivity. SMCs do not have the same magnetic properties as other soft magnetic materials though, with a much lower permeability than electrical steel laminations. It is for this reason that AM has been investigated for the processing of soft-magnetic materials. The ability to allow for 3D flux pathways whilst using the complexity and control afforded by AM to create geometry which may limit eddy currents, could provide an excellent route to enable new electric machine architectures with improved performance.

2.4 Characterisation of soft magnetic materials manufactured by AM

AM of soft magnetic materials is still in its infancy, with the first published research appearing in 2012 where Zhang et al. studied the microstructure and magnetic properties of Fe-30 wt%Ni produced by L-PBF (4). This research paved the way for an increasingly popular area of research that is AM of soft magnetic materials, which has been steadily growing over the last decade as shown in Figure 2-8.

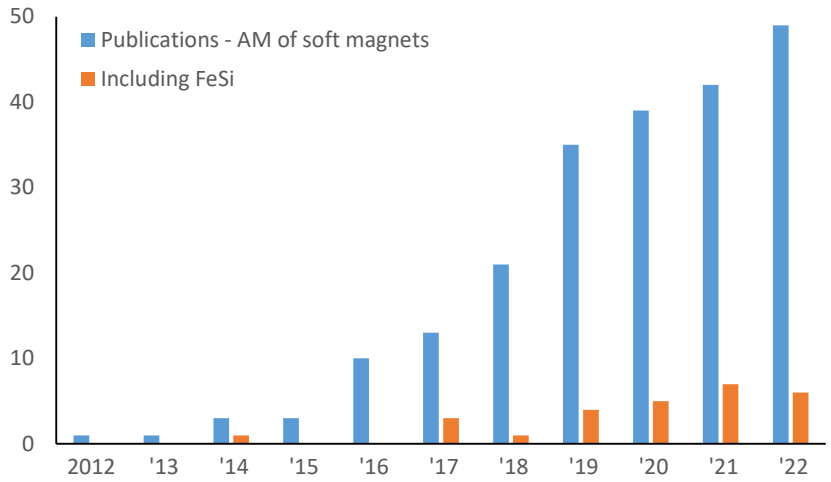

Figure 2-8 - Number of publications per year found using Scopus search terms, additive AND manufacturing AND soft AND magnet, and also including Fe*Si*.*

Zhang et al. published a trio of papers that characterises Fe-30 wt%Ni (4), Fe-80 wt%Ni (6) and different blends of Fe-30 wt%Ni (5). Due to the age of this work, these materials were processed with relatively low laser power ≈ 100 W for L-PBF, though the materials still exhibited some good magnetic properties. The saturation magnetisation and coercive force were shown to be dependent upon laser velocity, which impacted the phases present with Fe_3Ni_2, Fe and Ni peaks all present in the XRD traces (4). Zhang et al. also demonstrated the first in-situ alloying of a soft magnetic material when blending elemental powders of Fe and Ni to give Fe-80 wt%Ni, showing a higher fraction of $FeNi_3$ yielding a higher saturation magnetisation (6), although it seems there were difficulties obtaining samples without porosity, most likely due to the low laser power available, as laser power in excess of 100 W is normally used now to avoid lack of fusion defects caused by insufficient energy input.

High silicon electrical steel (Fe-6.5 wt%) was first reported by Garibaldi et al. (21) who studied the metallurgy of the alloy when processed using L-PBF, demonstrating the ability of AM to process high silicon electrical steel into a single phase material, avoiding the brittle ordered phases of B2 and D03, meaning the as-built material may be machinable whereas traditionally this alloy cannot be machined or rolled due to its lack of ductility. The processing of this alloy showed near-fully dense samples, however, it was shown that the processing window for this alloy may be very small. Normally too low energies produce lack of fusion and porosity, and too much energy creates cracks and keyhole porosity. This study showed that the samples with the lowest porosity already had some cracking, and no samples without cracks or porosity were presented (Figure 2-9). The samples were displayed to have a strong <001> texture in the build direction (Z axis of machine) with columnar grains oriented in the same direction. The study found a single ferritic phase using XRD traces, suggesting that the fast-cooling rates of AM can inhibit the ordered phases. This was proven by Lemke and Garibaldi et al. using differential scanning calorimetry (DSC) (22).

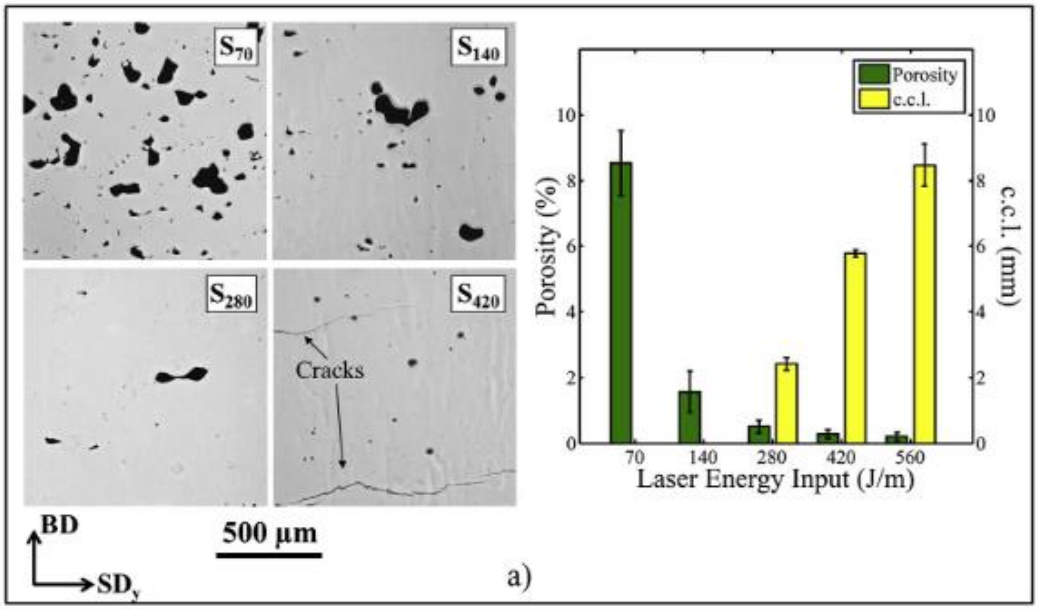

Figure 2-9 - Metallurgy of high silicon electrical steel showing porosity and cumulative crack length c.c.l. at different line energy densities (Laser power/Laser speed) of 70, 140, 280 and 420 J/m. Reproduced from (21)

Garibaldi et al. followed up this study with further work assessing the magnetic properties when the samples experience annealing at different temperatures from 400 – 1150°C (23). This study demonstrated an increase in maximum permeability from 2000 in the as-built condition, to approximately 9000 for the 900°C anneal after stress relief has occurred, but no grain growth. The final annealing temperature of 1150°C demonstrated a disproportionate increase in permeability as grain growth was demonstrated to have occurred. This change was attributed to grain growth, however it is possible that the heat treatment caused a phase change to include some ordered phases such as B2 and D03, which would naturally form during the slow furnace cooling at this silicon content (Fe-6.5wt%). XRD traces in this study did show an increase in D03, however this was not commented on with respect to magnetic properties. DC hysteresis loops were shown to have similar performance to the commercially available JNEX super core (24), though with much higher AC losses due to the eddy currents in the 2 mm thick samples, when compared to the 0.1 mm thickness of the JNEX laminations. This study did show that the <001> texture did persist through the heat treatment even after grain growth. This is important for FeSi as the <001> direction is magnetically soft and therefore has superior magnetic properties to the other crystallographic directions.

The next study from Garibaldi et al. focusses on assessing the effect of laser processing parameters on both the microstructure and magnetic properties of the as-built samples (25), though a stress relieving heat-treatment of 700°C was used as shown in the previous paper to not affect microstructure (23). This demonstrates small differences to occur with varying laser parameters, however, concludes that for use in practical applications a heat-treatment which incorporates grain growth is indispensable, and hence the as-built microstructure is not as crucial. This paper states that the differences in magnetic properties are caused mostly by porosity and differences in texture between the samples though no textural characterisation is completed for the different samples, and the porosity is not shown either. Hence this conclusion requires more evidence to be understood fully.

Further understanding of the effect of processing parameters on magnetic properties of Fe-6.5 wt%Si was developed by Goll et al. (26), showing an improvement in maximum permeability and coercive force of μ_{max} = 31,000 and Hc = 16 A/m respectively (Figure 2-10), with hysteresis losses

of 0.7 W/kg at 1 T. Significant improvement over the properties shown by Garibaldi et al. were achieved by utilising build platform pre-heating of temperatures between 200 – 600°C. Heat treatment was still required to achieve the excellent reported magnetic properties, but a large improvement in the as-built samples was demonstrated with the pre-heating. Grain size was larger with a higher pre-heat temperature in both the as-built and heat treated condition with a maximum grain size D_{50} of >1 mm after heat treatment with a build platform pre-heating of 600°C. Goll et al. also started to investigate methods to reduce eddy currents but this will be re-visited in the next section.

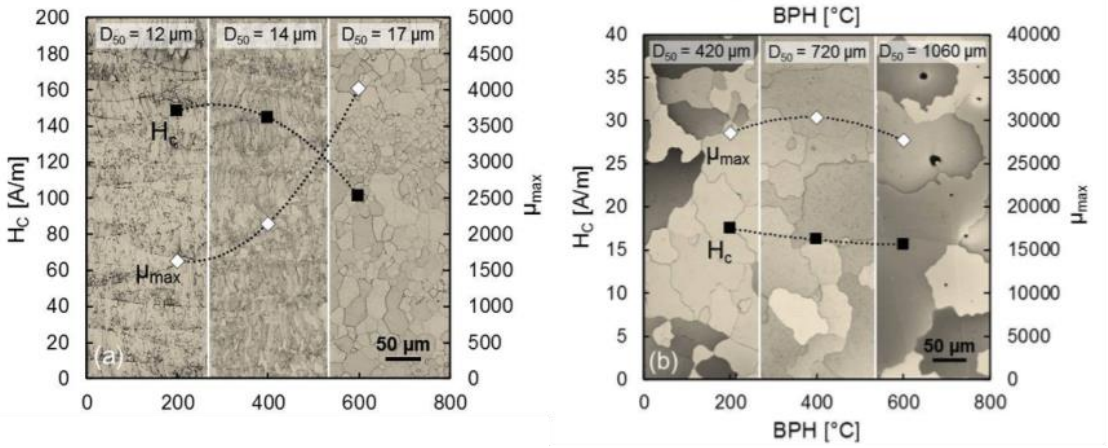

Figure 2-10 – Coercive force and permeability for as-built samples (left) and heat-treated samples (right). Reproduced from (26)

Plotkowski et al. also investigated electrical steel, but used a lower silicon content (27), showing that the strength of the <001> texture in the build direction can be increased from 2.5 multiple of uniform density (mud) to almost 8 mud in the XY plane, by using a double scan laser strategy, scanning each layer twice. Plotkowski et al. also show an improved surface roughness based on a laser scan tracks that follow the direction of the outer surface, similar to building a part using only contours. This paper also draws the conclusion that more research is required to identify heat-treatments for FeSi manufactured by AM, as the increase in grain size was dependant on the laser scan tracks used to create parts which had identical CAD geometry. This is similar to the findings of Goll et al. (26) who showed differing grain sizes post heat-treatment based on the build platform pre-heat temperature. Plotkowski et al. are the first authors who have separated the eddy current and hysteresis losses (27), calculating the eddy current and hysteresis loss coefficients, however this was measured with a “picture frame”, akin to a miniature Epstein frame. Whilst testing with this the magnetic circuit was not continuous as there are discrete joints in the corners. Due to this no permeability was measured, presumably as the discontinuities caused a large reduction in the measured permeability due to the reluctance of these gaps. As a positive, Plotkowski et al. are able to isolate one direction for their measurements, for which they choose to align the legs of the “picture frame” with the build direction, allowing the <001> direction to be aligned with the magnetic test direction. The authors suggest that this gives an improvement in properties similar to grain orientated electrical steel, however there is no experimental data to confirm this.

Tiismus et al. then also separated the hysteresis and eddy current losses (28), demonstrating a large improvement in the majority of properties with heat treatment, including coercive force and permeability. Tiismus et al. did use toroidal test samples and therefore didn’t have any discontinuities in the magnetic circuit allowing for measurements of permeability. For the first time as-built and heat-treated samples are compared directly, at several frequencies and a number of flux

densities ranging from 1-1.5 T. Interestingly the difference in performance between the as-built and heat-treated samples reduces as higher frequencies and flux densities are reached. It becomes apparent that the behaviour of the samples is dominated by their geometry, as eddy currents are increased with the square of the frequency and the performance of as-built and heat-treated samples gradually gets closer until they are not discernible at a flux density about 1.35 T and frequency of 50 Hz (Figure 2-11). 50 Hz was the highest measured frequency, though it is worth noting many electrical machines run at frequencies of 1 kHz or more, therefore a wider frequency range should be investigated. Tiismus et al. were also the first authors to report the electrical resistance of FeSi manufactured by AM (29), showing resistance ranging from 75-85 μΩ.cm for Fe-3 wt%Si and 120-140 μΩ.cm for Fe-6.5 wt%Si. The resistance values varied based on the orientation of the samples in the build chamber. These values for Fe-6.5 wt%Si are above the expected value of 82 μΩ.cm (20), though it is possible to observe cracks within the micrographs for these samples in the study, hence the resistivity measured is likely to be overestimated as defects such as cracks and porosity can cause an increase in resistance.

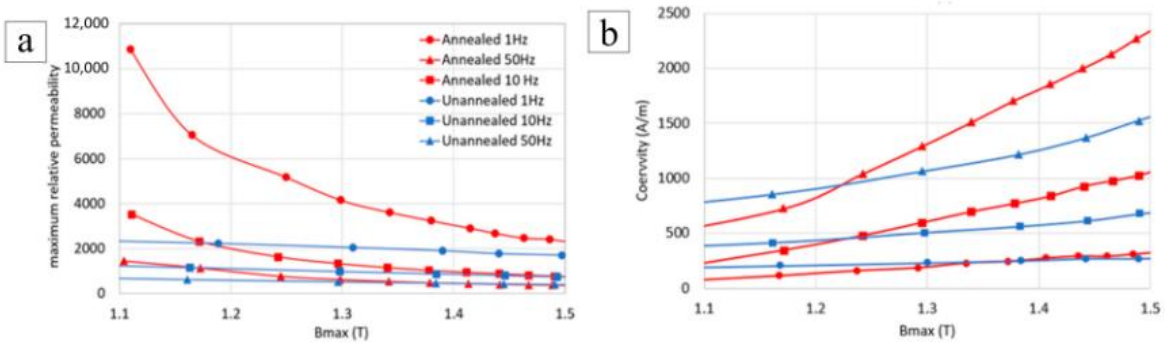

Figure 2-11 - Permeability and coercivity in the as-built and heat-treated condition, at a number of flux densities at 1, 10 and 50 Hz. Reproduced from (28).

Little investigation into the effect of build angle on the magnetic properties. It is well known that there is anisotropy in structural parts (30), and has been suggested by many authors with regards to magnetic anisotropy of FeSi built by AM (23,26,31–33) but the only literature exploring this is from Urban et al. (34), who built toroidal magnetic test samples at angles of 0°, 45° and 90° to the base plate. Using a t-test, no statistical difference was found in the magnetic properties between the samples, though the variance in this study was quite high. Heat-treatment was again found to be beneficial. This is also currently the only study that shows mechanical properties, showing a tensile strength of 100-500 MPa, and elongation to break at 5-12%. The samples built parallel to the build platform showed better mechanical properties than those at either 45° or 90°. Urban et al. also investigated the processing window of Fe-6.5 wt%Si (35), which Stornelli et al. also reported to be narrow (33).

Babuska et al. showed that the mechanical properties of Fe-50 wt%Co samples produced by AM avoided the brittle intermetallic phases and showed ductile behaviour in the as-built condition due to the high cooling rates of AM (36). Although FeSi components were also manufactured in this study, the mechanical properties of these were not analysed, therefore the same can be suspected about FeSi but has not been evidenced.

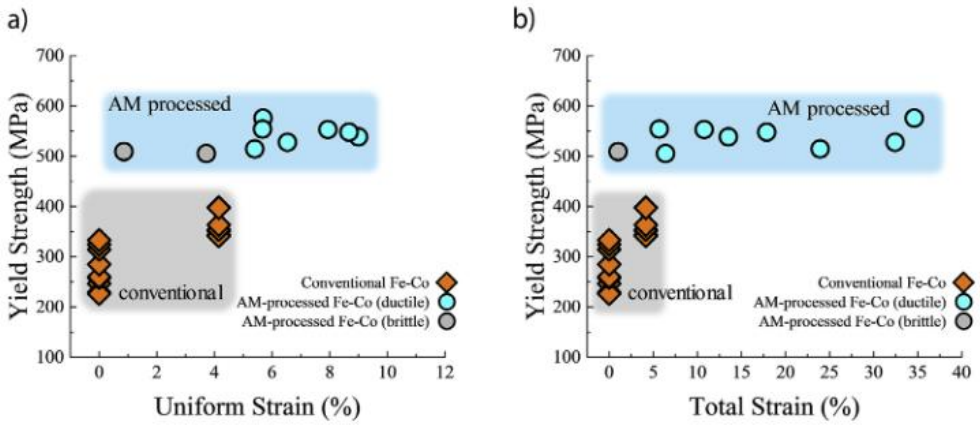

Figure 2-12 - Yield strength of binary FeCo showing both conventionally processed and AM processed data, showing a 300% increase in yield strength and large increase in ductility. Reproduced from (36).

This section has covered the key papers from literature relevant to this thesis, but for a comprehensive overview of the properties of soft magnetic materials processed by AM, review papers are available first from Périgo et al. (37), and then from Chaudhary et al. (7). This includes further studies on FeNi and using FeCo, which all show further successful case studies of using AM to process soft magnetic materials with properties close to that of the traditionally processed material, furthering the evidence of AM being a viable channel to process this material. All these studies suffer with high eddy currents due to the toroidal test rings having a large cross-sectional thickness (> 2 mm), when compared to electrical steel laminations (0.1-0.5 mm), however hysteresis losses, saturation magnetisation and DC permeability have all been shown to be competitive with non-AM processed material.

2.5 Use of soft magnetic materials manufactured by AM in electrical machines

To enable the use of soft magnetic materials in electrical machines, strategies to manage the eddy current losses need to be developed. Just as electrical steel was first processed into thin sheet, or laminations, soft magnetic material manufactured by AM and intended for use in AC machines cannot be processed as a bulk material with thick cross-sectional areas. Multiple authors have attempted such works with a variety of techniques, from trying to mimic laminations (26) to topological optimisation of the soft magnetic material to reduce eddy currents, whilst increasing flux linkage (38).

The first application of soft magnetic material manufactured by AM was for the soft magnetic core of surface-mounted permanent magnet motor (PMM) which was designed and developed by Garibaldi et al. (39). The authors developed a topological optimisation based on a finite element (FE) mesh, which attempted to improve torque density whilst maintaining structural integrity. The outcome of this study was the rotor of the machine with an organic three-dimensional geometry. Although this study did not attempt to quantify or reduce the eddy current losses, it displays a methodology that could be used based on a different set of equations that could be used to optimise for eddy current losses, whilst maintaining structural performance. It is noteworthy that manufacturing constraints were not taken into account during the analysis, and although the resulting part did not require supports and was easily manufacturable using L-PBF, this is likely down to the electrical machine geometry being a radial flux motor with a cylindrical shape. Other motor types such as axial flux motors may not be optimised into a manufacturable shape, and hence future topological optimisation studies for soft magnetic material should aim to reduce eddy currents,

increase a performance parameter such as torque density but have built in manufacturing and structural constraints. This adds another dimension of difficulty to the problem, and but whilst this methodology is still embryonic, structural topology optimisation shows the capacity to allow for this.

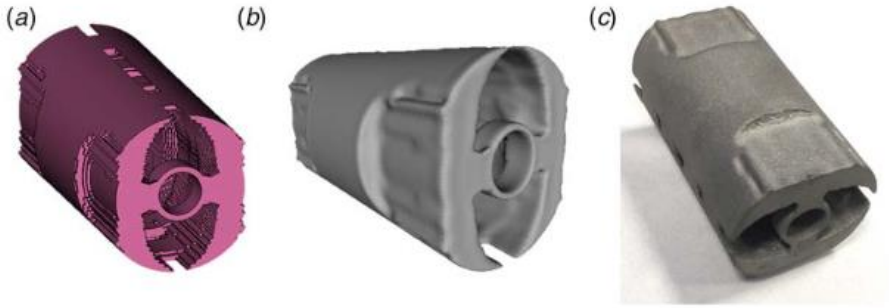

Figure 2-13 - Topology optimised PMM rotor showing optimisation results (a), post smoothing (b) and manufactured component (c). Reproduced from (39).

The only other reported use of topology optimisation of soft magnetic material was published in 2022 by Manninen et al. (38) who did optimise for minimum eddy current losses and maximum secondary flux linkage. The chosen sample was a toroidal ring sample, allowing for easy characterisation of the sample when manufactured. This study is also one of the few to directly compared to a laminated structure, although this time using FeCo rather than FeSi. The methodology, however, is material agnostic. In this study Manninen et al. demonstrated that the topology optimised sample demonstrated lower losses than the alternative tested which was manual designs of a grooved sample. The topology optimised sample showed slightly higher losses than that of the 0.35 mm thick laminations, although this is the closest reported in literature. The study also reports a reduction in flux linkage for the topology optimised samples, due to the reduction in volume of magnetic material inside the cross-section. The stacking factor is reduced to approximately 70% (calculated from the manuscript images using ImageJ). Further to this, the results of the topology optimisation were not implemented directly, but rather used for inspiration for a manually designed geometry, due to the manufacturing constraints of the AM process. Figure 2-14 displays the results of the topology optimisation, with areas circled in red that are typically not manufacturable in L-PBF due to overhanging surfaces, along with the actual geometry used to build the samples. It's also worth noting that the mesh used for the topology optimisation is fairly coarse as can observed by the pixelation in Figure 2-14, most likely due to the computational intensity of multi-physics simulations. This does however offer a benefit in that with a finer mesh, one may obtain features of a size below which the L-PBF process cannot maintain.

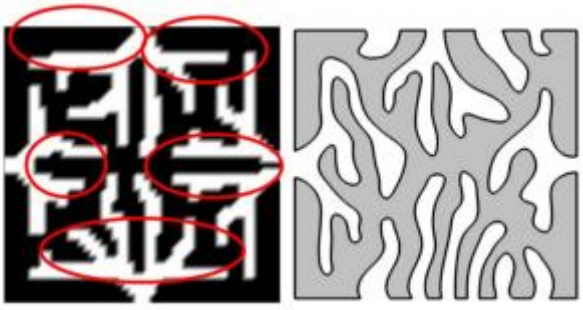

Figure 2-14 - Topology optimisation results (left) and implemented cross-sectional geometry (right) of a toroidal ring sample. Reproduced from (38).

Although topology optimisation of soft magnetic materials has shown promise, the majority of the research in this area is based on manually created designs. This can be quite a laborious task with a trial-and-error approach to what the cross-sectional geometry should be to reduce eddy currents. Goll et al. showed FE models of a slotted geometry along with experimentally built samples. It can be seen from the micrographs that issues with resolving this geometry were faced, as the structure has multiple horizontal overhanging surfaces with particles short circuiting the air gap. No optimisation of the size of this gap was undertaken to ensure no short circuiting between areas which should be electrically isolated (Figure 2-15). The other strategy employed by Goll et al. is to build with a multi-material layered structure, using alternating layers of pure Fe, with its good magnetic properties, with a relatively higher resistivity FeAl16 layer, though the resistivity of this layer is still similar to Fe-6.5 wt%Si. Therefore, in this configuration is not likely to offer low enough losses, however if a higher resistivity material was able to be used, such as a ceramic this may provide a good solution. Multi-material with metals is only just developing, and as such a metal-ceramic multi-material structure has still not yet been created using L-PBF, but other methods such as binder jet printing may offer a quicker route to a material like this.

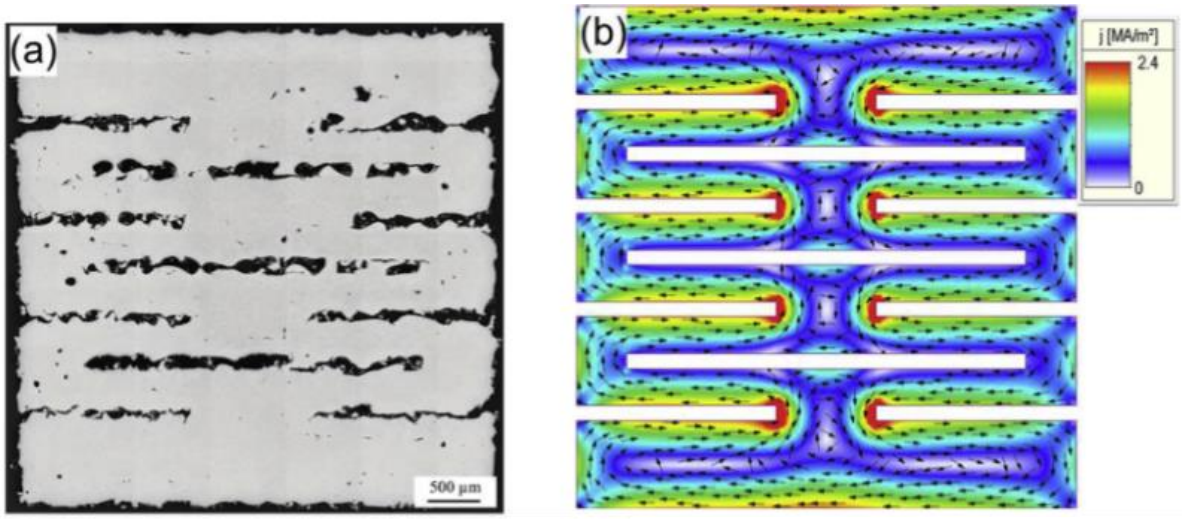

Figure 2-15 - The slotted structure shown by Goll et al., showing the micrograph of the printed sample (a) and the simulated eddy current behaviour of the ideal cross-section (b). Reproduced from (26).

Plotkowski et al. (27) also demonstrated geometrical control of eddy currents with several samples built using a laminated style pattern called ‘parallel plates’ with differing air gaps and stacking factors, along with a Hilbert pattern and Mesh pattern (Figure 2-16). This showed that for the thinnest plates, the highest eddy current losses occurred, the opposite of what would be expected with laminations. This is due to short circuiting between the plates, as the thickness of the plates were reduced to fit more plates into the same area, the gaps between the plates were also reduced below the accuracy of the machine causing the short circuiting between plates. Therefore, in AM it appears to be a trade-off between reducing the size of the gaps to as small as possible to increase the volume of magnetic material, whilst still maintaining electrical isolation. During this study, Plotkowski et al. demonstrated the Hilbert pattern to have the best performance with a loss density of approximately 4.5 W/kg for a BH loop with an applied field of 3000 A/m. It is difficult to compare the results in this study to others, as mentioned earlier there are discontinuities in the magnetic circuit. Therefore, the authors have not stated flux density in the samples, instead quoting losses at a given applied field value which is atypical. Most other papers report losses for a flux density of 1 T at a frequency of 50 Hz. Data sheets for electrical steel laminations show several frequencies and

flux densities, however as AM of these materials is still a recent development, it is useful for all investigators to report the same test conditions as these will likely scale predictably with frequency.

Plotkowski et al. used Fe-3 wt%Si in this first study (27), however followed up with a study using Fe-6.5 wt%Si as well, implementing the Hilbert pattern into a transformer (31) which showed performance comparable to non-orientated electrical steel laminations, though the thickness of these was not specified. Two other patterns were introduced in this study of radial and clock spring, though both of these sections showed higher losses than the Hilbert pattern. Again, all of these samples were built in the XY plane of the machine, which is the easiest direction to resolve complex shapes as the accuracy is dependent on the laser spot size and scan strategy, whereas resolution in the XZ plane is also dependant on laser burn through. Therefore, these samples are only capable of carrying magnetic flux in 2D, and it's unlikely that they will outperform laminations which are also capable of carrying magnetic flux in 2D. Some of these patterns may be suitable for 3D magnetic flux pathways with some development, though this isn't shown in the study. Urban et al. also investigated Hilbert type fill patterns showing both simulation and experimental validation (40), however the loss behaviour of these performed worse than those of Plotkowski et al.

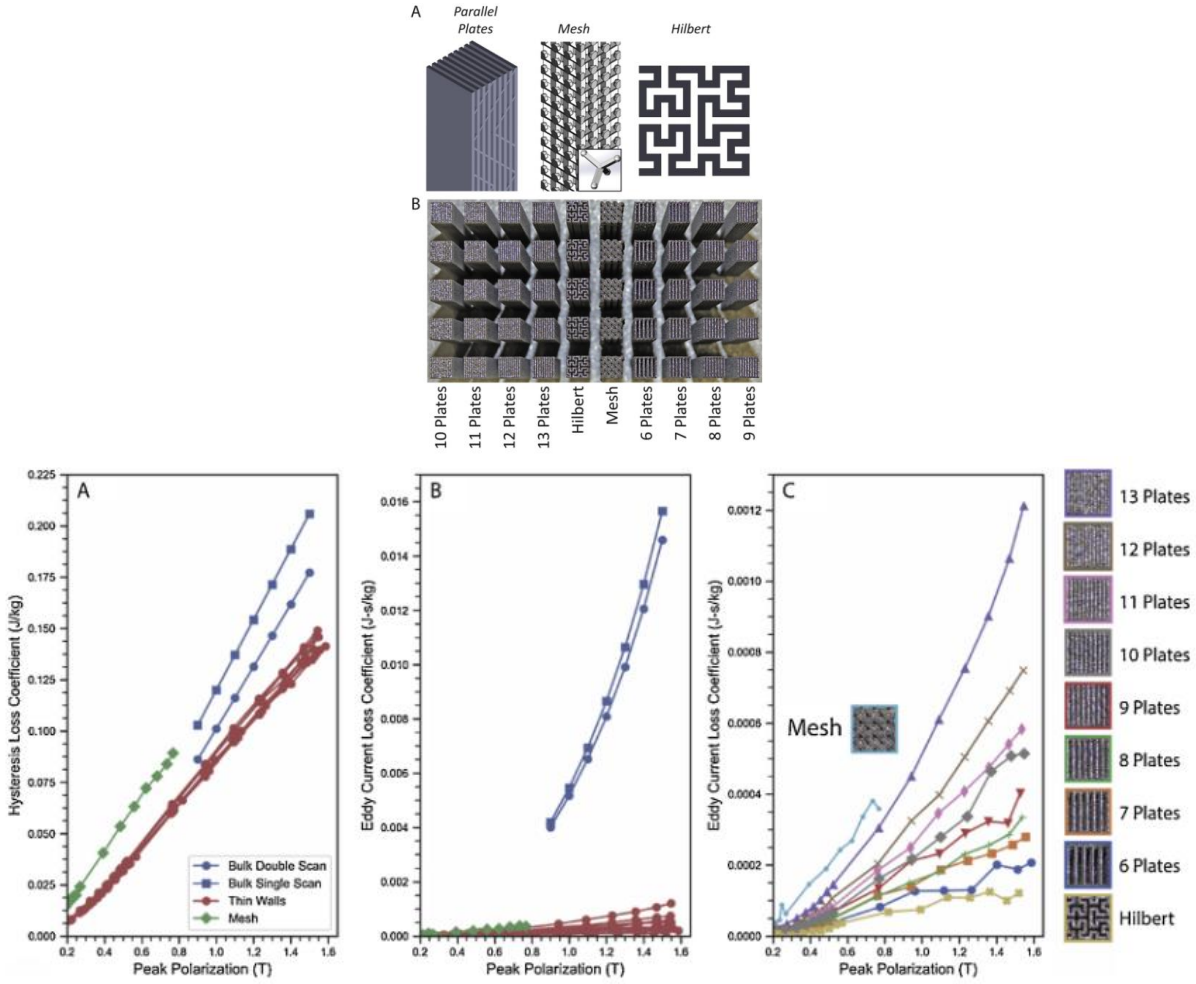

Figure 2-16 - Different strategies for geometrical control of eddy currents including parallel plates, Mesh, and Hilbert patterns. The Hilbert pattern showed the lowest eddy current coefficient. Reproduced from (27).

The best loss behaviour observed by AM soft magnetic materials is demonstrated by Koo et al. (41) with a "structurally-layered" material, which has a shape similar to electrical steel laminations with

alternating ends connected. This study shows the building of the sample in an expanded state, which reduces the probability of the electrical shorting across the air gaps. Following this, an insulating SiO_2 coating is crated using a sol-gel-based process. Following this the sample may be compressed easily due to its topology. This author was also able to successfully process walls as thin as 0.2 mm, due to an excellent as-built surface roughness, which is thinner than any other author has successfully reported. The measured core loss was extremely low, approximately 1 W/kg at 50 Hz and 1 T, but even more remarkably 52.5 W/kg at 1 kHz and 1T. This was then demonstrated in the stator of an axial flux machine though this was created from stainless steel rather than Fe-6.5 wt%Si, unlike the other samples in the study.

Optimisation of the horizontal gaps was first undertaken by Andreiev et al. (42) who also demonstrated a slits in the structure akin to electrical steel laminations, showing that the minimum gap is affected by the laser parameters and hence optimising the laser parameters to ensure these gaps existed without short-circuiting. The magnetic properties were also characterised showing losses of 11.2 W/kg at 50 Hz 1T, higher than most other authors though it is worth noting that Fe-2.7 wt%Si was used for this study which is less resistive.

Lindross et al. (43) also demonstrated a reduction of losses using geometrical features such as grooved structures when building with FeCo alloys. Topology optimisation is also touched upon and Manninen is one of the co-authors of this paper, who's work was described earlier.

Comprehensive review papers covering further details on soft magnetic materials and their use in electrical machines are available from Lamichhane et al. (44), Pham et al. (45), Naseer et al. (46) and Tiismus et al.(47,48).

Further to the work characterising these soft magnetic materials and coming up with design strategies to reduce eddy current losses, researchers have started to demonstrate these materials in applications. Transformers created by Plotkowski et al. (31) and Tiismus et al. (32) have already been discussed in this section. Electric motors have also been investigated such as the PMM (49) described by Urbanek et al. which uses extra slots in the soft magnetic rotor to insert copper wires, short circuiting the rotor coils. Urbanek et al. also demonstrated an improvement in cogging torque and reduction in in leakage flux (50). Kresse et al. (51) manufactured a transverse flux machine with geometry for loss reduction, showing a type of motor (that would be very difficult to manufacture from electrical steel laminations.

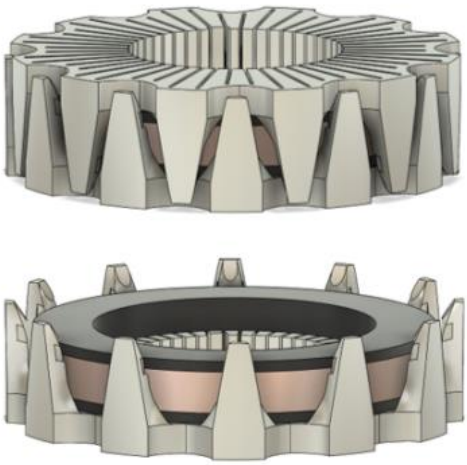

Figure 2-17 Stator half shells of the transverse flux machine shown by Kresse et al. (51) that are additively manufactured. Reproduced from (51).

2.6 Summary

This research context section has shown the literature surrounding the additive manufacturing of soft magnetic material, showing that authors have managed to successfully process near fully dense samples from common soft magnetic materials, but also from high silicon steel (Fe-6.5 wt%Si) (21) which is difficult to process traditionally. Materials processed with AM have typically shown magnetic properties below that of electrical steel laminations (25), though a small number of studies have managed to obtain properties which are comparable to electrical steel laminations (26,27). DC magnetic properties are often comparable, but large eddy current losses show a decrease in magnetic performance owing to the thicker cross-sections. This is somewhat combatted by using the higher silicon content, but Fe-3 wt%Si electrical steel laminations are still better for AC losses despite their lower resistivity, especially at high frequencies. A number of methods to reduce eddy currents have been investigated, with a variety of geometries from slotted (26) and slitted parts (51), to the Hilbert pattern (31,40). Topology optimisation has also been investigated but is far from maturity as the only observed use of this (38) resulted in a manually adjusted design to account for manufacturing constraints which were not factored in during the design phase.

Current gaps in the literature are apparent in the fundamental process-parameter relationship of soft magnetic materials in AM. The as-built properties and grain structures have been investigated however electrical steel is rarely used without a heat treatment, therefore further detailed study needs to be undertaken to investigate the effect of heat treatments linking back to the as-built geometry and grain structure. Further to this surface roughness has not yet been investigated although it is known that it has a large impact on magnetic behaviour, especially losses. Limited domain wall imaging has been used to observe the domain wall structure and propagation in the AM material, and this is likely to attract further research. The effect of grain orientation in both the as-built and heat treated states is also not well understood when compared to electrical steel laminations. The loss behaviour and stacking factor of soft magnetic material manufactured by AM is still not competitive with electrical steel laminations. To exploit the use of AM there must be some tangible benefit to using the 3D magnetic circuit, which will require the design of new motor architectures. Quantifying the possible increase in performance of these will become important to understand the minimum target properties of the AM processed material.

3 Importance of surface roughness on magnetic properties of additively manufactured FeSi thin walls

3.1 Journal details and author contributions:

Planned Journal – Acta Materialia (undergoing peer review)

Submission date – 30th January 2023

Author contributions:

Alexander Goodall – Conceptualisation, Methodology, data capture of all magnetic characterisation and half of surface roughness data, investigation, analysis, data curation and visualisation, writing original draft

Lova Chechik – Support with matlab and EBSD analysis and interpretation, writing review and editing

France Livera – Methodology and data capture of first set of surface roughness measurements. Support on interpretation of these results

Iain Todd – Support with methodology formal analysis, visualisation, writing review and editing, supervision.

3.2 Background

Electrical steel laminations are available in two categories, (GO) and non-GO. Non-GO electrical steel laminations have a random texture with no alignment of the crystallographic axes with the direction of magnetisation giving uniform magnetic properties in all directions. GO electric steel laminations use a series of rolling and annealing to create a Goss texture resulting in a strong <001> texture in the direction of magnetisation (52). This results in the easy axis of magnetisation being aligned with the magnetic flux, improving properties such as permeability and reducing hysteresis losses (53).

During L-PBF, a <001> texture is normally created aligned with the build direction (machine Z axis), due to the vertical growth of elongated grains throughout many layers (21). It has been suggested by multiple authors (23,26,31,33,47) that this texture will provide improved magnetic properties in the build direction, when compared to other orientations within the build chamber. This suggestion is sensical as if aligning the texture provides improved properties in GO laminations, and we can obtain this texture in AM components, it could be a fair assumption that this would provide an improvement in the build direction. However, this has not yet been experimentally validated.

This paper initially sets out to understand how the magnetic properties, namely susceptibility/permeability and a higher magnetisation at the knee point along the MH loop, also yielding a higher magnetisation for a given field. The saturation magnetisation is not expected to change as this is a single-phase material, hence at saturation the magnetic moment is dependent only on the volume of material and not on the crystallographic orientation. It was hypothesised that by building samples at an angle away from the build direction, the <001> texture would be controlled to an angle away from the long edge of the sample, and hence the magnetisation direction. As the sample passed 45° from the build direction, it would become closer to the <001> texture again and magnetic properties should increase again up to the 90° sample. As the paper shows the data did not show this to be the case.

After analysis of this data showed a trend of decreasing magnetic susceptibility with increasing angle from the build direction, other factors were investigated. Surface roughness was found to be an

important factor and further study was undertaken to understand this more, and improve the performance based on surface roughness improvements.

The heat-treatment initially used in this study was laid out by Garibaldi et al. (23) to enable grain growth and was shown to improve magnetic properties significantly. During our experimentation we did not find this to be the case, the susceptibility did not appear to improve with heat-treatment. This led to the suspicion that this heat-treatment did not allow the samples to fully recrystallise and then encourage grain growth, as increased grain size has been shown to be beneficial especially with respect to susceptibility. Hence a study was undertaken to investigate the effects of heat-treatment on the samples used, to try and understand why an established heat-treatment method did not work as intended for these components.

3.3 Paper

Importance of surface roughness on magnetic properties of additively manufactured FeSi thin walls

Alexander D. Goodall[a], Lova Chechik[a], Frances Livera[a], Iain Todd[a]

[a] Department of Materials Science and Engineering, University of Sheffield, Sheffield, UK

Corresponding Author – Alexander Goodall adgoodall1@sheffield.ac.uk

Keywords

Laser Powder Bed Fusion; Soft-Magnetic Material; FeSi: Anisotropy; Surface Roughness

Abstract

Thin-walled structures have been investigated for use in soft magnetic components manufactured by additive manufacturing to limit eddy current losses in AC machines. Fe-6.5 wt%Si has been shown to be a promising material in such components, however most characterisation has taken place using thicker bulk material. Thermal conditions and microstructure have been shown to differ with thin-walled structures, hence magnetic properties may differ also. This study characterises the magnetic properties of thin-walled structures, showing that the <001> texture usually apparent in laser powder-bed fusion does not persist in thin-walled samples built at an angle to the build platform. Surface roughness is shown to increase with build angle from 28 Sa when perpendicular to the build platform, to 80 Sa when parallel, causing a deterioration in magnetic properties such as susceptibility which is reduced by up to 25%. Improvements in magnetic properties are demonstrated for samples with lower surface roughness due to improved laser parameters, with even larger improvements available when using polishing as a post-process finishing operation which was shown to improve susceptibility by over 10%. This study enables the designers of soft magnetic components made by additive manufacturing the freedom to design magnetic flux paths at any angle in the build chamber and gives surface roughness as a key parameter to improve magnetic properties.

1. Introduction

Research interest in additive manufacturing (AM) of soft-magnetic materials started when Zhang et al. processed permalloy (Fe-30 wt%Ni) (4), and has greatly increased in the last decade with many authors contributing to the field (37,44,45) with studies focusing on the three most common soft-magnetic alloys of FeSi (26,27,54), FeCo (36,55,56) and FeNi (57–59). Of these materials, FeSi is commercially the most heavily used with a wide variety of applications. AM has been used to demonstrate manufacturing of transformers (31,32), electric machine stator cores and rotors (54,60). Throughout these applications, all of which operate using AC currents and magnetic fields, thin walled structures are deployed to reduce eddy currents and their associated joule heating losses (26,27,61), mimicking the behaviour of electrical steel laminations whereby eddy currents are confined to smaller cross-sectional areas normal to the magnetic flux. Although the material is normally used in a thin wall (<2 mm) structure, the properties have always been measured with cross-sectional dimensions above 4 mm (25–27), for ease of handling and characterisation and to abide by standards for characterisation such as BS 60404 (62).

Heat transfer in thin walls has been shown to behave differently than bulk material (> 4mm thickness) during AM (63), yielding differing microstructure based upon the geometry. Assuming this to be the case in AM of soft-magnetic materials, the microstructure and hence magnetic properties of these thin wall structures cannot be directly implied from measurements of the bulk material. Further to this, authors often refer to an improved performance in the build direction of Fe-6.5 wt%Si during L-PBF due to a strong <001> texture in this direction whilst avoiding the <111> direction (23,26,31–33). This texture has only been demonstrated in thicker samples, generally with a cuboidal structure unlike those likely to be used in an electrical machine. There is no evidence yet to suggest that the properties are different in different build orientations, however one study does investigate rings built at different build orientations (34), but fails to draw conclusive differences between the samples. In low silicon (Fe-3 wt%Si) electrical steel laminations grain orientation is often used to obtain better properties by aligning a Goss texture ({011}<100>) (64) with the magnetic flux direction, supported by measurements on single crystal materials (65) and polycrystal steel sheets (66). However high silicon electrical steel (Fe-6.5 wt%Si) has a magnetocrystalline anisotropy constant of k_1=3.4 x10^4 J/m^3, 20% lower than Fe-3 wt%Si at k_1=4.1 x10^4 J/m^3 (67). This means that at the higher silicon content of 6.5%, there is less difference between the easy <001> and hard <111> axes of magnetisation. There is a need for further understanding of the magnetic properties of soft-magnetic materials processed by AM, especially thin-walled components. Without this understanding it will not be possible for electrical engineers to simulate electrical machine performance, or design improved machines using the material produced by AM.

This study will investigate the grain orientation and surface roughness of thin-walled samples built at a variety of angles within the build chamber, characterising texture using electron backscatter diffraction (EBSD), and magnetic properties using vibrating sample magnetometry (VSM). By characterising samples at a variety of angles, it will be possible to test the magnetic properties at an angle to the build platform in L-PBF manufactured components. The effect of surface roughness on magnetic properties in thin-walled structures will also be investigated, and optimised build parameters and post-processing attempted to give an improvement.

2. Materials and Methods

2.1 Sample processing

All samples in this study were manufactured from high silicon steel powder (Fe-6.5 wt%Si) with a size range of 15-45 µm supplied by Höganäs using an AconityMINI (Aconity3D GmbH) L-PBF system, equipped with a 200 W ytterbium doped continuous wavelength laser (wavelength 1074 nm) which has a spot size of 70 µm. All samples were built using a meander scan strategy for the fill with laser power 170 W, laser speed 670 mm/s, and a hatch spacing of 70 µm which was previously found to give above 99.5% density in 5x5x5 mm cubes. The samples in this study were processed with a variety of contour parameters, ranging from 0-2 contours with varying volumetric energy density specified by using a full factor design of experiments, with laser speed using 4 levels between 500-1100 mm/s, and laser power using 4 levels between 130-190 W resulting in a volumetric energy density of 56-181 J/mm^3. Unless otherwise specified samples were built without contours. Sample orientation in the build chamber was varied from an angle of 0° to the machine Z axis, in increments of 15° about the Y axis until 90° as displayed in Figure 3-1, which also highlights machine coordinates. The Z axis is also referred to as the build direction. Samples were removed manually due to their size, by applying a small mechanical force at the base of the sample where it joins the baseplate which was made from stainless steel.

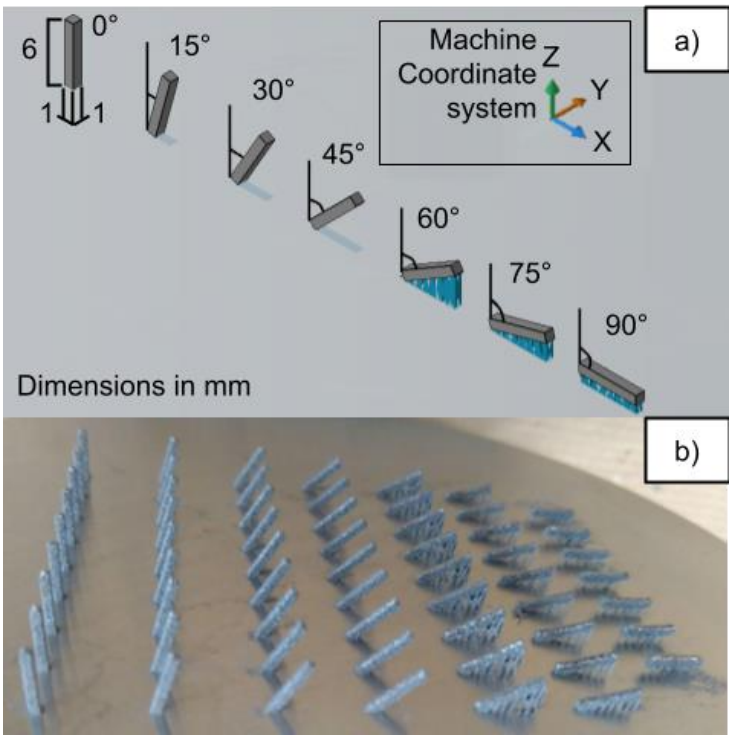

Figure 3-1 – Sample orientation, machine coordinate system and labelling nomenclature(a) with a photo of the samples in the as-built condition (b).

2.2 Sample preparation, optical microscopy and EBSD

Samples were prepared for both optical microscopy and EBSD by hot mounting then grind and polish. Hot mounting in Bakelite was completed using a Simplimet 1000 from Buehler. Grinding and polishing was completed using a Struers Tegramin 20 first with grinding papers of P1200 and P2400,

followed by 9 µm, 1 µm, and 0.25 µm diamond suspensions and a final polishing step using 0.05 µm MasterPolish all supplied by Buehler.

Optical microscopy was undertaken using an Olympus BX51 microscope paired with Clemex Vision PE system. All optical micrographs were taken in the XZ plane of the machine coordinate system. Density analysis was completed using the areal method by thresholding the image in ImageJ. Standard error (SE) was calculated for the density by taking 5 measurements of different cropped areas within the sample micrograph, and using the formula $SE = \sigma/\sqrt{n}$.

Samples remained in bakelite for EBSD analysis. EBSD analysis was conducted using a 7900F field emission gun (FEG) scanning electron microscope (SEM) manufactured by JEOL, fitted with an Oxford instruments symmetry EBSD detector. The accelerating voltage used was 20 kV with a step size of 1 µm. The Bakelite was reduced in size using hand tools, then mounted onto the SEM stub using silver paste. The software used to capture EBSD data was AZtec by Oxford Instruments, indexing Fe-6.5 wt%Si by using the library parameters for α-iron, (BCC). Only a single phase was detected with an index rate above 98%. Multiple frames were captured and aligned in the software before exporting to .CRC format.

Analysis of the data was completed using MTEX toolbox plugin for MATLAB R 2020a. First the data was aligned to the machine coordinate system in order to create consistency within the data. 10° was used to identify high angle grain boundaries and grain orientations were calculated. All orientation maps in this study are viewed on the XY plane. As per optical microscopy all EBSD maps were captured on the machine XZ plane. Grain size (GS) was averaged using this data taking the arithmetic mean of the grains identified in MTEX. Weighted grain size (WGS) was calculated using Equation 2, where n is the total number of grains.

$$WGS = \frac{\sum_{i=1}^{n} GS^2}{\sum_{i=1}^{n} GS}$$

Equation 2

Magnetic polarisation was calculated as a function of angle using the methodology from MTEX (68), based upon literature from several authors (69–72). This methodology calculates the value of the magnetic anisotropy constant k1 (Equation 3) and magnetic saturation J_s (Equation 4) based upon the composition of the FeSi alloy (67). The angle between each of the magnetically soft directions and the direction of magnetisation is calculated (Equation 5-7). Following this the magnetic anisotropy energy, E_a, is calculated based on the orientations of the grains within the EBSD map (Equation 8) and averaged into angled bins between -90° and +90° from the samples long edge. Then J_{50} is calculated based upon the mean magnetic anisotropy energies (Equation 9).

$$K_1 = 4.77 - 0.21256 \times Si\ content\ (wt\%) - 0.03816 \times Al\ content\ (wt\%)$$

Equation 3

$$J_s = 2.162 - 0.043 \times Si\ content\ (wt\%) - 0.0625 \times Al\ content\ (wt\%)$$

Equation 4

$$Cos_{[100]} = \cos(angle\ between\ Miller\ [100]\ and\ grain\ [100])$$

Equation 5

$$Cos_{[010]} = \cos(angle\ between\ Miller\ [010]\ and\ grain\ [010])$$

Equation 6

$$Cos_{[001]} = \cos(angle\ between\ Miller\ [100] and\ grain\ [001])$$

Equation 7

$$E_a = K_1\ \times (Cos_{[100]}{}^2 . Cos_{[010]}{}^2 + Cos_{[100]}{}^2 . Cos_{[001]}{}^2 + Cos_{[010]}{}^2 . Cos_{[001]}{}^2)$$

Equation 8

$$J_{50} = J_s(1 - 0.19\ \times average\ E_a)$$

Equation 9

2.3 Magnetic characterisation using VSM

Magnetic characterisation was completed using an MPMS 3 magnetometer from quantum design. Samples were mounted on a quartz rod using GE varnish with the long edge of the sample aligned parallel to the magnetisation direction. Sample offset was measured at a field of 1.5 kA/m and the sample was centred from this. All measurements were taken at 300 K in VSM mode. 6 quadrants of a MH loop (magnetic moment vs field) were measured to allow the sample to saturate before data was taken and avoid demagnetisation cycles, which went from a field of 0 kA/m, up to 1200 kA/m, returning back to -1200 kA/m before again going to 1200 kA/m and then back to 0 kA/m. Results reported are from the 5th Quadrant giving the magnetisation during a field change of 0 kA/m to 1200 kA/m, which was previously found to saturate the sample fully. 100 measurements were taken between 0-1200 kA/m using the uniform spacing$^{0.5}$ function, which gives a finer field spacing in lower values and a coarser spacing at higher values. The sample was held stable at each field, where a VSM measurement of amplitude 1 mm, averaging time 2 s was taken. All MH data plotted in this study uses normalised magnetic moment of M/M_s, which will allow for direct comparison of the shape of the loops whilst avoiding the requirement to correct for any radial offset or shape effects. It is possible to normalise this data in such a way as the sample is a single phase material and therefore the saturation magnetisation depends only on the volume of material. Heat-treatment may cause the introduction of B2 and D03 phases as the samples were furnace cooled, however should not impact on the saturation of the material (73). To ensure this is correct, several samples were tested before and after heat-treatment, and were found to have the same M_{sat} during VSM measures.

Normalised susceptibility is calculated by finding the gradient between measured points at 3 kA/m and 35 kA/m. This was then normalised to the 0° as-built sample to allow easier comparison between samples.

2.4 Heat Treatment

Heat treatment of samples, unless otherwise specified, was completed at 1150°C for 1 hour, with a heating rate of 5°C/min and furnace cooling as reported by Garibaldi et al. (23). This was undertaken in a tube furnace under argon. For other samples used different durations, the samples were removed from the furnace sequentially meaning that furnace cooling was not possible. Hence, the samples were removed from the furnace, kept in the ceramic boat, and placed in an insulating ITM-Fibermax 72 (Schupp) blanket to simulate furnace cooling. Samples were still not fully cooled after over an hour from removal; therefore, this was judged as an acceptable method.

2.5 Surface roughness measurements

Surface roughness measurements were carried out using an Alicona InfiniteFocusSl using the optical focus-variation technique. Objective magnification of 5x was used and an area of approximately 2x1 mm was measured for each sample. The surface arithmetic average roughness (Sa) was obtained from a smaller section of approximately 1x0.5 mm, to avoid including edges and corners in the measurement. Polishing of samples for improved magnetic performance used P1200 and P2400 grit paper grinding to improve the surface roughness by hand until an even finish was obtained. Error was measured by repeating this measurement 5 times for each sample, then using the standard error calculation as per Equation 10, where SE is standard error, σ is standard deviation and n is the number of samples, 5 for this study.

$$SE = \frac{\sigma}{\sqrt{n}}$$

Equation 10

3. Results

3.1 Effect of build angle on microstructure

FeSi built by AM has been reported to have an <001> texture in the build direction, Z, (21). To confirm if this <001> texture remains in the same direction, even when thin rods are built at an angle to the build direction, Z, samples were built at 15° intervals from Z (0°), to horizontal in the build chamber in the X direction (90°). As the removal of heat from the sample may flow through the component as the powder bed acts as an insulator relative to the solidified component, it was prudent to confirm that the <001> texture remained with the machine co-ordinate system or with the sample co-ordinate system, if it persisted at all.

Figure 3-2a shows the density of the samples as they move away from 0°, demonstrating near fully dense (>99.5%) for the 0° sample, and with some of the angled samples having a lower density. There does not appear to be a trend as the 15° and 60° samples have >99.5% density, whereas some of the other samples have lower density highlighting the need for either more detailed parameter optimisation based on build angle in thin-walled samples, or in-situ process control to allow fully dense samples at any build angle.

EBSD was captured for the XZ plane for all samples between 0-90°. The EBSD maps were used to plot orientations in the XY plane to confirm if the <001> texture remained with the machine co-ordinate system. EBSD maps for all samples are shown in Figure 3-3, demonstrating that the <001> texture remained for the 0° sample with a measure of at least 5 multiples of uniform density (MUD). The other samples all exhibited a weak texture with no apparent alignment to the machine coordinate system. The strength of the texture varied between samples, with all samples showing less than 2 multiple of uniform density (MUD), except the 0° and 30° sample. The 30° sample appears to have a small texture close to <100>, but much weaker than the 0° sample. Hence these results confirm that there is no <100> texture along the build direction for this sample geometry, when the samples move away from vertical (0°). The loss of the texture may be a result of the material being built above the powder bed, rather than above solid material when leaning at an angle. The first 0.5-1.0 mm above the powder bed is frequently small equiaxed grains, before a preferred growth

direction is selected. In these samples it is apparent that this preferred growth direction has not yet been selected. As these samples are only 1 mm thick the whole sample is left with little texture.

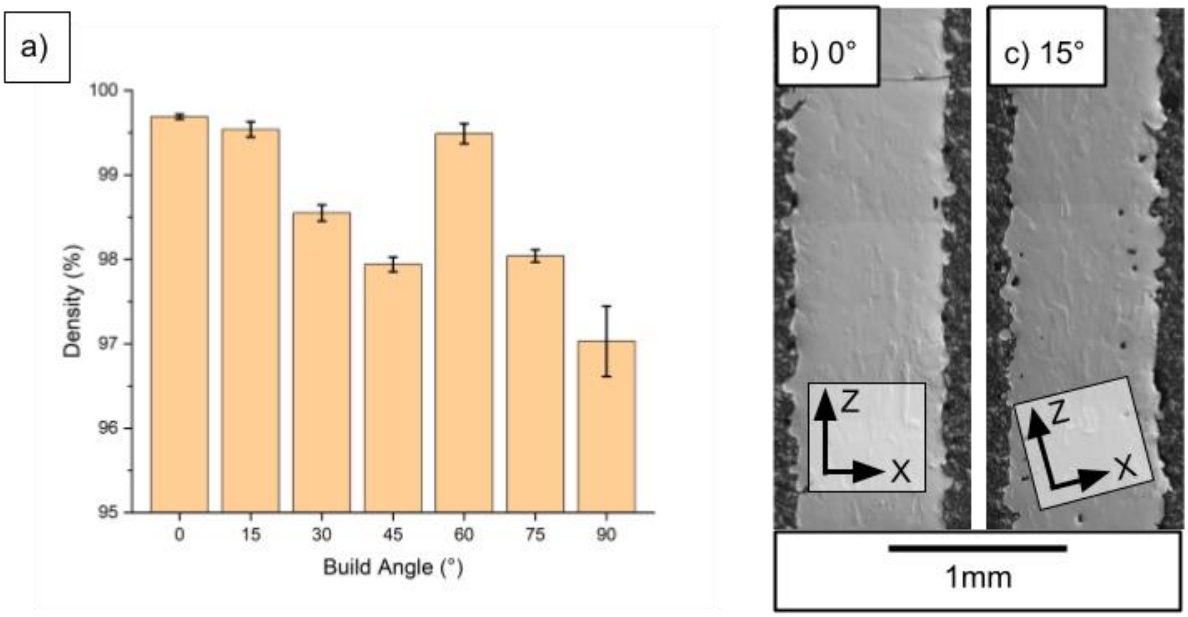

Figure 3-2 - Density vs build angle (a) with micrographs of 0° sample (b) and 15° sample (c) showing high density with a small amount of porosity present.

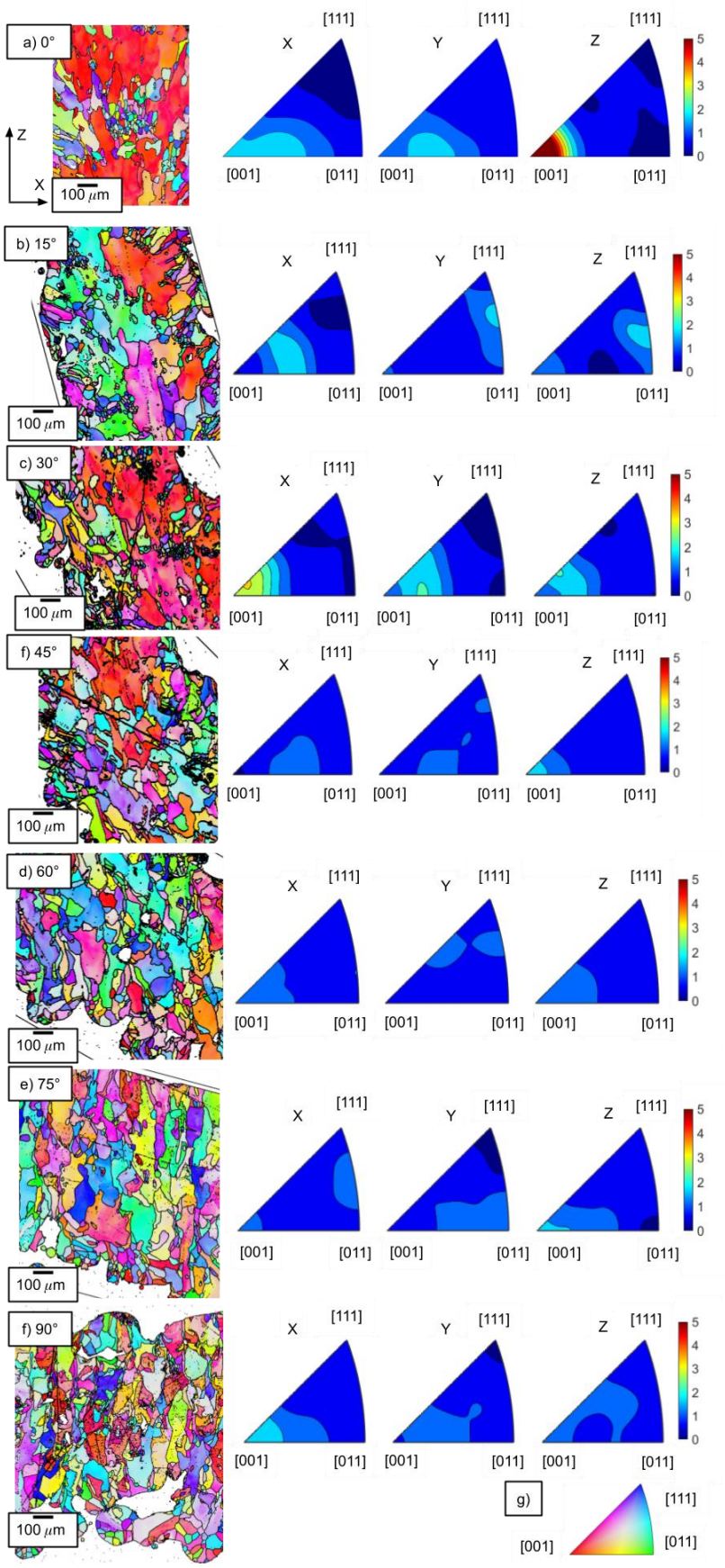

Figure 3-3 - EBSD data of 0° (a), 15° (b), 30° (c), 45° (d), 60° (e), 75° (f) and 90° (g). Showing maps of the XZ plane with grain orientation in the XY plane, demonstrating a strong <001> texture in the 0° sample but there is weak texture in the other samples.

With the EBSD data it is possible to estimate how the average magnetocrystalline anisotropy energy (E_a) will change when the samples are magnetised at different angles (68). From this it's possible to calculate the magnetic polarisation J_{50} (at a field, H, of 5000 A/m) which is shown in Figure 3-4. This demonstrates a small range of magnetic polarisations, which varies by only 3% when the magnetisation axis is rotated about the Y axis of the sample. Hence, from EBSD data we can predict little difference in magnetic performance between samples built at different angles. The data does show small variations with magnetisation angle that are present due to the weak texture of the samples. The peaks are not all centralised to a 0° magnetisation angle, showing that the weak texture does not always align with the long edge of the sample. It is not possible to obtain experimental data at different magnetisation angles due to the shape effects that would be caused by the cuboidal samples in this study. Therefore all the experimental data is from a 0° magnetisation angle.

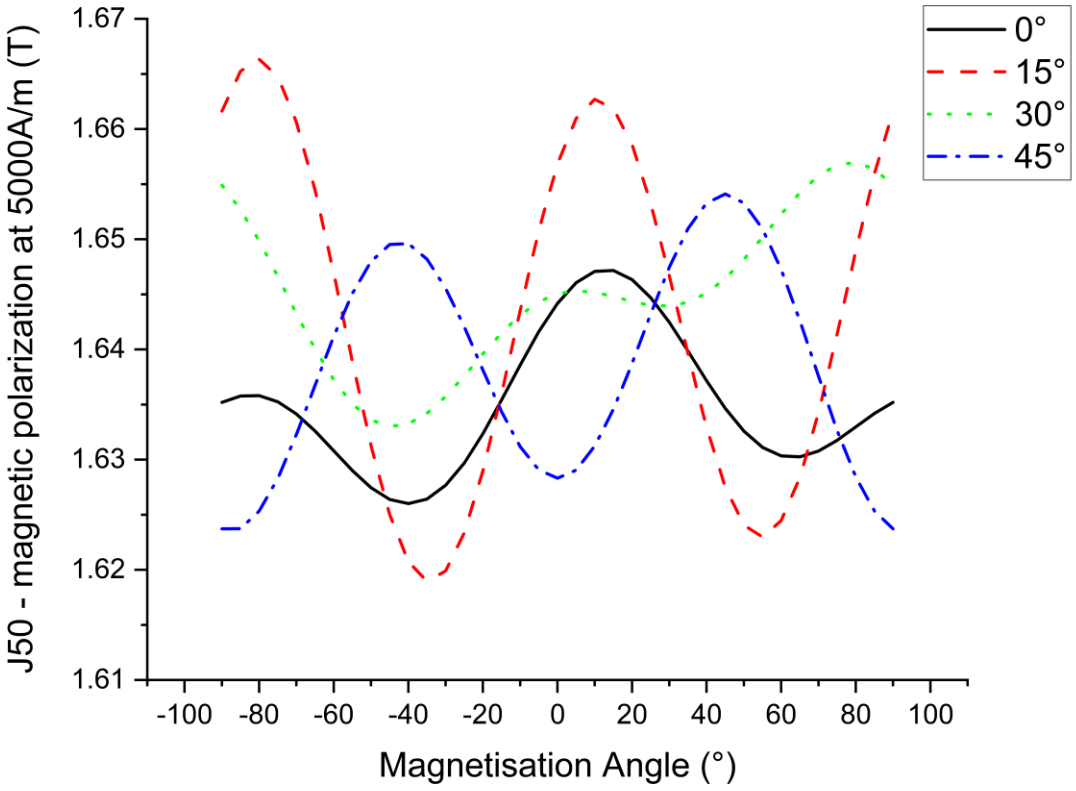

Figure 3-4 – Calculated changes in J_{50} (magnetic polarisation at 5000 A/m) with magnetisation angle (angle between the long edge of the sample and the magnetisation direction) using EBSD data, demonstrating a small change of less than 3% between all samples and orientations.

3.2 VSM measurements

MH loops were measured using VSM by magnetising the sample along its long edge. All samples had the same geometry and are single phase with the same material composition, therefore magnetic moments were plotted normalised to the magnetic saturation M_{sat} of the sample, which was taken as the magnetisation at 1200 kA/m, allowing more accurate comparison between the data and avoiding shape corrections necessary when using VSM (74). Figure 3-5 shows the first quadrant of the MH loops for all samples 0-90°, with the rest of the MH loop excluded for clarity.

When investigating the knee point there is a clear trend of decreasing performance with increasing build angle from sample 0° through to sample 75°, with the 90° sample being an anomaly to this pattern. This performance decrease is demonstrated by a lower magnetisation at a given field, hence a lower susceptibility (X_m), and a higher field required to saturate.

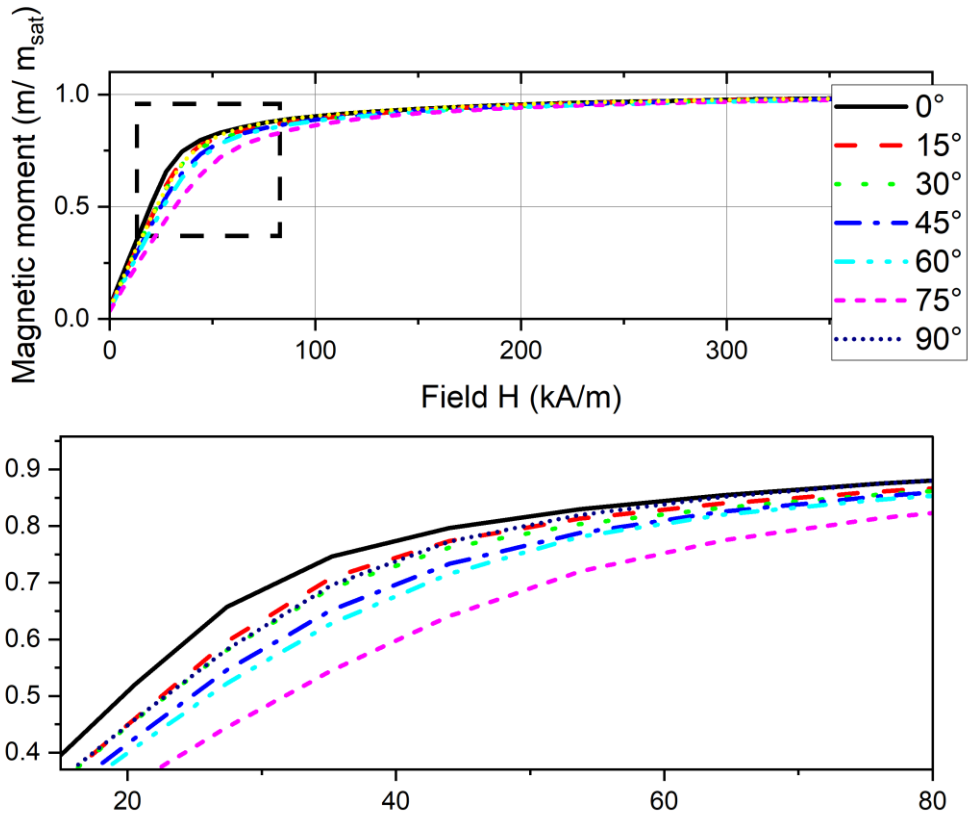

Figure 3-5 – First quadrant of the MH loop for as-built samples with varying build angle, 0-90°, demonstrating a reducing magnetic performance from 0° to 75°, with the 90° sample being an anomaly. Decreasing performance is indicated by a lower magnetisation at the knee point, and a reduced gradient before the knee point.

Observations from the EBSD data show that the samples had a weak texture therefore are not able to explain the differences in the magnetic properties, supported by the calculations of J_{50} in the previous section. With crystallographic texture not responsible for the change in properties, other factors which could impact the magnetic properties must be investigated such as residual stress, grain size and surface roughness.

To reduce residual stress and aim to increase the grain size and susceptibility, a heat-treatment (HT) can be used. Annealing 1150 °C for 1 hour has been shown to have a large positive effect on the permeability and hence susceptibility whilst increasing grain size (23,26) and therefore was used in this study. Figure 3-6 demonstrates that the HT has a negligible positive increase of around 1% in contrast to the other published studies which show order of magnitude improvements. Following HT to investigate if surface roughness may be having a significant impact on performance, all samples were ground and polished to a 2 Sa (2-dimensional Ra) roughness and re-tested. Results shown in Figure 3-6 demonstrate an increase in normalised susceptibility of at least 10% for all samples with polishing. Figure 3-7 shows the first quadrant of the MH loop for the 0° sample in the as-built, heat-treated, and polished with heat-treatment condition.

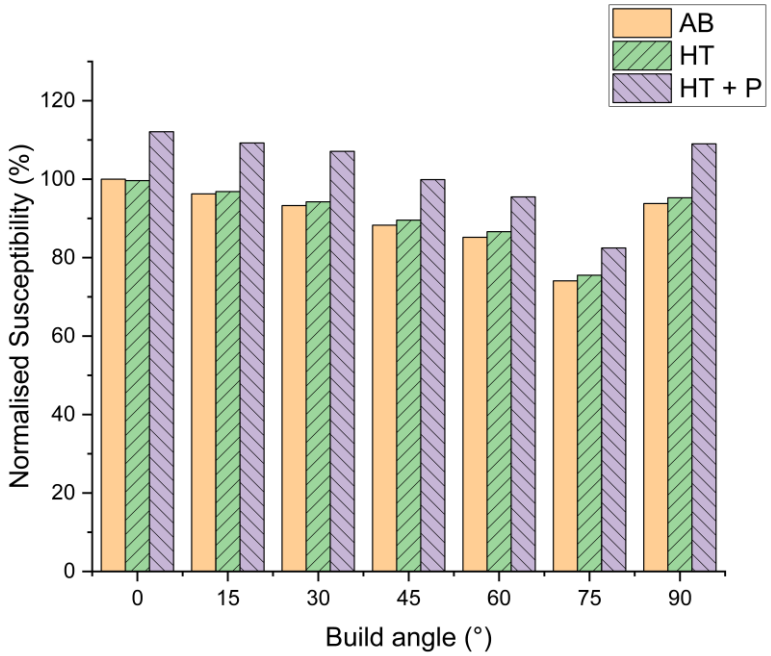

Figure 3-6 – Normalised susceptibility of as-built (AB), heat treated – 1hr @ 1150°C (HT), and heat treated with polishing (HT + P), demonstrating a small increase in susceptibility with heat treatment and a large increase with polishing. There is also a decrease in performance with increasing build angle away from vertical (0°). Results are normalised to 0° as-built sample.

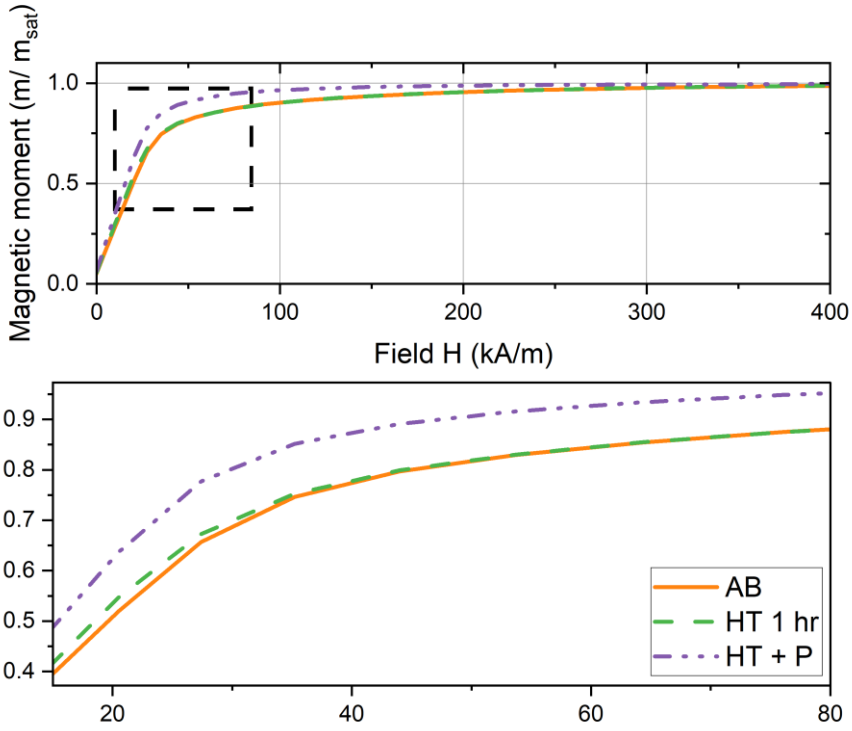

Figure 3-7 – First quadrant of the MH loop for the as-built, heat-treated, and heat-treated + polishing samples all built at an angle of 0°, showing that heat-treatment has a small positive effect but polishing gives a large improvement with a higher susceptibility and saturation knee point.

3.3 Surface roughness improvements

As polishing showed a significant increase in susceptibility, further investigation into the as-built surface roughness was undertaken. Surface roughness measurements from the as-built, 0-90° samples show an increasing surface roughness with build angle (Figure 3-8c) from 31 Sa at 0° to 136 Sa at 90°. To test if improving surface finish in the as-built condition improved magnetic properties, samples were manufactured with a build angle of 0°, with contours at a range of volumetric energy densities (VED) ranging from 50-180 J/mm^3 with either 0, 1, or 2 contours. By introducing contours the average surface roughness can be reduced from 27 Sa with no contours, to 8 Sa with one or two contours (Figure 3-8d), giving a visibly improved surface roughness, which is even more evident from optical 3D surface imaging (Figure 3-8a/b). Little difference was observed in the surface roughness by varying the VED used for the contours. Average values are calculated by measuring the roughness of all four of the long faces, whereas the highest roughness surface was the down skin surface in the build chamber, most likely due to building on top of the powder bed rather than on top of solid material.

Magnetic characterisation was completed for the samples with the highest and lowest surface roughness, of 44 Sa and 5 Sa respectively. These samples were tested in both the as-built and heat-treated condition and the first quadrant of the MH loop is shown in Figure 3-9. The results show a clear improvement of magnetic properties with a lower surface roughness, demonstrating a higher susceptibility, higher knee point, lower field for saturation. Again heat-treatment had a small positive impact, but this was small in comparison to the improvement gained with an improved surface roughness.

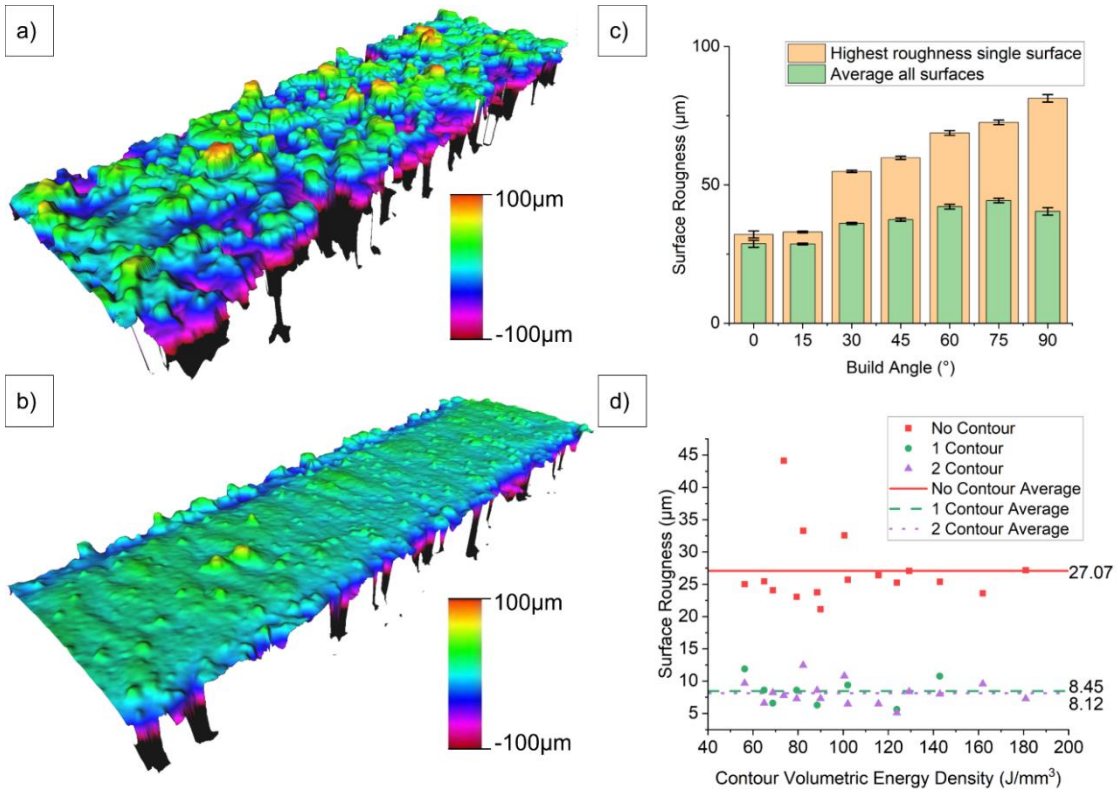

Figure 3-8 – Surface roughness study showing a sample without contours (a), a sample with 2 contours (b), surface roughness vs build angle (c) demonstrating an increasing roughness with build angle for the as-built samples, and surface roughness vs contour volumetric energy density (d), demonstrating a significant improvement in surface roughness with contouring but little difference between 1 or 2 contours.

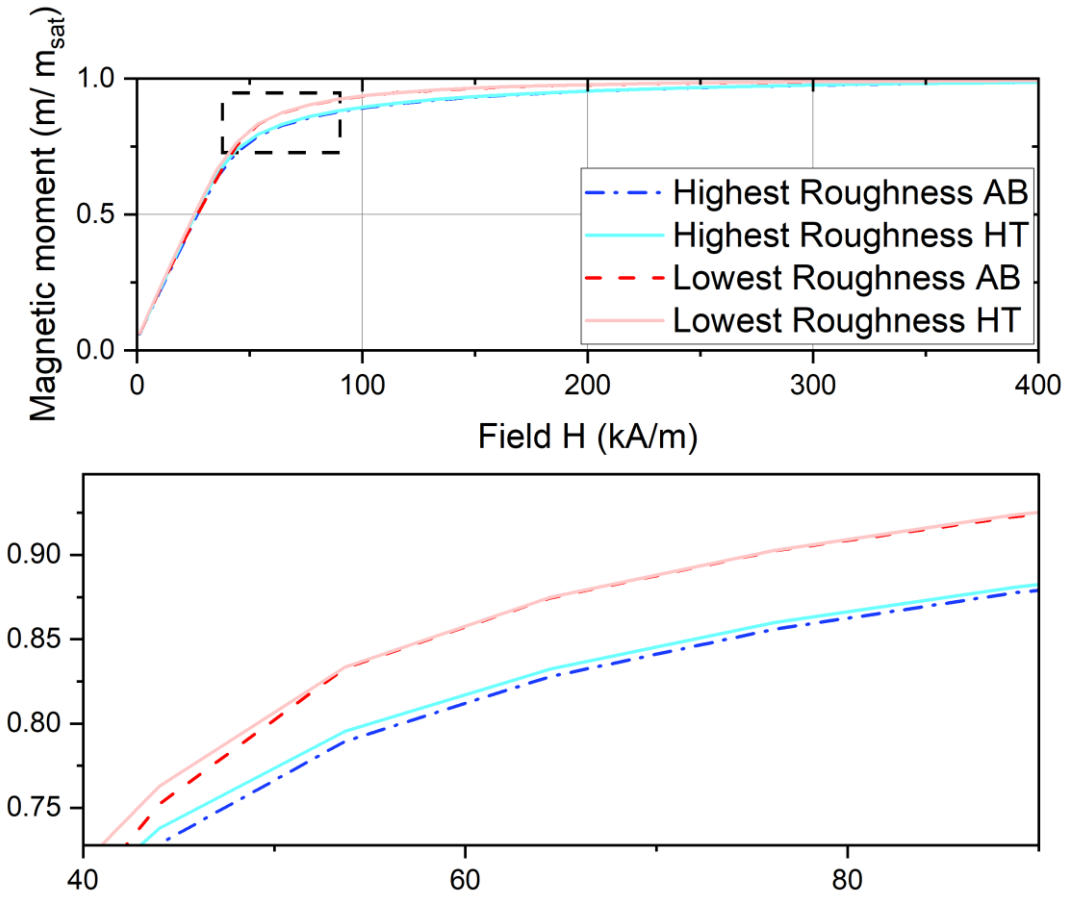

Figure 3-9 – First quadrant of MH loop demonstrating an improved magnetic performance with a lower roughness in both the as-built and heat-treated states. Heat-treatment has a small positive effect on the magnetic performance also. The highest and lowest roughness of the samples was 44 Sa and 5 Sa respectively.

3.4 Heat-treatment improvements

By utilising the heat-treatment demonstrated by Garibaldi et al. (23) of 1150 °C for 1 hr, followed by furnace cooling, this study showed a limited improvement in magnetic properties. Garibaldi et al. demonstrated the recrystallization and grain growth had occurred during this time window. The lack of improvement of magnetic properties suggest that grain growth had not occurred during the heat-treatment of the samples in this study, and to investigate this, EBSD was carried out for the heat-treated samples (1 hour) and the microstructure compared to the as-built samples for all angles. Figure 3-10d shows that for all the samples, the weighted average grain size reduced with the 1 hr heat treatment, demonstrating that partial recrystallisation had occurred but that there had not been sufficient time for grain growth.

To investigate when grain growth would occur in these samples, several samples were built at 0° and heat-treated for 1 hr, 3 hrs, 9 hrs, and 30 hrs. Figure 3-10e shows that grain growth is still happening up to 30 hrs, where grains of 1-2 mm were found in the sample (Figure 3-10b). At 30 hrs significant grain growth has occurred and the magnetic properties of the sample were characterised, as shown in Figure 3-10c. Interestingly the magnetic properties of this sample performed below that of the as-built sample demonstrating a lower normalised susceptibility of 92% (compared to as-built sample). There are multiple factors that could be impacting this, firstly a large amount of porosity was found in the sample after the heat treatment. Secondly, as the grains are now very large in relation to the sample, the texture of a small number of grains could have a significant impact on the magnetic properties. As shown in Figure 3-10b, the texture of the 30 hrs sample is much closer to the <111> direction, or the hard axis of magnetisation of the material. The last explanation could be due to oxidisation changing the phase from Fe-6.5 wt%Si to an Iron oxide, with significantly poorer magnetic properties. The heat-treatment was supposed to take place under argon; however, an oxide layer was found on the samples during EBSD. Oxygen may have entered into the furnace chamber whilst removing samples with a shorter heat-treatment duration.

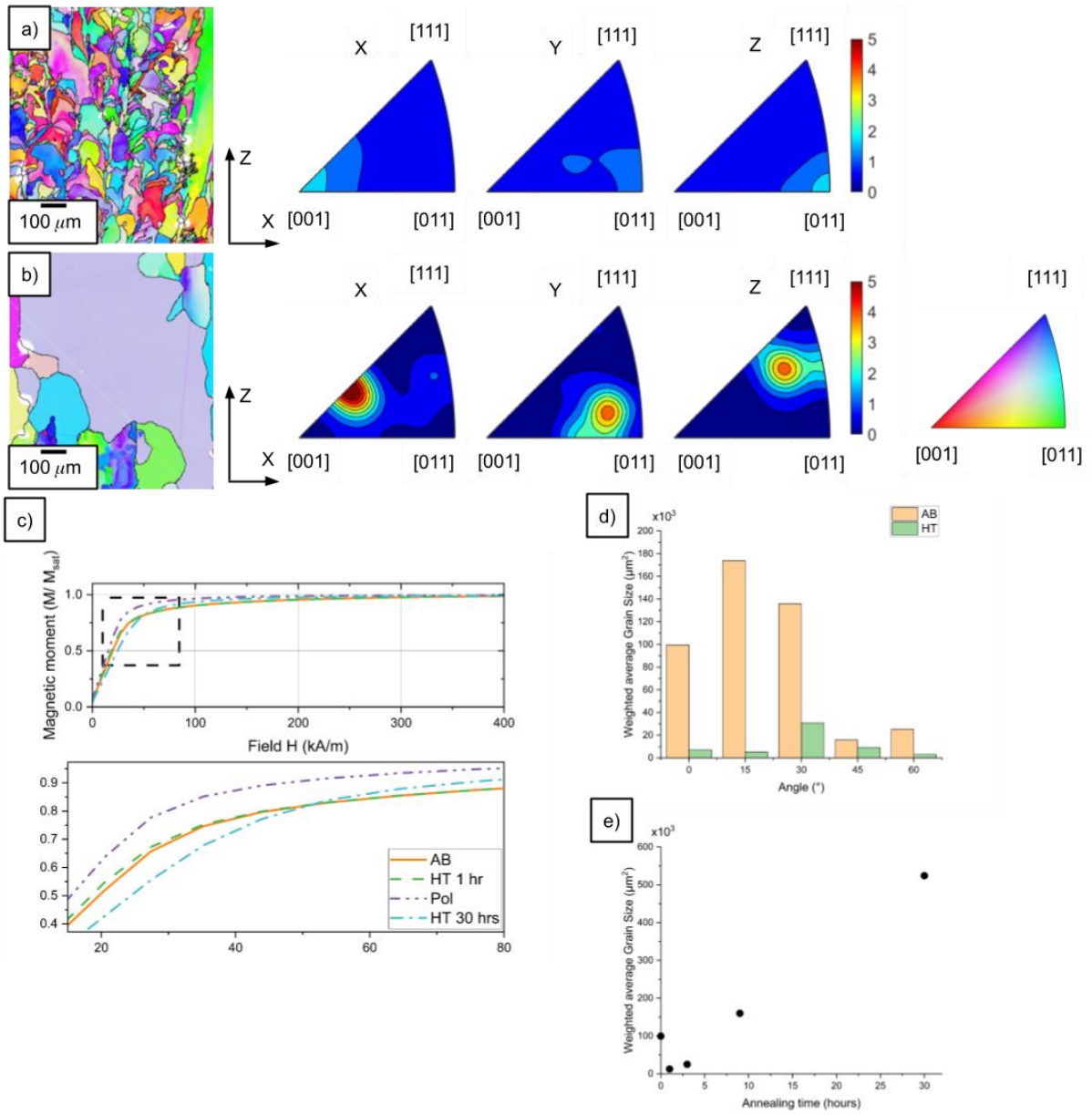

Figure 3-10 - EBSD data of as-built (a) and heat-treated (b) samples with a build angle of 0°, showing partial recrystallisation after heat-treatment for 1 hr. First quadrant of the MH loop for the heat treated samples (c), along with average grain size vs build angle (d) and annealing time (e).

4. Discussion

This study has shown that in this study, for the thin-walled samples of high silicon electrical steel, Fe-6.5 wt%Si, the crystallographic texture is not causing a significant difference in magnetic performance, contrary to the assumptions of multiple authors. EBSD data has shown the crystallographic texture does not persist with build angle, and the high silicon content already reduces the magnetocrystalline anisotropy making grain orientation less important. In this study the performance of thin-walled samples is currently limited mainly by surface roughness, possibly due to a larger surface to volume ratio inherent in thin-walled samples.

This study highlights the need for different parameters when building at different angles, which could be achieved either by a suite of parameters selectively chosen based upon local geometry, or more like in-situ control algorithms to ensure high density and consistent microstructure. The reduction in density of samples such as 45° did not appear to correlate with the decrease in magnetic properties, especially as the sample built at 90° had the lowest density but demonstrated third best performance as judged by the MH loops. However, it is likely that any porosity could act as a pinning site. The porosity was based on micrographs of the cross-section of the samples; however, a more accurate value may be obtained by X-ray computed tomography (XCT).

Surface roughness is shown to be heavily dependent on build angle, which has previously been reported in the literature (75). Improvements to surface roughness in the as-built condition are possible and have shown improvements in magnetic properties, however these are still not as good as when a post-process polishing operation was carried out giving a surface roughness of 2 Sa. This low roughness value is unlikely to be achievable with L-PBF in the near future, and hence other post-processing operations should be investigated such as chemical polishing or electro-polishing. Soft-magnetic materials are likely to require thin wall structures with internal features, making manual polishing difficult. The impact of surface roughness on the magnetic properties such as susceptibility could be due to the pinning of magnetic domains, which may be caused by factors such as excessive roughness or surface features such as partially melted powder particles and spatter.

For soft-magnetic materials increased pinning of magnetic domains causes a decrease in susceptibility, however for hard-magnetic materials the increased pinning caused by the rough surfaces will increase the coercive force and provide an improvement, as they would be harder to de-magnetise (76).

During this study the heat-treatment as specified by Garibaldi et al. (23) did not cause full recrystallisation and grain growth. The samples in this study had a small cross-sectional area of 1 mm^2, compared to the larger samples >15 mm^2 for Garibaldi et al. The reduction in cross-sectional area has also reduced the hatch length during the build, which has been positively correlated with residual stress in L-PBF (77), therefore shorter hatches would reduce the residual stress. Higher residual stress is known to lower the temperature of recrystallisation as the sample would have more internal energy and a larger driving factor for nucleation of new grains (78). The short duration of 1 hr may provide enough time in a larger bulk sample, but for thin-walled samples in this study it proved insufficient and a time of 3 hrs was required for some grain growth, and even after 9 hrs further grain growth was shown. Therefore, in the AM of soft-magnetic components which are likely to require thin wall structures to reduce eddy currents, optimum heat-treatment time may be related to component geometry. Hence, investigation will be required on a case-by-case basis, to reduce the heat-treatment time to the minimum required for recrystallisation and the desired level of grain growth and magnetic properties whilst remaining economical.

In this study the increased grain growth did not show improved magnetic properties, however this is more likely to other factors apparent with the 30 hrs heat treated sample such as oxidisation, increased porosity and change of crystallographic texture towards the harder <111> direction.

Magnetic testing during this study was conducted by using VSM on cuboidal samples. VSM testing does not have a flux closed state and hence the magnetostatic energy would be much higher than the magnetocrystalline anisotropy energy. This means that any shape effects would dominate any measurement of anisotropy if the shape was changed. For this study all the samples used are cuboids of 6x1x1 mm, hence should have the same magnetostatic energy, however these were removed from the baseplate by mechanical force and had the potential to leave the samples with slight differences at one of the ends.

5. Conclusion

In this study, thin-walled samples were manufactured using L-PBF, showing a weak texture when samples are not built perpendicular to the build platform. By building samples at incremental angles to the build platform, it was possible to magnetically characterise the samples along orientations within the build chamber, which showed a decreasing performance with angle. This decreasing performance was correlated to an increase in surface roughness, which is well-known to decrease with build angle during AM. The sample built at 90° (parallel to build platform) showed an exception to this rule, likely due to the better surface roughness of the top surface which would have no staircase effect. Improvements in performance were demonstrated by reduced surface roughness as a result of both improved build parameters and post-process polishing. A heat-treatment at 1150°C for 1 hr was shown to be insufficient to cause grain growth in these samples with a 1x1 mm cross-section, and grains were shown to still keep growing even after 9 hrs of heat-treatment.

Declaration of competing interest

None.

Author contributions

AG: Conceptualization; Data curation; Formal analysis; Investigation; Methodology; Writing - original draft. **IT:** Conceptualization; Data curation; Formal analysis; Methodology; Funding acquisition; Supervision; Visualisation; Writing - review & editing. **FL**: Methodology; Data curation **LC:** Software; Writing - review & editing. (MATLAB processing of EBSD)

Acknowledgements

We wish to acknowledge the Henry Royce Institute for Advanced Materials, funded through EPSRC grants EP/R00661X/1, EP/S019367/1, EP/P02470X/1 and EP/P025285/1, for access to the AconityMINI at The University of Sheffield.

4 Geometrical control of eddy currents in additively manufactured Fe-Si

4.1 Journal details and author contributions:

Materials & Design,

Volume 230,

2023,

112002,

ISSN 0264-1275,

https://doi.org/10.1016/j.matdes.2023.112002.

Author contributions:

Alexander Goodall – Conceptualisation, Methodology, data capture of all magnetic characterisation for samples with complex geometry, investigation, analysis of XCT data and magnetic characterisation data, data curation and visualisation, writing original draft

Georgios Yiannakou – Methodology set up and testing of bulk test rings (AB & HT), writing review and editing

Lova Chechik – support with analysis and interpretation, writing review and editing

Ria Mitchell – Methodology set up and testing of XCT samples, support with data analysis

Geraint Jewell – Support with simulation set up and analysis, support with analysis of BH loops and data interpretation, supervision

Iain Todd – Support with conceptualisation, formal analysis, visualisation, data interpretation, writing review and editing, supervision.

4.2 Background

Soft magnetic components used in alternating current (AC) machines are usually required to manage the eddy current losses, which are both geometry and material dependant. After characterising thin-walled structures, it is possible to start to investigate the types of geometries that may be used to reduce the eddy current losses in large bulk materials. Traditionally electrical steel laminations are used to reduce eddy current losses, however this normally limits EM design to 2D magnetic circuits. Electrical steel laminations have been processed into 3D magnetic circuits before (79), however there are many manufacturing constraints and difficulties and applying this to scale production has rarely been managed. When it has been used this is normally with coil wound laminations, again putting a significant constraint on the geometry.

AM has the ability to create geometrically complex forms, including internal cross-sectional patterns without the same constraints as laminations. However, AM cannot currently process material into sections as thin as laminations (≈0.1 mm), and may never be able to. The surface roughness, as shown in chapter 3, is also significantly worse than laminations. With these two factors, if a magnetic circuit can be manufactured using electrical steel laminations it is likely better to use this method than manufacturing by AM. Therefore, investigation into geometry to limit eddy currents is constrained to shapes that could be processed in any direction within the build chamber, as this is the only area that AM can provide a benefit. It is expected that components made by AM will have

higher losses than thin electrical steel laminations, but that a system level benefit may be achieved in an EM by a 3D magnetic circuit.

The other advantage AM can offer is the ability to process electrical steel with a high silicon content of 6.5 wt%. This material is normally brittle due to ordered phases which form during cooling, however, AM has the ability to process this material into net shape objects which do not require further machining or rolling and can therefore benefit from the increased resistivity that the higher silicon content provides.

This study quantifies the loss behaviour of complex cross-sections manufactured in high silicon steel using AM, with the aim of demonstrating performance close to that of thicker (≈0.5 mm) electrical steel laminations and outperforming SMCs. The ability to successfully resolve these cross-sections in 3D is also investigated, along with methods of improvement that can be used to reduce the likelihood of unwanted electrical shorting.

4.3 Further methodology

Due to the space restrictions in journal papers, the modelling techniques are not described in adequate detail to allow replication, therefore this section will explain the modelling in full. Geometry was created by modelling toroidal rings with dimensions; 30 mm ID, 38 mm OD, 4.5 mm thick, in PTC Creo 7 and then exported to .stp files.

Altair Flux 3D 2022 was used for electromagnetic simulations. Geometry was imported from the .stp files, which modelled 1/40th of the ring. A steady state AC magnetic simulation was used. After importing the geometry an infinite box area was set up using “infinite cylinder”, with inner radius of 22 mm, outer radius of 24 mm, inner half height of 6 mm and outer half height of 8 mm. The part was centred within this infinite box. Periodicity was implemented as 40 repetitions about Y, with even periodicity (cyclic boundary conditions).

Volume regions were then set up within the model. The soft magnetic material was assigned to a volume region defined as “core”, whilst the air surrounding the core was defined as “air”, and then air in the infinite box defined as “infinite”. The two volume regions containing air were set as “air or vacuum region”, whereas the core was given material properties as found in the section 3.1 within the chapter. This was set up as isotropic analytic saturation (arctg, 2 coef) of type BH curve as a “sine wave flux density”, with an initial relative permeability of 10,000 and a saturation magnetisation of 1.5 T. Electrical resistivity used was 82 μΩ.cm, and mass density was 7480 kg/m^3. Iron losses were calculated using the Bertotti method.

The model was meshed using the software’s built in aided mesh generator, using two aided meshlines. The first aided meshline was used along the edges of the soft magnetic core, with an absolute deviation of 80 μm. The second meshline was used along the edges of the infinite box to reduce the computational demands, with 20 segments per line and a ratio of progression R=1. The check mesh function was used to ensure there were less than 2% poor quality elements.

Non-meshed coils were implemented as rectangular coils of dimensions 5 x 5 mm, with a wire radius of 0.75 mm. By modelling one coil, and using duplication by the symmetries and periodicities the rest of the 40 primary coils were taken into account. These coils were connected in series. The electrical circuit consisted of a sinusoidal driven current source driven by a parameter controlled within the solver, a resistor of 1 μΩ, and the non-meshed coils all connected in series, with a connection to ground.

A post-processing support structure was implemented as a 2D grid, 4.5 x 4 mm (the whole cross-section), with 300x300 elements to allow measurement of the average flux density across the cross-section. Flux density was calculated using an operation type sensor, evaluating the average B on the 2D grid. The eddy current losses were also calculated using a sensor to evaluate the “losses by joule effect”, a predefined quantity, on the volume region of the soft magnetic core.

A solver was set up with multiple values of current and frequency. For each value of frequency, current was iterated by starting with two current steps of 0.5 A and 5 A. By interpolating the resulting average flux density, the current was manually iterated until the average flux density was 1.0 ± 0.01 T, at which point the joule losses were recorded. The default solver was used, which converged successfully for all but a few of the models. When the solver did not converge, the mesh was refined by reducing the value of the aided meshline on the core region to half the previous value (40 µm), and rerunning the solver. In this case all models converged correctly.

4.4 Paper

Geometrical control of eddy currents in additively manufactured Fe-Si

Alexander D. Goodall[a], Georgios Yiannakou[b], Lova Chechik[a], Ria L. Mitchell[a], Geraint W Jewell[b], Iain Todd[a]

[a] Department of Materials Science and Engineering, University of Sheffield, Sheffield, UK
[b] Department of Electronic and Electrical Engineering, University of Sheffield, Sheffield, UK

Corresponding Author – Alexander Goodall adgoodall1@sheffield.ac.uk

Abstract

Additive manufacturing has enabled the processing of high silicon electrical steels which have excellent soft magnetic properties. In bulk form, core losses as a result of eddy currents would be too large to allow their use in high frequency electrical machines, therefore strategies are needed to reduce eddy currents. Additive manufacturing affords high part complexity and provides the opportunity for cross-sectional patterns within the material to limit eddy current generation. This study investigates several designs including a novel hexagonal pattern which is shown to have the lowest eddy current loss coefficient of 0.0005, less than 25% of the bulk material which has an eddy current loss coefficient of 0.0021. Heat treatment is shown to increase the eddy current losses, demonstrating that for high frequency machines it may be beneficial to use the material in the as-built state. Physical samples were compared to their intended geometries showing there are defects in these complex cross-sections causing increased eddy currents when compared to simulations, but that geometrical accuracy can be improved by alternative design methodology which experimentally experiences smaller losses. These novel cross-sectional designs may be implemented into an electric machine which has a 3D magnetic flux pathway enabled by additive manufacturing, affording more flexibility for electrical engineers to design new motor architectures in the pursuit of higher power density machines.

Keywords

Soft Magnetic Material

Eddy Current Loss

Fe-Si

Electric Machine

Magnetic Characterization

Abbreviations

AB: as-built

HT: heat-treated

L-PBF: laser powder bed fusion

EM: electric machine

1. Introduction

Electric motors are one of the most widely used electric machine (EM), accounting for approximately 50% of energy consumption in industry (1). With a global drive to improve efficiency and reduce energy consumption, research efforts are being made to improve the performance of EMs, with high power density, fault tolerant and efficient machines for aerospace being a major research focus (80).

Additive manufacturing (AM) has the ability to manufacture parts with complex 3D geometry due to the layer-by-layer process. This technology could enable novel architectures for electric motors to give higher torque density, lighter mass and other benefits (81,82). AM has been used to process both soft magnetic materials (44) and copper (83), which are key materials to enable effective design of electric motors. However, to fully exploit the advantages afforded by AM, these materials must first be characterised, and then implemented using design strategies which capitalise on the advantages of AM.

Electrical steels (Fe-Si) are used extensively in soft magnetic applications due to their high saturation, permeability, and relatively high electrical resistance. Fe-6.5 wt%Si has been shown to exhibit some of the best properties for soft magnets (20,84), however currently Fe-3 wt%Si is used more frequently due to its workability with conventional processes (18). Stacked laminate sheets with a thin layer of insulation between layers is the most common approach to creating soft magnetic cores. By electrically isolating the layers, eddy current losses are greatly reduced, but this limits design freedom to two dimensional systems due to the difficulty of building 3D shapes from thin sheets. AM and specifically laser powder bed fusion (L-PBF) is capable of building complex 3D shapes from high silicon steels (27,85) and other soft magnetic materials (86,87), offering the geometrical freedom to manipulate both magnetic flux pathways and eddy current flows. The ability to improve upon one of more properties of EMs (88) has been demonstrated. Attempts have been made to characterise soft magnetic materials built using L-PBF (6,21,22,25,27,47,85,89,90), however in AM, the processing parameters can affect the magnetic properties important for EM design.

This paper gives an overview of the magnetic properties of L-PBF built Fe-6.5 wt%Si in the as-built (AB) and heat-treated (HT) conditions. Simulations assess the eddy current losses in several cross-sections, designed to capitalise on the geometrical freedom of AM to reduce eddy current losses. These cross-sections are tested experimentally at a range of frequencies between 5-1000 Hz, identifying the eddy current coefficient and quantifying the improvement that can be gained over the bulk. The cross-sections are critically analysed to investigate physical geometry compared to modelled geometry. This demonstrates how the losses in an additively manufactured EM core could be managed to enable three-dimensional magnetic circuits.

2. Experimental Methods

2.1 Sample Processing

High silicon steel powder (Fe-6.5 wt%Si) supplied by Höganäs AB was used for all samples in this paper. The particle size and chemical composition as stated by the supplier is in Table 4.

Table 2 - Fe-6.5 wt%Si Powder Details

Chemical Composition (wt%)						Size Distribution (µm)			
Iron	Silicon	Oxygen	Nitrogen	Carbon	Sulphur	X10	X50	X90	X99
93.735	6.200	0.036	0.016	0.01	0.003	15.67	25.72	42.07	57.23

This powder was processed using an AconityMINI from Aconity3D GmbH. This is a L-PBF machine which uses a 200 W ytterbium doped continuous laser with a spot size of 70 µm. During each layer the laser scans over the cross-sectional area, melting the material which solidifies creating the desired object, see Figure 4-1. The layer rotation angle (θ) was 67° between each layer. This process is completed under an argon atmosphere with an oxygen content of less than 100 ppm. The samples were built onto a stainless-steel build platform of 140 mm diameter with a constant layer thickness (l) of 30 µm. Hatch spacing (h), laser power (Q) and laser velocity (v) were all manipulated during this study. The samples with complex cross-sections were built using Q=140 W, v=0.7 m/s and h=70 µm. All samples were removed from the build platform by wire electrical-discharge machining.

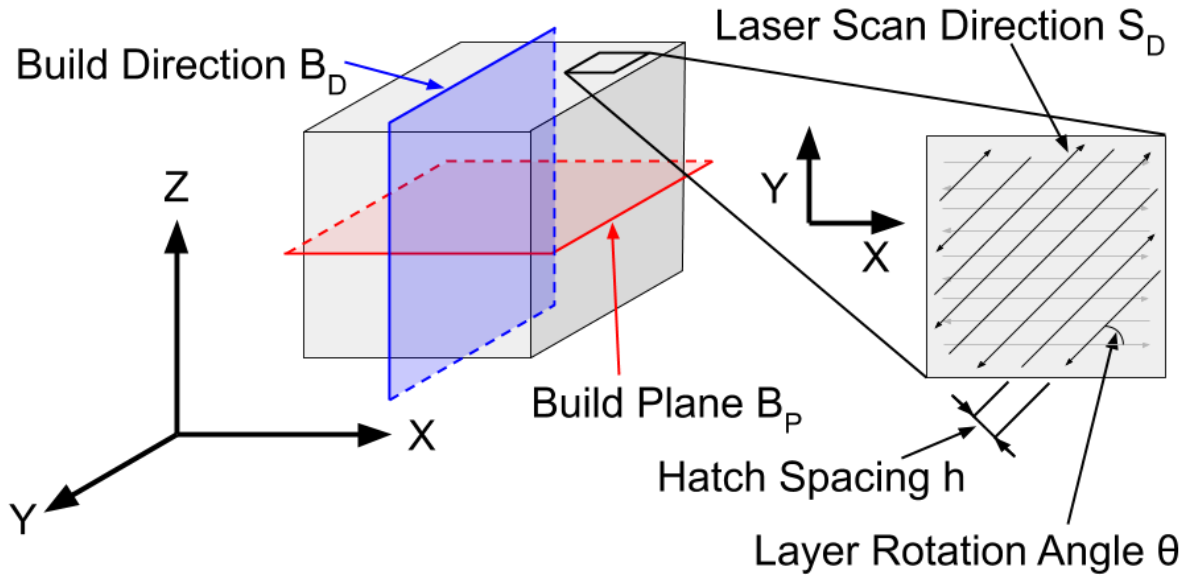

Figure 4-1 - Parameters relating to L-PBF sample processing showing build plane and build direction, laser scan direction, hatch spacing and layer rotation angle

5 mm cubic samples were initially built to understand how the laser parameters affect density, cracking, and microstructure. Volumetric energy density, $E=Q/vlh$, was varied between 37 - 115 J/mm^3 by using a two-level central composite design of experiments, varying the values of 1/h and Q/vl. These values were chosen based upon data available in literature shown to produce high density parts from additively manufactured high silicon steel (21,85).

2.2 Metallographic and Magnetic Characterisation

Cubes were sectioned along the build plane and build direction, see Figure 4-1, and prepared for microscopy using standard metallurgical techniques. An Olympus BX51 microscope was used in conjunction with Clemex Vision PE system to obtain optical micrographs, followed by analysis using ImageJ (91) to determine the density.

Magnetic properties were characterised by testing a toroidal sample with a rectangular section, using an AMH-1K Permeameter by Laboratorio Elettrofisico. The dimensions of the toroid were approximately 30/38 mm inner/outer diameter and 4.5 mm thickness, with each sample being measured accurately with a digital calliper. This was chosen to respect the sample dimensions in BS 60404-6:2018 (92). The secondary search coil used 0.35 mm single core insulated copper wire with 45 coils, whereas the primary driving coil used 1.5 mm multi core insulated copper wire with 40 turns in two layers. DC normal magnetisation curves were used to obtain the maximum relative permeability (μ_{max}) and coercive force (H_c) was measured using a quasi-static B-H loop to allow direct comparison with literature. AC power losses were obtained from B-H loops measured at various frequencies between 5-1000 Hz. For the complex cross-section samples, a full ring was used for magnetic characterisation and one quarter of a ring used to analysis the cross-section and stacking factor (SF) with optical microscopy. SF is the percentage volume of material/ total volume including insulation (air gaps).

Power losses during magnetic cycling can be described by Equation 11 (93).

$$P_{loss} = C_0 B_m^2 f + \frac{\pi^2 t^2}{6\rho}(B_m f)^2 + C_1 B_m f^{1.5} = P_h + P_{EC} + P_{Ex}$$

Equation 11

Where P_{loss} is the total power loss, f is the frequency, B_m is the flux density which is 1 T for this study, ρ is the resistivity of the material, t is the thickness of the material, C_0 & C_1 are constants, P_h, P_{EC} & P_{Ex} are hysteresis power loss, eddy current power loss and excess power loss respectively. This equation only applies to solid material and hence the $\frac{\pi^2 t^2}{6\rho}$ term can be replaced with a constant for this study C_{eddy}, which will express the benefit of the cross-sectional designs. The inclusion of C_1 did not improve fitting of the data and was set to 0 for this study. Hence the power losses in this study are described by Equation 12, with energy loss per cycle (E_{cycle}) described in Equation 13. B_m has been removed due to $B_m = 1\ T$.

$$P_{loss} = P_h + P_{EC} = C_{hysteresis} f + C_{eddy} f^2$$

Equation 12

$$E_{cycle} = C_{hysteresis} + C_{eddy} f$$

Equation 13

AC measurements were taken at a number of frequencies. By plotting energy loss per cycle vs frequency, and using a linear fit, the hysteresis ($C_{hysteresis}$) and eddy current loss coefficients (C_{eddy}) can be obtained, as demonstrated in Figure 4-7. Errors for C_{eddy} were calculated by using the sum of squares error method.

HT (heat treatment) of toroidal samples was performed in a tube furnace under an inert argon atmosphere using the best HT regime identified by Garibaldi (23), 1150°C for one hour, followed by furnace cooling to room temperature.

2.3 Electromagnetic Simulation

To observe and compare eddy current generation and flow inside the complex cross-sections and bulk material, multi-physics electromagnetic simulations were performed using a steady state AC model in Altair Flux. A model was set up to mimic the physical toroid using the same geometrical dimensions and number of turns in the primary coil. 1/40th (1 turn on the primary coil) of the system was simulated due to the symmetry of the system and to reduce the computational demand. Non-meshed coils were used, whilst the mesh was created with the aided mesh generator. The modelled electric circuit consists of the magnetisation winding connected to a sinusoidally driven current source of frequency 50 Hz. The amplitude of the current was varied to reach an average flux density value of 1 T, as measured by a radial-section cut-plane through the material. The measured Joule losses (P_{ec}) were then divided by f^2 to give C_{eddy} (Equation 2). It was confirmed that C_{eddy} was independent of frequency in the simulations by running the bulk cross-section at several frequencies between 5-1000 Hz. The material properties used are taken from the measurements of the bulk sample, and were inputted as type – "isotropic analytic saturation" (arctg, 2coef), with initial relative permeability of 10,000, saturation magnetisation of 1.5 T, with electrical resistivity set as "spatial isotropic resistivity" of 8.2 x 10^{-7} Ohm.m. An example of the model for the bulk cross-section is shown in Figure 4-2.

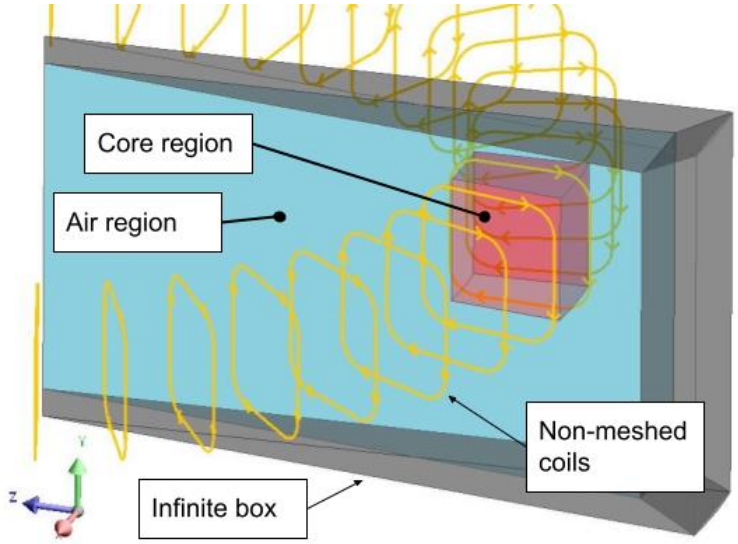

Figure 4-2 Altair flux 3D model used to simulate eddy current losses in toroidal samples, showing the different volume regions and the coils and symmetry used.

2.4 X-ray Computed Tomography (XCT) and analysis

A toroidal sample was mounted on a sample holder and scanned using a Zeiss Xradia 620 Versa X-ray microscope (XRM). X-rays were generated from a tungsten transmission target and collected on a CCD (charge coupled device) 16-bit 2000 x 2000 pixel detector. Approximately ¼ of the ring was scanned, achieving a voxel (isotropic 3D pixel) resolution of 16.7 µm. A filter (HE6) was inserted to reduce unwanted lower energy X-rays. 1601 projection images were collected per sample, and a 2 s exposure time was applied to improve signal-to-noise ratio. A filtered back projection method was

used to reconstruct the data, and reconstructed .txm volumes were converted to 8-bit greyscale image stacks (.tiff) using Zeiss Reconstructor software.

Tiff images were orientated to view the build plane (XY) in order to give a consistent cross-sectional pattern for the slotted sample. Using ImageJ (91), an area of 7 x 5 mm was cropped for analysis, and the image binarized by thresholding. By measuring the total width of the short circuit connections and dividing by total width, a % of electrical shorting can be measured (Figure 4-3). Through the sample, 10 images with 160 µm vertical (Z) gap between them were analysed for short-circuiting and the results averaged. For the hexagonal samples, 9 images were used, three from each of the vertical sides of the hexagons, separated by 100 µm.

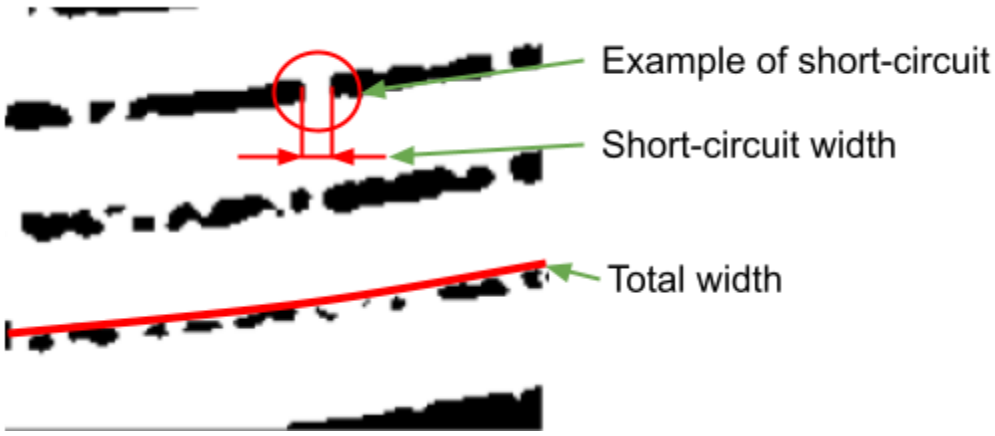

Figure 4-3 - Example of XCT short-circuiting analysis showing the binarized image with an example short-circuit and total length highlighted.

3. Results and Discussion

3.1 Bulk Processing and Magnetic Characterisation

5 mm cubes were used to assess the processing window for Fe-6.5 wt%Si. For all samples, the density in the build plane was higher than build direction, therefore the results shown are from the build direction to give a conservative approach. Lower energy density led to lack of fusion defects and low density, Figure 4-4b, whilst higher energy density introduces cracking and keyhole porosity, as shown in Figure 4-4d. The best parameters found to give a density of over 99.5% were Q=170 W, v=0.7 m/s and h=70 µm. This set of parameters has been used for all subsequent samples.

The thermal conditions during the build process for the toroidal samples are different to that of the cube despite the cross-sectional area being similar. The inter-layer time will be increased in the complex cross-sections, and the heat transfer out of the component will be changed due to the thinner walls, surrounded by powder which will act as an insulator when compared with bulk material. These differing thermal conditions may impact the microstructure of the toroidal samples compared to that of the cubes.

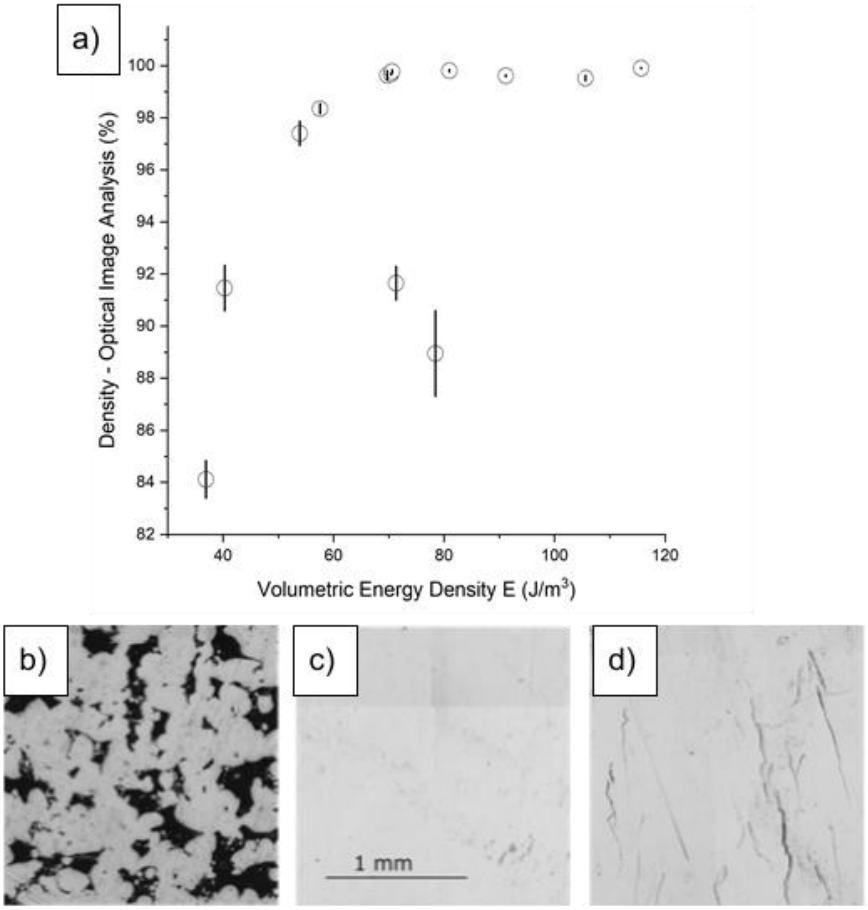

Figure 4-4 Results showing the effect of changing laser parameters on the density of Fe-Si samples. Error bars show standard error. The samples increase in density up to 70 J/mm³, whereby increasing energy density does not improve density. There are two outliers with density below 92% with an energy density of above 70 J/mm³ due to melt pools which have been modelled to be thinner than the hatch spacing. Lack of fusion (b) results from low energy density whereas cracking (d) occurs from too high energy density.

The magnetic properties of the bulk material were measured in both AB and HT conditions. The coercive force is measured at 143 A/m in the AB condition, which is reduced to 26 A/m for the HT sample. The maximum permeability achieved in this paper is 9,800 for the HT sample, significantly lower than Tiismus et al. who achieve 28,900 (61) and Goll et al. who achieve 31,000 (85). Hence there could be an improvement of the material properties in the bulk condition in this study, as factors such as density, grain size and surface finish could be optimised to yield an improvement but is outside the scope of this work.

The BH loops at 1 T for frequencies of 5 Hz and 1000 Hz are shown in Figure 4-5, demonstrating a large reduction in losses (BH loop area) with HT at 5 Hz, but an increase at 1000 Hz. Losses were measured at a variety of frequencies as shown in Figure 4-6, showing that at low frequency the HT sample outperforms the AB sample, whereas at high frequencies, this is reversed. The losses cannot demonstrate the full picture however as the shape of the BH loops in Figure 4-5 show, the knee point is lower, and a higher field is required to obtain the same flux density within the AB toroid especially at low frequencies. The stark difference between the shape of these BH loops (Figure 4-5) demonstrates the difference between hysteresis dominated losses at low frequency, and eddy current dominated losses at high frequency. At low frequency the hysteresis losses which are dependent on the material properties account for the majority of the losses. These can be improved by microstructural manipulation such as increased grain size, reduced residual

stress, reduced number of non-magnetic inclusions along with any other improvements that reduce the energy required for domain wall movement. Eddy current losses however are shape dominated and therefore we see little difference between the as-built and heat treated samples. To reduce eddy current losses, the only material property influencing this is resistivity which usually shows little change with heat treatment.

Further work is required to understand the lower losses of the AB sample at high frequency, but it is suspected that the larger grain size of the HT sample is causing an increase in eddy current losses (94). The losses at higher frequencies are dominated by eddy currents rather than hysteresis losses, hence the increased hysteresis losses of the smaller grains with higher grain boundary density are less impactful than the increased eddy currents given by the larger grains. As a result of this, the smaller grain size of the AB condition (23), could give a benefit in high frequency machines.

Figure 4-7 shows the data for the linear fit of Equation 13 with an R^2 value of 0.998, demonstrating that we can effectively calculate both the y intercept, $C_{hysteresis}$ (0.0419)and the gradient, C_{eddy} (0.0021). 1000 Hz measurements were excluded from this data set as the eddy currents get very large.

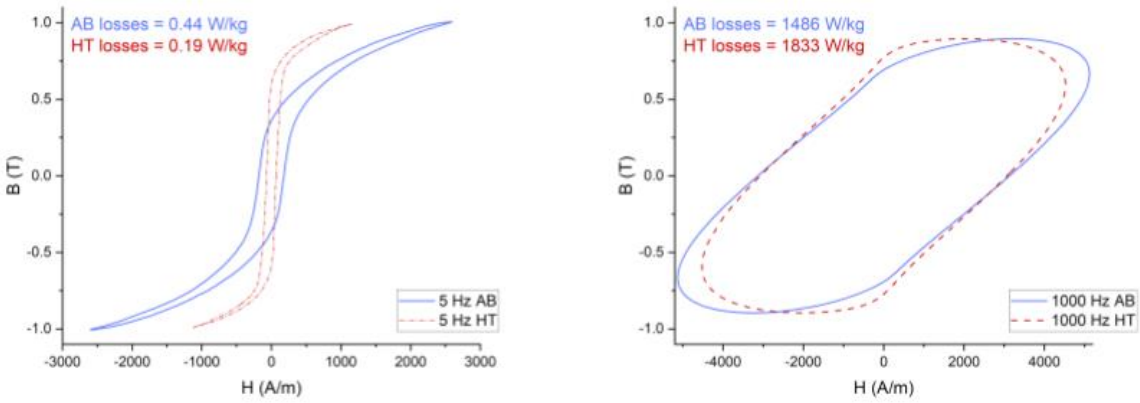

Figure 4-5 BH loops of the AB and HT condition at 1 T 5 Hz, and 0.9 T 1000 Hz, showing the specific losses (W/kg) demonstrating that HT gives an improvement at 5 Hz but performs worse at 1000 Hz. As this setup can only use a field of 5000 A/m, the 1000 Hz samples were measured at a lower flux density of 0.9 T.

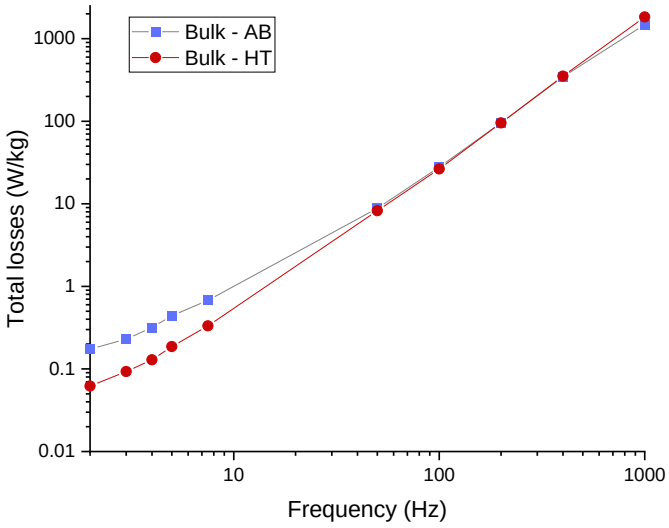

Figure 4-6 - Loss behaviour at flux density of 1T for various frequencies, showing that the HT gives an improvement in losses at low frequencies but above 400 Hz, the AB condition demonstrates lower losses.

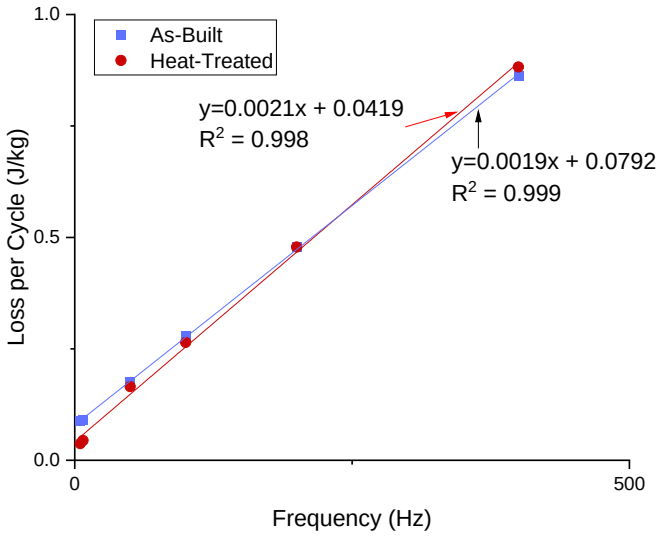

Figure 4-7 - Energy loss per cycle showing that the linear fit can successfully obtain C_{eddy} and $C_{hysteresis}$.

3.2 Complex cross-section eddy current losses

As the power losses at high frequencies are significantly above that of currently available soft magnetic materials, AM of bulk soft magnetic materials will be of little use in high frequency machines. Just as electrical steel laminations are used over bulk electrical steel, when utilising this material for AM, alternative strategies must be used to limit the eddy current generation. As shown by Goll, Plotkowski and Tiismus (27,61,85), features may be designed into the cross-section of the material to reduce the generated eddy currents by forcing them to experience a longer, more resistive path. The most complex of these is the Hilbert pattern (27), which has been demonstrated

in 2.5D, with a constant cross-section in the build plane. To capitalise on the geometric freedom of AM, flux pathways must be able to run in three-dimensional space, otherwise electrical steel laminations would likely experience lower losses at a lower cost. This study will only focus on complex cross-sections which could be produced at any angle in the build chamber. When the cross-section is resolved in the build plane, the laser accurately controls the edges, giving the best resolution, whereas in the build direction, the laser can often penetrate multiple layers, giving difficulty in precise control over horizontal or overhanging surfaces. When complex cross-section toroids are built, they use the same parameters as when processing bulk sections, however the cross-sectional area has multiple thin sections (≈1 mm). As can be observed in Figure 4-8, this has caused some porosity in the sample. This highlights the importance of tailoring parameters for each individual component or for process-control to give a consistent outcome.

To compare several cross-sections, electromagnetic simulations were carried out and the eddy current losses assessed (hysteresis losses are not included). The three best cross-sections are shown in this paper which are the Hilbert pattern first shown in this context by Plotkowski (27), the slotted pattern first shown by Goll (inner slits) (85) and a novel hexagonal design, designed to limit eddy currents to several separated segments. This hexagonal section has periodic (1 mm thick) supporting structures around the toroid which have been omitted from these figures for clarity. These cross-sections are shown in Figure 4-8. The simulations enable us to observe the current flow in the cross-section, which demonstrates a difference in the method of loss reduction between the slotted and Hilbert patterns, which direct the eddy currents over a longer path when compared to the hexagonal pattern, which contains the eddy currents within a smaller area as shown in Figure 4-9 (and in more detail in **Appendix 1**).

When compared to the bulk cross-section throughout the frequency range, the Hilbert and slotted cross-sections showed only 4% of the eddy current losses, with the hexagonal cross-section showing 10% of the losses. The eddy current coefficients of both the simulated and measured physical samples are shown in Figure 4-10, demonstrating that the simulations for the bulk cross-section have a good correlation to the measured results. The simulations are overly optimistic for the complex cross-sections, as although all of these patterns do show an improvement over the bulk material they do not perform as well as predicted in the simulation. For all the samples it is shown that C_{eddy} and hence eddy current losses, increase with heat treatment. This is likely due to microstructural changes such as increased grain size, reduced residual stress etc. Hence for high frequency machines it may be beneficial to not heat treat components, though further study is required to fully understand this. To be used in an EM, there are other important material performance parameters to inspect such as permeability, saturation and BH loop shape. Figure 4-11 demonstrates the BH loops for the best performing cross-section which is hexagonal. The area of the BH loop is smaller showing the decrease in losses, however the permeability is lower meaning that a machine would require a higher field to obtain the same flux density.

Simulations such as those above, could allow for design optimisation. Modifying the size of the hexagons based on their location, with larger hexagons at the centre and smaller hexagons at the edge where the eddy currents are higher, or differing average hexagon size based on the intended frequency of operation. The cross-sections used in the simulation also assume that the pattern is accurately resolved in the AM process, whereas Figure 4-8 shows that in the physical samples there are errors in the resolution of the desired design, with shorting between areas which should be electrically isolated and some cracking and porosity.

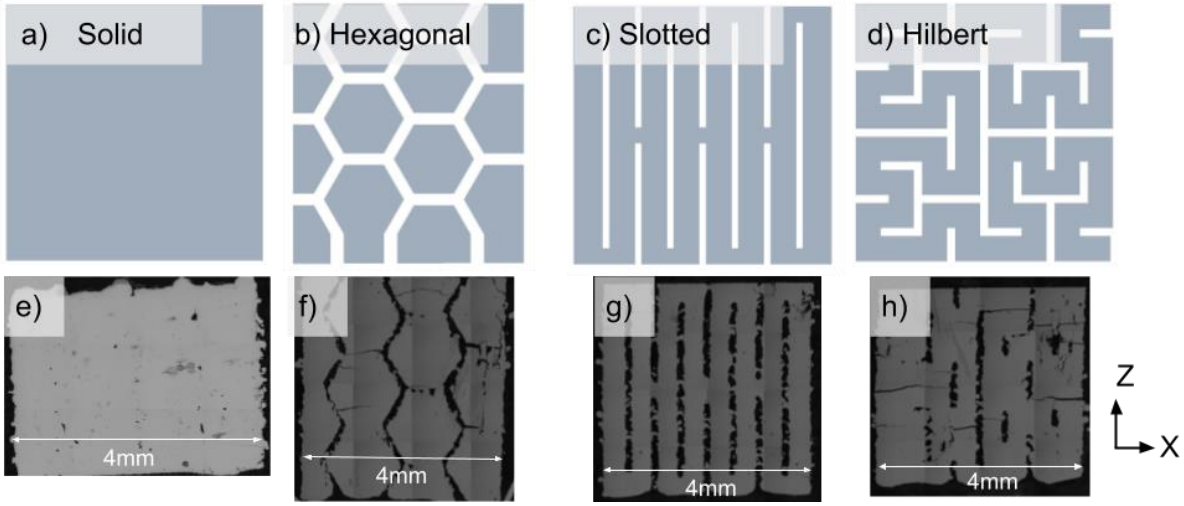

Figure 4-8 – Solid (a,e), Hexagonal (b,f), slotted (c,g) and Hilbert (d,h) cross-section showing a micrograph of the AB sample after removal from the baseplate (e,f,g,h), and the cross-section as per the design (a,b,c,d). Micrographs show the build direction (Figure 4-1)

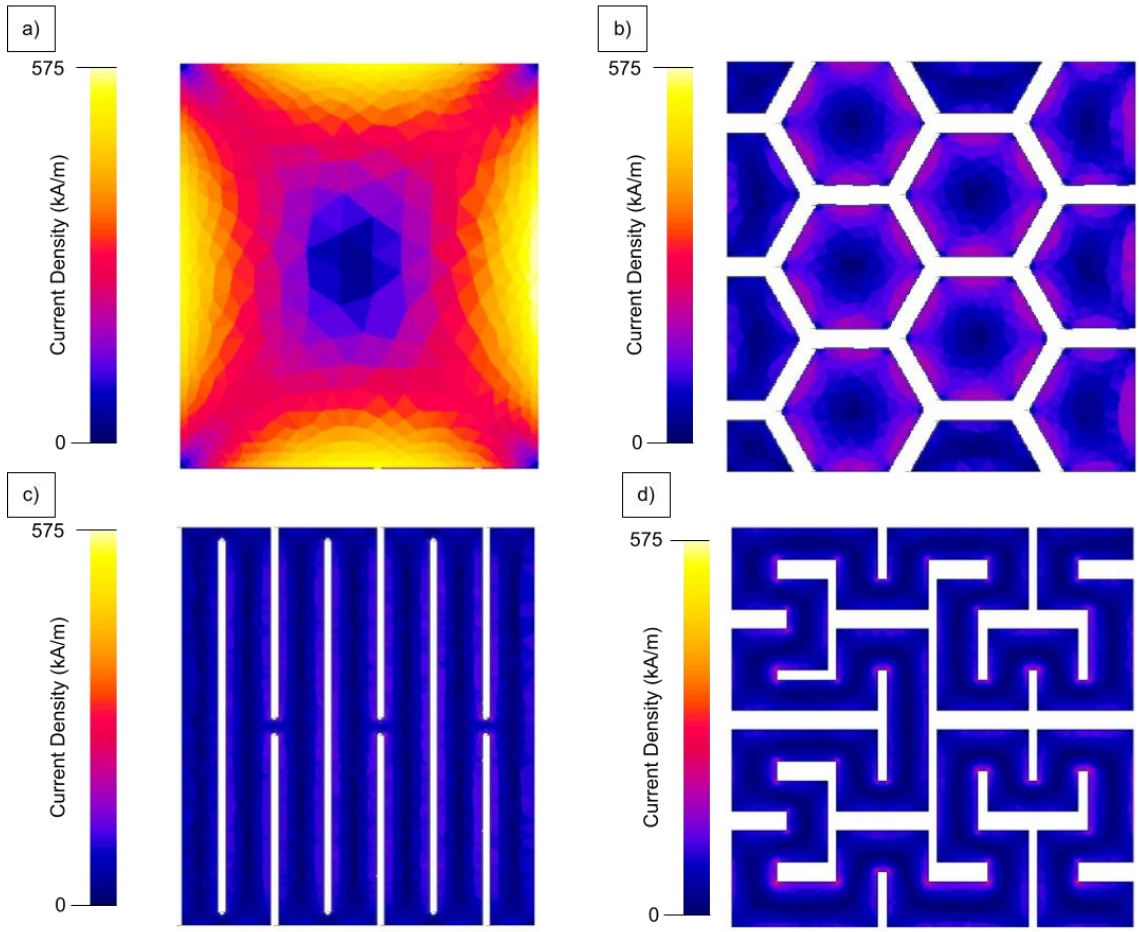

*Figure 4-9 - Display of eddy current density inside the bulk section and complex cross-sections, demonstrating a clear reduction in eddy current density for all the complex cross-sections. This enables the current paths to be observed showing the difference between the hexagonal section which constrains the eddy currents to smaller areas, and the slotted and Hilbert sections which force the currents over longer paths. Full images of each can be found in **Appendix 1** including arrows indicating current flow direction.*

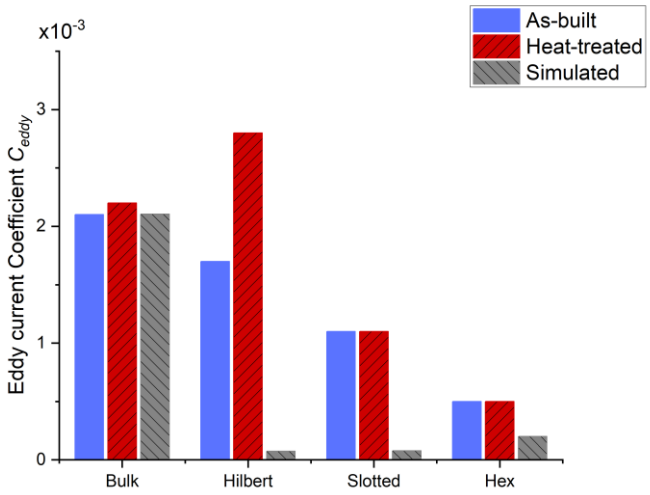

Figure 4-10- Eddy current losses during electromagnetic simulations of the complex cross-sections compared to the bulk cross-section, performed at a flux density of 1 T with varying frequencies. All the complex cross-sections showed an improvement over the bulk, with the hexagonal cross-section showing the lowest losses at approximately 6% of the losses of the bulk cross-section.

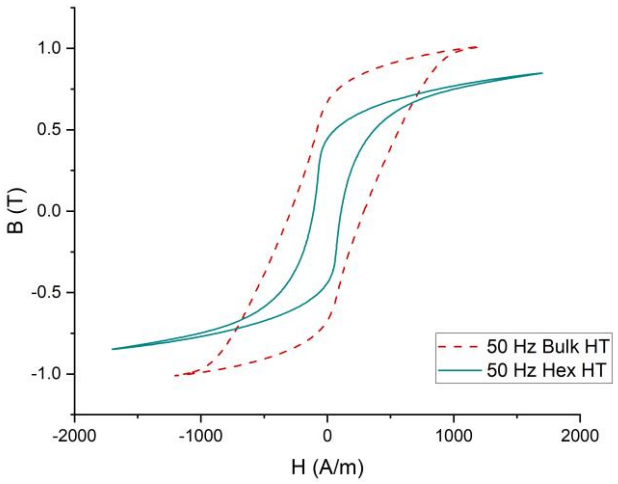

Figure 4-11 - BH loops of bulk and hexagonal cross-sections at 50 Hz, showing that although the hexagonal section has significantly lower losses, it requires a larger field to obtain the same flux density. The initial permeability is better for the hexagonal sample however the knee point of the BH loop is at a lower flux density, at approximately 0.5-0.6 T rather than 0.7-0.8 for the bulk cross-section.

As there is such a disparity between the simulated values and the measured values of C_{eddy} for the complex cross-sections, further investigation into the slotted sample was undertaken as this was the simplest geometry. Figure 4-12 shows a micrograph of the slotted cross-section, demonstrating a number of issues in the resolution of the desired geometry. Firstly, there are large pores which have the morphology of lack of fusion defects. This could be caused by using the same parameters for a 5 mm thick cross-section and a 0.5 mm thick cross-section which will have different thermal conditions. There is also some cracking apparent, which could be caused by the sharp changes in geometry giving rise to stress concentrations whilst cooling. There is also a possibility this cracking occurred during hot mounting. However, the most important issue for soft-magnetic components is surface roughness, which causes unwanted electrical contact between areas which should be

isolated, termed shorting. This gives pathways for eddy currents to circulate which are not intended in the design of the geometry.

To quantify the amount of shorting between areas which should be separate, XCT of the slotted sample was undertaken in order to give a three-dimensional representation of this defect (Figure 4-13). The XCT data achieved a voxel size of 16.72 µm, due to the sample thickness. This gives sufficient resolution to see defects which are causing connections. It was found that throughout the sample, 10 ± 2% of the area was electrically connected. This equated to an increase of C_{eddy} from the simulated value of 7.8 x10^{-5} to 110 x10^{-5}, over an order of magnitude larger. Therefore, to improve the performance of these cross-sections, improved surface finish would be required, which would reduce electrical shorting, providing large gains as shown by the disparity between simulated and physical results. There are multiple ways of doing this, such as optimising contour parameters during the process, or post processing operations such as electro-polishing.

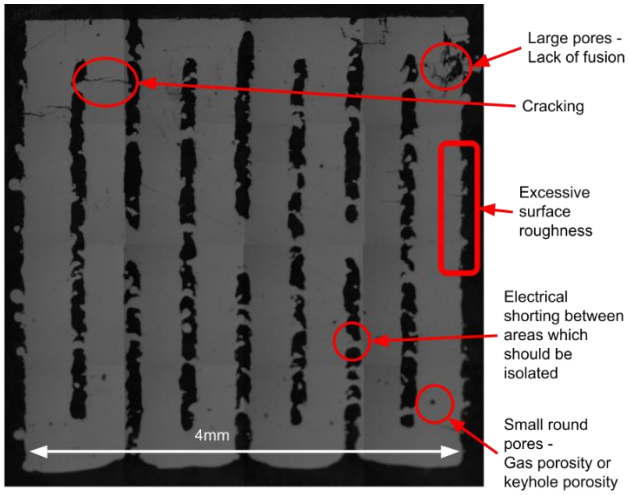

Figure 4-12 - Errors in resolution of cross-section such as shorting, missing air gaps or cracking/porosity.

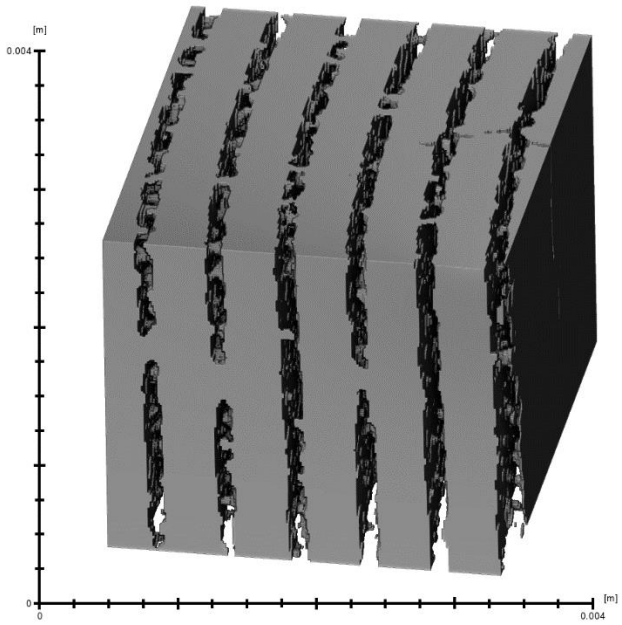

Figure 4-13 – XCT data of slotted ring showing the electrical shorting between areas which should be isolated. The voxel size attained is 16.72 µm due to the relatively thick sample.

3.3 Cross-section design and stacking factor

Further to the surface roughness, improvements in cross-sectional resolution can be obtained by design of the cross-section. Although it can be possible to build unsupported horizontal surfaces for short distances, in general, this is avoided in AM. Hence the Hilbert cross-section used throughout this study is unsuitable for use in any other than the build plane (XY plane), as demonstrated by Figure 4-14c which shows how poorly the physical sample resembles the intended design (Figure 4-14a). In order to ensure 3D flux pathway capability other designs are necessary which can be built in any orientation. Figure 4-14b shows a modified Hilbert cross-section which has been designed to enable building in any orientation in L-PBF by reducing overhanging surfaces to less than 45° overhang, which has been built in the build direction (Figure 4-14d). This section shows an improvement and demonstrates cross-section is almost as per the design, however, would need further optimisation to be the identical. The modified Hilbert cross-section shows a higher C_{eddy} in simulations, however the physical sample demonstrates an improvement with a lower C_{eddy} than the original Hilbert cross-section (Figure 4-14e). In order to further improve these cross-sections, a tool to optimise the topography based upon electromagnetic simulations with manufacturing constraints considered is needed, this would enable the optimum design to be found which would likely be both machine and location (within the machine) specific. Garibaldi et al. (39) have attempted topology optimisation for soft magnetics, considering both mechanical stress and magnetics to reduce the weight of a rotor, however this does not take into account eddy current behaviour. In a stator where the mechanical stresses are low, this optimisation would likely be able to ignore mechanical stress whilst optimising for magnetic performance (including losses). By ensuring the printability of the cross-section, air gaps can be minimised increasing the stacking factor (SF).

The SF is an important material selection parameter for soft magnetic cores, with a higher SF meaning there is more material to give a higher total flux with the same field. Modern electrical steel laminations can obtain SFs upwards of 95%, whereas the complex cross-sections shown so far in this paper have SFs of 90%, 86% and 91% for the hexagonal, slotted and Hilbert sections respectively. However, all these cross-sections show error in the resolution of the intended design, as demonstrated in Figure 4-12.

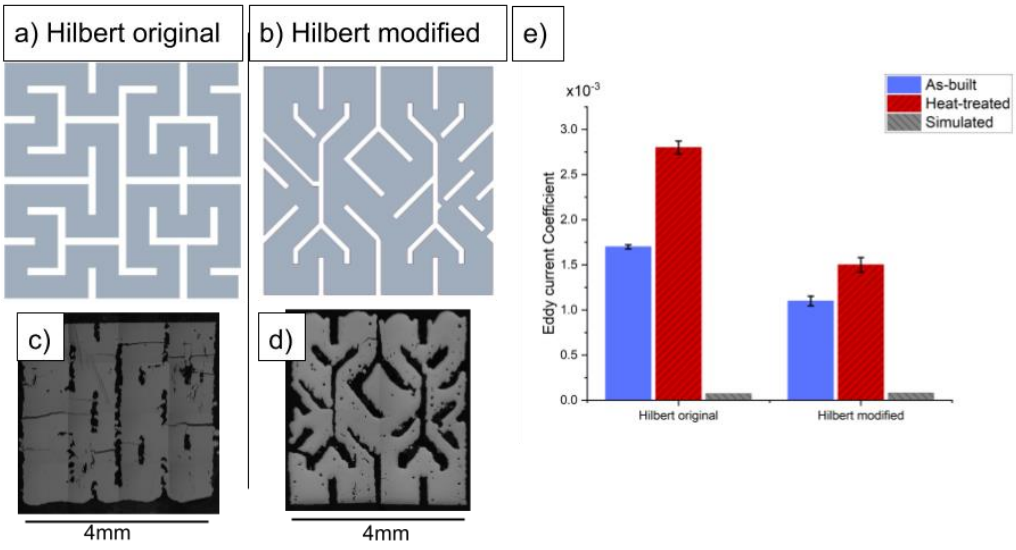

Figure 4-14 – Hilbert and modified Hilbert cross-sections, where the modified cross-section has no surfaces which would overhang by more than 45°. Micrographs of these sections demonstrate that the modified Hilbert section is more similar to the intended design. Losses are shown (e), whereas the Hilbert section shows lower losses in the simulation, the modified Hilbert section shows lower losses in the physical sample, due to more accurate representation to the desired geometry.

Another method to reduce the likelihood of shorting between areas which should be electrically isolated by an air gap is to increase the nominal width of the air gaps. By using a modified hexagonal section with no overhanging surfaces above 45° to the baseplate, the air gaps are modified in size as shown in Figure 4-15. Increasing these air gaps has a positive effect on the loss behaviour as shown in Figure 4-16, explained by reduced electrical shorting between areas which are supposed to be isolated, from 27% for the 100 µm gap sample to only 0.5% for the 200 µm gap sample. This does however have an undesirable effect on the SF, by increasing the air gaps the SF is reduced from 87% for the 100 um gap sample, to only 74% for the 200 µm gap sample. It's also worth noting that for the 200 µm sample other build defects were more prevalent that the other samples such as cracking or porosity, however there was very little electrical shorting. It appears that the support structures between the hexagons were not sufficient in the 200 µm sample as the hexagons at the top are not in the correct position and appear to be 'slumping' onto the ones below.

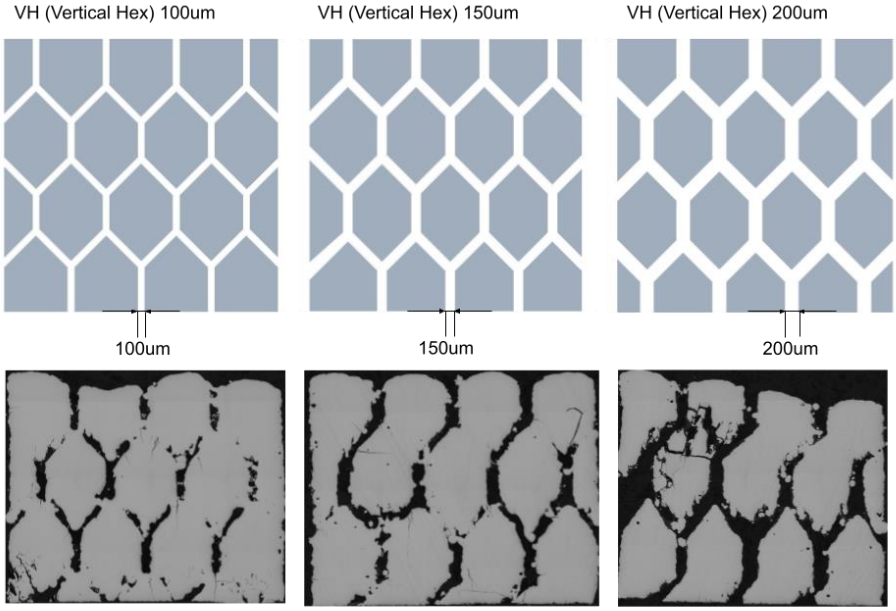

Figure 4-15 – Diagram showing the increasing size of the air gap between sections which need to be electrically isolated, demonstrating that the larger the gap, the less undesirable electrical shorting between areas which should not be connected. However, the larger the gap the less material in a given area and the lower the stacking factor.

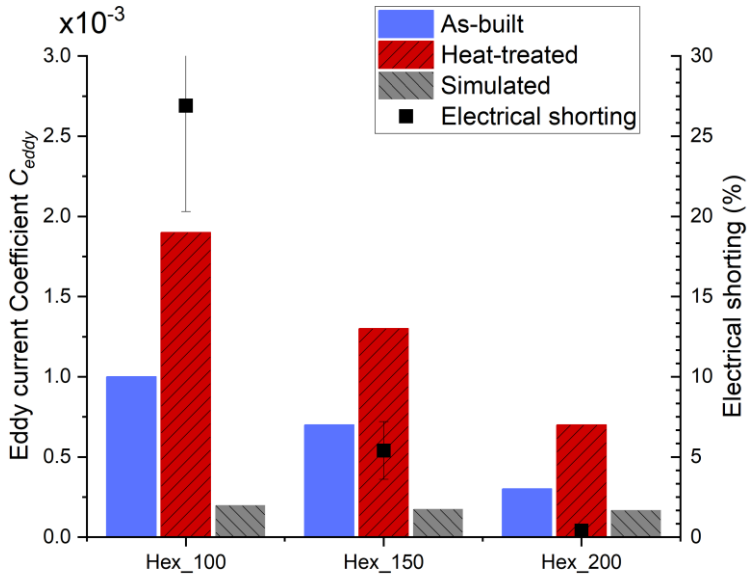

Figure 4-16 - Loss behaviour of hexagonal cross sections AB with differing air gaps and designs from Figure 4-15. The lowest losses are for the HH section with 200 um gaps, as can be seen in Figure 4-15 this has the best electrical isolation between the different sections. The VH sections show the losses reducing with an increasing air gap size, however this also reduces the SF from 87% to 74%.

To better resolve the cross-sections and decrease the air gap, the surface roughness of the builds could be improved. This would reduce the electrical shorting between areas which are intended to be insulated from each other by air but could also mean that the air gaps could be reduced in width, resulting in a higher SF. Improving the surface roughness may also improve the magnetic properties as the rough surface could act as pinning sites for magnetic domains, reducing the permeability and increasing the coercive force and losses. Post processing may also be used to improve this such as chemical polishing or electro-polishing.

4. Conclusion

In this paper we demonstrate an ability to process fully dense (>99.5 %) high silicon steel using L-PBF, with magnetic properties of H_c = 26 A/m, μ_{max} = 10,000 and B_{50} = 1.3 T, sufficient to be useable in an EM. A novel hexagonal cross-section was shown to significantly reduce the eddy current coefficient, $C_{eddy,}$ from the bulk value of 0.0021, to 0.0005. Simulations were shown to correlate well with the bulk cross-section, but physical samples with complex cross-sections underperformed when compared to the simulations. The hexagonal section outperformed both the Hilbert and slotted cross-sections previously produced in literature. Difficulties were found when trying to build the cross-sections in three-dimensions, which were shown to improve with modified cross-sectional geometry to reduce horizontal overhanging surfaces. Electrical shorting between areas which should be insulated from each other was shown to be approximately 10 % for the slotted cross-section, yielding an order of magnitude decrease in performance from that predicted by simulations. By increasing the air gap the electrical shorting was improved from 27% to 0.5% in the 100 µm and 200 µm gap hexagonal samples respectively, with the 200 µm gap sample being the closest to the simulated value at just under double the eddy current coefficient. Improvements in surface finish and accurate reproduction of the desired geometry is likely to give further performance benefits,

which could be achieved with either process parameter optimisation or post-processing, which will also aid in improving stacking factor to higher than 90%. The eddy current loss coefficient C_{eddy} was shown to increase in all samples after heat-treatment, suggesting that the as-built condition may give lower losses for high frequency machines.

Declaration of competing interest

None.

Author contributions

AG: Conceptualization; Data curation; Formal analysis; Investigation; Methodology; Writing - original draft. **IT:** Conceptualization; Data curation; Formal analysis; Methodology; Funding acquisition; Supervision; Visualisation; Writing - review & editing. **LC:** Software; Writing - review & editing. **RM:** Data curation; Methodology. Support in design of experiments and data capture of XCT. **GJ:** Data curation; Methodology. Support in design of experiments, data capture and analysis of magnetic measurements. **GY**: Data curation; Methodology. Support in design of experiments and data capture of magnetic tests.

Acknowledgements

We wish to acknowledge the Henry Royce Institute for Advanced Materials, funded through EPSRC grants EP/R00661X/1, EP/S019367/1, EP/P02470X/1 and EP/P025285/1, for access to the AconityMini at The University of Sheffield. We also acknowledge Sheffield Tomography Centre and University of Sheffield funding from EPSRC (EP/T006390/1) for use of the Zeiss Xradia 620 Versa X-ray microscope.

Appendix 1

Full size images of the eddy current simulations which give further clarity than Figure 4-9.

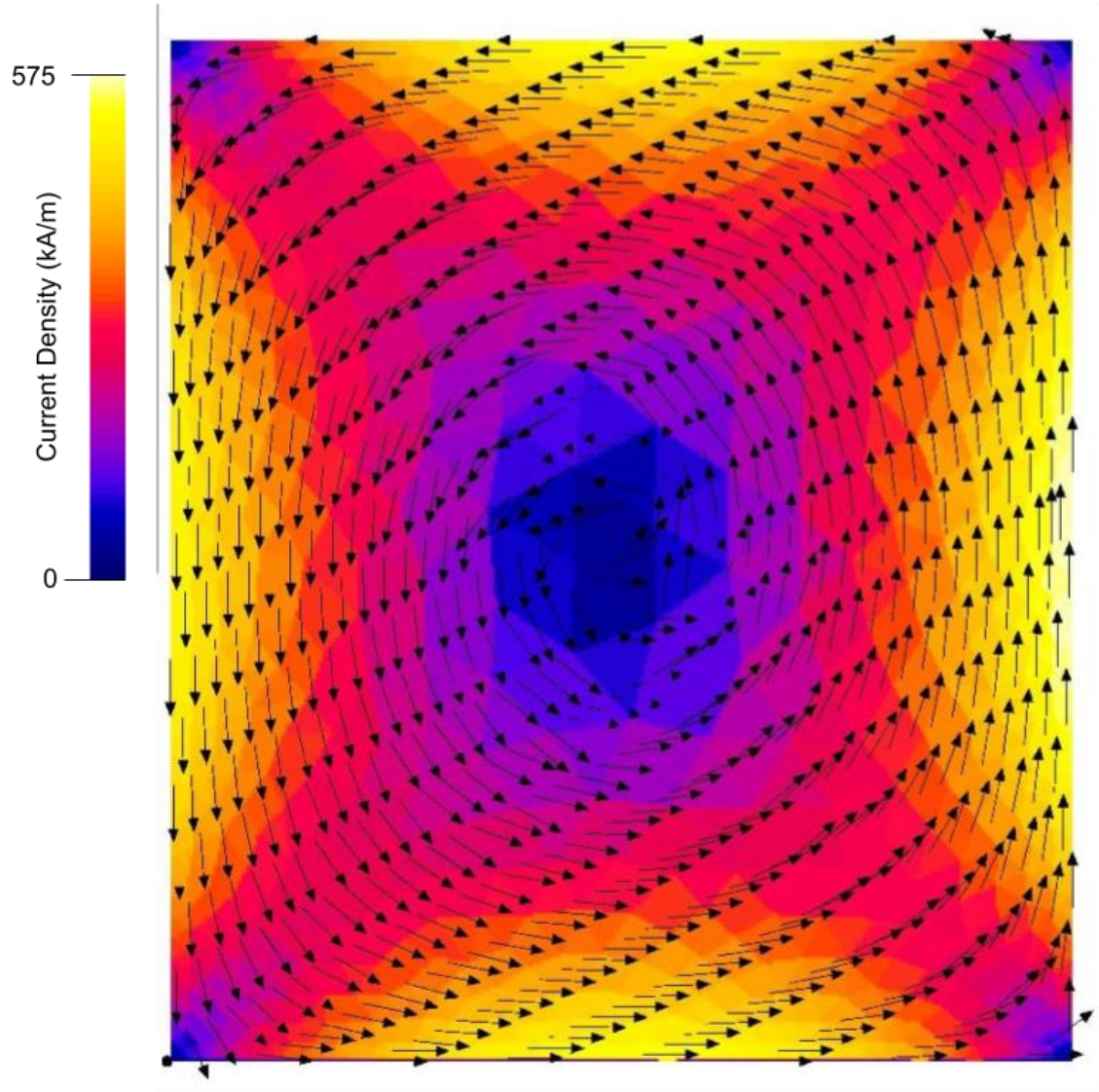

Figure 4-17 - Full size image showing solid cross-section eddy current density with arrows to show current direction

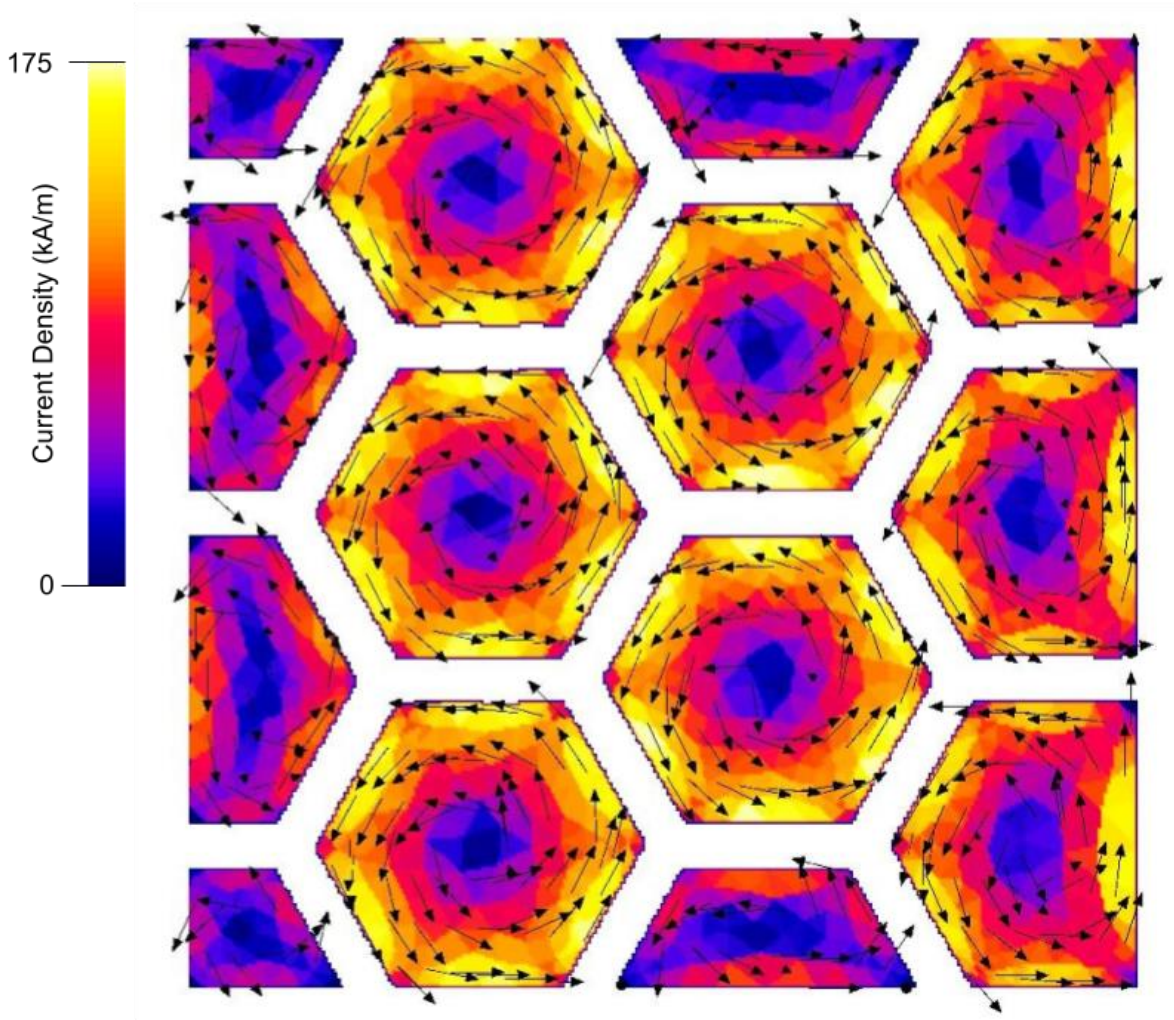

Figure 4-18 Full size image showing hexagonal cross-section eddy current density with arrows to show current direction, using a more suitable scale than Figure 4-9.

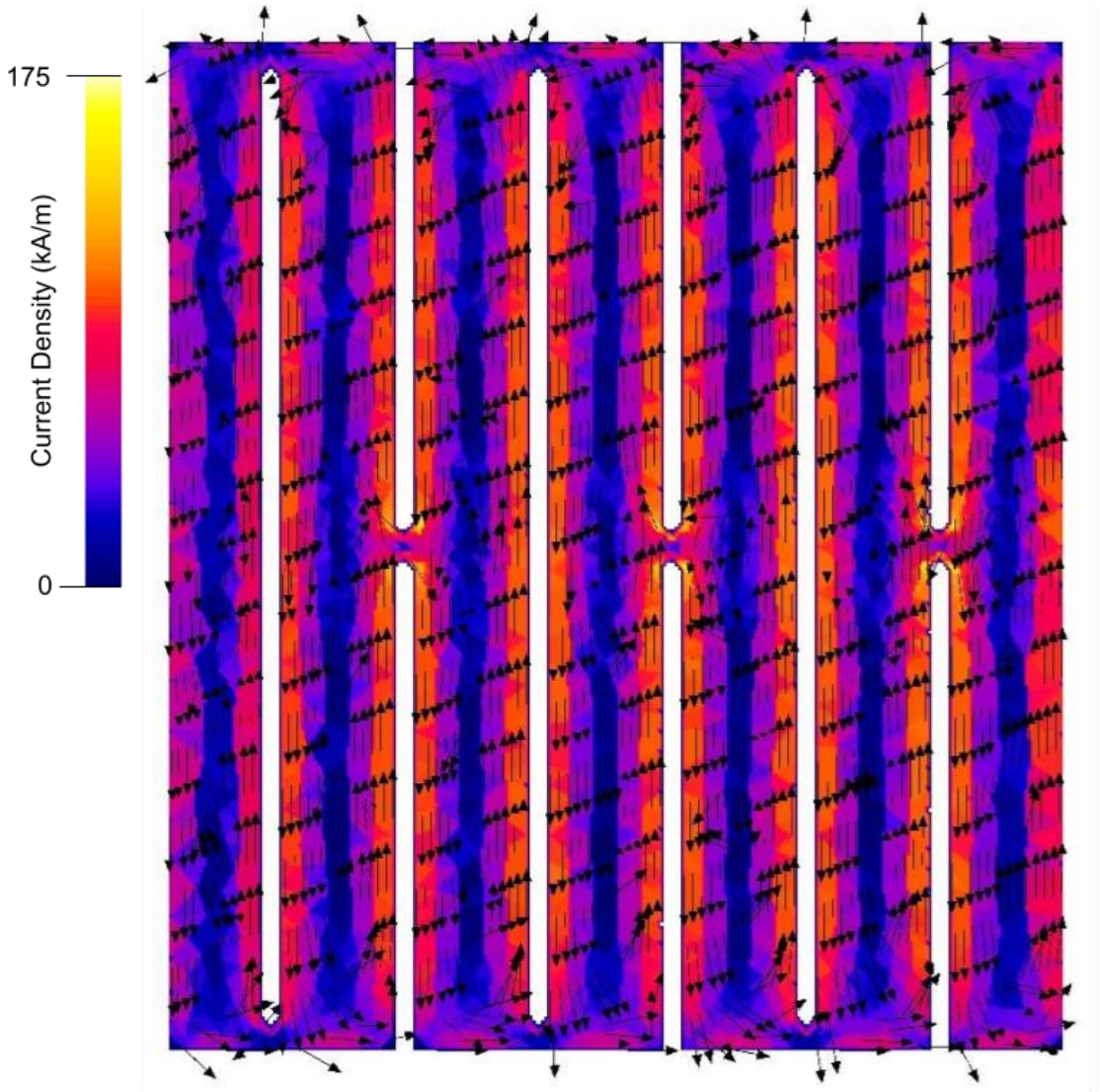

Figure 4-19 Full size image showing slotted cross-section eddy current density with arrows to show current direction, using a more suitable scale than Figure 4-9.

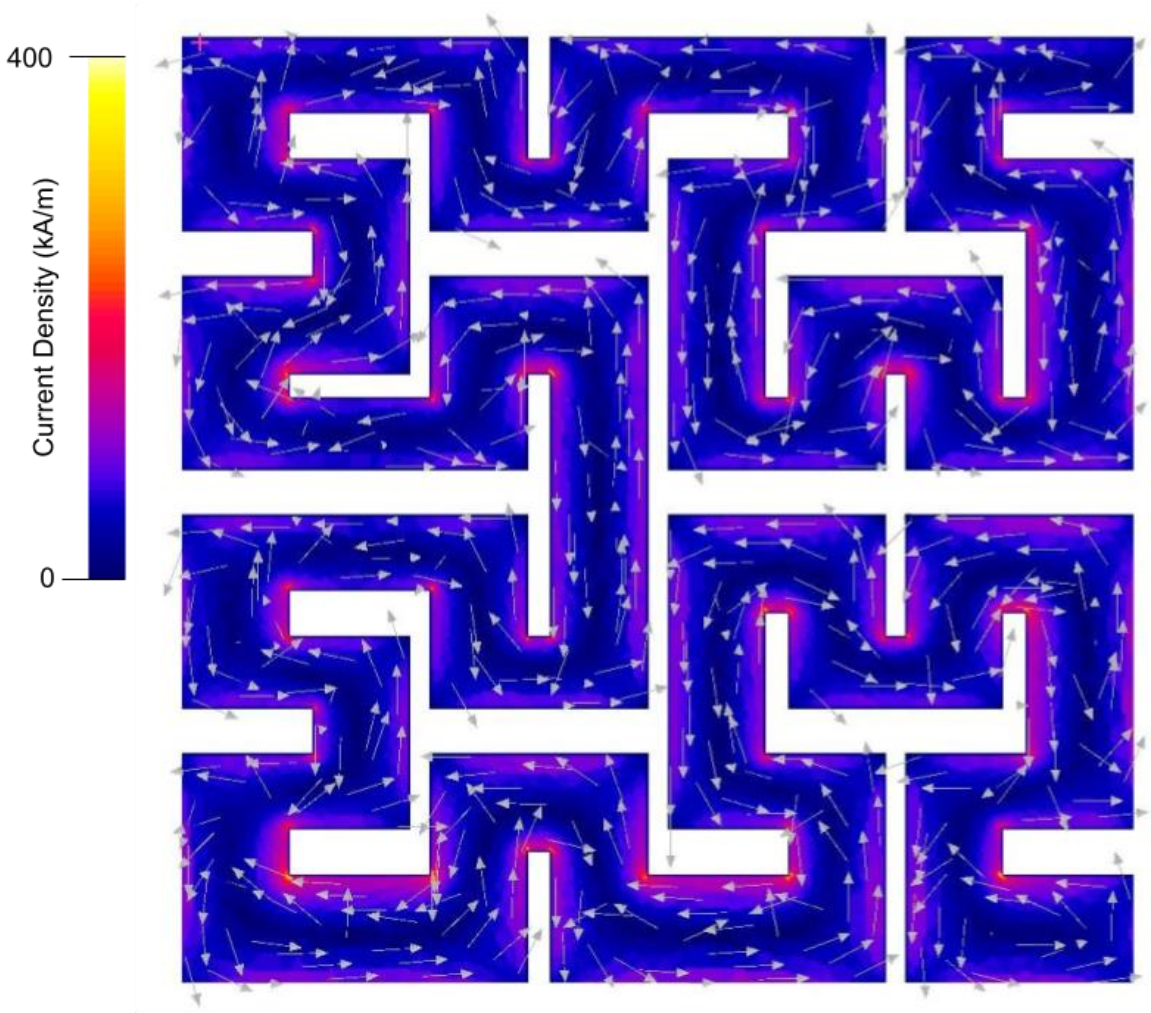

Figure 4-20 Full size image showing Hilbert cross-section eddy current density with arrows to show current direction, using a more suitable scale than Figure 4-9.

5 Loss performance of an additively manufactured axial flux machine stator with an eddy-current limiting structure

5.1 Journal details and author contributions:

Materials Today Communications,

Volume 35,

2023,

105978,

ISSN 2352-4928,

https://doi.org/10.1016/j.mtcomm.2023.105978.

Author contributions

Alexander Goodall – Conceptualisation, forming the collaboration with Wempec at the University of Wisconsin, all AM sample design and manufacture, characterisation of toroidal ring samples. Data processing and analysis of the stator rig tests. Characterisation and creation of the design rule for minimum gap and writing of the original draft

FNU Nishanth – Creating of stator from electrical steel laminations, all FEA work, winding and rig testing of the stators including data collection. Writing – section 2.4 and 2.5 and review and editing of rest of the paper

Eric Severson – Support with methodology for rig testing and analysis, supervision, writing – review and editing

Iain Todd – Support with methodology formal analysis, visualisation, writing review and editing, supervision.

5.2 Background

The Hilbert structure has been characterised by Plotkowski et al (27) and tested in a transformer with 2D flux pathways (31). Chapter 4 shows the manufacture and characterisation of this cross-sectional geometry using a toroidal ring, which has flux pathways parallel to the build platform, in the most difficult to process orientation. Following from this work, Chapter 5 implements the Hilbert cross-sectional geometry into the stator of an Axial flux permanent magnet machine designed and developed by collaborators at the University of Wisconsin (79). The axial flux is an appropriate place to attempt to use this methodology, as it has 3D flux pathways whilst being difficult to manufacture using electrical steel laminations. During this study, it was found that the volume production of this stator using electrical steel laminations would not be possible due to manufacturing defects caused by machining the slots after coil winding of the stator.

Two stators were manufactured for this work in the hope of characterising the stator in both the as-built and heat-treated conditions, however unfortunately the as-built stator was damaged during transit. This work reiterates the characterisation of the Hilbert cross-sectional geometry, and compares it with the calculated losses of two different thickness electrical steel laminations, both 3% silicon with thicknesses of 0.127 mm and 0.35 mm. The performance of this AM Hilbert stator is then characterised and compared with the 0.127 mm electrical laminations.

During this study the design of the AM Hilbert stator was investigated in more detail, showing the difficulties of resolving these complicated cross-sectional geometries using AM, which follow 3D magnetic flux pathways. This work focussed again on using 3D flux pathways as for 2D magnetic circuits electrical steel laminations were suspected to always outperform additively manufactured parts, and data shown in this study would support that hypothesis.

5.3 Paper

Loss performance of an additively manufactured axial flux machine stator with an eddy-current limiting structure

Alexander D. Goodall[a], FNU Nishanth[b], Eric L. Severson[b], Iain Todd[a]

[a] Department of Materials Science and Engineering, University of Sheffield, Sheffield, UK
[b] Department of Electrical and Computer Engineering, University of Wisconsin-Madison, Madison, USA

Corresponding Author – Alexander Goodall adgoodall1@sheffield.ac.uk

Keywords

Laser Powder Bed Fusion; Soft-Magnetic Material; FeSi: Axial flux machine; Electrical machine design

Abstract

AC electrical machines have mostly been limited to 2D magnetic circuits due to the use of electrical steel laminations, however in recent years advances in non-traditional motor architectures such as axial flux and conical machines show promise for increased efficiency, torque and power densities. These motors are enabling electrification of our transportation industries including more electric aircraft, allowing reduced carbon emissions. 3D magnetic flux pathways as required by axial flux motors are difficult to manufacture using laminations, and for other architectures impossible. Soft magnetic composites can enable 3D flux pathways but come at the expense of magnetic properties. In this study the stator of an axial flux motor is fabricated from high silicon electrical steel (Fe-6.5 wt%Si) using additive manufacturing with a Hilbert cross-sectional geometry to limit eddy current losses. It is tested and compared with electrical steel laminations of 0.127 mm and 0.35 mm, with the results showing comparable performance between the additively manufactured Hilbert stator and 0.35 mm laminations at frequencies below 500 Hz. A torque loss of approximately 20% was observed due to 34% less magnetic material in the Hilbert stator compared to the 0.127 mm laminations, but an improved torque density for the stator by 13%. By using design for additive manufacturing, tooth area could be scaled up providing an electrical machine with 3D magnetic flux pathways could be created with acceptable loss behaviour and good magnetic circuit properties, enabling further flexibility to electrical engineers in their pursuit of higher torque and power density.

1. Introduction

Electrical steel laminations have been used to reduce eddy current losses in electrical machines (EMs) (95) for decades. By limiting the generated eddy currents to a thin sheet of material the generated currents are smaller and hence losses via Joule heating are also reduced. However, laminations restrict the magnetic flux circuit to two dimensions as the magnetic flux must run in the plane of the lamination. This has made 3D magnetic flux circuits rare, and when used alternatives such as soft magnetic composites (SMCs) are often used to reduce the core loss especially at high frequencies (96), however this comes at the cost of magnetic properties such as permeability. Axial flux machines have shown potential for achieving high torque density (97), however these machines require a 3D magnetic circuit. Techniques available to manufacture the stator cores of axial flux machines and axial flux topologies are reviewed in (97) It is possible to achieve this by using coil wound electrical steel laminations, however any advances on this design to enable things such as magnetically levitating bearings (98,99) or more complex flux pathways will not be possible to be fabricated in this way as the radial dimensions will not be constant. SMCs have also been used for axial flux stators (100–102), demonstrating lower core loss than electrical steel laminations at high frequencies, but again have limitations on shape due to the uniaxial pressing operation. As the capacity to create 3D magnetic circuits with acceptable loss behaviour has not yet been possible, machines using this configuration have rarely been investigated.

Further to this, high silicon electrical steel (Fe-6.5 wt%Si) has been shown to be a promising soft-magnetic material for future electrical machines (20) with a higher resistivity yielding lower core loss, however the brittle nature of this alloy has posed difficulties with processing meaning that rolling into thin sheets is not a commercially viable option. Alternative methods such as diffusion of Si into Fe-3 wt%Si sheets have been used with some success (103), but not yet widely adopted, and as a result Fe-3 wt%Si is more commonly used (18).

Additive manufacturing (AM) has the ability to combat both of these issues, having been shown to successfully process high silicon electrical steel effectively (21,27), near fully dense and with good magnetic properties such as permeability up to 30,000 (85). This is enabled by the high cooling rates of the AM process avoiding the ordered phases that cause embrittlement in the high silicon alloy. Therefore, soft magnetic components can be processed via AM, however the process does not have the ability to mimic the small material thickness and surface quality of electrical steel laminations, therefore alternative methods to avoid large eddy currents in bulk sections must be investigated. Cross-sectional geometries have been shown to reduce the eddy current losses such as slotted geometries similar to laminations (26), and complex geometries such as the Hilbert pattern demonstrated first by Plotkowski et al (27). This Hilbert pattern was built with the cross-sectional geometry being resolved perpendicular to the build platform, which is the easiest orientation to achieve high resolution in laser powder bed fusion (L-PBF), however this restricted Plotkowski et al. to building 2D flux pathways. As such testing of these materials required a mini-Epstein frame style fixture to join together 4 legs of material to enable a magnetic circuit to be created. For characterising the losses of this geometry this is an effective method, however for AM to be useful in electrical machines it must be able to achieve continuous 3D flux pathways, otherwise electrical steel laminations are likely to outperform electrical steel produced by AM. Plotkowski et al. have also demonstrated this pattern in an real world application by building a transformer (31), however this again has 2D flux pathways and multiple locations where the magnetic circuit is not continuous.

This study will characterise the Hilbert cross-sectional geometry when built parallel to the build platform, the most difficult orientation for this pattern due to horizontal overhung surfaces. A design rule will be established to reduce electrical shorting across areas which should not be connected. Once enabled in this direction the Hilbert cross-sectional geometry could be implemented into any orientation in the build chamber, and therefore the stator of an axial flux permanent magnet (AFPM) machine is designed and built using AM, which has 3D magnetic flux pathways. The performance of this stator is compared to that of a prototype stator built using electrical steel laminations but is not suitable for volume production.

2. Materials and Methods

2.1 Additive Manufacturing and heat-treatment

All AM samples were manufactured using L-PBF. AM of toroidal ring samples for magnetic characterisation and samples for determining minimum gap sizes were built using an AconityMINI from Aconity3D GmbH with a build platform of 140 mm diameter. This machine uses a 200 W ytterbium doped continuous laser with a spot size of 70 µm. The AM Hilbert stator was manufactured using an AconityLAB from Aconity3D GmbH, with a larger build platform of 170 mm diameter, equipped with a 400 W ytterbium doped continuous laser with a spot size of 70 µm. The vertical direction normal to the build platform, also known as the build direction is referred to throughout this work as the Z axis, whereas the orthogonal directions parallel to the build platform are referred to as X and Y.

All samples were built using high silicon electrical steel powder (Fe-6.5 wt%Si) supplied by Höganäs AB, with a powder size of 15-45 µm. Layer thickness was kept constant at 30 µm, with a 67° layer rotation. The process is completed under an argon atmosphere, with oxygen content kept below 400 ppm. All samples were built onto stainless steel baseplates. Laser power and laser speed were kept constant at 170 W and 0.7 m/s respectively. Wire electrode discharge machining (EDM) is used to removal all samples from the build platform. All samples are removed before heat-treatment except for the AM Hilbert stator, which was removed after heat-treatment.

All samples were designed using Creo 8 provided by PTC. After exporting to .STL files, Netfabb premium 2021 (Autodesk) was used to arrange parts on the build platform and assign parameters, before creating .ILT files which can be used directly by the Aconity machines. Hatch offset and fill offset were 0.1 mm and 0.15 mm respectively, with a hatch spacing of 70 µm.

Heat-treatment was done in-house using a tube furnace for the toroidal ring samples and externally by MSL heat treatment LTD for the AM Hilbert stator. All heat-treatments used a heating rate of 5°C per minute, then held at a temperature of 1150°C for 1 hr, followed by furnace cooling, as demonstrated by Garibaldi et al. (23). All heat-treatments were completed in an argon atmosphere.

2.2 Metallographic preparation and microscopy

Samples were cross-sectioned using a Secotom 50 (Struers), then hot mounted using a Simplimet mounting press (Buehler). Grinding and polishing was completed using a Tegramin 20 (Struers) with several steps which were; Grinding using P1200 grit paper, grinding using P2400 grit paper, polishing using 9 µm diamond suspension, polishing using 1 µm diamond suspension, polishing using 0.25 µm diamond suspension and finally polishing using Masterpolish, all supplied by Buehler.

Optical microscopy was captured using an Olympus BX51 microscope on conjuction with Clemex Vision PE system, using a 50x magnification lens. Measurements for gaps were taken directly from the micrographs in the Clemex software.

2.3 Magnetic characterisation – ring samples

Toroidal ring samples were used to characterise the material using an AMH-1K Permeameter by Laboratorio Elettrofisico. These samples had a rectangular cross-sectional area of approximately 4x4 mm, however this was measured accurately for each sample. The toroid had an outer diameter of 38 mm, hence the samples respect the dimensions in BS 60404-6:2018 (62). Samples were wound with a search coil using 0.35 mm diameter, single core copper wire with 45 turns, and a driving coil of 40 turns using 1.5 mm diameter multi-strand copper wire with PVC insulation. BH loops were measured at several frequencies from 5 Hz to 1000 Hz, which is the maximum the machine can provide, allowing for the core loss to be measured. For each toroid, a secondary sample of only ¼ of a ring was built, sectioned and imaged to provide a stacking factor, defined as the percentage area of magnetic material / the total area including air gaps. This stacking factor was implemented into the measurements in the Neon software (Laboratorio Elettrofisico), used to control the Permeameter in order to take account of the air gaps within the material.

2.4 FEA simulations and lamination loss calculations

The stator of the axial flux machine designed and optimized in (79) was selected for prototyping using AM. Two electrical steel laminates of thickness 0.127 mm and 0.36 mm were considered for comparison with the AM stator. The B-H data and the loss coefficient terms in the Steinmetz equation (equation 14) for the 0.127 mm and 0.35 mm laminations were obtained from the library material models from the manufacturer in Simcenter MAGNET (104). The material model used for the 0.127 mm lamination was that of Arnon 5, while the model of M-19 29 Ga was used for the 0.35 mm lamination. Two sets of 3D transient electromagnetic simulations were performed to compute the stator iron losses by assigning i) the 0.127mm steel material and ii) the 0.35 mm steel material for the stator core. The 3D FEA model is shown in Figure 5-1. The rotor yoke and permanent magnets were set up as a motion component and configured to the rated speed. Sinusoidal 3 phase current excitation, with a peak value of 140 A (rated current) was applied to the stator windings. The frequency of the current excitation was 800 Hz for the rated speed. A fixed time step of $1/20^{th}$ of the fundamental time period (1.25 ms) was used for the transient FEA. Full details of the FEA model can be found in (79).

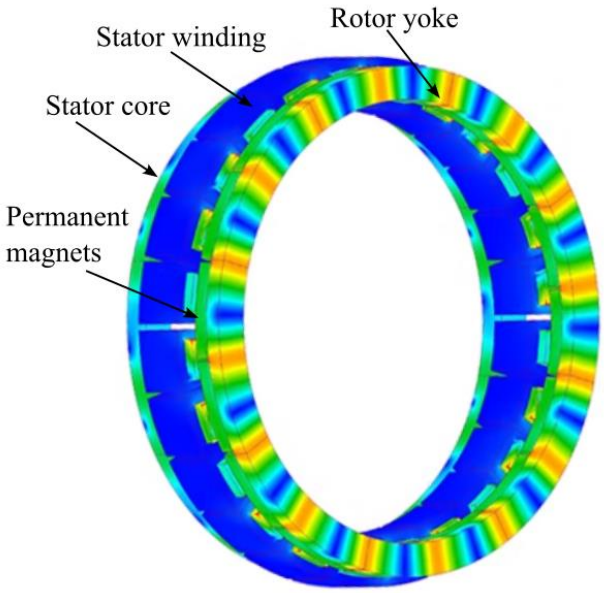

Figure 5-1 – 3D FEA model showing stator, rotor, permanent magnets and stator windings.

2.5 Stator winding and testing

The laminated stator was fabricated by machining slots into a tape wound core. A strip of 0.127 mm thick laminations was wound into a ring-shaped core with the same dimensions as the stator dimensions of the electric machine. The tape wound core was then bonded using an inorganic insulating adhesive to improve structural strength and prevent the layers from splaying. Next, slots were machined into the tape wound core. Finally, a layer of insulating material was coated on the machined stator core.

Rectangular 12 AWG equivalent copper wire was used to make the stator coils for the conventional and the additive stators to achieve high copper fill factors. Each coil had 7 turns and the stator had 24 coils. The finished stator was glued to an aluminium baseplate using a structural adhesive.

A CNC mill configured as a contact free dynamometer was used to characterize the conventional and additive stators. A 16-pole rotor was mounted in the spindle collet while the stator was mounted on a 6-axis load cell fixed to the mill bed. The load cell was used to measure the axial forces and the reaction torque on the stator. Static torque measurement tests described in (17) were performed at different stator currents up to the rated current to validate the torque capability of the machine.

To compare the iron losses, no-load test was performed. The stator terminals were open circuited, and the rotor was rotated at different speeds up to 6000 RPM (corresponds to an electrical frequency of 800 Hz), using the mill spindle speed control function. The reaction torque on the stator was measured using the load cell at each speed. The product of the reaction torque T in Nm on the stator and the speed ω in rad/s was computed to obtain the stator iron losses $P_{stator} = T\omega$.

3. Results

3.1 Loss performance of Hilbert shaped magnetic circuit

The Hilbert space filling curve pattern has been shown to be effective at managing eddy current losses in additively manufactured Fe-Si (27,31). These have always been built with the cross-sectional geometry being resolved in the XY plane of the L-PBF machine. The major advantage of using AM to build soft-magnetic material is to enable 3D flux pathways. Restraining the cross-sectional geometry to one plane also limits the magnetic circuit to a 2D path, therefore in this study the Hilbert cross-section is built in the XZ plane, as this will be the most difficult to successfully resolve the intended geometry due to burn through of horizontal gaps from the layers above. To find out the minimum sized gap in the XY plane a test sample was made with nominal gaps ranging from 50-500 µm, showing that in this plane a 50 µm gap was successfully maintained (Figure 5-2a). Demonstrating this on a 4x4 mm cross-section, it is shown that this cross-sectional geometry will resolve correctly in the XY plane (Figure 5-2b), with gaps this small, but when attempted in the XZ plane the horizontal gaps suffer from burn through, rendering the geometry unrecognisable (Figure 5-2c).

The minimum gap in the XZ direction was found to be 250 µm, hence we can create a design rule for the minimum permissible gap to allow for air gaps to be maintained. The gap will differ depending on the angle of the surface being built, as shown in Figure 5-2d, where the required gap to allow for 250 µm between surfaces in the Z direction is dependent on the Cosine of angle of the surface. This is plotted graphically in Figure 5-2e demonstrating a sinusoidal reduction in gap from horizontal surfaces (build angle 0°), to a minimum of 50 µm at approximately 80 which is then maintained until 90°.

This experiment was done using constant laser parameters. It is possible that the roughness of the downfacing surfaces may be optimised for a lower roughness, meaning that a gap smaller than 250 µm could be used. For these soft-magnetic material structures, it is very important to have complete isolation between the surfaces. As additive manufacturing is inherently stochastic at the scale of surface roughness, due to differences in powder spreading, powder quality, laser interaction with the powder bed and thermal conditions, there could be some events causing short-circuiting between areas which should be electrically isolated.

The nominal gap in the CAD design is not the only factor affecting this gap, other factors such as hatch spacing, melt pool width, surface roughness and hatch offset (distance from edge of CAD model to laser hatch line) can all have an impact on this gap. By using constant laser parameters during this study these parameters were kept uniform, however when transferring between different machines or software it is important to control all of these parameters.

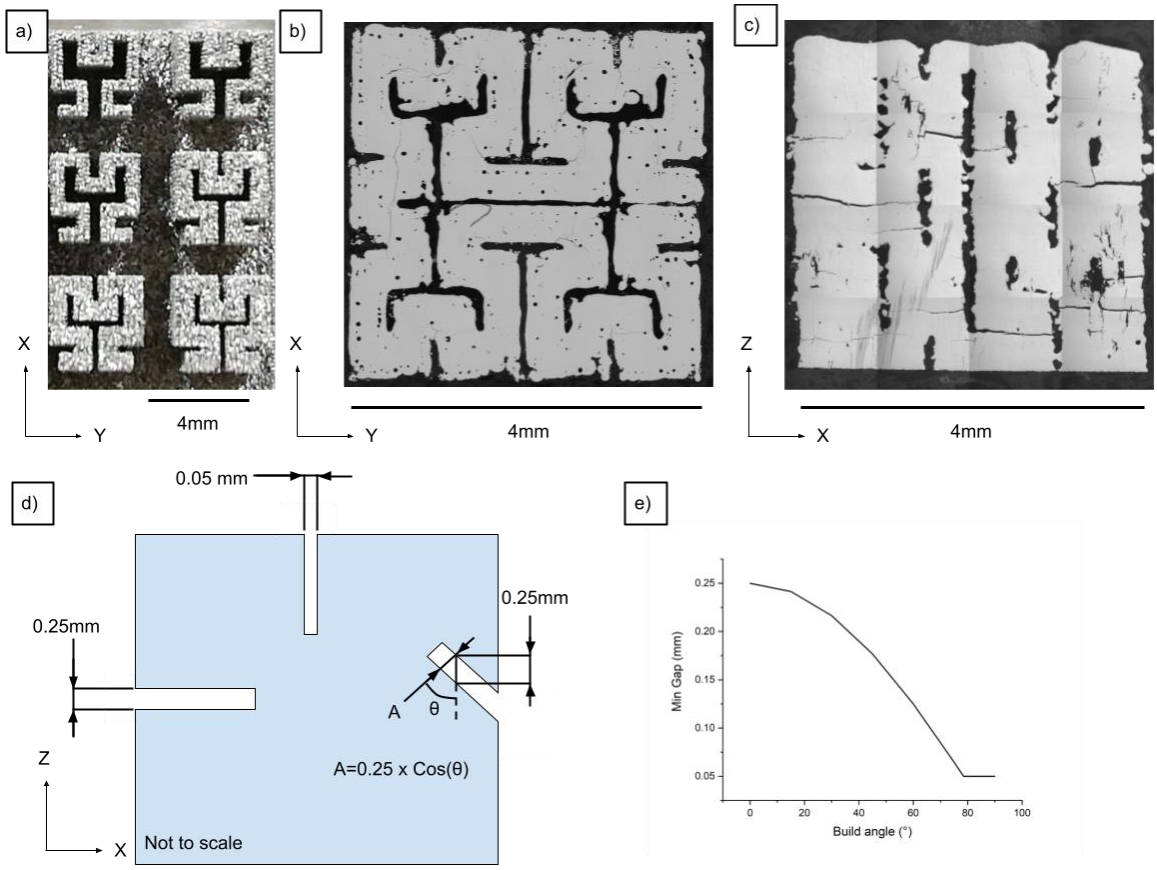

Figure 5-2 - Hilbert shape filling curve used to manage eddy currents, showing a test to check for the minimum sized gap in the XY plane (a), the resultant Hilbert cross-sectional geometry when the pattern is built in the XY plane (b) and XZ plane (c), along with the schematic showing the minimum gap design rule (d) and the graphical representation of the minimum gap design rule (e).

Toroidal ring samples which used a Hilbert space filling curve based cross-sectional geometry were built with the cross-sectional pattern in the XZ plane in order to test the magnetic properties. BH loops were measured at a variety of frequencies from 5 Hz up to 1 kHz, which was the maximum permissible by the testing equipment used. Measurements were taken manipulating the magnetic field, H, until a flux density of 1 T was measured in the sample. BH loops for ideal soft-magnetic materials are demonstrated by a high initial gradient, and hence relative permeability (μ_r), followed by the knee point occurring at a high flux density, giving a higher flux density for a given magnetic field (H). Other desirable features are high magnetic saturation, low core losses represented by the area inside the loop, and low coercive force (H_c). Samples were tested in the as-built condition, then heat-treated at 1150°C for 1 hr using the procedure from Garibaldi et al. (23) and characterised. Resulting BH loops are shown in Figure 5-3 demonstrating a reducing permeability and increasing core losses with an increase in frequency.

Heat-treatment of the samples yields an improvement in magnetic properties, especially permeability as the BH loops have a steeper gradient prior to the knee point. The knee point is also evidently higher. At higher frequencies such as 1 kHz, there is less difference in the BH loop shape as the eddy currents start to dominate the loss behaviour due to proportionality with the square of the frequency. This behaviour is more heavily dependent on the shape of the samples rather than the microstructural properties and therefore to be expected. Even in the heat-treated samples, the knee

point is lower than would be expected from Fe-Si, where it would normally occur at approximately 1.5 T.

The core losses are plotted in Figure 5-4 showing a small improvement in loss behaviour with heat-treatment for the additively manufactured Hilbert samples, with core losses at 1 kHz being 1727 W/kg and 1065 W/kg for the as-built and heat-treated samples respectively. These are plotted against core losses calculated using the Steinmetz equation (105) for electrical steel laminations of 0.127 mm and 0.35 mm. The Steinmetz equation is shown in Equation 14, where P is the total core loss, K_h and K_e are the hysteresis and eddy current loss coefficients respectively, f is the frequency, B is the flux density and α and β are constants.

The core losses at frequencies of 50 Hz and above are lower in electrical steel laminations than those in the additively manufactured Hilbert samples, owing to their lower wall thicknesses that cannot be reproduced using current AM technology. Eddy current losses are increased with a larger wall thickness and the wall thickness in the Hilbert structure is nominally 0.5 mm thick. At 1 kHz the core losses for the 0.127 mm and 0.35 mm laminations are calculated at 106 W/kg and 50 W/kg respectively, an order of magnitude smaller than those from the Hilbert samples. The trend also shows the difference increasing with frequency.

$$P = K_h f^{\alpha} B^{\beta} + K_e f^2 B^2$$

Equation 14

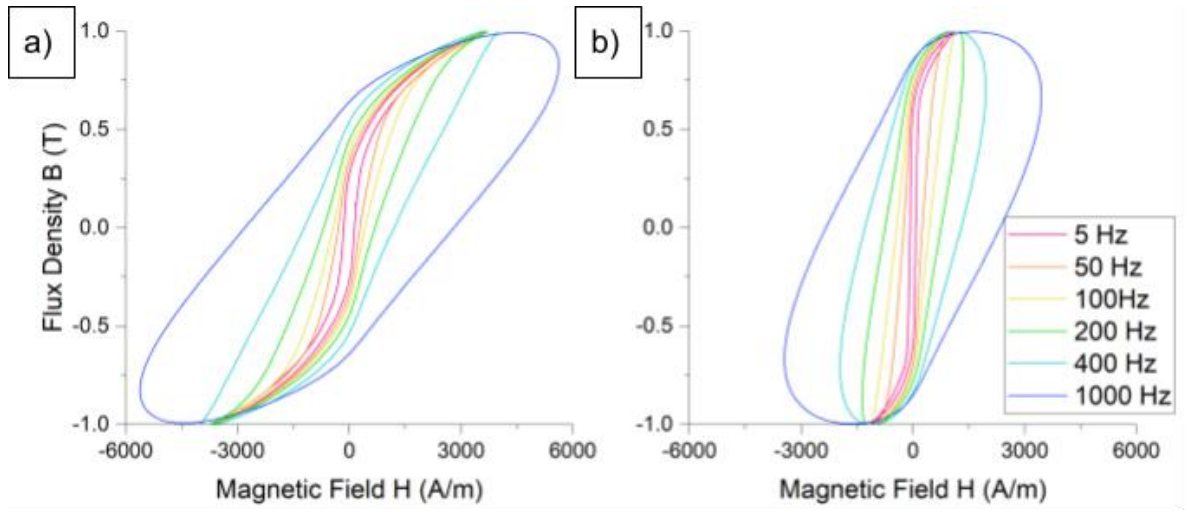

Figure 5-3 - BH loops of toroid samples with Hilbert cross-sectional geometry, for the as-built state (a) and heat-treated state (b). BH loops were measured at several frequencies 5-1000 Hz at a flux density of 1 T.

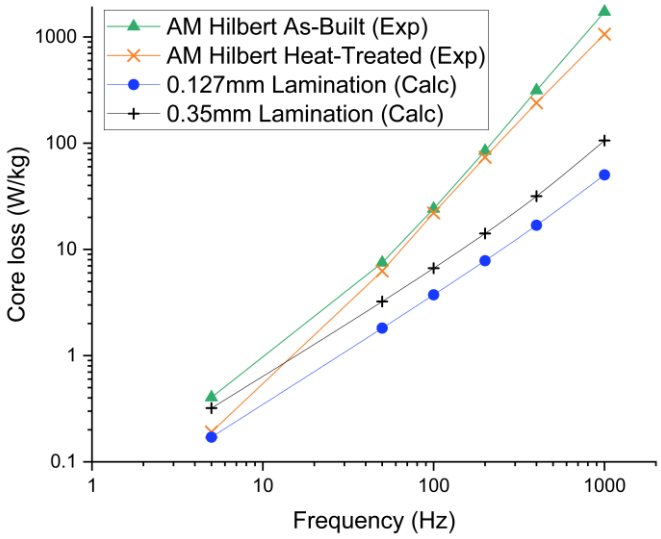

Figure 5-4 – Experimentally measured loss behaviour of the Hilbert ring manufactured by AM, in the as-built and heat-treated conditions, compared with data calculated for two thicknesses of laminations.

3.2 Design and manufacture of electrical machine stator

Having established a design rule for the minimum gaps to give electrical isolation, the design for an electrical machine stator was created using the Hilbert cross-sectional geometry. This was developed for the axial flux permanent magnet (AFPM) motor demonstrated by Nishanth et al. (79), which was designed to use a stator consisting of ring wound electrical steel laminations, 0.127 mm thick. The stator has an outside diameter of 164.5 mm and has an axial length of 35 mm. By building the Hilbert stator using AM, it is possible to obtain a direct comparison with the electrical steel laminations used in the original design.

The design of the Hilbert stator is shown in Figure 5-5. There are two main regions which are the tooth and back iron of the stator. As the majority of the flux pathway within the stator is in the tooth, this region is kept in the XY plane of the AM machine in order to obtain the smallest possible air gaps within the cross-section. This allows for a higher stacking factor, which is the volumetric ratio of magnetic material to insulation, which in this case is air. The other main region is the back iron which runs circumferentially around the bottom of the stator. This must have non-uniform air gaps as the horizontal surfaces require a gap of >250 µm, whereas the vertical surfaces require a gap of only 50 µm.

This back iron region has an approximately square cross-sectional area therefore implementing the Hilbert space filling curve is done with relative ease (Figure 5-5c). However, the tooth has a non-regular shape owing to its outer and inner surfaces falling on the outer and inner diameters of the stator. The central region of this is filled with the Hilbert space filling curve, whilst the edges are modified in a way so as to keep the intent of the shape, whilst attempting to reduce any large cross-sectional areas of bulk material (Figure 5-5d). The flux pathways in this stator are axially along the tooth, circumferentially around the back iron, hence this is the direction the Hilbert cross-section is implemented. In the region where the tooth and back iron meet, the flux may run in several directions, either skipping the tooth and running circumferentially, or by leaving the tooth and running through the back iron in either direction. Due to this, the magnetic flux can be running in one of three directions in the region underneath the tooth. Therefore, the Hilbert cross-section has

been implemented in these three directions, where the flux pathways interfere with each other a simple rule was used to implement solid material or air gap. In any location, if at least one of the flux pathways' Hilbert cross-sectional pattern required solid material, then solid material is selected. The outcome of this is that in some areas where there is supposed to be an air gap, this air gap is filled with solid material from the cross-section of a different flux pathway. The full stator is shown in Figure 5-5b.

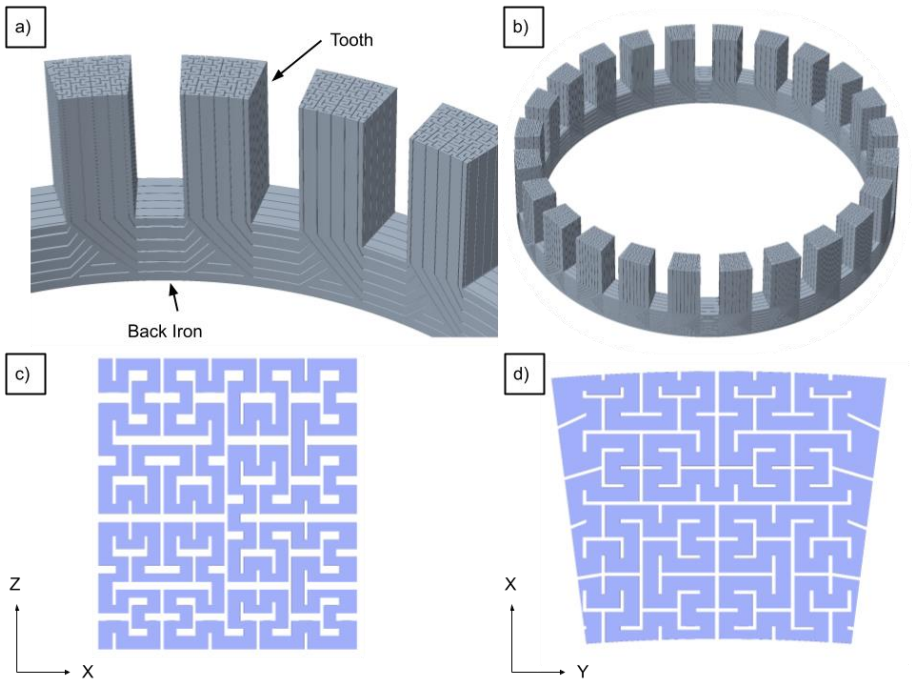

Figure 5-5 - Hilbert stator for AFPM machine designed to be manufactured using AM (a,b). The stator has a toothed region which has a uniform air gap size for the XY plane of the AM machine (d), with a back iron region with non-uniform air gaps showing more clearance in the Z direction than the X direction (c).

This stator was designed in 3 days and successfully built in approximately 80 hrs. The stator was then heat-treated at 1150°C for 1 hour, in order to relieve residual stress, drive recrystallisation and encourage grain growth, shown to improve the properties of Fe-6.5 wt%Si build by AM (23). The component was left attached to the baseplate during heat-treatment to allow a flatness tolerance of 0.03 for the lower face, and a parallel tolerance of 0.03 for the upper face, to be achieved upon removal of the component using wire electrode discharge. If the removal of the component was completed before heat-treatment, there were concerns that the part may distort and be unable to achieve the required tolerance.

Images of the stator are shown in Figure 5-6 demonstrating the successful resolution of the tooth profile. It has not yet been possible to check the cross-sectional profile of the back iron as sectioning and polishing would render it unusable. Following EDM removal from the baseplate the component shows oxidisation throughout due to the sensitive nature of this alloy and the contact with water during the EDM process. The oxidisation is not suspected to have a significant impact on the performance of the component, however in the future methods to prevent this such as coating prior to EDM could be easily implemented. The stator mass is 0.66 kg, giving a stacking factor of 65-70%. The original electrical steel lamination stator has a mass of 0.97 kg with a stacking factor of approximately 91%. A comparison of time and cost to manufacture both prototype stators are shown in Table 3. The processing cost for the AM stator includes machine time ($1200), heat

treatment ($350) and EDM removal ($100), whereas for the laminations this includes winding, bonding, welding, milling and insulating.

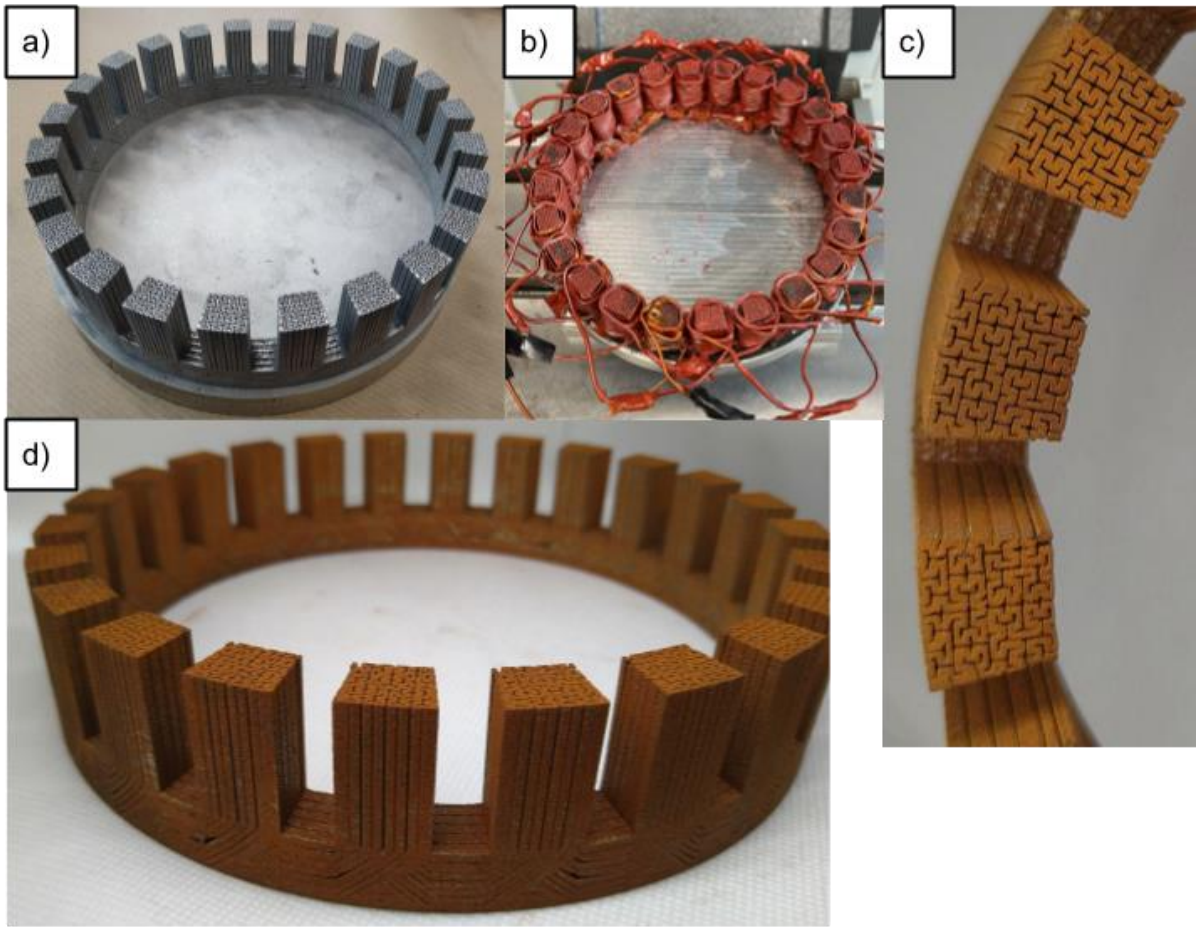

Figure 5-6 - Images of the Hilbert stator showing the as-built component still attached to the build plate (a), the part after removal from the build plate (d), and the successfully resolved tooth profile (c), both showing severe oxidisation. The stator is also shown in the wound state ready for rig testing (b).

Table 3 - Time and cost of manufacturing Hilbert AM and 0.127 mm electrical steel lamination

	Raw material ($)	Processing cost ($)	Processing time (weeks)
Hilbert AM	40	1650	3
0.127mm Laminations	20	2500	12

3.3 Characterisation of Hilbert AM stator

A rig test was used to determine the torque and loss behaviour. The AM Hilbert stator was tested and compared with a 0.127 mm lamination stator, and the core loss behaviour was also calculated using FEA for both 0.127 mm lamination and with a 0.35 mm lamination. The torque curves are shown in Figure 5-7a, normalised to the rated torque of 18 Nm and rated current of 140 A. The AM Hilbert stator shows a decrease in torque throughout the full range of tested values, with a 17% decrease at 20 A (14% of rated current) through to a 23% decrease at 140 A. This trend shows a

higher difference between the laminations and AM Hilbert stators with increasing current. This is unsurprising considering the mass difference between the two stators, with less material giving a lower magnetic flux in the machine. Gravimetric torque density was calculated at 100% of the rated current (140 A) for the stator only, showing 18.3 Nm/kg for the 0.127 mm lamination stator and 20.7 Nm/kg for the AM Hilbert stator.

The core loss behaviour of two experimentally tested stators are displayed in Figure 5-7b along with the FEA results from laminations of two different thicknesses. The FEA of the 0.127 mm lamination shows good correlation with the experimental data for 0.127 mm laminations, displaying that the FEA model is successful in its loss predictions. FEA data for a 0.35 mm lamination stator was also created. The AM Hilbert stator shows higher core loss than all the other samples at higher frequencies above 500 Hz, with the core loss at 800 Hz being 543 W, 27% higher than the 0.35 mm laminations and 210% higher than those of the 0.127 mm laminations. At lower frequencies the performance of the AM Hilbert stator is comparable to both the 0.127 mm and 0.35 mm laminations.

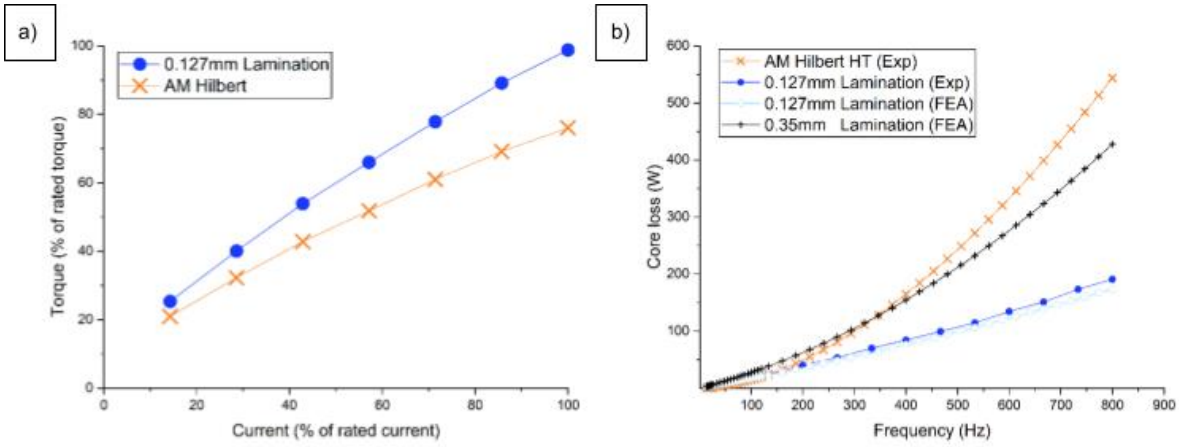

Figure 5-7 - Torque performance of AM Hilbert stator and 0.127 mm laminations stator (a), demonstrating a reduction in torque of approximately 20% throughout the whole operating range. Loss performance (b) measured at several frequencies showing that the AM Hilbert stator has higher core loss than the 0.127 mm laminations, but is comparable to 0.35 mm laminations through a range of frequencies.

4. Discussion

Resolving the Hilbert cross-sectional pattern is difficult in the XZ plane of the machine as the laser melts through multiple layers for each hatch, enabling a 3D component to be created. However, when trying to resolve cross-sections which have gaps where no material should be, this laser burn through melts powder which should not be melted. In this study we created a design rule to allow this to be managed through the design of the component however other strategies are available. Different parameters can be used for the upskin surfaces to reduce the laser power or increase the speed, giving a shallower melt pool and hence less burn through. Optimisation studies into this method could yield further improvements in the minimum gap distance and hence increase the stacking factor of these components. Another possible improvement to the cross-sectional resolution and prevention of short circuiting could be in post-processing the components using a chemical or electro-polishing process. This would preferentially remove material from things like partially melted particles or thin sections due to their high surface area to volume ratio, enabling the reduction of undesirable short circuits from the component. Other methods to do this could be

abrasive flow machining (AFM) if the cross-section had a closed shape or by using a fixture for this. As a secondary benefit from this, it is possible that a component with a smoothed surface could demonstrate softer magnetic performance as the rough surfaces may act as pinning sites for magnetic domains.

Other cross-sectional geometries may offer improvement over the Hilbert space filling curve design. Hilbert geometry has been shown to provide improvement over other sections such as a lamination style design (27), however with AM there is an enormous design space to explore. Multi physics simulations including the magnetic performance and loss behaviour are computationally expensive for these complex geometry components. Further to this, these simulations must be completed in 3D as any magnetic circuit in 2D would currently perform better with laminations. The simulation of the Hilbert stator used in this study were attempted but not possible to solve based on computational demands. The Hilbert geometry has many overhanging horizontal surfaces which is known to be difficult to process via AM. Other geometries may be more friendly to the AM process whereby overhanging surfaces are limited to below angles approximately 45°. In order to obtain the optimal geometry for a given machine, new software capable of topology optimisation based upon magnetic performance would be required, whilst respecting manufacturing constraints. This would allow the best shape to be obtained for a given application, in the same way as structural parts are intelligently optimised with topology optimisation currently.

The geometry of the final component depends not only on the CAD file, but also the processing parameters such as hatch spacing, melt pool width and hatch offsets from the edge of the part. All of these parameters can influence the position of the components surface in relation to the CAD surface. Hence, optimisation of these parameters could also reduce the minimum gap required to ensure electrical isolation.

The stator in this study suffered from oxidisation due to the EDM process being completed in water. Although oxidisation can have an impact on the magnetic properties (95), it was judged that this thin layer of oxidisation which was easily removed with a wire brush wouldn’t have a significant impact on the magnetic performance of the component in rig tests. This oxidisation could be avoided by completing the EDM process in oil rather than water. Future work could verify if there is a deterioration of properties from this surface oxidisation. It would be unlikely to be acceptable in the manufacture of an electrical machine for use in an application as the oxidisation could deteriorate the performance over time.

The reduction in torque of the AM Hilbert stator can be expected as there is a lower volume of magnetic material when compared to the laminated stator. However, the gravimetric torque density of 20.7 Nm/kg for the AM Hilbert stator, which is 13% higher than that of the 0.127 mm laminated component, shows the AM Hilbert stator outperforming that of the laminated stator for the same mass. Enabled by AM, to allow for the same amount of torque it would be possible to increase the cross-sectional area of the tooth of the stator, whilst reducing the area of the slot and therefore being able to manage the low stacking factor. By using AM to also create the copper windings the same amount of conductive material could be used, whilst increasing the amount of soft-magnetic material in the core within the same volumetric envelope. An example of these windings were created (Figure 5-8), showing that the slot fill factor could be doubled, as it was possible to create windings with a cross-sectional area of 2.4x2.7 mm with AM, whereas due to winding constraints the original machine used conductors with a cross-section area of 1.2x2.7 mm. By reducing the slot size and increasing the tooth area, it would be possible to maintain the same level of torque.

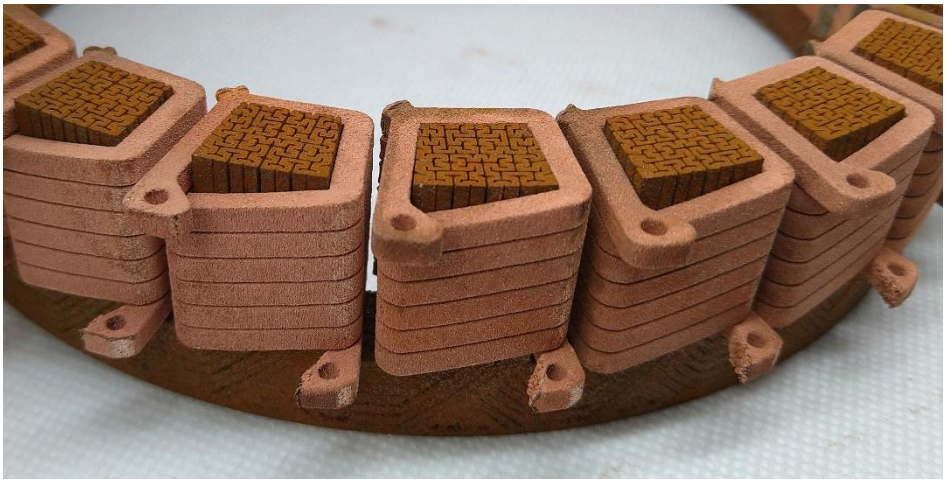

Figure 5-8 - Increasing the slot fill factor is demonstrated using L-PBF of pure copper, doubling the slot fill factor

The core loss of the AM Hilbert stator was higher than that of the laminations, re-affirming that if a 2D magnetic circuit is needed then laminations are still the preferred method. The core loss is close to that of the thicker lamination showing promise for enabling electrical machines with 3D flux paths. The 0.127 mm laminated stator shown in this study had a large cost due to it being a low volume prototype, however many issues were found with manufacturing this component making it unsuitable for volume production. Winding and bonding the laminations is a difficult process and machining the slots after this can cause issues with delamination and show areas of insufficient bonding (Figure 5-9). If this component were possible to mass manufacture, the cost would likely be significantly lower than the AM component. The AM component was also manufactured more quickly in only a few weeks, compared to the 12 week lead time for the prototype laminated stator. This can enable a larger design space to be explored in the same amount of time, allowing electrical engineers greater freedom to manipulate the machines architecture. The AM stator also had some build defects (Figure 5-9). For prototypes this is likely to be an acceptable compromise, however for production components improvements would be required in the build to reduce or eliminate these defects.

The core loss of this part was measured with a heat-treated sample which is likely to have recrystallized and experienced grain growth, similar to the components reported by Garibaldi et al. (23). Grain growth up to a size of 5-7 mm has been shown to improve properties at a frequency of 50-60 Hz, however smaller grain size has been shown to have reduced losses at high frequencies (106). Therefore, the as-built condition with its smaller grain size of 10-100 µm may have lower losses at higher frequencies. A sample was built to investigate this, however it was unfortunately broken during transit. This was caused by the weld lines created by attempts to improve the build time.

Build time was quite large at 80 hrs due to the complex scanning pattern required, a large area in the centre of the build without any material, meaning lots of time is spent with the laser traversing this region without melting any material. It was possible to reduce this to approximately 25 hours by splitting the component into quarters, however this can create a weld line and it is not known the affect that this may have on the magnetic properties of the component. For the component that broke due to these weld lines, the joints were orientated vertically, meaning that any faults between the segments were stacked on top of each other. In further work, this split should be angled in order to allow the penetration of multiple layers by the laser, to bridge the gap between the segments and create a better joint. The impact on magnetic properties of these joins should also be investigated.

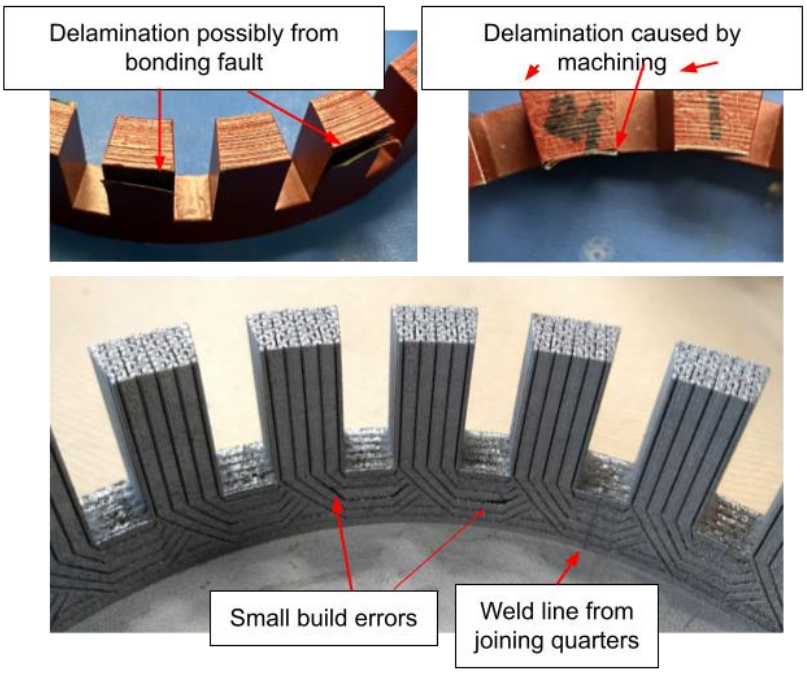

Figure 5-9 – Delamination from bonding and machining shown for the 0.127 mm laminated stator, and build defects of the AM Hilbert stator showing a weld line from splitting the component into four segments, and small errors where the geometry is not exactly as intended.

This study, to the authors knowledge, is the first use of 3D magnetic flux paths in an electrical machine stator made with eddy current limiting geometry. This technology can enable different architectures of electrical machine that require these 3D flux paths, as this has previously not been possible there has been little development of motors of this type, however some examples could be conical motors with magnetically levitating bearings (98,99), or any motor where SMC has previously been used. By using AM to process the functional materials required for electrical machines, the limitations are now in the mind of the designer, and it is possible to realise architectures never before possible.

A demonstrator motor was created to start to showcase the possibilities of using AM for electrical machine design (Figure 5-10). The housing can be made from lightweight material and have additional functionality built into it such as heat exchangers. The stator can be spatially graded to have different structures depending on the flux pathway or direction, and can possibility incorporate air or liquid cooling when using cross-sectional geometries such as the Hilbert pattern. Conductive coils can have spatially varied cross-sectional area (107) to reduce losses, have better slot fill factors due to pre-shaping and also have higher temperature insulators as there is little need to deform the part and hence brittle ceramics can be used to insulate conductors for the first time.

Axial flux machines have been shown to have potential for high torque density (97) and possess a much smaller axial length than more common radial flux machines. However, radial flux machines are more commonly used as they are inexpensive and have high efficiency owing to the use of electrical steel laminations. Each application will be case specific, but axial flux machines are more likely to be used in high value applications where size and weight are a constraint and a high level of performance is required.

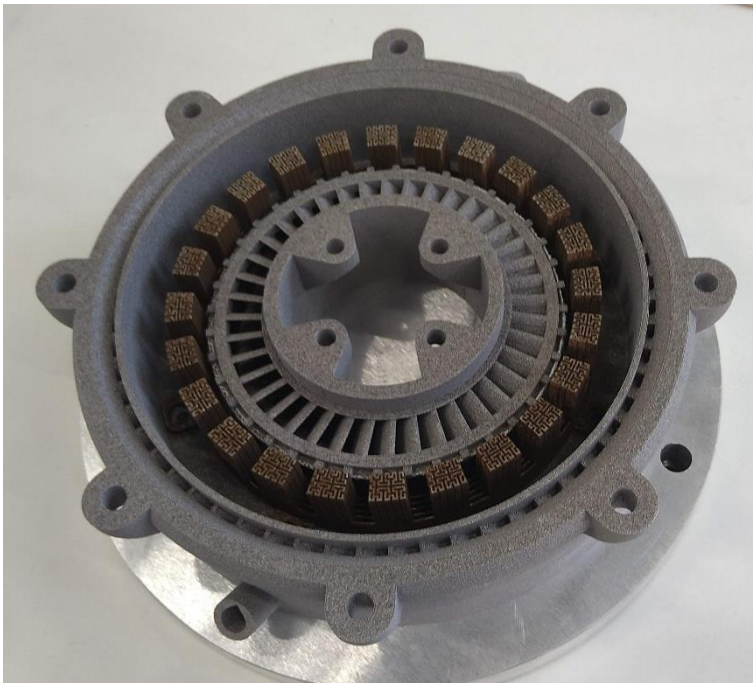

Figure 5-10 - Demonstrator motor created mostly with AM, showing a soft magnetic FeSi stator core and rotor back iron, an aluminium housing and rotor. The bearings and permanent magnets are not created using AM.

5. Conclusion

Toroidal ring samples were built using AM, from high silicon electrical steel powder (Fe-6.5 wt%). These ring samples were designed with a Hilbert cross-sectional geometry implemented to reduce eddy current losses during AC excitation. Heat-treatment was found to improve the properties of these toroidal rings by increasing permeability and reducing core losses, 'squaring' the BH loop. This Hilbert cross-sectional geometry was then implemented into the 3D magnetic flux pathways of an axial flux permanent magnet electrical machine, which was then compared experimentally to a 0.127 mm thickness electrical steel laminations (Fe-3 wt%Si) and by using FEA with 0.35 mm thick electrical steel laminations (Fe-3 wt%Si). The AM Hilbert stator was 66% lighter than the 0.127 mm laminations and showed an average of 20% reduction in torque throughout the operating range. The torque density of the AM Hilbert stator was 13% higher at 20.7 Nm/kg (stator only) than the 0.127 mm laminations. Core losses in the AM Hilbert stator were higher than the 0.127 mm laminations, but comparable to 0.35 mm laminations in frequencies below 500 Hz. At 1000 Hz the experimental core loss of the AM Hilbert stator was 543 W, compared to 428 W for the 0.35 mm laminations calculated using FEA. To the authors knowledge, this is the first time an additively manufactured soft-magnetic component has been directly compared to electrical steel laminations in an application using 3D magnetic flux pathways. Improvements in the AM Hilbert stator could have been obtained by reducing the undesired electrical shorting between areas of material that should be electrically isolated, and by improving AM build parameters to reduce the size of insulating air gaps, hence increasing the stacking factor. Future work will address the loss of torque due to the reduction of total magnetic material, and offsetting this by increasing the area of the stator tooth, whilst reducing the size of the slots. The same amount of conductive material could be used by utilising AM to manufacture the windings, allowing the full torque to be obtained.

Declaration of competing interest

None.

Author contributions

AG: Conceptualization; Data curation; Formal analysis; Investigation; Methodology; Writing - original draft. **FN:** Data curation; Formal analysis; Methodology: Investigation; Writing – review and editing. **ES:** Methodology; Supervision; Writing – review and editing. **IT:** Conceptualization; Data curation; Formal analysis; Methodology; Funding acquisition; Supervision; Visualisation; Writing - review and editing.

Acknowledgements

We wish to acknowledge the Henry Royce Institute for Advanced Materials, funded through EPSRC grants EP/R00661X/1, EP/S019367/1, EP/P02470X/1 and EP/P025285/1, for access to the AconityMINI and AconityLab at The University of Sheffield. We also wish to acknowledge Prof. Geraint Jewell for support in the design and manufacture of the demonstrator motor, and for access and support to the AMH-1K Permeameter. The authors are grateful to the Wisconsin Electric Machines and Power Electronics Consortium (WEMPEC) at the University of Wisconsin-Madison for providing access to the electric machine prototype testing facilities. Electromagnetic simulation tools used in this study at the University of Wisconsin-Madison were generously provided by Mentor Graphics, a Siemens business.

6 Cracking of soft magnetic FeSi to reduce eddy current losses in stator cores

6.1 Journal details and author contributions:

Additive Manufacturing,

Volume 70,

2023,

103555,

ISSN 2214-8604,

https://doi.org/10.1016/j.addma.2023.103555.Journal – Additive manufacturing

Author contributions

Alexander Goodall – Conceptualisation, Methodology, data capture of all magnetic characterisation and electrical resistivity measurements, investigation, analysis of XCT data and magnetic characterisation data, data curation and visualisation, writing original draft

Lova Chechik – support with scripting of XCT analysis and EBSD analysis, writing review and editing

Ria Mitchell – Methodology set up and testing of XCT samples, support with data analysis

Geraint Jewell – Support with electrical resistivity methodology and analysis, support with analysis of BH loops and data interpretation, supervision

Iain Todd – Support with conceptualisation, formal analysis, visualisation, data interpretation, writing review and editing, supervision.

6.2 Background

During optimisation of the cross-sectional geometries for eddy current control, it was found that surface roughness and resolution caused a lower limit on the size of the air gaps used for electrical insulation. Ideally this gap would be as small as possible but without being short circuited by things such as un-melted particles. It is a well-known phenomenon in L-PBF fusion that too much energy input can cause cracking in certain alloys, and Fe-6.5 wt%Si certainly exhibits this behaviour. These cracks are usually in the order of 1-10 µm wide and cause the complete separation of the material for the length of the crack, with no areas touching. These cracks are then much smaller than the gaps obtained by designing the cross-sectional geometry.

Hence, this chapter started with the aim of inducing these cracks intentionally, in order to create a structure that limits eddy currents. When it was found to be possible, further work was undertaken to understand how the laser parameters and scan strategies impacted upon the crack density and crack orientation. The crack density and orientation were hypothesised to effect electrical resistivity which is proportional to the eddy current losses. Therefore, the research undertaken in this chapter set out to both control the density and orientation of the cracks, hence impacting the resistivity, and to characterise this material magnetically to understand the loss behaviour. It was suspected that the thin cracks could provide a much higher stacking factor than the geometries presented in chapter 4.

6.3 Paper

Cracking of soft magnetic FeSi to reduce eddy current losses in stator cores

Alexander D. Goodall[a], Lova Chechik[a], Ria L. Mitchell[a], Geraint W Jewell[b], Iain Todd[a]

[a] Department of Materials Science and Engineering, University of Sheffield, Sheffield, UK
[b] Department of Electronic and Electrical Engineering, University of Sheffield, Sheffield, UK

Corresponding Author – Alexander Goodall adgoodall1@sheffield.ac.uk

Abstract

To enable use of additively manufactured (AM) soft-magnetic material in electric machines, large bulk cross-sections must be avoided due to reduced efficiency, stemming from the large eddy currents they allow. Fe-6.5 wt%Si is an excellent soft magnetic material but is brittle. In this study we employ this inherent characteristic of the material to develop crack networks within the additively manufactured material to inhibit parasitic eddy currents. By manipulating the laser parameters and scan strategy to induce cracking, the effective resistivity of the material can be increased to 206 μΩ.cm, 250% of the materials' already high resistivity of 82 μΩ.cm. Crack density is shown to increase with decreasing laser speed and calculated electrical tortuosity shown to correlate to effective resistivity. Different scan strategies are shown to alter the orientation of the cracks, demonstrating that the crack orientation could be controlled in relation to the magnetic flux, providing high electrical resistance in the plane of the eddy currents, whilst maintaining magnetic properties. This method yielded a high stacking factor of >97%, low losses of 2.2 W/kg at 1 T, 50 Hz and outperformed other methods used in additive manufacturing of soft magnetic material, showing promise for manufacturing stators of complex electric machines.

Keywords

Laser Powder Bed Fusion; Cracking; Soft-Magnetic Material; Eddy currents; FeSi

1. Introduction

AM has been revolutionary in enabling the manufacture of high performance and lightweight structural parts (108), allowing for topological optimisation and reduced part mass and material usage. Described as having high geometrical freedom (109), AM, however, has its drawbacks including the generation of processing defects such as porosity and cracking (21), and whilst this is undesirable in structural parts, these features may be beneficial in some instance such as in the case of Titanium orthopaedic implants where high porosity facilitates bone ingrowth (110). Other types of functional materials have received recent interest such as soft magnetic materials, first additively manufactured by Zhang et al. (4). Since this initial work alloys such as Fe-Ni (57,111), and Fe-Co (56,112) have been successfully manufactured via AM to generate fully dense components. Most research in this area focusses on Fe-Si (21,23,25,47), however, as this is the most commonly used soft magnetic material in industry. Silicon content is typically kept to less than 3% to allow the material to retain some degree of "workability" (18) and allows rolling into thin sheets known as electrical steel laminations, which when insulated and stacked upon each other form the basis of most electrical machine (EM) stators. These laminations limit the eddy currents within the thickness of the lamination giving rise to low losses. Higher silicon content electrical steel with 6.5% rather than 3 wt.% Si, has soft magnetic properties such as high permeability, high saturation magnetisation and low magnetostriction (20) similar to that of Fe-3 wt%Si, but has almost double the resistivity at 82 μΩ.cm, and is a desirable material for use in electrical motors (EMs). However, it is difficult to process to form laminations by rolling as a result of the embrittling effect of the ordered phases (B2, D03) which form above 5% silicon content.

AM has been shown to effectively process fully dense Fe-6.5 wt%Si (21) and the design freedom of AM could revolutionise EM design and manufacture for More Electric Aircraft (MEA) (113). However, to fully capitalise on the ability to additively manufacture this soft magnetic material, strategies must be implemented to reduce losses, specifically eddy current losses caused by large bulk cross-sectional areas in planes perpendicular to the magnetic flux pathway. AM affords the geometrical freedom to introduce thin air gaps between areas of deposited material. By using these air gaps as electrical insulators the eddy currents can be confined to smaller cross-sectional areas, resulting in reduced eddy current losses. Plotkowski et al. showed a Hilbert pattern can reduce losses to 1.34 W/kg at 1 T, 50 Hz (27) whereas Goll et al. (26) showed that a slotted pattern, similar to electrical steel laminations, could reduce losses also. Both of these methods use air gaps as electrical insulators in their design, and other authors such as Koo et al. have processed air gaps to be as thin as 50 μm (41), however these often have unwanted shorting between adjacent sections due to surface roughness and partially melted particles, and still yields a low stacking factor (volume of magnetic material/volume of magnetic and insulation material) of only 80%. A stacking factor (SF) this low could impact upon the minimum size of an EM, an important selection parameter especially in the transportation and aerospace sector.

In this study the possibility of introducing stochastic cracking by manipulating process parameters is investigated. These result in structures which limit eddy currents using cracks of widths 1-10 μm, instead of designed air gaps approximately 100 μm, hence increasing the stacking factor. Scan strategy and laser parameters are manipulated to yield different crack patterns which can provide an advantage when orientated with respect to the magnetic flux path. These are investigated using X-ray computed tomography (XCT) and the effective electrical resistivity is measured. Finally, a ring sample is used to compare the magnetic performance between bulk,

cracked and a Hilbert cross section similar to that of Plotkowski et al. (27) demonstrating that this is a promising method for processing soft magnetic material via AM.

2. Materials and Methods

2.1 Sample processing

High silicon steel powder (Fe-6.5 wt%Si) supplied by Höganäs was used for all samples in this paper. The particle size and chemical composition, as stated by the supplier, are presented in Table 4.

Table 4 - Fe-6.5 wt%Si Powder Details

Chemical Composition (wt%)						Size Distribution (µm)			
Iron	Silicon	Oxygen	Nitrogen	Carbon	Sulphur	D10	D50	D90	D99
93.735	6.2	0.036	0.016	0.01	0.003	15.67	25.72	42.07	57.23

This powder was processed using an AconityMINI (Aconity3D GmbH). This is a laser powder bed fusion (L-PBF) manufacturing system which employs a 200 W ytterbium doped continuous wavelength laser (wavelength 1074 nm) with a spot size of 70 µm. This process is completed under an argon atmosphere with an oxygen content maintained at less than 100 ppm. The samples were built onto a stainless-steel build platform of 140 mm diameter with a constant layer thickness (l) of 30 µm. Hatch spacing was also held constant at 100 µm for all experiments and the laser power used was 195 W in all cases except for sample 1_ref, which uses a laser power of 170 W. The parameter set 1_ref had been found previously to give the highest density via a design of experiments methodology, which was used to optimise processing parameters for the manufacture of fully dense parts. Laser scanning speed (v) and scan strategy were the two main variables explored in this study. Laser parameters and scan strategies are listed in Table 5 and scan strategies employed are shown, schematically, in Figure 6-1. All samples were removed from the build platform by wire electrical-discharge machining.

Table 5 - Sample processing parameters and scan strategy

Sample ID = ID_laserspeed_scanstrategy	**Laser Speed (mm/s)**	**Scan strategy**	**Inter - Layer Rotation (degrees)**
1_ref (optimum bulk parameters)	700	B (Bidirectional)	67
2_300_B	300	B	0
3_400_B	400	B	0
4_600_B	600	B	0
5_800_B	800	B	0
6_400_BR	400	BR (Bidirectional with rotation)	90
7_400_S	400	S (Stripe)	0
8_400_SR	400	SR (Stripe with rotation)	90

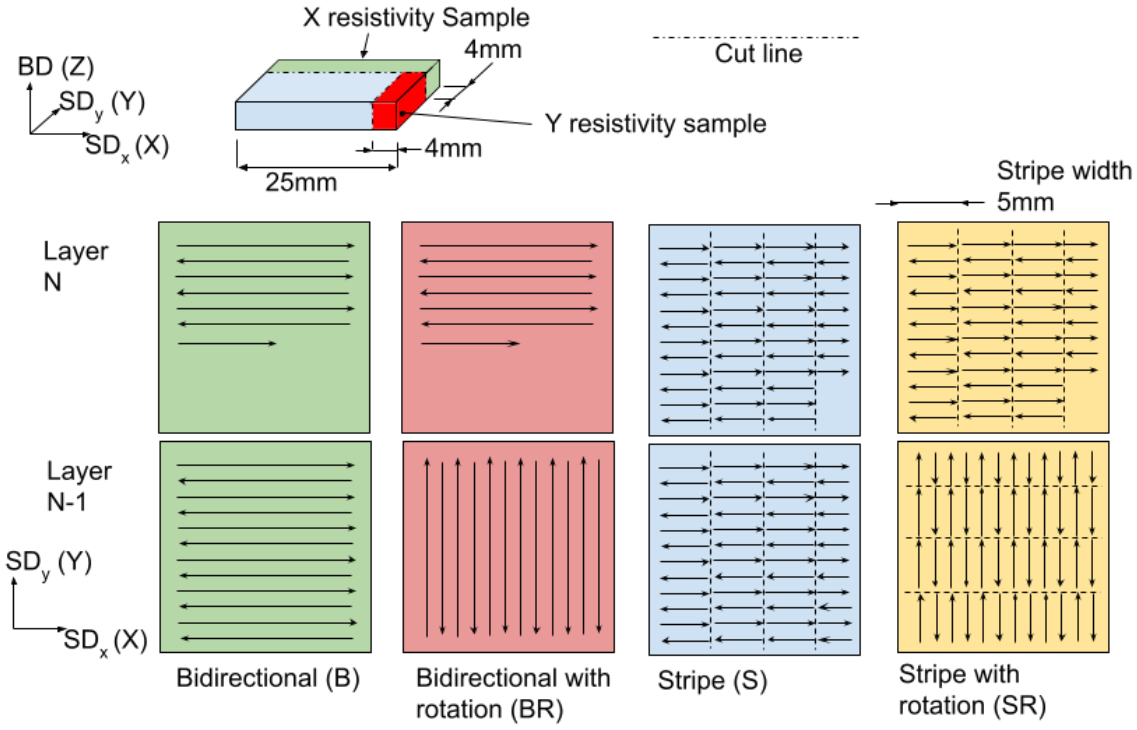

Figure 6-1 Sample size shown along with X and Y resistivity samples, and scan strategies used in this study which include scan strategies that do not have any later rotation, such as bidirectional (B) and stripe (S), along with scan strategies with a 90˚ layer rotation such as bidirectional with rotation (BR) and stripe with rotation (SR). Stripe width was kept constant at 5mm in this study.

2.2 Metallographic and cracking characterisation

25x25x4 mm (X, Y, Z) cuboidal samples were built to understand how laser parameters and scan strategy affected crack density and crack orientation. These samples were sectioned, polished using standard metallurgical techniques and optical micrographs taken of the XY and XZ planes using an Olympus BX51 microscope in conjunction with Clemex Vision PE system.

Throughout this study, it is evident that the cracking behaviour is complex and it is not possible to understand this from a single optical micrograph, hence XCT was used to gain a 3D understanding of the cracking through a larger volume. Samples of 20x2x2 mm (X, Y, Z) were mounted on a sample holder and then scanned using a Zeiss Xradia 620 Versa X-ray microscope (XRM). X-rays were generated from a tungsten transmission target and collected on a CCD (charge coupled device) 16bit 2000 x 2000 pixel detector. Rather than scanning the whole sample, a smaller region of interest with a field of view approximately 2x2x2 mm was scanned using the 4x objective, resulting in a spatial resolution of 1.9 µm. An accelerating voltage of 110 kV, and a source power of 15.5 W were used, while a filter (HE6) was inserted to reduce unwanted lower energy X-rays which can create scan artefacts. 1601 projection images were collected per sample, and a 2 s exposure time was applied to reduce noise and improve scan quality. Scans were achieved at a voxel (isotropic 3D pixel) of 2.76 µm. A filtered back projection method was used to reconstruct the data, and reconstructed .txm volumes were converted to 8 bit greyscale image stacks (.tiff) using Zeiss Reconstructor software.

Tiff stacks of approximately 1000 images were analysed using the batch solver and a custom macro in ImageJ (91) in both the XY plane and the XZ plane. The ImageJ macro rotated the tiff to obtain the correct orientation in relation to the build direction, cropped to the area of interest and auto-thresholded using the 'Triangle' method (114). Particles smaller than 10 pixels and a circularity

of greater than 0.5 were removed to reduce noise and exclude porosity, and the remaining particles analysed. Using an automatic process ensures greater consistency between samples than manual thresholding. The outlines of these particles were saved as tiff images and a small sample of these are compared with the original tiff images to ensure that only cracks are recorded, not porosity or other features. Once all 1000 images were processed, the data for each of these particles is saved, which includes the angle of a best fit ellipse and the Feret length, which were taken as approximations of crack orientation and length respectively. These data sets were processed using MATLAB R2020a (115) to calculate the crack density and orientation, which was separated into 5° bins and plotted on a histogram. These data sets have between 20,000 -70,000 records. An example of this workflow is shown in Figure 6-2. The error in the crack density values was obtained by manually thresholding the image and obtaining crack data from a random image, repeating this 5 times and then calculating standard error. This error value is used for all crack density values given. For each image, crack density was calculated as the total length of cracks divided by the image area.

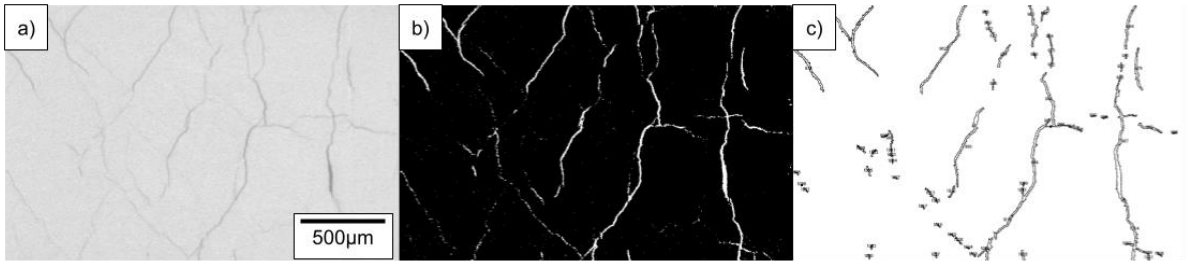

Figure 6-2 Crack analysis workflow showing the cropped image from the XCT data (a), the auto-thresholded and binarised image (b), and the outlines of the particles analysed by ImageJ (c). This shows that only cracks are identified but that the total cracks are underestimated as some faint cracks are not identified, and some larger cracks have their length underestimated.

Electrical conductivity and tortuosity have been shown to correlate in porous materials (116), often used in the geotechnical industry measuring the conductivity of a pore network filled with a fluid. Tortuosity can be calculated using several different methodologies (117), where usually the pore space is the conducting medium. In this study Avizo 3D (118) is used to calculate the electrical tortuosity where the solid medium, which is the Fe-6.5 wt%Si, is the conducting medium and the crack and pore space is assumed to be perfectly insulating.

First the tiff stacks created with XCT were imported into Avizo 3D. These data sets were then cropped to remove the empty space in the scan and the ends of the sample to improve segmentation, as these display some beam hardening which would make this difficult. Following this, a median filter was applied, the solid material segmented from the cracks and pores and a formation factor experiment used to investigate the tortuosity of the electrical path. The formation factor experiment imposes a potential difference at each end of the sample, whilst the surfaces parallel to the current flow have a 1 voxel thickness insulator added to the outside. A schematic of this is shown in Figure 6-3, demonstrating a 2D tortuosity. The formation factor calculates a 3D approximation of the tortuosity. Using Ohms Law and conservation of charge averaged over a volumetric area, it is possible to calculate a formation factor which is “directly linked with the electrical conductivity through its inverse: the electrical resistivity” (119). Full details of the calculation can be found in the Avizo user guide (119).

Using the result of this formation factor experiment, electrical tortuosity was calculated using a plugin (120) that defines electrical tortuosity as shown in Equation 15, where F = formation factor and φ = Volume Fraction of Pore space. Tortuosity is a measure that describes a ratio between actual flow path length to the straight distance between the ends of the sample, as shown in Figure 6-3.

$$\tau = \sqrt{F\varphi}$$

Equation 15

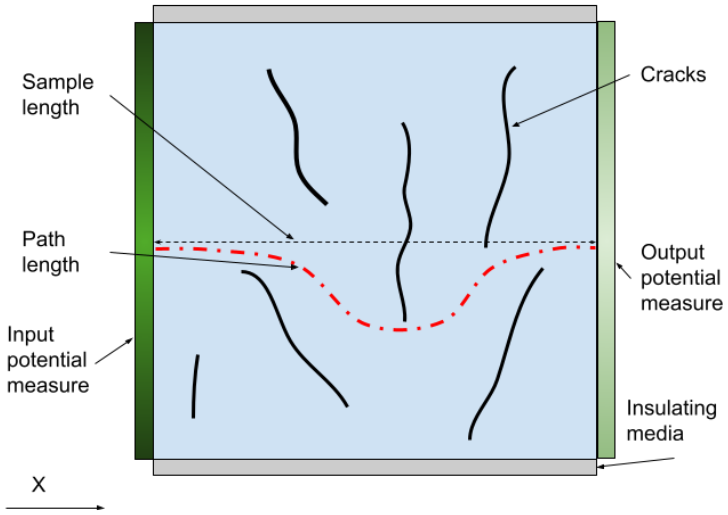

Figure 6-3 Schematic showing tortuosity calculation, the path which must travel around the cracks within the sample. A potential is imposed at the input and output, whilst an insulating wall of 1 voxel thickness is applied at the surfaces parallel to the current direction (X).

2.3 EBSD data collection and processing

EBSD (Electron backscatter diffraction) samples were prepared by sectioning and polishing in the YZ plane to enable observation normal to the scan tracks in the B scan strategy. The microscope used was a 7900F field emission gun (FEG) SEM manufactured by JEOL, fitted with an Oxford Instruments Symmetry EBSD detector, used with a 20 kV accelerating voltage and step size of 1 µm. The samples were mounted on the SEM stub using silver paste. AZtec by Oxford Instruments was used to capture and process the EBSD data, indexing the FeSi samples using the default parameters for α-iron, (BCC). The index rate was over 98% for all samples inspected. Following the data acquisition, AZtec was used to align the EBSD map which has multiple frames, before exporting to .crc file format.

Analysis of EBSD data was performed in MATLAB R 2020a using the MTEX toolbox plugin. The data was imported and aligned to the coordinate system of the base plate, to allow the data to be compared between samples. Then high angle grain boundaries were identified (>10˚) and orientation maps and pole figures were plotted to view the data graphically. Orientation maps are viewed on the XY plane, although the samples were inspected and are displayed in the YZ plane.

2.4 Resistivity and magnetic characterisation

Further segments were sectioned from the larger cuboid to obtain samples suitable for resistivity testing. The X-resistivity samples were approximately 25x4x4 mm (X, Y, Z) and the Y-resistivity samples approximately 4x20x4 mm (X, Y, Z) as per Figure 6-1. A digital calliper was used to measure the length and cross-sectional area, which was taken as the average of the cross-section measured at each end. The resistance of these samples was measured 5 times using a Cropico DO5000 microhmmeter by Seaward, reversing the polarity after 3 measures, and converted to resistivity using Equation 16.

$$\rho = \frac{RA}{L}$$

Equation 16

where $\rho = resistivity, R = resistance, A = area, L = length$. Throughout this paper effective resistivity is used rather than resistivity, as intrinsic material properties are not being stated but the measured value from the system of material with cracks. Effective resistivity has been expressed through this paper as a percentage of the bulk resistance which is 82 µΩ.cm as measured and reported in literature (20). 5 samples were taken from sample 1_ref and the resistivity measurements repeated; the standard error was then calculated, and this value of error is used for all effective resistivities.

BH loops and loss behaviour were measured using a toroidal sample of 30 mm inner diameter (ID), 38 mm outer diameter (OD), and approximately 4 mm thickness respecting the sample dimensions in BS 60404-4:2018 (62). These toroidal rings were tested using an AMH-1K Permeameter by Laboratorio Elettrofisico controlled using Neon software. The rings were first wound with a single insulating layer of Kapton tape, then wound with 45 turns on the secondary search coil using 0.35 mm diameter single core copper wire and 40 turns on the primary coil using 1.5 mm diameter multi core wire. The cross-section of the ring was measured in three places using a digital calliper and the average taken, and the mass was measured using laboratory scales. The specific power losses are calculated as per Equation 17, where density is 7480 kg/m^3 (20).

$$P_l = \frac{A \times f}{\rho}$$

Equation 17

where P_l *= power losses, A = cycle area, f = frequency and ρ = density*.

3. Results and discussion

3.1 Effects of scan strategy and laser speed on resistivity

By changing the laser speed whilst keeping laser power, hatch spacing and scan strategy constant (sample 2-5), it is possible to observe that the slower the laser speed, the higher the crack density (Figure 6-4). It is well known that excessive energy input can cause cracking in AM parts of certain alloys (121), however as the tendency is to eliminate cracking from parts, there has been little study on the crack density variation with processing conditions. The limited data from this study shows a trend for lower laser speeds to increase the crack density, but the nature of this relationship is not fully understood. It is likely that there is a lower limit for laser speed at which parts will not build successfully as a result of excessive balling or other build defects, and a higher limit at which cracking no longer occurs and eventually the samples will exhibit lack of fusion (LOF) defects. By altering the scan strategy there is also an impact on crack density. By adding a 90° inter-layer rotation, as with scan strategies BR and SR, the crack density is elevated when compared to the B and S strategies.

Higher crack densities would give more opportunities for electron scattering when passing an electrical current, however as shown in Figure 6-5, there is not a simple relationship between crack density and effective resistivity. For samples with the bidirectional scan strategy (B), it would appear that higher crack density yields a higher effective resistivity, although one of the samples

with high laser speed 5_800_B shows a higher resistivity than 4_600_B despite a lower crack density. Upon further investigation it was found that sample 5_800_B had a number of LOF defects (Figure 6-6) which are likely to increase the effective resistivity whilst not being accounted for in the value for crack density. The sample with the S scan strategy exhibits relatively high effective resistivity of approximately 200%, whilst having a lower crack density than some of the other samples with lower effective resistivity. Based on this analysis it is clear that crack density alone cannot predict the changes in electrical resistance observed.

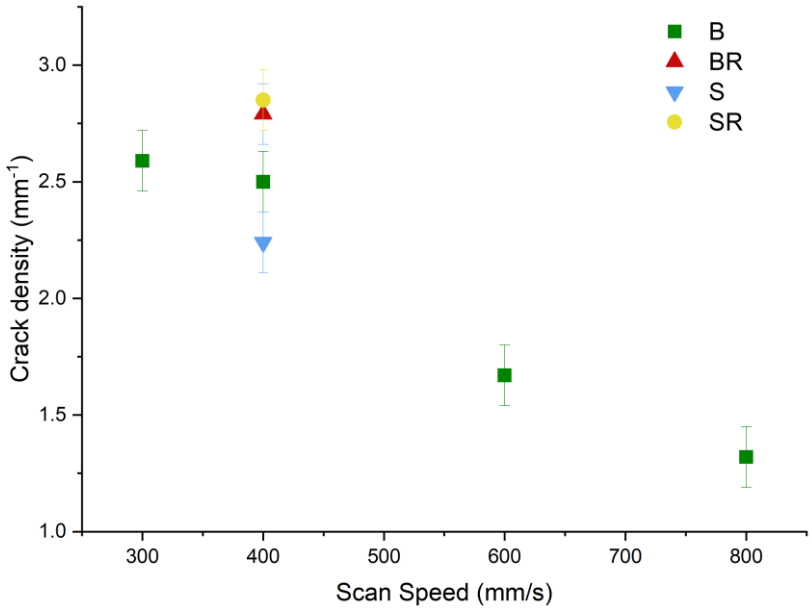

Figure 6-4 Laser speed vs crack density showing that the slower the laser speed, the higher the crack density within the sample. It is likely at higher laser speeds cracking will stop as LOF starts to become apparent. At lower laser speeds than 300 heavy balling occurs, and the samples are not built successfully. By changing the scan strategy whilst maintaining laser speed, there is an effect on the crack density within the samples.

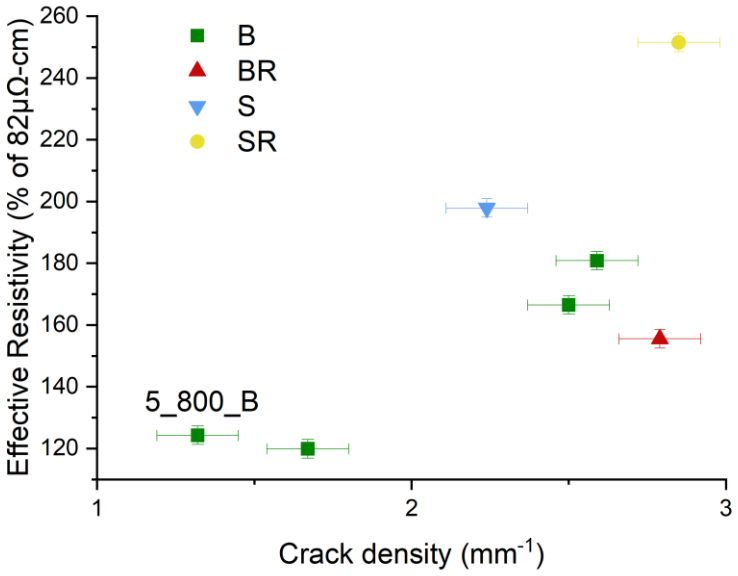

Figure 6-5 Graph showing that in general the more cracks a sample has, the higher the effective resistivity. The sample at the highest laser speed 5_800_B exhibited both cracking and LOF defects. This may explain why the first data point has a higher resistivity than the second, even though it showed a lower crack density.

.

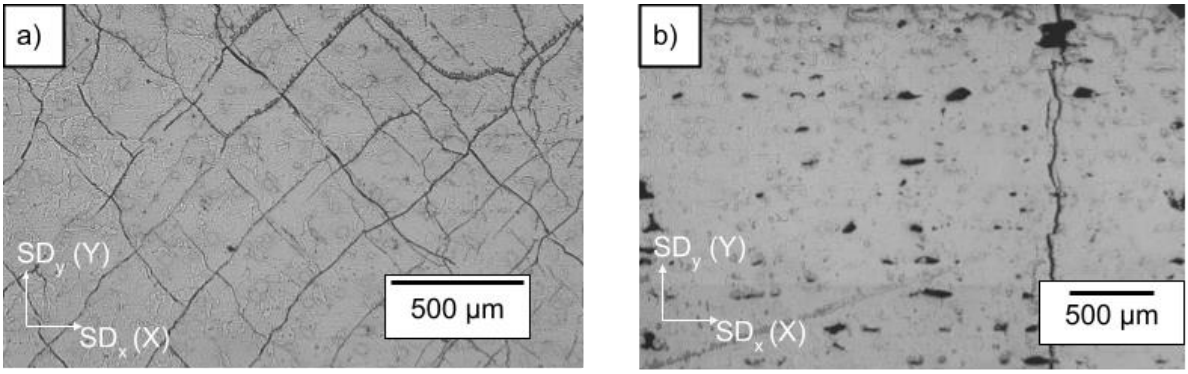

Figure 6-6 Optical micrograph of 2_300_B sample (a) XY plane showing that the cracking shows a distinct pattern with the cracks running in preferred directions of 45 and 135˚. As there are a large number of cracks, it would be unsuitable to infer the crack distribution throughout the whole sample using only one micrograph. Sample 5_800_B (b) showing both cracking and LOF defects.

As crack orientation varies significantly between samples, investigating a 2D cross-section cannot infer the crack distribution through the sample. It is not possible, from such images, to tell the depth or changing paths of the cracks, so, XCT was used to enable the crack networks to be viewed and analysed more fully in 3D. The XCT data was obtained to have sufficient resolution to be successfully thresholded to facilitate the segmentation of the cracks and pores from the solid material, whilst maintaining the largest field of view possible. Using the XCT data the electrical tortuosity could be calculated in Avizo 3D for the same direction as the physical measurements (X), which considers not only crack density, morphology and orientation but also how the cracks are positioned relative to each other. Calculated electrical tortuosity shows a linear relationship with the effective resistivity, as shown in Figure 6-7.

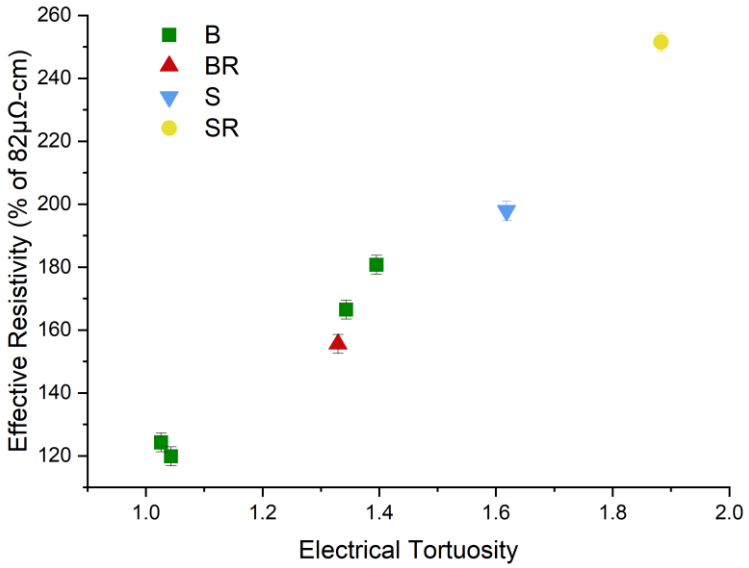

Figure 6-7 The electrical tortuosity calculated from the XCT data shows approximately a linear relationship, demonstrating that the scan strategy can create more tortuous pathways without increasing the crack density, as the sample with the S scan strategy shows.

3.2 Effects of scan strategy on crack orientation

Additive manufacturing allows a level of control to spatially vary microstructure and processing parameters unavailable in many traditional processes. To allow the magnetic flux to run in three dimensions in an electric machine, it may be possible to tailor the orientation of the cracking within the material to yield the highest possible resistivity in the plane in which eddy currents will circulate, hence reducing the losses. This could give a spatially graded material with anisotropic effective resistivity, providing electric machine designers unprecedented freedom over the magnetic flux pathways in the magnetic circuit, previously limited to 2D by electrical steel laminations or to materials with poorer properties such as soft magnetic composites (SMC).

The first of the scan strategies used in this study, B, scans the material in the same direction each layer. As residual stress has been shown to be higher normal to the scan direction (77), it is expected that cracks would occur normal to the scan direction as well, which would yield a higher tortuosity in the scan direction (X) than the perpendicular (Y) as most cracks would align with current flow in the Y direction, giving a lower tortuosity. Therefore, for samples 2-5 where the scan direction is restricted to hatch only in the X direction, cracks would increase the electrical tortuosity more for electrical current running in the X direction than the Y direction. To investigate this samples were taken from both the X and Y direction and their effective resistivity measured as displayed in Figure 6-8. As predicted, this shows that for bidirectional hatching, the effective resistivity in the X direction is significantly higher than that in the Y direction. Hence if the eddy currents are generated in the XZ plane they would experience higher resistivity than if they were in the YZ plane. In this way it is possible to tailor the anisotropy of the material based upon the electric machine design, to ensure the highest level of resistance in the plane in which eddy currents generate. The orientation of these cracks is shown in Figure 6-9, demonstrating that in the XY plane, the cracks are mostly orientated between 45˚ and 135˚ from the X direction, whereas in the ZX plane the orientation of the cracks is also centred around 90˚ from the X direction but with much less variation from this value.

By adding a layer rotation of 90˚, sample 6_400_BR shows a decrease in anisotropy between the X and Y samples effective resistivity, demonstrating that with scan strategy the anisotropy can be preferentially selected based upon the electric machine design. If the magnetic flux will always run in a single direction such as the tooth of an axial flux machine, the cracks can be heavily orientated to optimise for one direction, similar to a grain-orientated electrical steel. If the magnetic flux is required to change direction within the material such as in the back iron of a machine, scan strategies can be manipulated to yield an even crack distribution delivering an equal but lower electrical performance in every direction in a manner similar to non grain-orientated electrical steel.

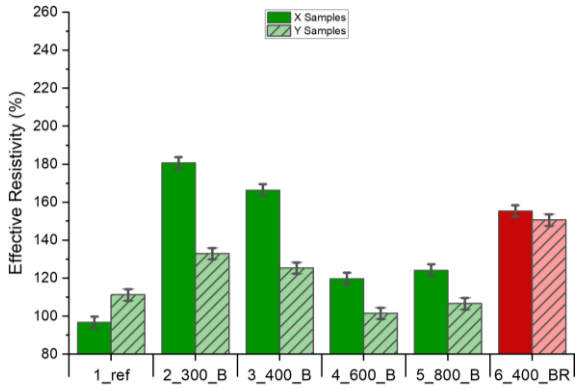

Figure 6-8 Difference in effective resistivity between X and Y samples, showing that with a bidirectional scan strategy, the samples have a higher resistance in the X direction, parallel to the scan direction. By introducing a rotation into the scan strategy, the anisotropy is reduced. The reference sample has higher than expected resistivity in the Y sample.

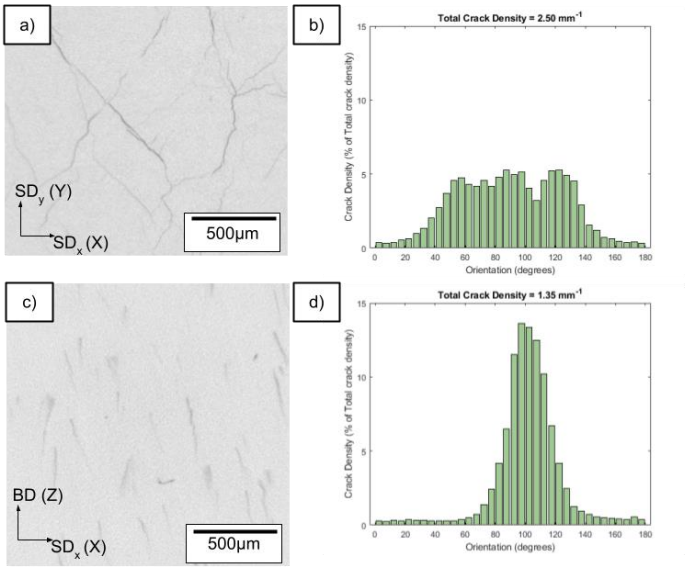

Figure 6-9 An example XCT slice from sample 3_400_B in the XY plane (a) and XZ plane (c) and their respective histograms (b, d), showing that in the XY plane there is a strong preference for cracks which are between 45-135˚, showing a spread centred around 90˚ (normal to the scan direction),, whereas in the XZ plane, cracks have a much smaller spread around 90˚.

A number of scan strategies were used in this study, and crack orientation is investigated for each. The crack orientation in the XZ plane was similar for all the scan strategies and an example of this for 3_400_B can be seen in Figure 6-9d.

Figure 6-10 shows an optical micrograph of samples for each of the scan strategies, along with histograms of the crack orientation in the XY plane which differs for each sample. The highest anisotropy is observed for the S scan strategy, showing cracks mainly at 90˚ to the scan direction (X), but also with a number of cracks parallel to the scan direction. Both strategies with a layer rotation (BR, SR) show a lower anisotropy than without (B, S). Depending on the design of the electric machine, the most appropriate scan strategy could be used to ensure the cracks are in the orientation that best serves the machine, increasing the electrical tortuosity of the eddy current flow path. The stripe with rotation (SR) sample shows the highest effective resistivity of 250% of the bulk resistivity at 206 µΩ.cm. Residual stress is expected to be highest in the plane normal to the scan direction, hence for the B scan strategy the cracks would be expected to be concentrated at 90°. Figure 6-10b shows this to be the case, with some variation about 90°.

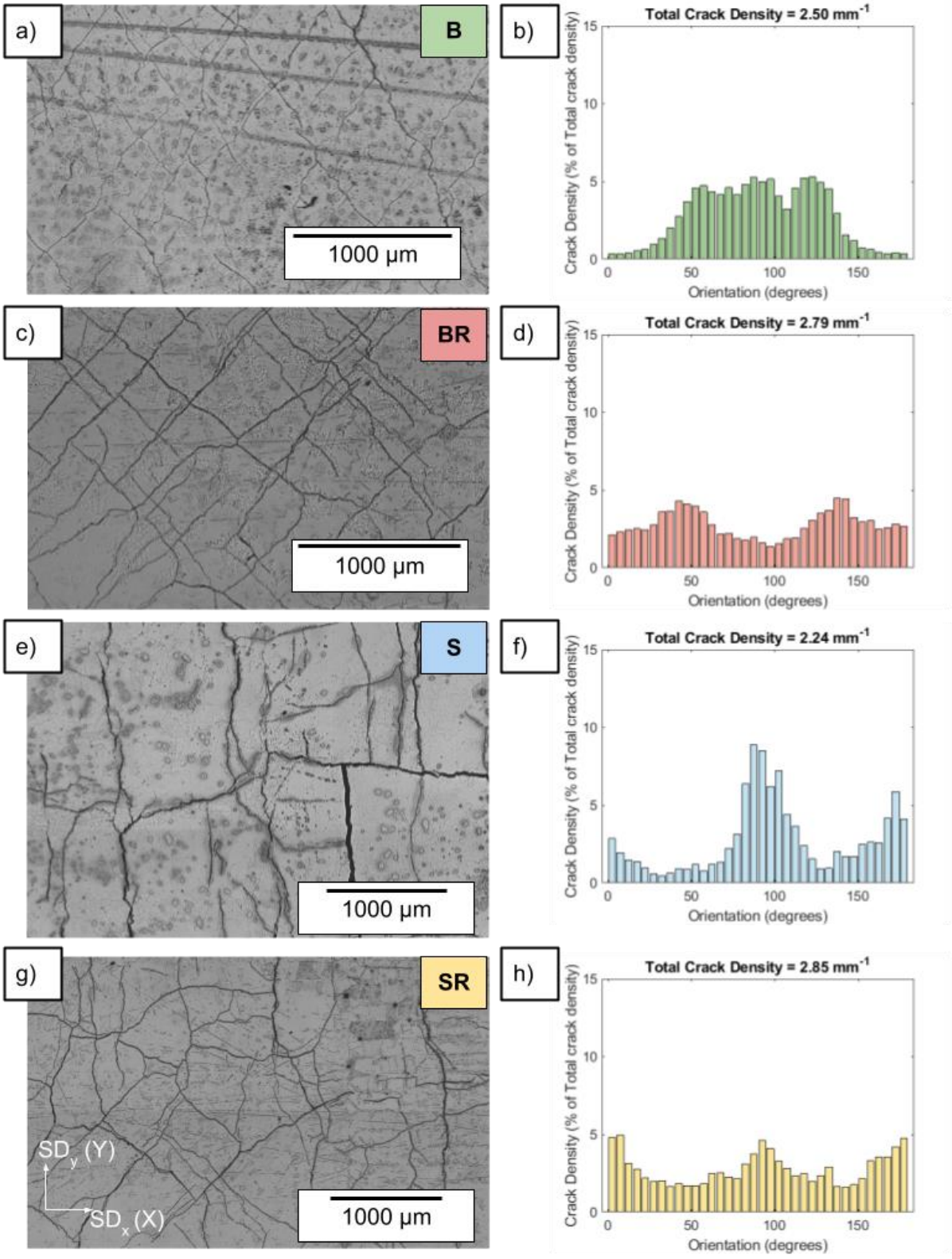

Figure 6-10 Optical microscopy images of samples 3_400_B (a), 6_400_BR (c), 8_400_S (e) and 9_400_SR (g) with their respective crack density histograms (b,d,f,h) showing the orientation of the cracks within the sample in the XY plane. 6_400_BR shows cracks mostly in the 45˚ and 135˚ directions whereas 8_400_SR shows cracking mostly in either the 0˚ or 90˚ direction.

3.3 Investigation of the residual stress and microstructure

Aside from the stochastic cracking within the samples, other factors such as residual stress, grain size and microstructure could have an impact on the effective resistivity. To ensure that the observed behaviours are an outcome of stochastic cracking, investigation into the other aspects is carried out for validation. To test the effect of residual stress and grain size, the samples were annealed at 1150˚C for 1 hr, as shown by Garibaldi et al. (23) to give the best magnetic properties. By using this heat treatment, residual stress will be relieved which may increase or decrease effective resistivity depending on the residual stress profile. The grain size will also grow, reducing grain boundary density and is expected to decrease effective resistivity. Figure 6-11 shows that after heat treatment the effective resistivity of the majority of samples change by less than 10%, with most samples displaying a small increase in resistance. Hence both residual stress and grain size/grain boundary density could not account for the magnitude of increase in effective resistivity shown by the samples in the as-built condition, adding further confidence that the cracking is the source of the increased effective resistivity. It may be possible that the thermal stress induced in the part during heat treatment caused some cracks to grow, which would increase the effective resistivity.

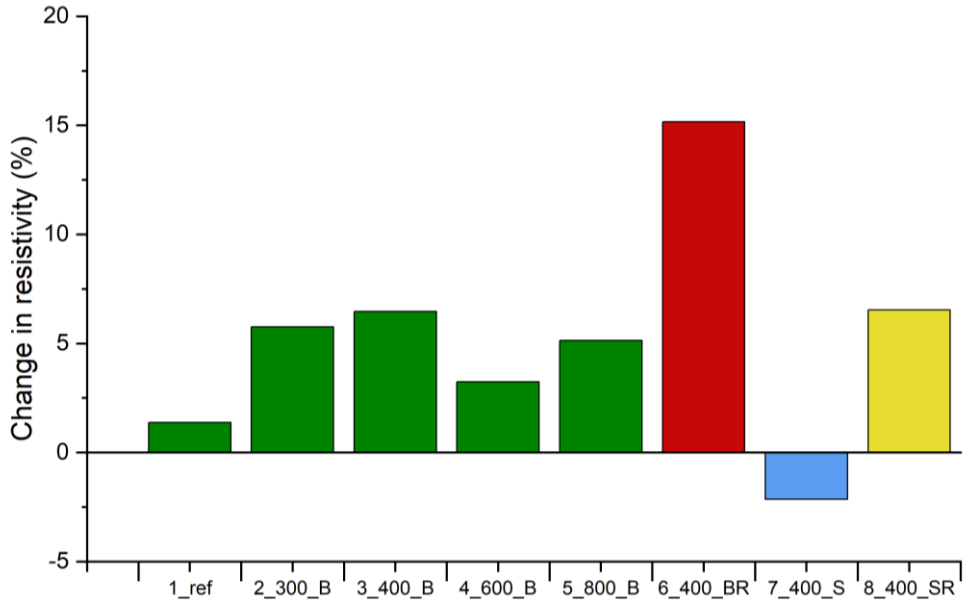

Figure 6-11 The percentage change in effective resistivity of each sample post heat-treatment, showing that on average there is less than a 10% difference between pre and post heat treated samples.

EBSD analysis was undertaken for all the samples to observe the as-built microstructure. Shown in Figure 6-12 is the data for 3_400_B and 8_400_SR as these samples use the same laser speed and power but exhibit large differences in effective resistivity, 166.5% 251.5% respectively. Sample 8_400_SR shows a common L-PBF microstructure, with a preferred orientation of the <001> crystallographic direction aligned to the build direction (Z), with elongated grains along this same axis, although the grain size is larger than average with some grains extending over 1 mm. Sample 3_400_B exhibits an unusual microstructure for L-PBF, with a preference for the <111> texture aligned with the build direction (Z). The texture does show elongated grains up to 0.75 mm long in the build direction (Z), however these are not as large as for 8_400_SR where some grains are >2 mm long.

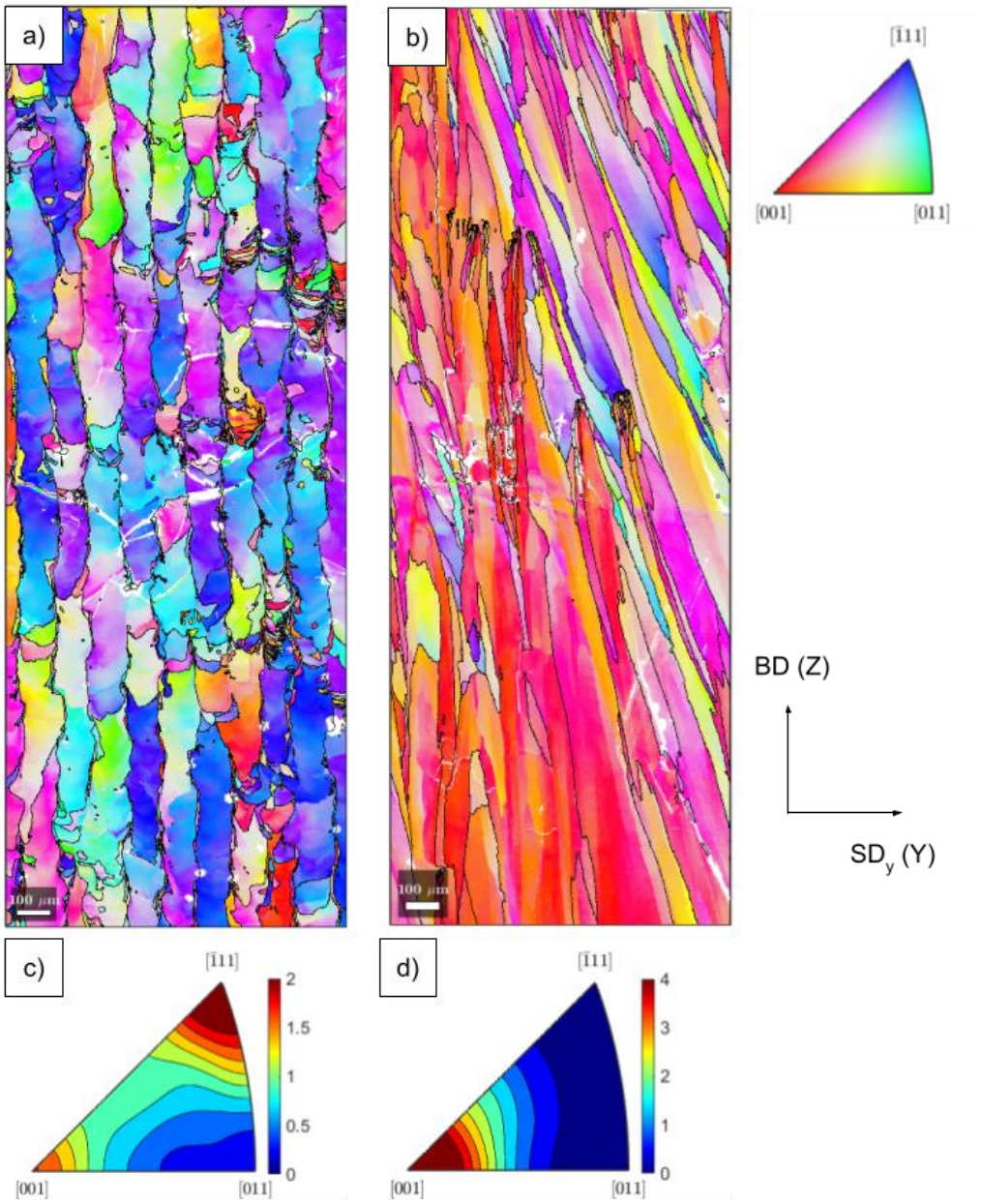

Figure 6-12 YZ view of EBSD data showing orientation maps for samples 3_400_B (a) and 8_400_SR (b) and pole figures respectively (c,d). The grain orientation is plotted with respect to the XY plane, showing that 3_400_B has a <111> texture in the build direction (Z), whereas 8_400_SR has a stronger <001> texture in the build direction (Z).

3.4 Magnetic characterisation

This work has demonstrated the possibility to increase the effective resistivity of Fe-6.5 wt%Si, by manipulating the laser parameters and scan strategy to introduce stochastic cracking. However, to be used in an EM, electrical resistivity is not the only important parameter, hence the impact of the cracks on the other magnetic properties must be investigated. To do this, ring samples were additively manufactured using solid bulk material, a cracked ring and a Hilbert ring similar to that reported by Plotkowski et al. (27), an example cross section of which is shown in Figure 6-15a. The cracked ring was manufactured using parameters 8_400_SR as this showed an average increase in effective resistivity up to 250%, whilst having a lower anisotropy as shown in Figure 6-10h. As shown in Figure 6-13, the Hilbert and cracked rings both have a significantly smaller area inside the BH loop

demonstrating lower losses. This is confirmed for the full frequency range tested of 5-1000 Hz (machine limits) in Figure 6-14. The shape of the BH loop shows that for the cracked sample, the permeability is reduced below that of the bulk as the Field increases, hence requiring a higher field to reach the same flux density. The drop in permeability is likely due to cracks or air gaps in the material, as these will act as pinning sites for the domain walls and may also make domain rotation more difficult.

The knee point appearing at a lower flux density than that of the bulk material is an issue for EM design, as this would require a higher field to get an equivalent flux density. Heat treatment could improve the permeability as shown by Garibaldi et al. (23), though it may not be possible to achieve the same value as the bulk material due to the extra material defects. The stacking factor of the cracked sections is >97%, which is much higher than that of the Hilbert section at 83.5% as shown in Figure 6-15, and likely to remain higher than any cross-sectional design due to the small width of the cracks (<10 µm) compared to the minimum width of a designed air gap, which is at least 50 µm. Further to this, cracks provide electrical insulation without any shorting as there will be no contact between the cracked surfaces. This is unlike the designed cross sections where there is often unwanted shorting between areas which should be electrically isolated (8). Having a higher stacking factor is another enabler to reducing machine size. However, as the cracking is stochastic, there may be higher variability between samples and in order to quantify this variability as a result of the stochasticity of the defect population a larger data set would be needed, which falls outside of the scope of this initial study. The number of cracks detected by the XCT and analysed was very large at 20,000 - 80,000 for a sample only approximately 2x2x2 mm, hence for the full sample of 25x25x5 mm it is possible that there are sufficient cracks for the material performance to be predicted statistically. The number of cracks is overstated as the cracks will be counted multiple times (once per slice) due to the nature of the analyse, but this systematic error is accounted for throughout the paper by using crack density.

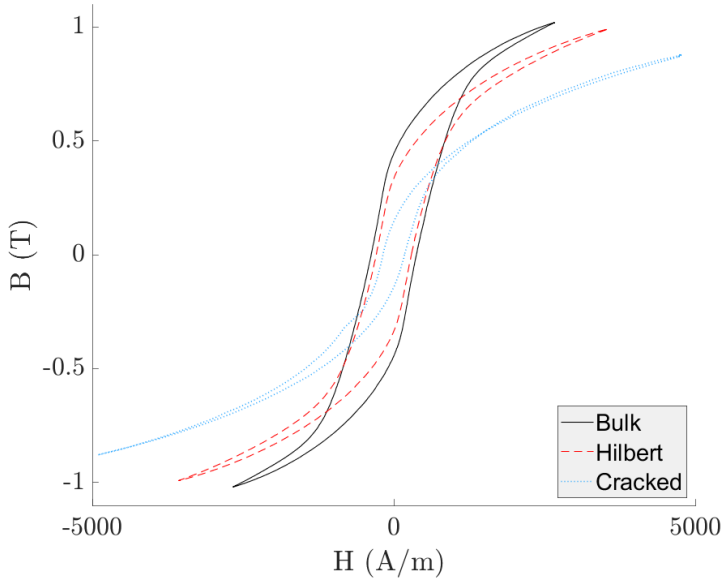

Figure 6-13 BH loops of bulk, cracked and Hilbert rings at 50 Hz, 1 T. The Hilbert ring shows lower losses than bulk (area), and the cracked section shows lower losses than both of the other samples. For both the cracked and Hilbert samples, the permeability (gradient) is reduced when compared to the bulk, especially after the knee point in the loop

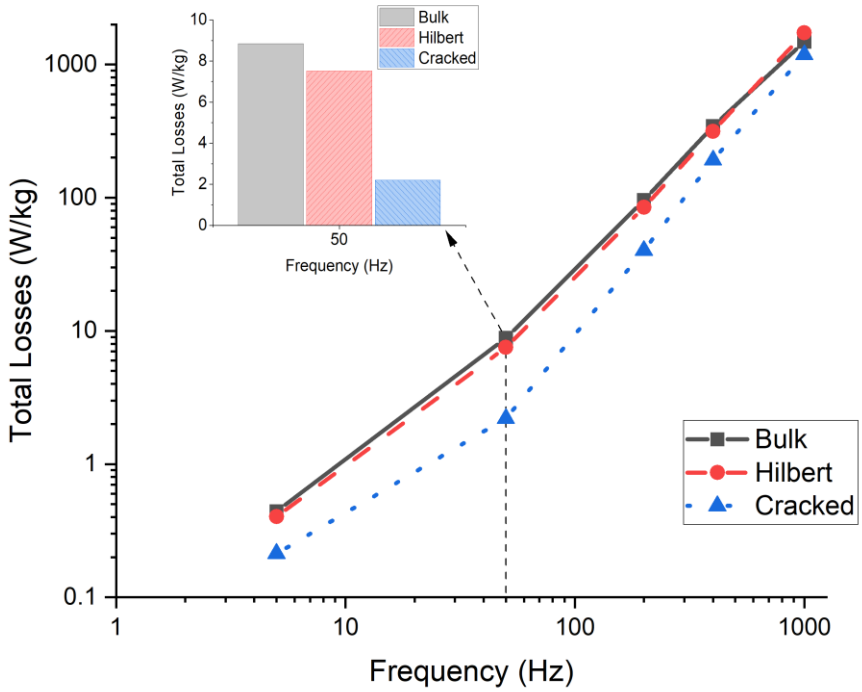

Figure 6-14 Loss behaviour of bulk, Hilbert and cracked samples at 1 T, showing that the Hilbert section provides an improvement over bulk, however the cracked ring yields lower losses through the whole frequency range tested than both the other samples.

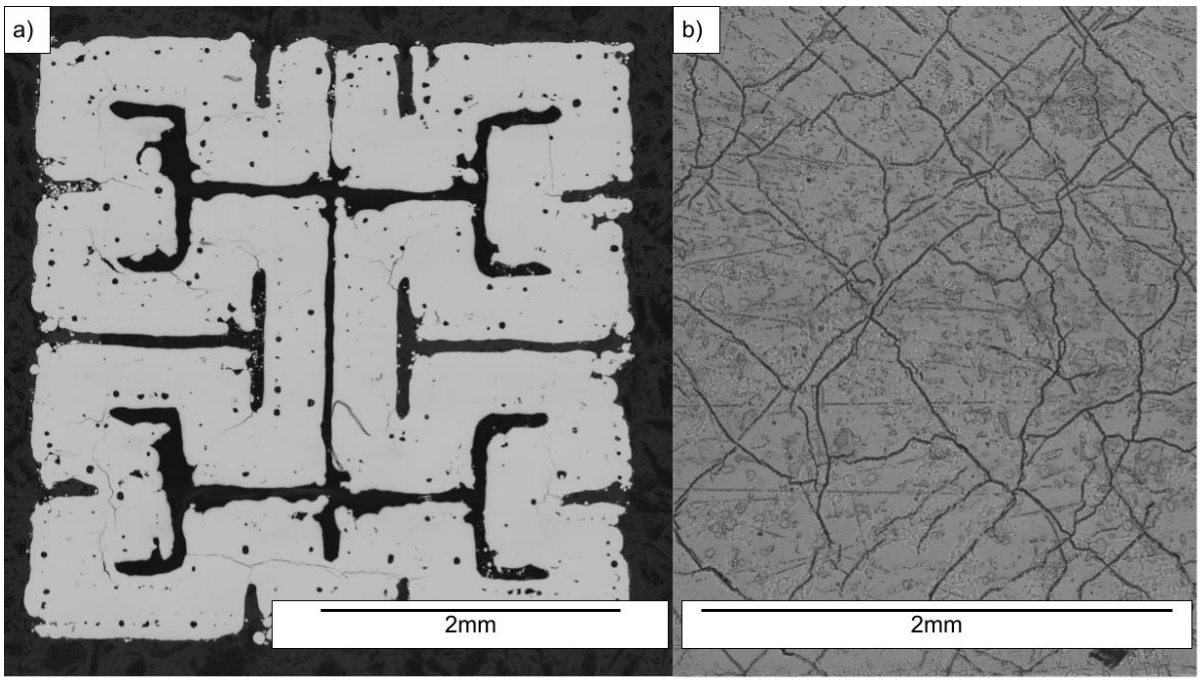

Figure 6-15 Micrographs of cross-sections of a Hilbert style pattern (a) with a stacking factor of 83.5% and a cracked section (b) using parameters 6_400_BR with a stacking factor of 97%, showing that the cracked section can yield a much higher stacking factor whilst still having lower losses. The Hilbert section has some porosity as the parameters used were optimised for bulk sections, rather than thin walls.

The cracked samples exhibit higher effective resistivity, lower losses, and a higher stacking factor than the Hilbert cross-section, however there are several more issues to discuss. Firstly, the volume and orientation of cracks will be dependent upon the part geometry, as this will change the thermal conditions in the build. The residual stress is correlated to the hatch length and cross sectional area (77), if the cross section is changing the residual stress will also vary. As this paper shows, a striped scan strategy could be implemented whilst still maintaining a high level of cracking which is a potential solution to this as any cross-section can be broken down into a number of uniform width stripes. Furthermore, the complex geometries found in EMs make it very difficult to characterise the material or magnetic properties of a stochastically cracked component in an actual machine.

Most tests to understand material properties require standard test sample geometries. If one were to use the same parameters to create a small magnetic test ring with a 5 mm cross-section and a stator with a cross section of 20 mm, it is likely that there would be a difference in crack density and/or orientation, and hence magnetic properties between the two parts. Additionally, there would also be a need to model this magnetic behaviour, otherwise components would have to be made by trial and error by manufacturing components and testing their properties. Models that are able to understand this behaviour are computationally expensive, and are generally limited to a small volume which would not allow a good understanding of the macro-scale behaviour. With further understanding of the underlying process simpler models may be able to be used to aid design.

Electrical resistivity was physically characterised, and electrical tortuosity calculated based on the XCT data in this study. In both cases these measures use a linear current, whereas eddy currents are generally circulating around a cross-section, with a non-uniform amplitude depending on the spatial position. The magnitude of eddy currents is proportional to the material resistivity therefore this is not expected to have a significant impact on the results. Utilising the electrical tortuosity calculations, it would be possible to define a circuit path and measure the tortuosity around this path, although to the authors' knowledge, no software currently has this capability. Further to this, the electrical tortuosity calculations are based on geotechnical work, with a solid non-conducting phase which is often a type of rock, and a liquid conducting phase filling the pore space. This is the opposite to the samples analysed in this study where the solid is the conducting phase. For our samples the tortuosity was between 1-2, which is relatively low, whereas most work validating these models and calculations use higher tortuosity values. The data in this study shows a good correlation between the measured effective resistivity values and the calculated electrical tortuosity, however as this is not a standard use case for this software more validation work would be needed to confirm its applicability.

The mechanical properties of the stochastically cracked samples have not yet been analysed but are assumed to be inferior to the bulk material and depending upon loading conditions, may also be lower than that of any designed cross sections such as the Hilbert pattern. Due to extensive cracking, it may not be possible to use stochastic cracking to reduce losses in the rotor of an EM due to the high centrifugal loading; however, the stator has relatively low mechanical requirements and so this methodology should be applicable in this case. The fatigue behaviour through repeated magnetisation and thermal loading would also need to be well understood before this method could be used, as there are concerns that the cracks may propagate and cause the loss of structural integrity. As Fe-6.5 wt%Si has almost zero magnetostriction of 0.01 ppm (20), yielding low stresses through the magnetisation cycle, it is likely the best composition to use, however cyclic thermal loading will cause expansion and contraction of the material, which may lead to crack growth and

failure. That said, all the samples in the current work possess sufficient structural integrity to handle and process.

The directionality of cracks may be beneficial for EM design, by aligning the cracks parallel to the flux direction this will give the highest resistivity in the plane in which eddy currents would circulate, whilst causing the least disruption to the magnetic flux. An Epstein frame style test could be used to quantify the benefit of this anisotropy, by aligning the cracks along the legs of the Epstein frame to give the highest performance. The design flexibility of the AM process allows for alteration to the scan strategy and laser parameters for different areas of a component, meaning that at every point in the stator the cracks could run parallel with the magnetic flux even when using a complex 3D flux path.

The loss behaviour of the stochastically cracked parts is comparable to other materials in production and industrial use today. As shown in Table 6, the losses are lower than both an SMC and a relatively thick low-silicon steel lamination, however thin high-silicon steel laminations still outperform the material characterised in this study. It has been demonstrated, in this study, that it is possible to process material with three-dimensional flux paths, with losses below that of traditionally manufactured Fe-3 wt.%Si electrical steel laminations. By directly manufacturing the stator via AM there will also be a reduction in component count and assembly time and cost when compared to a laminated electrical steel stator. This methodology could enable novel electric machine architectures which capitalise on this geometrical freedom to give performance benefits which have been unfeasible with laminations or SMC.

Table 6 - Loss behaviour of various materials at 50 Hz and 1 T

Material	Stochastic cracked Fe-6.5 wt%Si (this study)	AncorLam SMC (122)	JFE 65JN1600 3 wt%Si lamination 0.65mm (123)	JNEX-Core 6.5 wt%Si lamination 0.1mm (124)
Losses @ 50Hz 1T (W/kg)	2.2	9.0	7.1	0.5

4. Conclusion

In this paper, the ability to manipulate the nature of stochastic cracking in Fe-6.5 wt%Si, a high silicon electrical steel, has been demonstrated. It is shown that by reducing the laser speed, the crack density within the material increases, and that by changing the scan strategy the orientation of the cracks can be influenced. By cracking the material using this methodology, an increase in effective electrical resistance up to 206 μΩ-cm, 250% of the expected bulk resistance has been observed in sample 8_400_SR when using a stripe with rotation (SR) scan strategy with a laser speed of 400 mm/s. The total AC losses for this sample at 50 Hz 1 T are 2.2 W/kg, which shows a reduction in losses to below that of a cross-section with air gaps such as for the Hilbert section (6.8 W/kg, 50 Hz, 1 T), designed to reduce eddy currents. The cracked material shows a higher stacking factor of >97%, compared to only 83.5% for the Hilbert section.

The ability to orient the cracks parallel to the flux path allows for spatial grading of areas to ensure the cracks are always orientated to increase the resistance in the plane in which eddy currents circulate. It is also possible to correlate electrical tortuosity calculated from XCT data with the measured effective resistivity. With lower losses and a higher stacking factor, stochastic cracking

is a promising solution to implementing AM processed soft magnetic material into the stator of an EM, enabling a 3D magnetic flux path with low losses.

Declaration of competing interest

None.

Author contributions

AG: Conceptualization; Data curation; Formal analysis; Investigation; Methodology; Writing - original draft. **IT:** Conceptualization; Data curation; Formal analysis; Methodology; Funding acquisition; Supervision; Visualisation; Writing - review & editing. **LC:** Software; Writing - review & editing. Support in creating and modifying MATLAB code. **RM:** Data curation; Methodology. Support in design of experiments and data capture of XCT. **GJ:** Data curation; Methodology. Support in design of experiments, data capture and analysis of magnetic measurements.

Acknowledgements

We wish to acknowledge the Henry Royce Institute for Advanced Materials, funded through EPSRC grants EP/R00661X/1, EP/S019367/1, EP/P02470X/1 and EP/P025285/1, for access to the AconityMINI at The University of Sheffield. We also acknowledge Sheffield Tomography Centre and University of Sheffield funding from EPSRC (EP/T006390/1) for use of the Zeiss Xradia 620 Versa X-ray microscope. We also acknowledge Professor Geraint Jewell and Georgios Yiannakou in the Department of Electronic and Electrical Engineering at the University of Sheffield for access to and training on the AMH1K Permeameter by Laboratorio Elettrofisico.

7 Mechanical properties of stochastically cracked components

7.1 Journal details and author contributions:

Planned Journal – Additive manufacturing letters

Planned submission date – September 2023

Alexander Goodall – Conceptualisation, Methodology, data capture of tensile test data with Jared Uramowski, investigation, analysis, data curation and visualisation, writing original draft

Jared Uramowski – Tensile testing and DIC methodology, and support with data capture

Chadwick Sinclair – Data analysis and interpretation, supervision

Iain Todd – Support with methodology formal analysis, visualisation, writing review and editing, supervision.

7.2 Background

Following on from chapter 6 where stochastically cracked material was shown to have good magnetic properties, there were concerns on the mechanical properties and ability of this material to sustain the required loads inside an electrical machine. As most research focuses on reducing the appearance of cracks, to the authors knowledge no work has been undertaken to characterise material which is so heavily cracked. Therefore, this chapter sets out to understand the basic mechanical properties to check whether the material is strong enough to be used in the electrical machine shown in chapter 5.

Uniaxial tensile testing was chosen as the simplest way to start to understand the mechanical properties, and DIC was used as the non-uniform nature of the material meant that the deformation and failure was hypothesised to give unusual behaviours. More comprehensive testing such as fatigue testing was planned, but the difficulties of setting up the experiments especially with regard to the clamping of the samples, meant that this was pushed beyond the scope of this project. The first batch of samples created for these experiments did not use the interlocking area between the stochastic cracked and solid regions, instead using a straight vertical joint where the segments were overlapped by 2 mm. This caused a band of heavy porosity between the regions, and the first batch of samples failed in this area every time yielding no useful data, as we were unable to obtain the properties of the stochastically cracked section. The first samples also used standard tensile test specimen geometry, however after these failures a non-standard sample shape was used in order to ensure the failure in the correct region.

To keep the same thermal conditions, the stochastically cracked region was built with a 25x25 mm cross-section, and then cut down using EDM to the correct geometry. It is not yet fully understood how changing the hatch length will affect the crack density or orientation, though it is suspected at least the crack density will change. This gives a large space for investigation as different scan strategies, laser speeds and geometries can cause different outcomes, and as shown in chapter 6, the crack density can change by up to 3x, and hence a large variation in mechanical properties can be expected. Therefore, until the stochastic cracking is fully understood, it is likely that each application will need specific quantification to check if the magnetic and mechanical properties are satisfactory. This chapter serves as a feasibility study to check if one of the combinations of laser speed and scan strategy can be implemented into a specific electrical machine.

7.3 Paper

Mechanical properties of stochastically cracked soft magnetic material

Alexander D. Goodall[a], Jared Uramowski[b], Chawick Sinclair[b], Lova Chechik[a], Iain Todd[a]

[a] Department of Materials Science and Engineering, University of Sheffield, Sheffield, UK
[b] Department of Materials Engineering, The University of British Columbia, Vancouver, Canada

Corresponding Author – Alexander Goodall adgoodall1@sheffield.ac.uk

Keywords

Laser Powder Bed Fusion; Cracking; Soft-Magnetic Material; Mechanical characterisation; FeSi

Abstract

Processing of soft magnetic materials with additive manufacturing has shown capability to deliver good magnetic properties and increased silicon content of Fe-6.5 wt%Si, however methods must be used to reduce the eddy currents in large bulk cross-sections in components created by additive manufacturing. Geometrical design has been shown to do this effectively, however stochastically cracked parts show similar magnetic performance with a large increase in stacking factor. To enable their use in electrical machines the mechanical properties of this material must be understood, therefore this study uses uniaxial tensile testing to start to gain a picture of the mechanical performance. The ultimate tensile strength of the material in the as-built condition was 17.85 MPa (σ=4.47 MPa), which was improved by 40% to 25.45 MPa (σ=5.68 MPa) by infiltrating the cracks with a low viscosity resin. This brings the material strength to more than three standard deviations from the required strength of 7 MPa to be used in a specific axial flux machine. The material exhibited a maximum strain of 8-10%, showing that the suppression of ordered phases by high cooling rates have improved the ductility of the material. Hence, the stochastically cracked parts appear to have sufficient properties to be used in the 3D magnetic circuits of electrical machines.

1. Introduction

Additive manufacturing (AM) has recently been used to process soft-magnetic materials such as FeSi (21), FeNi (5)and FeCo (56), showing sufficient magnetic properties (26,27) for usefulness in electrical machines (EMs). Mechanical properties such as elastic modulus, ultimate tensile strength (UTS) and elongation are rarely reported for these alloys after processing by AM. FeSi is the most common soft-magnetic material and normally has low silicon content around 3%, where the alloy avoids brittle ordered phases B2 and D03 (125) during processing, allowing the alloy to be rolled into thin sheets. At 3% silicon content the elongation is 8-11 %, and UTS is 310-357 MPa (123). Higher silicon content such as 6.5% has been shown to improve certain magnetic properties such as higher resistivity and lower magnetostriction, and as such is promising for future use in efficient EMs (20). Higher silicon content, however, means that brittle ordered phases will form during normal cooling (20), creating difficulties in processing the material into the thin sheets that are commonly used in EMs. Other methods have been used to enable processing of 6.5% Si content such as post-rolling diffusion of silicon into Fe-3 wt%Si (24), however there is yet to be any scalable technology that allows processing of homogenous Fe-6.5 wt%Si. At 6.5% silicon content the elongation to break and strength is decreased (126). AM has a very high cooling rate, enabling some alloys such as binary FeCo to exhibit improved ductility by suppressing the brittle ordered phases formed under normal cooling conditions (36). Currently, no such study has been completed on FeSi, but it is possible that a similar effect could be found.

To enable their use in alternating current (AC) EMs, soft-magnetic material is normally rolled into thin sheets to reduce parasitic eddy current losses. Similarly with AM, processing large bulk sections should be avoided, and therefore some cross-sectional geometries have been explored which achieve this such as lamination style slots (26), Hilbert space filling curve based cross-sections (27), and others (41,42,61). In chapter 6, the current author has shown that good magnetic performance can be achieved by utilising processing parameters to induce stochastic cracking of Fe-6.5 wt%Si, reducing eddy current losses and demonstrating improved performance when compared to designed geometries such as Hilbert space filling. To enable the adoption of this technology and use in an EM, the mechanical properties of this material must be understood.

In an EM, the stator or soft-magnetic core has relatively low mechanical requirements. This part is usually not rotating or structurally stressed, therefore the only loading on the component is the forces from the magnetic circuit. Axial flux motors are a natural application for soft magnetic material processed by AM, as the 3D flux pathways increase the difficulties of using thin laminations making AM more appealing. In a motor designed by Nishanth et al. (79), the tensile load requirements are 900 N for a cross-sectional area of 130 mm^2, hence the stator tooth must survive a maximum stress of approximately 7 MPa.

In this study, the mechanical response in uniaxial tension of the stochastically cracked material is investigated, to determine if the strength of the material is sufficient for use in the stator of an electric machine. Digital image correlation (DIC) is used to estimate the local strain values and inspect the failure modes of the material in uniaxial tension, as the material is highly non-uniform with a number of stress concentrations. The variability is assessed, and a method to improve the materials robustness and mechanical properties is proposed, wherein the cracks are filled with epoxy resin.

2. Materials and Methods

2.1 Sample manufacture

Samples used in this study were created using Fe-6.5 wt%Si powder supplied by Höganäs, with a particle size of 15-45 µm. This powder was processed on an AconityMINI (Aconity3D GmbH) laser powder-bed fusion machine, equipped with a 200 W ytterbium doped continuous wavelength laser (wavelength 1074 nm) with a spot size of 70 µm. Samples were manufactured directly onto stainless steel build platforms, followed by sample removal using wire electrical discharge machining (EDM). Laser power of 195 W and laser speed of 0.4 m/s was used for stochastically cracked regions, whereas laser power of 140 W and laser speed of 0.7 m/s was used for solid regions of high density. Both regions use a layer thickness of 30 µm and a hatch spacing of 100 µm. The scan strategy used was 5 mm wide stripes, with a layer rotation of 90° for stochastic cracked regions and 67° for solid regions. This refers to the parameter set 8_400_SR detailed in chapter 6.

Tensile test samples were built by creating a 25x25x10 mm stochastically cracked region, flanked by 25x25x10 mm solid regions as per Figure 7-1. These sections were interlocked with a 2 mm wide region which alternated between solid and cracked every second layer. This provided a structurally sound joint between regions, allowing the sample to fracture within the gauge length rather than at the weld line between the regions. Flat tensile test samples were then machined from these blocks via EDM, cutting the tensile test bar outline first, with a gauge length of 10 mm, gauge width of 6 mm and a corner radius of 6.5 mm, then slicing into samples 3 mm thick, giving approximately 18 mm^2 cross-sectional area in the gauge length. This was measured for each sample with a set of digital callipers.

Solid tensile test samples were also built using the parameters for the solid region throughout the whole part. These were then machined into the same sample size using EDM.

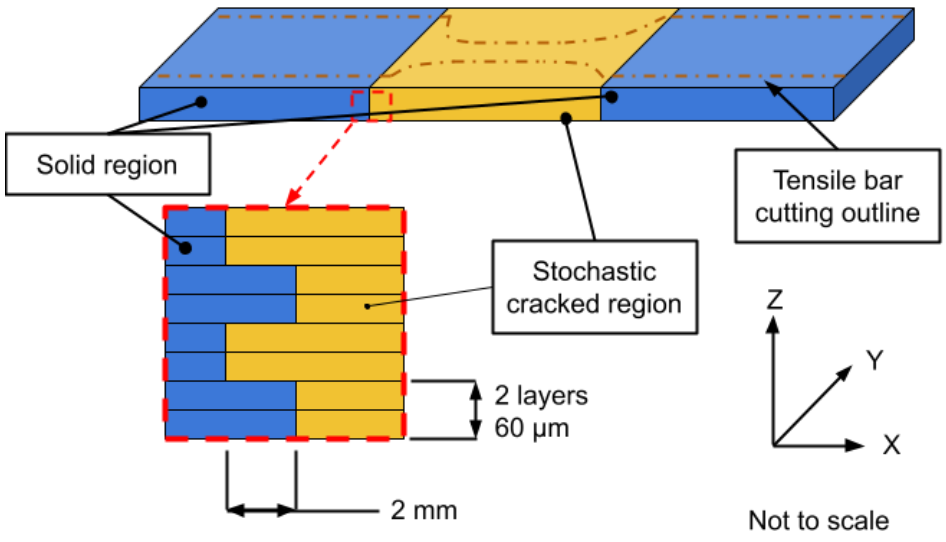

Figure 7-1 – Details of the additively manufactured blocks, that tensile test samples were machined from.

2.2 Tensile test and DIC

Tensile testing was performed on an Instron 8896 Universal Testing Machine, with a 25 kN load cell. Samples were deformed at a constant rate of 0.005 mm/s until ultimate fracture, while the load and crosshead extension were recorded at a rate of 10 Hz. Samples were pre-loaded to no more than 100 N prior to testing, thereby eliminating any fixture slip and ensuring the sample was adequately seated in the grips.

Due to the highly non-uniform distribution of cracks in the material, calculating strain by gauge length extension was deemed inappropriate, and instead optical DIC was used. A pattern was created using aerosol paint, first applying a white background before carefully applying the black speckle pattern. A consistent pattern was created for all samples, giving acceptable spatial resolution for displacement field calculation. On average, the size of each speckle was 0.35 mm and spaced by 0.3 mm. The system was calibrated for displacement and corrected for the camera angle using a standard 2.5 mm spaced grid pattern of 1mm crosses. Images were taken with a LaVision Imager QE camera through a 60 mm lens at an aperture of 5.6, acquired at a rate of 5 Hz for the duration of the test, storing the load data for each image. The distribution of strain was visualized using Davis version 10 software, where images were processed using the sum of differential method, at a subset and step size of 23 and 7 pixels respectively.

Due to noise in the data, smoothing was applied to the results to allow for better clarity. A Lowess method was applied using a span of 10 data points. For solid samples this was applied over the whole range. For the stochastic cracked samples, the data was split into 3 sections to avoid reducing the value of UTS due to smoothing. The three sections were the region until the first failure, the plateau between the first and second failures and the section after the second failure. The impact of this smoothing can be observed in Figure 7-3b.

2.3 Epoxy resin reinforcement

Filling of the cracks with epoxy resin was attempted to improve the mechanical performance of the stochastically cracked samples. An ultra-low viscosity epoxy was used from NextStar (127) to allow the epoxy to penetrate the microscopic cracks. The epoxy was applied by submerging the samples in a vat of resin, then placing inside a vacuum chamber for 30 minutes. Following this the epoxy was allowed to cure for approximately 5 hours at room temperature, at which point the viscosity of the epoxy had increased significantly. The samples were then removed from the vat of epoxy, whereby the excess epoxy could drain from the exterior surfaces of the sample, with the assumption that any epoxy inside the cracks would have too high of a viscosity to leave the sample. The samples reinforced with epoxy were then left to cure for the remainder of the four-day cure time.

3. Results

3.1 Tensile test results, solid

Tensile testing was conducted on 5 samples which were built using parameters intended for solid material without any cracks. These were tested to give a baseline to compare the stochastically cracked samples to, as there are no studies in literature characterising Fe-6.5 wt%Si, manufactured by AM. Stress-displacement data is shown in Figure 7-2. The average UTS was 57 MPa with a standard deviation of 6.36 MPa. The average elastic modulus was 98 GPa, with a standard deviation of 6.7 GPa, found using a linear fit on the data below 30 MPa to stay in the linear region, as the 0.2%

strain measurement is unsuitable for this material. Sample B was excluded from the elastic modulus calculation due to the high stress at the start of the test.

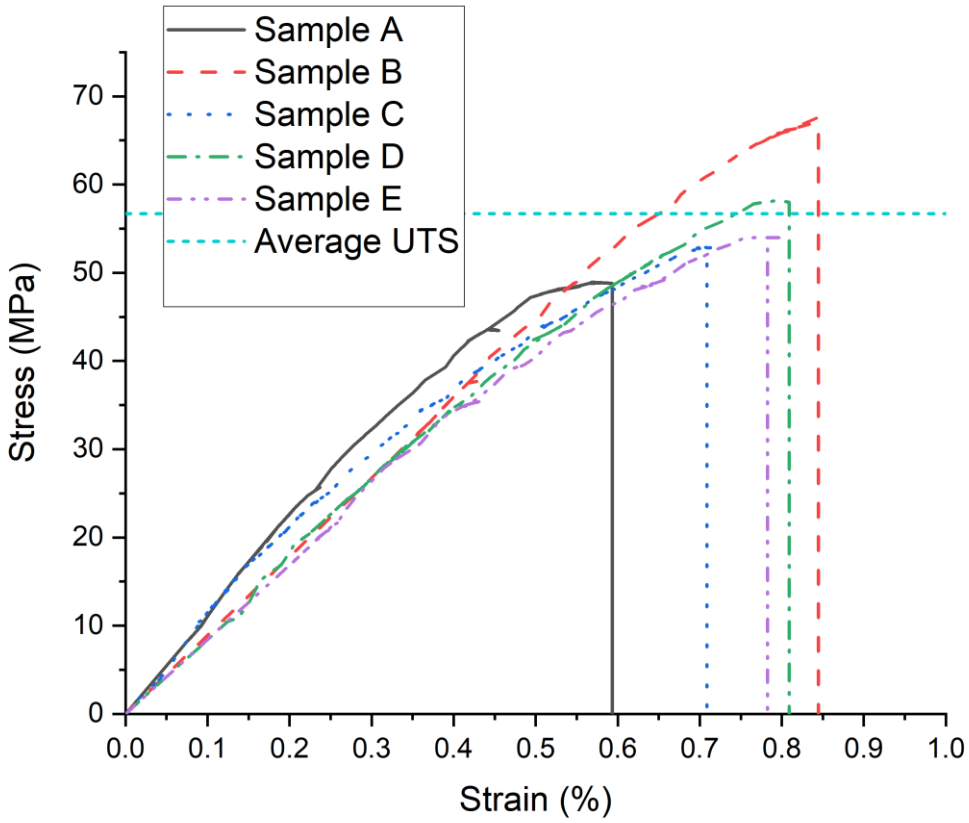

Figure 7-2 – Tensile test results of as-built Fe-6.5 wt%Si with solid cross-section, showing an average UTS of 57 MPa.

3.2 Tensile test results, stochastically cracked

Tensile testing was conducted on 8 samples with stochastic cracking in the as-built condition. One of the samples has been excluded from the results as it fractured outside of the gauge length along the radius between the gauge length and clamping face. The remaining samples show an unusual stress-strain curve (Figure 7-3a) starting with a linear elastic region, with a small area of yield followed by failure at ultimate tensile stress (UTS). After this failure the stress-strain curve continues with at least one lower plateau, followed by a gradual decrease to zero-stress. The samples show an average UTS of 17.85 MPa, with a standard deviation of 4.48 MPa. The minimum recorded UTS was 9.58 MPa for sample 7. Strain in the samples is concentrated into distinct bands, perpendicular to the loading direction due to the pre-existing cracks in the material causing distinct changes in cross-sectional area (Figure 7-3c/d). Due to the non-uniformity of the strain throughout the samples, stress is plotted against machine displacement instead of strain. Using a stress-strain curve could cause confusion on the strain to failure of the material. Figure 7-3b highlights different regions and suspected failure modes throughout the test.

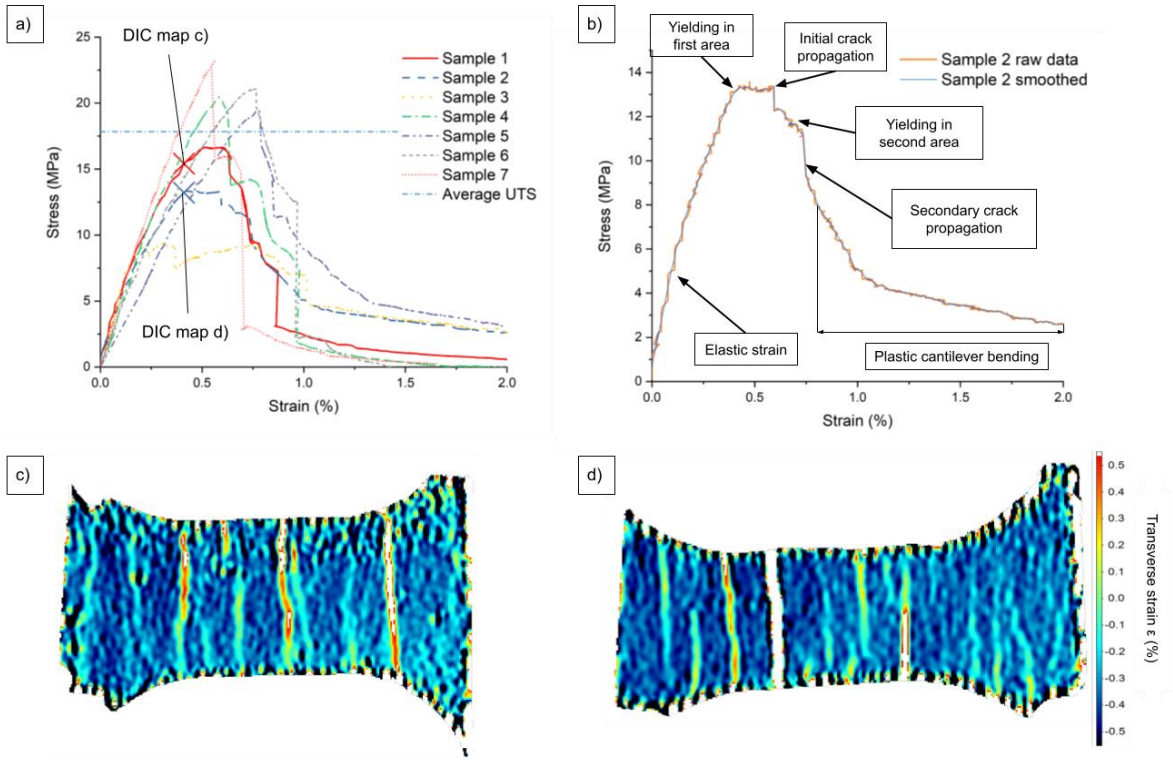

Figure 7-3 - Tensile test results showing stress vs displacement (a). All samples show a linear elastic region, followed by a small area of yielding and a sharp decrease in stress carrying capacity. The effect of data smoothing is shown in (b) along with the suspected failure modes of each area of the curve. Stress concentrates into distinct bands, with examples from sample 1 as shown(c) and sample 2 (d), demonstrating the likelihood of underlying cracks perpendicular to the force. Areas of white have exceeded the scale and are not yet cracks.

DIC was used to qualitatively show the strain behaviour throughout the test. By using the raw images to observe the cracks in the gauge section, and the processed images to find the strain, a deeper understanding of the stress curve in Figure 7-3b is obtained. There is a region of linear elastic strain initially. An effective elastic modulus can be calculated from this linear region; however, the strain is highly non-uniform (Figure 7-4a) and the effective cross-sectional area is unknown, therefore this is a property of the system rather than a material property. The average elastic modulus is 4.93 GPa with a standard deviation of 1.37 GPa. Following the linear elastic region there is a small region of plastic deformation where the material yields. Yield stress is normally quoted as a proof stress, an offset of the linear elastic region starting at a strain of 0.2%. This is an unsuitable measure for these samples as this would often be beyond the UTS. The next significant area on the curve is the first failure or crack initiation which can be observed in the DIC images (Figure 7-4b). XCT shows that there are pre-existing cracks in the material (chapter 6), therefore these images show the point at which this crack propagates to the external surface and hence the material can no longer take load in this area. This appears to happen with very little yield; however, it is not possible to conclude that the material is demonstrating a brittle failure due to noisy data. As the average elastic modulus is at least an order of magnitude smaller than the expected value for non-ordered Fe-6.5 wt%Si of 100 GPa, found in both literature (128) and by tests on solid components, we can conclude that the stress is concentrated into a much smaller cross-sectional area than the full gauge section.

Once this first crack has penetrated to the surface, there appears to still be load carrying capacity which must occur on the other side of the pre-existing crack. At this point, it is hypothesised that there is movement in both the first crack continuing to propagate, and a second area of material yielding. Following this there is another distinct failure where the stress carrying capacity drops

instantly, which is believed to be a second crack opening (Figure 7-4g-i). It is likely that this will happen on the opposite side of the gauge section than the first crack, as the first crack will stop the load path along this edge. Following this second crack, a cantilever beam type scenario occurs, whereby there is a beam which is fixed at both ends with a perpendicular force at each end (Figure 7-4j-l). This has significantly less resistance to axial stress and hence a lower stress carrying capacity, however it allows large displacements before one of the cracks eventually propagates all the way through the cross-section when the stress drops to zero.

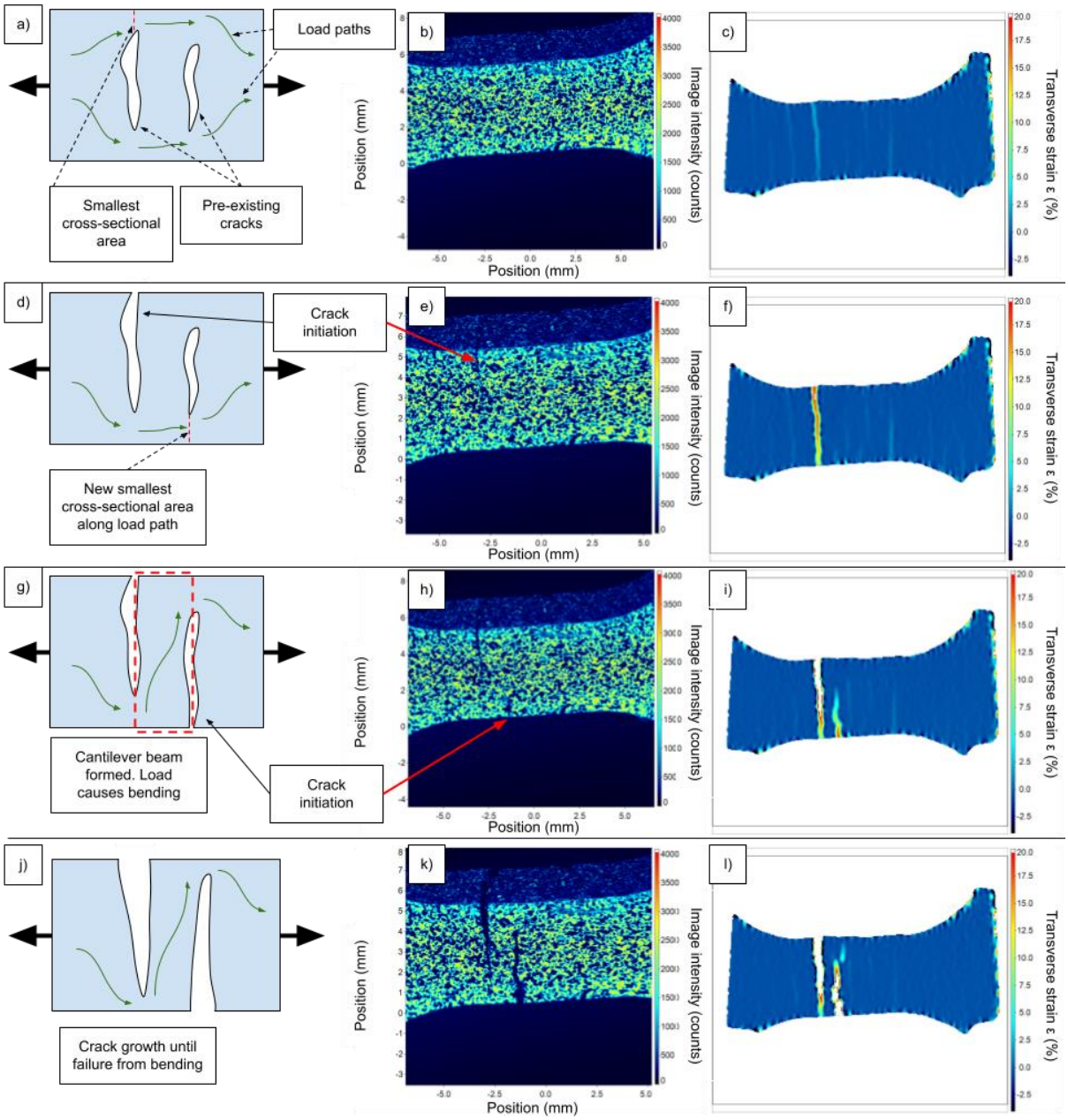

Figure 7-4 – DIC showing the progression of cracks through the gauge section, along with simplified sketches explaining the strain patterns observed

During additive manufacturing, the high cooling rates have been shown to supress the ordered phases B2 and D03 in Fe-6.5 wt%Si (21). These ordered phases are responsible for the brittle behaviour of this alloy, therefore if these phases are suppressed it is possible that the ductility of the material will increase. From DIC data it is possible to observe the local strain before crack propagation which is recorded at 8-10%, as shown in Figure 7-5 for sample 6 but is similar for all the samples. This is close to that of Fe-3 wt%Si which is 8-11%, therefore the ductility of Fe-6.5 wt%Si is improved when processing via AM, avoiding the ordered phases due to high cooling rates.

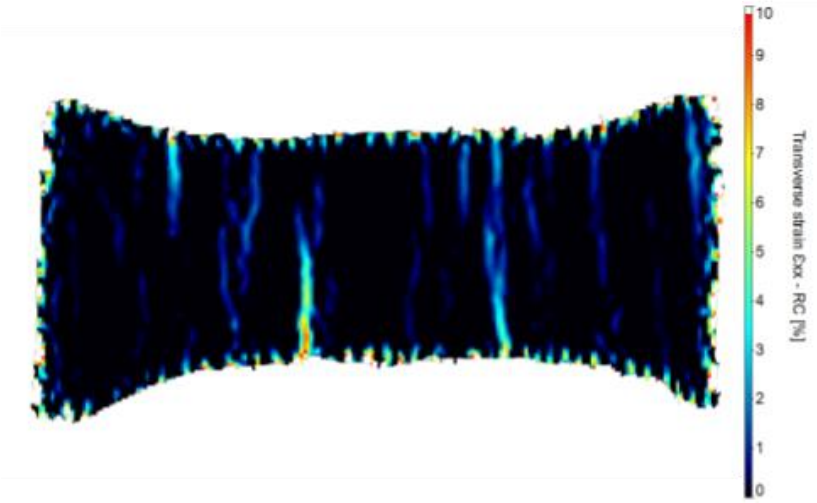

Figure 7-5 - Localised strain values prior to new crack initiation during tensile test, showing the local maximum strain is 8-10%.

3.3 Tensile test results, epoxy reinforced

In an electric machine, once the coils have been wound, the stator and coil assemblies are often potted with epoxy resin to ensure no movement of the coils and reduce likelihood of electrical shorting or insulation failure throughout the service life, as well as improve thermal conductivity between the parts. This potting could also be used as a way of infiltrating the cracks in this material with epoxy resin, improving the mechanical properties. Hence, this study tested 5 samples which have had the cracks filled with an epoxy resin. Figure 7-6 shows the stress-displacement data for these samples, which show an average UTS of 25.5 MPa with a standard deviation of 5.68 MPa. There is an average of 40% improvement of the epoxy filled samples compared to the as-built samples, with a 95% increase in the minimum value to 18.8 MPa. This material would surpass the mechanical requirements needed for many electric machine stators, including that introduced previously (79).

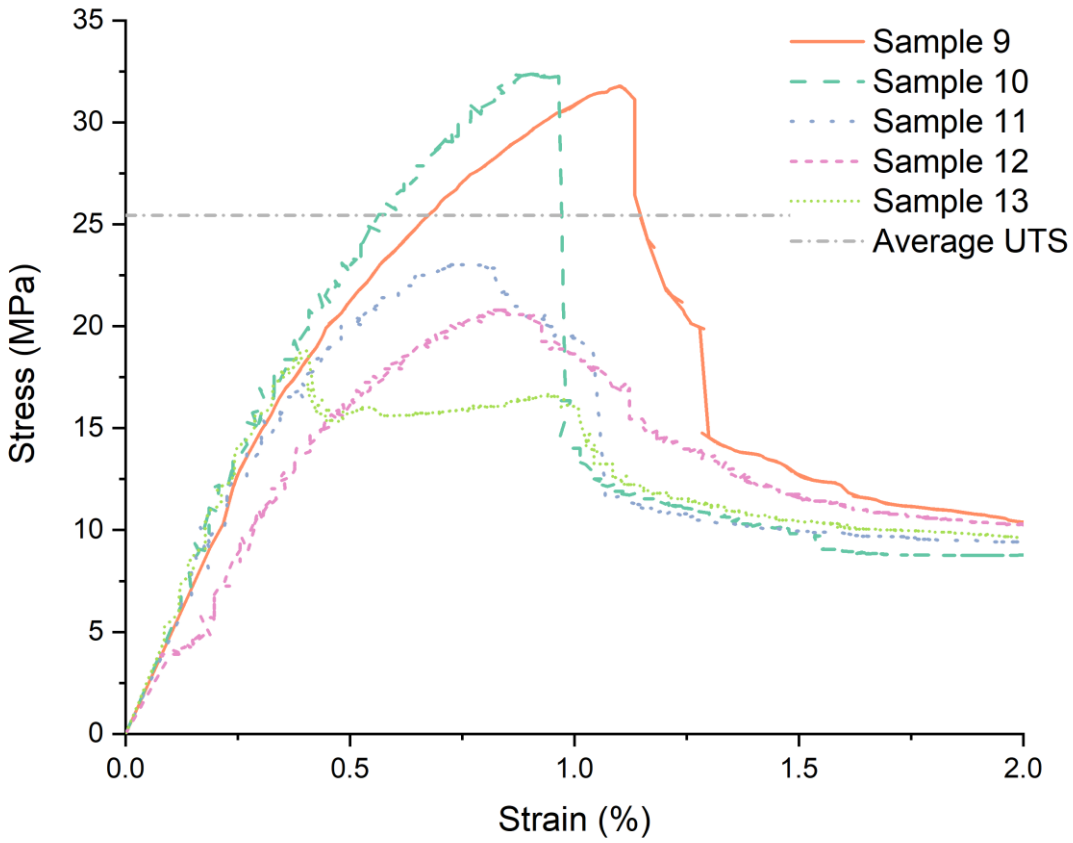

Figure 7-6 - Stress-displacement data for the samples reinforced with epoxy resin, demonstrating an average UTS of above 25 MPa.

XCT and optical microscopy were used to attempt to quantify the penetration of the epoxy into the cracks, however due to the high density of the Fe-6.5 wt%Si relative to the epoxy resin and the very small thickness of the cracks, it was not possible to clarify that the epoxy resin has infiltrated the cracks. Results show a significant change however, therefore it is demonstrated that the addition of the epoxy resin has caused in improvement in mechanical properties even if all of the cracks have not been infiltrated with epoxy. A summary of the key findings is given in Table 7.

Table 7 – Overview of ultimate tensile properties found in this study.

Sample type	Ultimate tensile stress (MPa)	Ultimate tensile stress st. dev. (MPa)	Minimum ultimate tensile stress (MPa)
Solid	56.7	6.36	49.2
As-built	17.8	4.48	8.0
Epoxy filled	25.5	5.68	18.8

4. Discussion

It is important to acknowledge potential errors in the test method presented in this work. Firstly, the noise apparent in the load-displacement data. This is a result of a low measured load (0.5 kN) relative to the capacity of the load cell (25 kN). A test was run for a similar period with no sample present, and the load was found to vary within +0.00050 kN and -0.00055 kN of the initial (zero) load. Similarly, the displacement varied within only +0.0018 mm and -0.0018 mm of the initial (zero) displacement. These values are small in comparison to the recorded load and variability between samples, and therefore have little impact the results of this work but create noisy data. If this work was repeated, data with less noise could be obtained by using a 1 kN/5 kN load cell. Further to this, the clamps on the tensile test machine have a flexible coupling to prevent the introduction of non-axial forces. At these low forces, the weight of the flexible coupling causes a small non-axial force on the sample, which would normally be orders of magnitude smaller than the applied axial load. For these samples however, some visible deformation occurred during clamping and two samples broke during clamping due to this. Once clamped successfully, there was often a small load already registering on the load cell. Normally this would be circumvented by using a pre-load, however the forces involved in these tests were prohibitive for applying any regular pre-load. This clamping force could introduce some non-axial force, however using DIC means that we can correlate the axial force with a transverse strain, yielding useful data.

While DIC can be a reasonable method for strain measurement, there are some limitations. For example, speckle patterns that are manually created may have a limit to the speckle size and consistency of the pattern across the sample. The speckle pattern used was created using aerosol paint giving a speckle pattern with circles approximately 0.1-0.3 mm, with occasional paint speckles up to 1 mm. Therefore, measuring maximum strain values could understate the localised maximum strain. Processing artefacts near edges and cracks may also appear artificially as areas under high strains, so maximum strain values were taken away from the edge of the sample. The size of the subset used can also influence resolution. This paper states the maximum strain to be 8-10% which would be a reasonable value for α-phase non-ordered Fe-Si, but to state material properties for this material in an as-built state, further tensile tests should be carried out using fully dense material which would allow accurate measurement of the mechanical properties of the bulk material. The aims of this study were to ascertain the UTS of the material, and strain measurements were used qualitatively to gain an understanding of failure mechanism rather than absolute values. Further to this, DIC was only performed on one surface, and it may be possible that crack growth occurred or originated on another surface first. Hence, there may be additional cracking that was not recorded by these images. DIC is showing data for the external surface and therefore it is not possible to infer the development of internal stresses from one DIC plot.

The average UTS of the solid samples is 57 MPa. There is no literature available regarding the mechanical properties of additively manufactured Fe-6.5 wt%Si as most studies focus on magnetic properties. However, data from melt spun samples report an elastic modulus of 100 GPa (128), which compares well with the results in this study showing the elastic modulus is 98 GPa, though no data for ultimate tensile stress was available. A more comprehensive study into the solid samples is required to understand the low UTS of the additively manufactured samples. The parameters used were demonstrated to give density above 99.5% in 5x5x5 mm cuboidal samples, however with the larger cross-sectional area of 25x25 mm the thermal conditions for these samples may require different process parameters to achieve high density, hence there could be some small cracking and porosity present in the solid samples which is reducing the UTS. Further to this, the as-built grain

microstructure could yield different mechanical properties than those resulting from different manufacturing methods such as melt spinning.

The mechanical requirements for an electric machine stator are generally low, and for the specific machine considered in this work, the required tensile stress is 7 MPa. In the as-built condition, the stochastically cracked material had an average UTS of 17.85 MPa, but with a large variability, therefore, to allow for 3 standard deviations the stress should be kept under 4.4 MPa. This would be insufficient for the application as there would be little safety factor. Reinforcing with epoxy resin improved this UTS to 25.5 MPa, and three standard deviations below would be 8.45 MPa. Therefore, even with the high variability, this material is strong enough to withstand the static loading on the stator within three standard deviations, showing promise as a soft-magnetic material that can enable 3D magnetic flux pathways, reduce eddy currents to compete with electrical steel laminations, and have sufficient mechanical properties.

It is noted that after fracture the epoxy-filled samples converge to a higher stress. Inspection of the samples reveals that this is due to a thin layer of excess epoxy on the outside of the gauge section, in the width direction, which is effectively carrying some amount of load during the final stage of the test, and therefore the test terminates with higher than zero stress as the thin area of epoxy has not broken due to its higher ductility. This does not impact the result, as the ultimate strength is still much higher in the epoxy-filled samples, and in practice, an electric motor stator prepared in this manner would also experience excess surface epoxy. It has not been shown in this study the effect the epoxy may have on the magnetic properties, though as the epoxy is replacing air, it is not expected to significantly reduce the magnetic properties of the soft magnetic material.

Tensile testing was attempted on samples with differing gauge sections. Those with smaller gauge section (5x2 mm) were difficult to handle and test, however initial results suggested that the UTS was lower than samples with a larger gauge section (6x3 mm). With the stochastic nature of the cracking, it is possible that there is a size dependency on material properties, with very small cross-sections having decreased performance. Due to magnetic circuit requirements, the cross-sectional area is unlikely to be this small, however future work is suggested to investigate the size dependency of mechanical properties. Further, no fatigue testing has been carried out at this time. Though before usage in a machine, the thermal, magnetic, and mechanical fatigue behaviour would need to be understood. As Fe-6.5 wt%Si has very low magnetostriction (0.01 ppm (20)), thermal and mechanical fatigue are likely to be more important factors.

The cracks in this material are interconnected as shown by XCT data allowing infiltrating with epoxy to be possible, which was shown to be effective in increasing the UTS. This does add a step to the manufacturing and assembly process for electric machines, however for machines that are currently potted it is not a large change. The epoxy resin may not fully infiltrate all of the cracks; however, it has been shown to have a positive effect on the properties using the methodology in this study. Further optimisation of this filling process may allow for even better mechanical properties. Heat treatment may be required to obtain optimum magnetic properties (23), which may allow ordered phases to become present in the material. This could decrease the ductility but is unlikely to have a negative effect on the UTS of the material. This heat treatment would need to be done prior to filling with epoxy, which would not interfere with the assembly process and order.

5. Conclusion

In the as-built condition, stochastically cracked Fe-6.5 wt%Si has inadequate mechanical properties for use in an electric machine, owing to relatively low UTS of 17.85 MPa with a high variability (σ=4.47 MPa). By reinforcing the material with a low-viscosity epoxy resin, mechanical properties were significantly improved, giving an average UTS of 25.45 MPa (σ=5.68 MPa). With the epoxy reinforcement this material would withstand the loading requirements of an electric machine stator (7 MPa), giving a soft-magnetic material which can enable 3D magnetic flux pathways, with high magnetic performance and eddy current losses competitive with electrical steel laminations.

Declaration of competing interest

None.

Author contributions

AG: Conceptualization, Data curation, formal analysis, investigation, methodology, visualisation, writing – original draft. **JU:** Data curation, formal analysis, investigation, methodology, writing – review and editing. **CS:** Investigation, methodology, supervision, validation, writing – review and editing. **LC:** visualisation, writing – review and editing. **IT:** Conceptualization, formal analysis, funding acquisition, methodology, supervision, validation, writing – review and editing.

Acknowledgements

We wish to acknowledge the Henry Royce Institute for Advanced Materials, funded through EPSRC grants EP/R00661X/1, EP/S019367/1, EP/P02470X/1 and EP/P025285/1, for access to the AconityMINI at The University of Sheffield. We also acknowledge Sheffield Tomography Centre and University of Sheffield funding from EPSRC (EP/T006390/1) for use of the Zeiss Xradia 620 Versa X-ray microscope.

8 Discussion, Conclusions and future work

8.1 Discussion

The overall objective of this thesis was to enable 3D magnetic circuits with the use of additively manufactured soft magnetic material in an electrical machine, with performance comparable to electrical steel laminations. This was partially achieved in that the stator for an electric machine with a 3D magnetic circuit was manufactured, however the performance was degraded when directly compared with electrical steel laminations, with higher losses and a reduced torque, albeit an improved torque density. The shortfall in performance can be attributed to several factors, which have been investigated in turn throughout this thesis.

Firstly, the material properties achieved by the bulk material in this study is below that of the state of the art. The permeability reached a maximum of approximately 10,000 as shown in Chapter 4, lower than other authors using AM and also lower than commercially available electrical steel. This could be improved through process optimisation but was outside the scope of this work which focussed on the eddy current losses, which are more geometry dependant with less influence from material properties.

To achieve the objective of loss performance comparable to electrical steel laminations, geometrical control of eddy currents was investigated in Chapter 4. By using air gaps to separate areas of material the eddy currents were shown to decrease. Difficulties were faced here in resolving the intended design of the cross-section without using support structures, where experimental samples showed a large amount of electrical shorting through the air gap which is intended to provide insulation. Simulations showed that excellent loss performance is possible, comparable to that of electrical steel laminations, however physical samples were unable to attain this performance due to the difference between samples and intended design. It was shown that improvements could be made by closing the gap between intended geometry and realised geometry, but this must be taken further to match the simulated losses. Other authors such as Plotkowski et al. (27) have demonstrated lower losses from the Hilbert pattern than this work, however this was not done for a 3D flux path. Loss performance comparable to electrical steel laminations has been achieved using AM by Koo et al. (41) for a 3D flux path, therefore showing that the state of the art in AM can compete with electrical steel laminations. The limitations of this method are the minimum size of the air gap before shorting occurs. This is likely to always remain a challenge in AM due to the surface roughness caused by partially melted powder.

This surface roughness was investigated in Chapter 3, showing that a large improvement in susceptibility could be achieved by improving the surface roughness of the AM samples. To implement this along with the geometrical eddy current control using air gaps would require a process other than manual polishing due to access to the surfaces. This study intended to investigate post processing methods to improve the surface finish such as chemical and electro-chemical polishing, however time restrictions didn't allow for this. The state of the art can progress to reduce the minimum size of this gap, however it appears unlikely that the air gaps will ever reach the thickness of insulation coatings on electrical steel laminations due to process limitations such as powder size, and melt pool variability. The outcome of this will be an upper limit on the stacking factor estimated at around 90% whereas electrical steel laminations can achieve stacking factors of 97-98%. During the processing of this material cracking was observed during the process. These cracks were usually around 1-10 µm, therefore, providing a smaller more consistent insulating air

gap than the geometrical control. Hence Chapter 6 investigated this phenomenon to ascertain if it may be possible to control and use the cracking for the management of eddy currents.

By investigating stochastic cracking, it was found the size of the insulating air gaps can be reduced by an order of magnitude, from approximately 50-100 µm when using geometrical control to 1-10 µm when using stochastic cracking. This was shown to increase the stacking factor up to 97%. The loss performance of the stochastically cracked material was investigated and shown to be comparable to a thicker electrical steel lamination of 0.65 mm. The orientation and density of the stochastic cracking was not optimised, therefore with alignment of the cracks with the magnetic flux direction to cause the highest resistance in the plane eddy currents would circulate, and increasing of the crack density to the highest value whilst maintaining sufficient mechanical properties, the authors believe that the stochastically cracked material could compete with thinner electrical steel laminations closer to 0.2 mm. After showing the magnetic performance of the material has promising properties, the first question to ask is will this material survive the loading conditions of an electrical machine. If the cracking causes a decrease in mechanical properties so severe that it is unusable, it would be wasted resource to continue optimising this material. Therefore, uniaxial tensile tests were carried out and reported in chapter 7, whereby it was shown that with vacuum impregnation of epoxy resin, the material was able to match the mechanical demands of the motor demonstrated in Chapter 5.

Despite this progress in the AM of electrical steel, the state of the art still lags behind electrical steel laminations for loss behaviour and this appears to be the biggest challenge of processing soft magnetic material with AM. Electrical steel laminations are highly optimised after decades of research and development, and there are fundamental process limitations within AM that mean electrical steel laminations are likely to always possess lower losses than AM manufactured electrical steel. Therefore, for the AM of electrical steel to provide benefits these must be gained through the use of 3D magnetic flux pathways which electrical steel laminations are unable to provide. Hence, it is within the design of the electrical machine architecture where improvements in power density and torque density may be found, aiming to get as close as possible to the loss behaviour of electrical steel laminations. By enabling 3D magnetic flux pathways, this work has enabled electrical engineers the freedom to design magnetic circuits that are highly optimised and not restricted to 2D. Whether real benefits can be obtained will be down to the next generation of electrical machines that capitalise on this.

The industrial relevance of this work is currently limited, without demonstrating a clear improvement over the current state of the art of electrical machines for either power density or loss behaviour, the additive manufacturing of soft magnetic materials does not yet provide a valid industrial use case. The academic relevance however is prevalent and with increasing research interest in the field, the next major steps which can be undertaken in parallel will be to optimise the processing to improve the material properties, and to start design work on new electrical machine architectures which can provide improved power density by utilising the 3D flux pathways enabled by AM.

This thesis adds to the current literature by providing a novel methodology to address the most difficult research challenge to overcome high eddy current losses in soft, along with the improvement of geometrical control of eddy currents. The material properties have also been further understood especially with respect to the texture, which has been assumed by many to improve magnetic performance, when this work has shown that before the benefits of texture can be realised the surface roughness must be addressed.

8.2 Conclusions

This project was defined to understand and enable to additive manufacture of soft magnetic materials, specifically high silicon electrical steel, into 3D flux pathways for electrical machines. The main focus was overcoming the issue of eddy current losses in thick cross-sectional areas.

Chapter 3 demonstrated the processing of Fe-6.5 wt%Si into thin-walled structures. Magnetocrystalline anisotropy was quantified and found to have little impact on the magnetic properties with respect to build angle due to a weak texture, whereas surface roughness was found to have a high influence. Improvements in surface roughness in the as-built condition were shown to greatly improve the susceptibility. Heat-treatment at 1150°C for 1 hr did not fully recrystallise the samples, without grain growth there were no significant improvement of properties. Grain growth was displayed for samples heat-treated for up to 30 hrs. This implies that heat-treatment must be tailored with respect to sample geometry, and it is suggested that residual stress is the underlying factor causing this geometry dependence. The hypothesis is that smaller samples are built with shorter hatches, which cause less residual stress and hence there is less of a driving force for the recrystallisation, but further work must be undertaken to evidence this.

Thin-walled structures were then built into the cross-sections of toroidal samples in chapter 4 in order to reduce eddy current losses. A large difference in simulated and experimentally measured losses were found due to the incorrect resolution of intended geometry, and unwanted electrical short circuiting between areas which should have been isolated from each other. The size of the air gaps is found to be a trade off as smaller gaps increase the stacking factor and volume of magnetic material present, whereas larger gaps reduce the short circuiting and improve the loss behaviour. This issue is complicated by the requirement for gap size being different in the XY plane and XZ/YZ planes of the AM machine, meaning that careful design is required to implement these complicated geometries in 3D flux pathways.

The Hilbert cross-sectional geometry was implemented into an axial flux electrical machine with 3D magnetic flux pathways, and the performance reported in chapter 5. Implementing the Hilbert cross-sectional geometry caused a loss in volume of magnetic material, which in turn reduced the torque of the machine by approximately 20%, however torque density was increased by 13%. The total core loss of this stator was shown to be comparable to 0.35 mm thick electrical steel laminations at frequencies below 500 Hz.

An alternative method of reducing the eddy current losses using stochastically cracked material, enabled by the precise process control afforded by AM was investigated in chapter 6. This method demonstrated total core losses lower than that of the geometrical control cross-sections investigated in chapter 4. Electrical resistance was shown to be proportional to the tortuosity of the cracks within the section, which were characterised using XCT. Crack density was shown to be controllable using laser speed, and crack orientation was shown to be affected by the scan strategy. The stacking factor of the stochastic cracking method is above 97%, a large improvement on the stacking factors of <90% demonstrated in chapter 4. This may provide a path to retain the full torque of the electrical machine shown in chapter 5 with improved eddy current losses, without changing any of the geometry.

The mechanical properties of the stochastically cracked material were investigated using uniaxial tensile tests in chapter 7, demonstrating that in the as-built condition the material did not have high enough mechanical strength for implementation in the electrical machine shown in chapter 5. However, by vacuum infusion of ultra-low viscosity resin into the cracks, the strength was increased enough to be suitable for the required loading conditions in the stator.

Overall, this thesis has shown that soft magnetic material produced by AM is still underperforming magnetically when compared to electrical steel laminations, however AM does enable 3D magnetic circuits. If improvements in electrical machine properties are available by utilising a 3D magnetic circuit, AM could be a suitable candidate for the manufacture of the soft magnetic material. Magnetic properties of electrical steel produced by AM still have room for improvement with further research efforts. The work presented in this thesis has characterised the magnetic properties of high silicon electrical steel, as manufactured by AM, whilst enabling the use of this material in 3D magnetic flux pathways by demonstrating two alternative methods of reducing eddy currents to give losses comparable to that of thicker electrical steel laminations, and shown one of these in an axial flux electrical machine.

8.3 Future work

There is wider scope to follow on from much of the work in this thesis:

- Conduct a comprehensive trial regarding the heat-treatment of Fe-6.5 wt%Si manufactured by AM, investigating not only the time required to encourage grain growth and the improvement in magnetic properties, but also to focus on the geometrical dependency of the heat-treatment. It was shown in chapter 3, that for the thin-walled samples, the 1 hr heat treatment did not provide enough time for the samples to recrystallise and allow for grain growth. Residual stress was suspected to be lower in the thin-walled samples, however a full study is needed to understand this relationship fully.

- Investigate post processing treatments for improving the resolution of the complex cross-sectional geometries such as the slotted and Hilbert patterns shown in chapter 4. By using abrasive flow machining, chemical polishing or electropolishing, the surface finish could be improved whilst also preferentially removing particles causing short-circuits due to their high surface area to volume ratio. Other benefits from the improved surface finish could be improved magnetic performance as was demonstrated in chapter 3.

- The design and manufacture of an electrical machine similar to that shown in chapter 5, which scales the size of the tooth area up, and the size of the slot down allowing for the same amount of torque even with the reduced stacking factor. This would be enabled by the AM of the copper coils to allow an increase in stacking factor, and the same amount of conductive material even with a reduced slot size.

- Further work into the stochastic cracking methodology could include creating a magnetic test geometry allowing the characterisation of the material with the cracks orientated to the magnetic flux direction. By aligning the cracks parallel to the flux direction, it is suspected that performance gains above that shown in chapter 6 may be possible. As an unintended consequence, mechanical properties may increase compared to those measured in chapter 7 due to the angle of the cracks with respect to the loading direction in the machine.

- The manufacture and characterisation of another stator for the same motor as displayed in chapter 5, using the stochastically cracked material demonstrated in chapter 7 and 8. This would allow the characterisation of this material in an application, and provide a comparison with the designed geometries as well as electrical steel laminations.

- Further mechanical characterisation of the stochastically cracked samples should be undertaken, to understand the size dependence and fatigue properties of the material. Other methods for enhancing the mechanical properties should also be investigated, such as potting the whole stator and winding assembly, allowing for further improvements to be gained from the epoxy resin.

Future work in the area of additive manufacturing of soft magnetic materials is likely to focus on improving the surface finish of components, as well as developing the methodology for keeping eddy current losses low. Following this, more research into microstructural benefits such as spatially controlled texture may be investigated to align the <100> direction with the magnetic flux direction. In the wider field, more electrical machines with 3D flux pathways will be investigated now that AM can provide freedom over the shape of the magnetic circuit. Topology

optimisation on a machine level is likely to provide fruitful developments. To be industrially relevant these machines must exhibit higher power density than current machines, with loss behaviour similar to current machines.

9 References

1. Wadie, Paul, Brunner, Conrad U. Energy-Efficiency Policy Opportunities for Electric Motor-Driven Systems [Internet]. 2011 May [cited 2020 Jun 17]. (IEA Energy Papers; vol. 2011/07). Report No.: 2011/07. Available from: https://www.oecd-ilibrary.org/energy/energy-efficiency-policy-opportunities-for-electric-motor-driven-systems_5kgg52gb9gjd-en

2. Sarlioglu B, Morris CT. More Electric Aircraft: Review, Challenges, and Opportunities for Commercial Transport Aircraft. IEEE Trans Transp Electrification. 2015 Jun;1(1):54–64.

3. Dilberoglu UM, Gharehpapagh B, Yaman U, Dolen M. The Role of Additive Manufacturing in the Era of Industry 4.0. Procedia Manuf. 2017 Jan 1;11:545–54.

4. Zhang B, Fenineche NE, Zhu L, Liao H, Coddet C. Studies of magnetic properties of permalloy (Fe–30%Ni) prepared by SLM technology. J Magn Magn Mater. 2012 Feb 1;324(4):495–500.

5. Zhang B, Fenineche NE, Liao H, Coddet C. Microstructure and Magnetic Properties of Fe–Ni Alloy Fabricated by Selective Laser Melting Fe/Ni Mixed Powders. J Mater Sci Technol. 2013 Aug 1;29(8):757–60.

6. Zhang B, Fenineche NE, Liao H, Coddet C. Magnetic properties of in-situ synthesized FeNi3 by selective laser melting Fe-80%Ni powders. J Magn Magn Mater. 2013 Jun 1;336:49–54.

7. Chaudhary V, Mantri SA, Ramanujan RV, Banerjee R. Additive manufacturing of magnetic materials. Prog Mater Sci. 2020 Oct 1;114:100688.

8. Fortunati S, Cicalé S, Schneider J, Franke A, Kawalla R. Developments in the Field of Electrical Steels over the Last Years. 2016.

9. Milewski JO. Additive Manufacturing of Metals [Internet]. Cham: Springer International Publishing; 2017 [cited 2022 Nov 29]. (Springer Series in Materials Science; vol. 258). Available from: http://link.springer.com/10.1007/978-3-319-58205-4

10. Travitzky N, Bonet A, Dermeik B, Fey T, Filbert-Demut I, Schlier L, et al. Additive Manufacturing of Ceramic-Based Materials. Adv Eng Mater. 2014;16(6):729–54.

11. ASTM 52900, 2015. Additive manufacturing, General principles, Terminology. ASTM International; 2015.

12. Ganguly S, Margel S. 3D printed magnetic polymer composite hydrogels for hyperthermia and magnetic field driven structural manipulation. Prog Polym Sci. 2022;131.

13. Khatri B, Lappe K, Noetzel D, Pursche K, Hanemann T. A 3D-printable polymer-metal soft-magnetic functional composite-development and characterization. Materials. 2018;11(2).

14. Bollig LM, Hilpisch PJ, Mowry GS, Nelson-Cheeseman BB. 3D printed magnetic polymer composite transformers. J Magn Magn Mater. 2017;442:97–101.

15. Bollig LM, Patton MV, Mowry GS, Nelson-Cheeseman BB. Effects of 3-D Printed Structural Characteristics on Magnetic Properties. IEEE Trans Magn. 2017 Nov;53(11):1–6.

16. Spaldin NA. Magnetic Materials: Fundamentals and Applications [Internet]. 2nd ed. Cambridge: Cambridge University Press; 2010 [cited 2023 Jul 8]. Available from:

https://www.cambridge.org/core/books/magnetic-materials/4C8C2C5DF32C9E8D528E1E8D26381C1F

17. Jiles D. Introduction to magnetism and magnetic materials [Internet]. Third edition. Boca Raton ; London ; New York: CRC Press is an imprint of the Taylor & Francis Group; 2016 [cited 2022 Nov 27]. Available from: https://ebookcentral.proquest.com/lib/sheffield/detail.action?docID=5338615

18. Krings A, Cossale M, Tenconi A, Soulard J, Cavagnino A, Boglietti A. Magnetic Materials Used in Electrical Machines: A Comparison and Selection Guide for Early Machine Design. IEEE Ind Appl Mag. 2017 Nov;23(6):21–8.

19. Boll, Richard. Soft Magnetic Materials. 3rd ed. Heyden & Sons Ltd; 1979. 353–353 p.

20. Ouyang G, Chen X, Liang Y, Macziewski C, Cui J. Review of Fe-6.5 wt%Si high silicon steel—A promising soft magnetic material for sub-kHz application. J Magn Magn Mater. 2019 Jul;481:234–50.

21. Garibaldi M, Ashcroft I, Simonelli M, Hague R. Metallurgy of high-silicon steel parts produced using Selective Laser Melting. Acta Mater. 2016;110(C):207–16.

22. Lemke JN, Simonelli M, Garibaldi M, Ashcroft I, Hague R, Vedani M, et al. Calorimetric study and microstructure analysis of the order-disorder phase transformation in silicon steel built by SLM. J Alloys Compd. 2017 Oct 25;722:293–301.

23. Garibaldi M, Ashcroft I, Lemke JN, Simonelli M, Hague R. Effect of annealing on the microstructure and magnetic properties of soft magnetic Fe-Si produced via laser additive manufacturing. Scr Mater. 2018 Jan 1;142:121–5.

24. JNEX product data [Internet]. Available from: https://www.jfe-steel.co.jp/en/products/electrical/catalog/f1e-002.pdf

25. Garibaldi M, Ashcroft I, Hillier N, Harmon SAC, Hague R. Relationship between laser energy input, microstructures and magnetic properties of selective laser melted Fe-6.9%wt Si soft magnets. Mater Charact. 2018 Sep 1;143:144–51.

26. Goll D, Schuller D, Martinek G, Kunert T, Schurr J, Sinz C, et al. Additive manufacturing of soft magnetic materials and components. Addit Manuf. 2019 May 1;27:428–39.

27. Plotkowski A, Pries J, List F, Nandwana P, Stump B, Carver K, et al. Influence of scan pattern and geometry on the microstructure and soft-magnetic performance of additively manufactured Fe-Si. Addit Manuf. 2019 Oct 1;29:100781.

28. Tiismus H, Kallaste A, Belahcen A, Vaimann T, Rassõlkin A, Lukichev D. Hysteresis Measurements and Numerical Losses Segregation of Additively Manufactured Silicon Steel for 3D Printing Electrical Machines. Appl Sci. 2020 Jan;10(18):6515.

29. Tiismus H, Kallaste A, Vaimann T, Rassõlkin A, Belahcen A. Electrical Resistivity of Additively Manufactured Silicon Steel for Electrical Machine Fabrication. In: 2019 Electric Power Quality and Supply Reliability Conference (PQ) 2019 Symposium on Electrical Engineering and Mechatronics (SEEM). 2019. p. 1–4.

30. Buchanan C, Matilainen VP, Salminen A, Gardner L. Structural performance of additive manufactured metallic material and cross-sections. J Constr Steel Res. 2017 Sep 1;136:35–48.

31. Plotkowski A, Carver K, List F, Pries J, Li Z, Rossy AM, et al. Design and performance of an additively manufactured high-Si transformer core. Mater Des. 2020 Sep 1;194:108894.

32. Tiismus H, Kallaste A, Belahcen A, Rassõlkin A, Vaimann T, Shams Ghahfarokhi P. Additive Manufacturing and Performance of E-Type Transformer Core. Energies. 2021 Jun 3;14:3278.

33. Stornelli G, Faba A, Schino A, Folgarait P, Ridolfi MR, Cardelli E, et al. Properties of Additively Manufactured Electric Steel Powder Cores with Increased Si Content. Materials. 2021 Mar 18;14:1489.

34. Urban N, Detrois J, Franke J. Correlation between Residual Stress, Building Angle and Illumination Parameters of Additive Manufactured FeSi6.5 and Mechanical and Magnetic Properties. In: 2020 10th International Electric Drives Production Conference (EDPC). 2020. p. 1–7.

35. Urban N, Bauch L, Armbruster R, Franke J. Evaluation of Soft Magnetic Ferrosilicon FeSi 6.5 for Laser Beam Melting. In: 2019 9th International Electric Drives Production Conference (EDPC). 2019. p. 8138–43.

36. Babuska TF, Wilson MA, Johnson KL, Whetten SR, Curry JF, Rodelas JM, et al. Achieving high strength and ductility in traditionally brittle soft magnetic intermetallics via additive manufacturing. Acta Mater. 2019;180:149–57.

37. Périgo EA, Jacimovic J, García Ferré F, Scherf LM. Additive manufacturing of magnetic materials. Addit Manuf. 2019;30.

38. Manninen A, Pippuri-Mäkeläinen J, Riipinen T, Lindroos T, Metsä-Kortelainen S, Antikainen A. The Mitigation of Eddy-Current Losses in Ferromagnetic Samples Produced by Laser Powder Bed Fusion. IEEE Access. 2022;10:115571–82.

39. Garibaldi M, Gerada C, Ashcroft I, Hague R. Free-Form Design of Electrical Machine Rotor Cores for Production Using Additive Manufacturing. J Mech Des [Internet]. 2019 Jul 1 [cited 2019 Oct 9];141(7). Available from: https://asmedigitalcollection.asme.org/mechanicaldesign/article/141/7/071401/727196/Free-Form-Design-of-Electrical-Machine-Rotor-Cores

40. Urban N, Masuch M, Paduch J, Franke J. An Approach to Eddy Current Reduction in Laser Powder Bed Fused High Silicon Steel Considering Manufacturing Influences. In: 2021 11th International Electric Drives Production Conference (EDPC). 2021. p. 1–5.

41. Koo B, Jang MS, Nam YG, Yang S, Yu J, Park YH, et al. Structurally-layered soft magnetic Fe-Si components with surface insulation prepared by shell-shaping selective laser melting. Appl Surf Sci. 2021 Jul 1;553:149510.

42. Andreiev A, Hoyer KP, Dula D, Hengsbach F, Haase M, Gierse J, et al. Soft-magnetic behavior of laser beam melted FeSi3 alloy with graded cross-section. J Mater Process Technol. 2021 Oct;296:117183.

43. Lindroos T, Riipinen T, Metsä-Kortelainen S, Pippuri-Mäkeläinen J, Manninen A. Lessons learnt - additive manufacturing of iron cobalt based soft magnetic materials. J Magn Magn Mater. 2022;563.

44. Lamichhane TN, Sethuraman L, Dalagan A, Wang H, Keller J, Paranthaman MP. Additive manufacturing of soft magnets for electrical machines—a review. Mater Today Phys. 2020 Dec 1;15:100255.

45. Pham T, Kwon P, Foster S. Additive Manufacturing and Topology Optimization of Magnetic Materials for Electrical Machines—A Review. Energies. 2021 Jan;14(2):283.

46. Naseer MU, Kallaste A, Asad B, Vaimann T, Rassõlkin A. A Review on Additive Manufacturing Possibilities for Electrical Machines. Energies. 2021 Jan;14(7):1940.

47. Tiismus H, Kallaste A, Rassõlkin A, Vaimann T. Preliminary analysis of soft magnetic material properties for additive manufacturing of electrical machines. Key Eng Mater. 2019;799 KEM:270–5.

48. Tiismus H, Kallaste A, Vaimann T, Rassõlkin A. State of the art of additively manufactured electromagnetic materials for topology optimized electrical machines. Addit Manuf. 2022 Jul 1;55:102778.

49. Urbanek S, Ponick B. Surface Eddy Current Loss Reduction in Additively Manufactured Permanent Magnet Rotor Active Parts. In: 2018 XIII International Conference on Electrical Machines (ICEM). 2018. p. 1317–22.

50. Urbanek S, Keuter R, Peter E, Ponick B. Effects of Continuous Rotor Skewing in Additively Manufactured Permanent Magnet Rotors. In: 2020 International Symposium on Power Electronics, Electrical Drives, Automation and Motion (SPEEDAM). 2020. p. 662–9.

51. Kresse T, Schurr J, Lanz M, Kunert T, Schmid M, Parspour N, et al. Additively Manufactured Transverse Flux Machine Components with Integrated Slits for Loss Reduction. Metals. 2022 Nov;12(11):1875.

52. Hayakawa Y. Mechanism of secondary recrystallization of Goss grains in grain-oriented electrical steel. Sci Technol Adv Mater. 2017 Jul 14;18(1):480–97.

53. Arai KI, Ishiyama K. Recent developments of new soft magnetic materials. J Magn Magn Mater. 1994 May 1;133(1):233–7.

54. Garibaldi M. Laser Additive Manufacturing of Soft Magnetic Cores for Rotating Electrical Machinery: Materials Development and Part Design. 2018 Dec;262.

55. Kustas AB, Susan DF, Johnson KL, Whetten SR, Rodriguez MA, Dagel DJ, et al. Characterization of the Fe-Co-1.5V soft ferromagnetic alloy processed by Laser Engineered Net Shaping (LENS). Addit Manuf. 2018 May 1;21:41–52.

56. Riipinen T, Metsä-Kortelainen S, Lindroos T, Keränen J, Manninen A, Pippuri-Mäkeläinen J. Properties of soft magnetic Fe-Co-V alloy produced by laser powder bed fusion. Rapid Prototyp J. 2019 May 13;25(4):699–707.

57. Mazeeva AK, Staritsyn MV, Bobyr VV, Manninen SA, Kuznetsov PA, Klimov VN. Magnetic properties of Fe–Ni permalloy produced by selective laser melting. J Alloys Compd. 2020 Jan 25;814:152315.

58. Li B, Fu W, Xu H, Qian B, Xuan F. Additively manufactured Ni-15Fe-5Mo Permalloy via selective laser melting and subsequent annealing for magnetic-shielding structures: Process, micro-structural and soft-magnetic characteristics. J Magn Magn Mater. 2020 Jan 15;494:165754.

59. Schönrath H, Spasova M, Kilian SO, Meckenstock R, Witt G, Sehrt JT, et al. Additive manufacturing of soft magnetic permalloy from Fe and Ni powders: Control of magnetic anisotropy. J Magn Magn Mater. 2019 May 15;478:274–8.

60. Gargalis L, Madonna V, Giangrande P, Rocca R, Hardy M, Ashcroft I, et al. Additive Manufacturing and Testing of a Soft Magnetic Rotor for a Switched Reluctance Motor. IEEE Access. 2020;8:206982–91.

61. Tiismus H, Kallaste A, Belahcen A, Tarraste M, Vaimann T, Rassõlkin A, et al. AC Magnetic Loss Reduction of SLM Processed Fe-Si for Additive Manufacturing of Electrical Machines. Energies. 2021 Jan;14(5):1241.

62. BSI. BS60404-6-2018 Methods of measurement of the magnetic properties of magnetically soft metallic and powder materials at frequencies in the range 20 Hz to 100 kHz by the use of ring specimens. British Standarad Instituion; 2018.

63. Chechik L, Christofidou KA, Markanday JFS, Goodall AD, Miller JR, West G, et al. Hardness variation in inconel 718 produced by laser directed energy deposition. Materialia. 2022 Dec 1;26:101643.

64. Mehdi M, He Y, Hilinski EJ, Kestens LAI, Edrisy A. The Origins of the Goss Orientation in Non-Oriented Electrical Steel and the Evolution of the Goss Texture during Thermomechanical Processing. Steel Res Int. 2019;90(7):1800582.

65. Williams HJ. Magnetic Properties of Single Crystals of Silicon Iron. Phys Rev. 1937 Oct 1;52(7):747–51.

66. Paltanea VM, Paltanea G, Gavrila H, Dumitru L. Experimental analysis of magnetic anisotropy in silicon iron steels using the single strip tester. In: 2015 9th International Symposium on Advanced Topics in Electrical Engineering (ATEE) [Internet]. Bucharest, Romania: IEEE; 2015 [cited 2021 Mar 15]. p. 456–9. Available from: http://ieeexplore.ieee.org/document/7133857/

67. Yonamine T, Landgraf FJG. Correlation between magnetic properties and crystallographic texture of silicon steel. J Magn Magn Mater. 2004 May;272–276:E565–6.

68. Magnetic Anisotropy | MTEX [Internet]. [cited 2022 Nov 11]. Available from: https://mtex-toolbox.github.io/MagneticAnisotropy.html

69. Wu W, Cao H, Ou H, Chen Z, Zhang X, Luo Z, et al. Effects of punching process on crystal orientations, magnetic and mechanical properties in non-oriented silicon steel. J Magn Magn Mater. 2017 Dec 15;444:211–7.

70. Bunge HJ. Texture Analysis in Materials Science: Mathematical Methods. Elsevier; 2013. 614 p.

71. Bunge H. Texture and Magnetic Properties. Textures Microstruct. 1989 Jan 1;11:75–91.

72. Landgraf F, Yonamine T, Takanohashi R, Silva QF, Tosetti J, Beneduce F, et al. Magnetic properties of silicon steel with as-cast columnar structure. J Magn Magn Mater - J MAGN MAGN MATER. 2003 Jan 31;254:364–6.

73. Roy R, Ghosh M, Panda A, Ghosh R, Mitra A. Development of rapidly solidified 6.5 wt% silicon steel for magnetic applications. Trans Indian Inst Met. 2010 Aug 1;63:745–50.

74. Amorim CO, Mohseni F, Dumas RK, Amaral VS, Amaral JS. A geometry-independent moment correction method for the MPMS3 SQUID-based magnetometer. Meas Sci Technol. 2021 Jul;32(10):105602.

75. Delfs P, Ťows M, Schmid HJ. Optimized build orientation of additive manufactured parts for improved surface quality and build time. Addit Manuf. 2016 Oct 1;12:314–20.

76. Kim JHKJH, Shin SCSSC. High Coercivity in Co/Pt Multilayers. Jpn J Appl Phys. 1996 Jan 1;35(1S):342.

77. Mercelis P, Kruth J. Residual stresses in selective laser sintering and selective laser melting. Rapid Prototyp J. 2006 Jan 1;12(5):254–65.

78. Toda Caraballo I, Chao J, Lindgren LE, Capdevila C. Effect of residual stress on recrystallization behavior of mechanically alloyed steels. 2010 Jan [cited 2022 Nov 15]; Available from: https://digital.csic.es/handle/10261/35935

79. Nishanth F, Bohach G, Nahin MM, Van de Ven J, Severson EL. Development of an Integrated Electro-Hydraulic Machine to Electrify Off-highway Vehicles. IEEE Trans Ind Appl. 2022;1–12.

80. Cao W, Mecrow BC, Atkinson GJ, Bennett JW, Atkinson DJ. Overview of Electric Motor Technologies Used for More Electric Aircraft (MEA). IEEE Trans Ind Electron. 2012 Sep;59(9):3523–31.

81. Zhang Z, Jhong KJ, Cheng C, Huang P, Tsai M, Lee W. Metal 3D printing of synchronous reluctance motor. In: 2016 IEEE International Conference on Industrial Technology (ICIT). 2016. p. 1125–8.

82. Huang PW, Jiang IH, Tsai MC, Chen GM. New Hybrid Stator Design for High-Speed PMSMS Based on Selective Laser Melting of 3-D Printing. IEEE Trans Magn. 2019 Jul;55(7):1–4.

83. Jiang Q, Zhang P, Yu Z, Shi H, Wu D, Yan H, et al. A Review on Additive Manufacturing of Pure Copper. Coatings. 2021 Jun;11(6):740.

84. Littmann M. Iron and silicon-iron alloys. IEEE Trans Magn. 1971 Mar;7(1):48–60.

85. Goll D, Schurr J, Trauter F, Schanz J, Bernthaler T, Riegel H, et al. Additive manufacturing of soft and hard magnetic materials. Procedia CIRP. 2020 Jan 1;94:248–53.

86. Freeman FSHB, Lincoln A, Sharp J, Lambourne A, Todd I. Exploiting thermal strain to achieve an in-situ magnetically graded material. Mater Des. 2019 Jan 5;161:14–21.

87. Yakout M, Elbestawi MA, Wang L, Muizelaar R. Selective laser melting of soft magnetic alloys for automotive applications. 2019 Sep;4.

88. Strecker Z, Kubík M, Vítek P, Roupec J, Paloušek D, Šreibr V. Structured magnetic circuit for magnetorheological damper made by selective laser melting technology. Smart Mater Struct. 2019 Apr;28(5):055016.

89. Pham TQ, Do TT, Kwon P, Foster SN. Additive Manufacturing of High Performance Ferromagnetic Materials. In: 2018 IEEE Energy Conversion Congress and Exposition (ECCE). 2018. p. 4303–8.

90. Yamaura S, Furuya Y, Watanabe T. The effect of grain boundary microstructure on Barkhausen noise in ferromagnetic materials. Acta Mater. 2001 Sep 3;49(15):3019–27.

91. Schneider CA, Rasband WS, Eliceiri KW. NIH Image to ImageJ: 25 years of image analysis. Nat Methods. 2012 Jul;9(7):671–5.

92. BS 60404-4 DC measurements [Internet]. [cited 2021 Jan 14]. Available from: https://bsol-bsigroup-com.sheffield.idm.oclc.org/Bibliographic/BibliographicInfoData/000000000030313864

93. Tumanski S. Handbook of Magnetic Measurements. CRC Press; 2016. 398 p.

94. Cullity BD, Graham CD. Introduction to Magnetic Materials. John Wiley & Sons; 2011. 684 p.

95. Beckley P. Electrical Steels for Rotating Machines. IET; 2002. 334 p.

96. Schoppa A, Delarbre P. Soft Magnetic Powder Composites and Potential Applications in Modern Electric Machines and Devices. IEEE Trans Magn. 2014 Apr;50(4):1–4.

97. Nishanth F, Verdeghem JV, Severson EL. Recent Advances in Analysis and Design of Axial Flux Permanent Magnet Electric Machines. In: 2021 IEEE Energy Conversion Congress and Exposition (ECCE). 2021. p. 3745–52.

98. Kascak P, Jansen R, Dever T, Nagorny A, Loparo DrK. Bearingless Five-Axis Rotor Levitation with Two Pole Pair Separated Conical Motors. In: 2009 IEEE Industry Applications Society Annual Meeting. 2009. p. 1–9.

99. Messager G, Binder A. Derivation of forces and force interferences in a double conical high-speed bearingless permanent magnet synchronous motor. In: 2017 IEEE International Electric Machines and Drives Conference (IEMDC). 2017. p. 1–8.

100. Wang Y, Lu J, Liu C, Lei G, Guo Y, Zhu J. Development of a High-Performance Axial Flux PM Machine With SMC Cores for Electric Vehicle Application. IEEE Trans Magn. 2019 Jul;55(7):1–4.

101. Sun S, Jiang F, Li T, Xu B, Yang K. Comparison of A Multi-Stage Axial Flux Permanent Magnet Machine With Different Stator Core Materials. IEEE Trans Appl Supercond. 2020 Jun;30(4):1–6.

102. Kim CW, Jang GH, Kim JM, Ahn JH, Baek CH, Choi JY. Comparison of Axial Flux Permanent Magnet Synchronous Machines With Electrical Steel Core and Soft Magnetic Composite Core. IEEE Trans Magn. 2017 Nov;53(11):1–4.

103. Tian G, Bi X. Study on the Si penetration into Fe sheets using PVD method and its application in the fabrication of Fe-6.5wt.% Si alloys. Surf Coat Technol. 2010 Jan 15;204(8):1295–8.

104. Siemens Digital Industries Software [Internet]. [cited 2022 Nov 27]. Simcenter MAGNET | Siemens Software. Available from: https://www.plm.automation.siemens.com/global/en/products/simcenter/magnet.html

105. Rashid MH. Power Electronics Handbook. Butterworth-Heinemann; 2017. 1510 p.

106. Cullity BD. Introduction to magnetic materials [Internet]. 2nd ed. Hoboken, N.J., Hoboken, N.J. ; Chichester: Wiley for IEEE, Wiley; 2009 [cited 2022 Jan 17]. xvii+544. Available from: http://www.vlebooks.com/vleweb/product/openreader?id=USheffield&isbn=9780470386316

107. Simpson N, Munagala SP, Catania A, Derguti F, Mellor PH. Functionally Graded Electrical Windings Enabled by Additive Manufacturing. In: 2022 International Conference on Electrical Machines (ICEM). 2022. p. 1477–83.

108. Zhu J, Zhou H, Wang C, Zhou L, Yuan S, Zhang W. A review of topology optimization for additive manufacturing: Status and challenges. Chin J Aeronaut. 2021 Jan 1;34(1):91–110.

109. Emmelmann C, Herzog D, Kranz J. 10 - Design for laser additive manufacturing. In: Brandt M, editor. Laser Additive Manufacturing [Internet]. Woodhead Publishing; 2017 [cited 2022 Mar 18]. p. 259–79. (Woodhead Publishing Series in Electronic and Optical Materials). Available from: https://www.sciencedirect.com/science/article/pii/B9780081004333000105

110. Singh R, Lee PD, Dashwood RJ, Lindley TC. Titanium foams for biomedical applications: a review. Mater Technol. 2010 Sep 1;25(3–4):127–36.

111. Mikler CV, Chaudhary V, Borkar T, Soni V, Jaeger D, Chen X, et al. Laser Additive Manufacturing of Magnetic Materials. JOM. 2017 Mar 1;69(3):532–43.

112. Yang X, Liu J, Cui X, Jin G, Liu Z, Chen Y, et al. Effect of remelting on microstructure and magnetic properties of Fe-Co-based alloys produced by laser additive manufacturing. J Phys Chem Solids. 2019 Jul 1;130:210–6.

113. Garibaldi M, Gerada C, Ashcroft I, Hague R, Morvan H. The Impact of Additive Manufacturing on the Development of Electrical Machines for MEA Applications: A Feasibility Study. In: MEA2015 More Electric Aircraft [Internet]. Toulouse, France; 2015 [cited 2022 Mar 18]. Available from: https://hal.archives-ouvertes.fr/hal-01178353

114. Zack GW, Rogers WE, Latt SA. Automatic measurement of sister chromatid exchange frequency. J Histochem Cytochem. 1977 Jul 1;25(7):741–53.

115. Mathworks. Matlab R2020a [Internet]. Mathworks; 2020. Available from: https://uk.mathworks.com/products/matlab.html

116. Ghanbarian B, Hunt AG, Ewing RP, Sahimi M. Tortuosity in Porous Media: A Critical Review. Soil Sci Soc Am J. 2013;77(5):1461–77.

117. Matyka M, Koza Z. How to Calculate Tortuosity Easily? AIP Conf Proc. 2012 Mar 26;1453:17–22.

118. ThermoFisher Scientific. Avizo 3D [Internet]. ThermoFisher Scientific; Available from: https://www.thermofisher.com/uk/en/home/electron-microscopy/products/software-em-3d-vis/avizo-software.html#applications

119. ThermoFisher Scientific. User's Guide Avizo Software 2019 [Internet]. ThermoFisher Scientific; 2019 [cited 2022 Jul 15]. Available from: https://assets.thermofisher.com/TFS-Assets/MSD/Product-Guides/users-guide-avizo-software-2019.pdf

120. ThermoFisher Scientific. Simulation-Based Tortuosity Estimation of Porous Media [Internet]. 2019. Available from: https://xtras.amira-avizo.com/xtras/simulation-based-tortuosity-estimation-of-porous-media

121. Oliveira JP, Santos TG, Miranda RM. Revisiting fundamental welding concepts to improve additive manufacturing: From theory to practice. Prog Mater Sci. 2020 Jan 1;107:100590.

122. Hoeganaes. AncorLam Materials Datasheet [Internet]. [cited 2022 Jul 6]. Available from: https://www.gknpm.com/globalassets/downloads/gkn-hoeganaes/pm-materials/engineered-solutions-for-pm/ancorlam.pdf/

123. JFE Steel Corporation. ELECTRICAL STEEL SHEETS [Internet]. [cited 2022 Jul 6]. Available from: https://www.jfe-steel.co.jp/en/products/electrical/catalog/f1e-001.pdf

124. JFE Steel Corporation. Super Core - Electrical steel sheets for high-frequency applicatoin [Internet]. [cited 2022 Jul 6]. Available from: https://www.jfe-steel.co.jp/en/products/electrical/catalog/f1e-002.pdf

125. Iron - binary phase diagrams. Berlin : Düsseldorf: Springer ; Verlag Stahleisen; 1982.

126. Seifert H, Jurisch M, Tobisch J, Oertel CG. Mechanical properties of Fe-4.5-6wt.%Si double roller ribbons. Mater Sci Eng A. 1991 Mar 15;133:292–6.

127. ULV #4 Ultra Low Viscosity Epoxy For Super Small Cracks [Internet]. [cited 2022 Oct 13]. Available from: https://nextstar.ca/shop/item.aspx/ulv-4-ultra-low-viscosity-epoxy-for-super-small-cracks/12/

128. Ouyang G, Jensen B, Tang W, Dennis K, Macziewski C, Thimmaiah S, et al. Effect of wheel speed on magnetic and mechanical properties of melt spun Fe-6.5 wt.% Si high silicon steel. AIP Adv. 2018 May;8(5):056111.